

UNIVERSITY OF SOUTHAMPTON

FACULTY OF ENGINEERING, SCIENCE AND MATHEMATICS

School of Chemistry

**PORPHYRIN-DNA AS A SCAFFOLD FOR
NANOARCHITECTURE AND NANOTECHNOLOGY**

by

ThaoNguyen Nguyen

Thesis for the degree of Doctor of Philosophy

May 2011

UNIVERSITY OF SOUTHAMPTON

ABSTRACT

FACULTY OF ENGINEERING, SCIENCE AND MATHEMATICS
SCHOOL OF CHEMISTRY

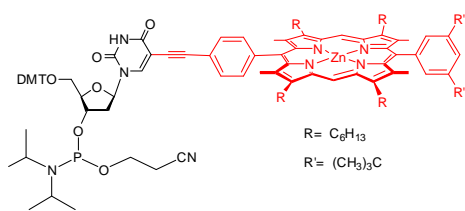
Doctor of Philosophy

PORPHYRIN-DNA AS A SCAFFOLD FOR NANOARCHITECTURE AND
NANOTECHNOLOGY

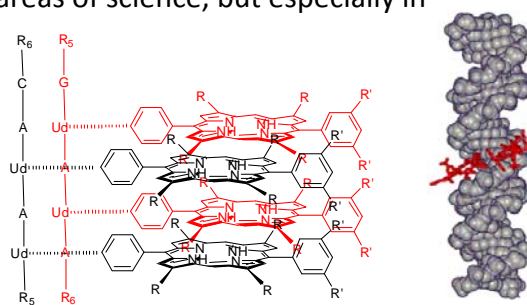
by ThaoNguyen Nguyen

Porphyrins, a substance class that can be found in diverse materials including green leaves and red blood cells, have been studied extensively over many years due to their potential industrial applications, *e.g.* in making optical electronic devices, in artificial photosynthesis or in sensors. In contrast, DNA has only recently been found to be a good scaffold for the construction of functional molecules. Combining the chemical properties of porphyrins and DNA could open the door to the production of multiporphyrin arrays using DNA as a scaffold; such materials could have multiple applications, an example being molecular electronic devices.

The work described in this thesis reports on further investigations of the synthesis of the porphyrin-nucleotide and its incorporation into DNA sequences, in order to study the structural, chemical and electronic properties of the porphyrin-modified DNA. The analytical results, obtained from employing a variety of techniques such as UV-vis and fluorescence spectroscopy, UV-vis and fluorescence melting studies, circular dichroism spectroscopy and EPR (electron paramagnetic resonance) spectroscopy showed electronic interaction between porphyrins stacked on DNA. Metallation with zinc or copper of different porphyrins (namely diphenyl porphyrins and tetraphenyl porphyrins) was also successfully achieved, after they had been attached onto DNA. Based on EPR measurements, evidence was found for intermolecular stacking of the porphyrin-DNA which leads to self-assembled higher order structures. The EPR investigation also demonstrated that different oxidation states of metals held inside porphyrin-DNA could be monitored. Using CD spectroscopy based on a synchrotron light source, the first measurements were made of DNA in the far UV region (< 200 nm). All the results obtained in this work and elsewhere during the past few years show that DNA based materials are highly promising for future applications in many areas of science, but especially in electronics and health care.



Porphyrin-nucleotide



Porphyrin-DNA

CONTENTS

Abstract	iii
Contents	v
Declaration of authorship	ix
Acknowledgements	xiii
Abbreviations	xv
DNA nomenclature	xxi
CHAPTER 1: INTRODUCTION	1
1.1 DNA in nanotechnology	1
1.1.1 Structures of DNA	1
1.1.1.1 Basic components of DNA	1
1.1.1.2 Hydrogen-bonding in DNA	2
1.1.1.3 Double helix DNA	3
1.1.2 Synthesis of DNA	6
1.1.2.1 Reactivity of DNA	6
1.1.2.2 DNA automated solid-phase synthesis	9
1.1.3 DNA as scaffold in supramolecular chemistry	11
1.1.4 DNA: From supramolecular chemistry template to a scaffold for nanotechnology	15
1.1.4.1 The origin of nanotechnology	15
1.1.4.2 DNA: From building block of life to building block for nanostructures	17
1.1.4.3 Applications of DNA in nanotechnology	21
1.2 Porphyrin-DNA as a scaffold for nanoarchitecture	26
1.2.1 Structures and properties of porphyrins	26
1.2.2 Porphyrins in supramolecular chemistry	30
1.2.3 Porphyrin modified DNA in nanotechnology	34
1.3 Project aims	39

CHAPTER 2: SYNTHESIS AND CHARACTERISATIONS OF PORPHYRIN-DNA	43
2.1 Synthesis of the 5'-O-DMT-dU^{ZnDPP} phosphoramidite 1	43
2.1.1 Synthesis of 3-hexylpentane-2,4-dione 3a	44
2.1.2 Synthesis of hexyl substituted dipyrromethane 7	45
2.1.3 Synthesis of protected zinc diphenyl-substituted porphyrin 9	46
2.1.4 Synthesis of 5'-O-DMT-dU ^{ZnDPP} 13 via formation of deprotected zinc diphenyl-substituted porphyrin 12	47
2.1.5 Synthesis of monomer 5'-O-DMT-dU ^{ZnDFP} phosphoramidite 1	48
2.2 Incorporation of porphyrin building block onto DNA and purifications	49
2.2.1 Automated solid-phase DNA synthesis	49
2.2.2 Purification methods for oligonucleotides	52
2.2.2.1 Fluorous affinity purification of oligonucleotides	52
2.2.2.2 Nap-5 purification of oligonucleotides	53
2.3 Post-synthetic metallations of porphyrin-DNA	54
2.3.1 Zinc metallation of porphyrin-DNA	54
2.3.2 Copper metallation of porphyrin-DNA	56
2.4 RP-HPLC analysis of oligonucleotides	59
2.5 Conclusion	68
CHAPTER 3: PHYSICOCHEMICAL ANALYSES OF PORPHYRIN-DNA	69
3.1 UV-vis measurements of porphyrin-DNA	69
3.1.1 Theory of UV-vis spectroscopy	69
3.1.2 UV-vis spectra of porphyrin-DNA	70
3.2 Fluorescence emission measurements of porphyrin-DNA as a complementary tool to UV-vis spectroscopy	74
3.2.1 Theory of fluorescence emission spectroscopy	74
3.2.2 Fluorescence emission spectra of porphyrin-DNA	77

3.3	UV-vis temperature and melting profiles of porphyrin-DNA arrays	82
3.3.1	UV-vis temperature profiles of porphyrin-DNA single strands	82
3.3.2	UV-vis melting profile of porphyrin-DNA double strands	83
3.3.3	UV-vis melting profiles of porphyrin-DNA mismatched double strands	86
3.4	Fluorescence temperature and melting profiles of porphyrin-DNA arrays	89
3.5	Circular dichroism (CD) analysis of porphyrin-DNA	92
3.5.1	Theory of circular dichroism spectroscopy	92
3.5.2	Circular dichroism spectra of porphyrin-DNA	94
3.5.2.1	CD spectroscopy of porphyrin-DNA measured with the Chirascan spectrophotometer	94
3.5.2.2	CD spectroscopy of porphyrin-DNA measured with the Olis DSM20 spectrophotometer	103
3.5.3	Circular dichroism of DNA as a function of time	107
3.6	Native PAGE of oligonucleotides	109
3.7	Conclusion	112

CHAPTER 4: ELECTRON PARAMAGNETIC RESONANCE (EPR) INVESTIGATION OF PORPHYRIN-DNA COMPLEXES

		115
4.1	Introduction to EPR	115
4.1.1	Basic principles of EPR	116
4.1.2	EPR parameters	120
4.1.3	“Forbidden” transitions in EPR	123
4.1.4	Components of EPR spectrometer	123








4.2	EPR results and discussion	125
4.2.1	EPR study of copper porphyrin building blocks	126
4.2.1.1	Copper porphyrin building blocks preparation for EPR	127
4.2.1.2	Fine powder measurements of CuDPP and CuTPP	128
4.2.1.3	Fluid solution measurements of CuDPP and CuTPP	131
4.2.1.4	Frozen solution measurements of CuDPP and CuTPP	137
4.2.1.5	Spectral simulations of frozen solution CuDPP and CuTPP	141
4.2.1.6	Interpretation of EPR spectra of copper porphyrin	143
4.2.1.7	EPR binding study of CuDPP	145
4.2.2	EPR study of porphyrin-DNA	149
4.2.2.1	Early EPR study and synthesis of CuDPP-DNA	150
4.2.2.2	EPR study of porphyrin-DNA single strands	154
4.2.2.3	EPR study of porphyrin-DNA double strands	157
4.2.2.4	EPR study of porphyrin-DNA dilutions	159
4.2.2.5	EPR spectral interpretation of porphyrin-DNA	161
4.2.2.6	Distance calculation of porphyrin-DNA by EPR	168
4.3	Conclusion	172
4.4	Future work	174

CHAPTER 5: EXPERIMENTAL	177
5.1 General synthetic procedures	177
5.2 Analytical experiments	178
5.2.1 NMR spectroscopy	178
5.2.2 EPR spectroscopy	178
5.2.3 UV-vis spectroscopy	179
5.2.4 UV-vis melting studies	181
5.2.5 Fluorescence emission spectroscopy	181
5.2.6 Fluorescence emission melting studies	181
5.2.7 Circular dichroism spectroscopy	182
5.2.8 Mass spectrometry	183
5.2.9 Analytical HPLC	183
5.2.10 Gel electrophoresis	184
5.3 DNA syntheses and purifications	185
5.3.1 DNA solid phase synthesis	185
5.3.2 DNA hybridisation	185
5.3.3 DNA purifications	185
5.3.3.1 Fluorous affinity purification of oligonucleotides	186
5.3.3.2 Nap-5 purification of oligonucleotides	188
5.3.3.3 Poly-pak II purification of oligonucleotides	188
5.3.3.4 Glen-pak purification of oligonucleotides	190
5.3.4 Solvents for DNA chemistry	191
5.4 Experimental procedure	192
REFERENCES	215

DECLARATION OF AUTHORSHIP

I, ThaoNguyen Nguyen declare that the thesis entitled “Porphyrin-DNA as a scaffold for nanoarchitecture and nanotechnology” and the work presented in the thesis are both my own, and have been generated by me as the result of my own original research.

I confirm that:

-  this work was done wholly or mainly while in candidature for a research degree at this University;
-  where any part of this thesis has previously been submitted for a degree or any other qualification at this University or any other institution, this has been clearly stated;
-  where I have consulted the published work of others, this is always clearly attributed;
-  where I have quoted from the work of others, the source is always given. With the exception of such quotations, this thesis is entirely my own work;
-  I have acknowledged all main sources of help;
-  where the thesis is based on work done by myself jointly with others, I have made clear exactly what was done by others and what I have contributed myself;
-  parts of this work have been published as:

1. Title: Duplex Stabilization and Energy Transfer in Zipper Porphyrin-DNA,

Author(s): Nguyen, TN.; Brewer, A.; Stulz, E.*

Source: Angewandte Chemie-international edition Volume: 48 Issue: 11 Pages:
1974-1977 Published: 2009

2. Title: Supramolecular helical porphyrin arrays using DNA as a scaffold

Author(s): Bouamaied, I.; Nguyen, TN.; Rühl, T.; Stulz, E.*

Source: Organic & BioMolecular Chemistry Volume: 6 Issue: 21 Pages: 3888-3891
Published: 2008

Signed:

Date:

ACKNOWLEDGEMENTS

At first, I would like to acknowledge Dr. Eugen Stulz for his supervision, guidance and support towards my study for the degree of Doctor of Philosophy at the University of Southampton.

With the oversight of my main supervisor, editorial advice has been sought from Prof. Bernard Albert Goodman (Guangxi University, China). No changes of intellectual content were made as a result of this advice. I would also like to express my gratitude to the editor for his effort.

Thanks are due to Thomas J. Bandy, Ashley Brewer, Michele Carboni, Jonathan R. Burns, Dr. Gabriella Marth, Daniel Singleton, who are members of the Stulz group for help and for making my PhD experience an enjoyable one; in particular to past members Dr. Imenne Bouamaied for sharing her experience on porphyrin synthesis and Dr. Simon R. Gerrard for advices on general practical experiments and moral support.

I wish to show appreciation towards my collaborators for EPR study at the EPSRC EPR National Service centre, University of Manchester, namely Prof. Eric McInnes, Dr. Joanna Wolowska, Daniel Sells, and especially to Prof. David Collison for his invaluable expertise and Dr. Ruth Edge for her training, patience and countless sample measurements. With this, I extend the acknowledgements to Dr. Par Hakansson (University of Southampton), Prof. Tatsuhisa Kato (Josai University), Dr. Olav Schiemann (University of St. Andrew) for external advices on the subject of EPR; and especially to Prof. Bernard Albert Goodman (Guangxi University, China) for his scientific mentoring and for introducing the technique.

Acknowledgements for the CD training are attributed to Dr. Giuliano Siligardi, Dr. Rohanah Hussain, and Dr. Daniel Myatt at Beamline 23, Diamond Synchrotron.

Many thanks to Dr. Ali Tavassoli for his support and advice towards my thesis corrections. I am thankful for the assistance from the mass spectrometry staff (Dr. John Langley, Ms. Julie Herniman) and the NMR spectroscopy staff (Dr. Neil Wells), Mrs. Joan Street at the School of Chemistry, University of Southampton.

I would like to acknowledge Dr. Dorcas Brown (ATD Bio), Prof. Tom Brown (University of Southampton), and his group members for their help with DNA synthesis and for letting me use their laboratory instruments. Special thanks are for Dr. Nittaya Gale and Dr. Afaf El-Sagheer for teaching me gel electrophoresis.

I am immensely grateful for the advices and supports from Prof. Gerard Bodeker (University of Oxford) and my friends (Helen Brown, Dr. Charlotte Coles, Maxie Roessler, Keziah Jacombs), and especially Dr. Asha Brown for giving me the encouragements and strength that are required to complete a PhD.

Last but not least, I would like to thank the EPSRC for funding this PhD study and show my appreciation to Dr. Josephine M. Peach (University of Oxford), to whom without early supervision, I may not have started the PhD.

ABBREVIATIONS

The following abbreviations are used throughout this report.

Structural

A	Adenine
C	Cytosine
Cu	Copper
CuDPP	Copper(II) ditert-butyl diphenyl porphyrin
CuTPP	Copper(II) acetylene tetraphenyl porphyrin
DMT	4,4-dimethoxytrityl
DNA	<i>Deoxyribo-Nucleic Acid</i>
DPP	Diphenyl-substituted porphyrin
dU	Modified iodouracile nucleoside
Et	Ethyl
G	Guanine
Me	Methyl
N	Nitrogen
P	Porphyrin derived molecule
R	Alkyl
T	Thymine
TPP	Tetraphenyl-substituted porphyrin
Zn	Zinc

Solvents

CHCl ₃	Chloroform
DCM	Dichloromethane
DMF	<i>N,N</i> -dimethyl formamide
DME	1,2-Dimethoxyethane
EDTA	ethylenediamine tetra acetate
Et ₂ O	Diethyl ether

EtOAc	Ethyl acetate
H ₂ O	Water
HOAc	Acetic acid
MeCN	Acetonitrile
MeOH	Methanol
PbOAc ₄	Lead (IV) acetate
THF	Tetrahydrofuran

Reagents

APS	Ammonium persulphate
CuI	Copper iodide
Cu(OAc) ₂ ·H ₂ O	Copper(II) acetate monohydrate
DDQ	2,3-dichloro-5,6-dicyano-1,4-benzoquinone
EDTA	Ethylenediaminetetraacetic acid
FAM	Carboxyfluorescein
H ₂	Hydrogen gas
HCl	Hydrochloric acid
HFIP	Hexafluoroisopropanol
K ₂ CO ₃	Potassium carbonate
LiAlH ₄	Lithium aluminium hydride
MgCl ₂	Magnesium dichloride
MgSO ₄	Magnesium sulphate
NaHCO ₃	Sodium hydrogen carbonate
NaI	Sodium iodide
NaNO ₂	Sodium Nitrite
NaOMe	Sodium methoxide
Na ₂ SO ₄	Sodium sulphate
NEt ₃	Triethyl amine
Pd/C	Palladium on carbon
TBE	Tris-borate-EDTA
TEA	Triethylamine

TEAA	Triethylammonium acetate
TFA	Tetrafluoro acetic acid
TMED	Tetramethylethylenediamine
Zn(OAc) ₂ ·2H ₂ O	Zinc(II) acetate dihydrate

Experimental

A	A-value
Å	Angstrom
Abs.	Absorbance
AFM	Atomic force microscopy
aniso	Anisotropic
aq.	Aqueous
a.u.	Arbitrary unit
br	Broad
C	Concentration
°C	Degree Celsius
CD	Circular Dichroism
conc.	Concentrated
d	Doublet
dd	Doublet of doublets
dt	Doublet of triplets
δ _H	Hydrogen chemical shift
ds	Double strand
ε	Molar extinction coefficient
<i>E</i>	Energy
Emis	Emission
EPR	Electron paramagnetic resonance
eq.	Equivalence
ESI	Electron spray ionisation
g	g-value
G	Gauss
GHz	Giga Hertz

h	Hours
h	Planck constant
hfs	Hyperfine structure
Hz	Hertz
iso	Isotropic
J	Coupling constants
k	Kilo
K	Kelvin
I	Transmitted intensity
I_0	Incident intensity
l	Path length
m	Metre
m	Multiplet
M	Mega
M	Molecular mass
MALDI-ToF	Matrix-assisted Laser Desorption Ionisation Time-of-Flight
max	Maximum
μL	Micro litre
μmol	Micro mole
μM	Micro molar
mL	Milli litre
min	Minutes
mmol	Milli mole
mM	Milli molar
mp	Melting point
MS	Mass spectrometry
mW	Milli Watt
m/z	Mass/charge ratio
n	Nano
nmol	nanamole

NMR	Nuclear magnetic resonance
Norm.	Normalised
PAGE	Polyacrylamide gel electrophoresis
PCR	Polymerase chain reaction
ppm	Parts per million
quin	Quintet
rel. int.	Relative intensity
rf	Reference on TLC plate
RP-HPLC	Reverse Phased-High Performance Liquid Chromatography
r.t.	Room temperature
s	Singlet
shfs	Superhyperfine structure
ss	Single strand
STM	Scanning tunnelling microscopy
t	Triplet
<i>T</i>	transmittance
TLC	Thin layer chromatography
T_m	Melting temperature of duplex
T_p	Turning point of single strand
UV-Vis	Ultraviolet visible spectroscopy
ν	Frequency
V	Voltage

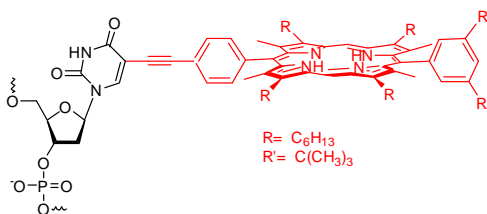
Other

Lit.	Literature
RP	Reverse phase
approx.	Approximate

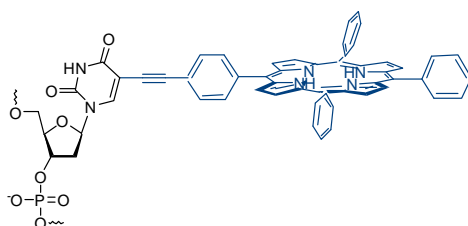
DNA NOMENCLATURE

ODN1	5'-CAT CGT AGT TTT PAP TTT TCC GTA CTC-3'
ODN2	5'-CAT CGT AGT APA PAP APA TCC GTA CTC -3'
ODN3	5'-GAG TAC GGP APA CCG TAC TC-3'
ODN4	5'-TAC GAT TCG TPT CTA GCT AGC-3'
ODN5	5'-GAG TAC GGA AAA ATA AAA ACT ACG ATG-3'
ODN6	5'-GAG TAC GGA TAT ATA TAT ACT ACG ATG-3'
ODN7	5'-GAG TAC GGT ATA CCG TAC TC-3'
ODN8	5'- CAT CGT AGP APA PAP APA PCC GTA CTC-3'
ODN9	5'-GAG TAC GGA PAP APA PAP ACT ACG ATG-3'
ODN10	5'-GAG TAC GGA AAA ATA AAA ACT ACG ATC-3'
ODN11	5'-GAT CGT AGT TTT TAT TTT TCC GTA CTC-3'
ODN12	5'-TAC GAT TCG AAA CTA GCT AGC-3'
ODN13	5'-GAG TAC GGA AAA APA AAA ACT ACG ATC-3'
ODN14	5'-GAT CGT AGT TTT PAP TTT TCC GTA CTC-3'
ODN15	5'-GCT AGC TAG PPP CGA ATC GTA-3'
ODN16	5'-CAT CGT AGT ATA PAT ATA TCC GTA CTC-3'
ODN17	5'-CAT CGT AGT TTT PAP TTT TCC GTA CTC-3'
ODN18	5'-CAT CGT AGT ATP PAT ATA TCC GTA CTC-3'
ODN19	5'-CAT CGT AGT ATA TAT ATA TCC GTA CTC -3'
ODN20	5'- FAM GAG TAC GGA TAT ATA TAT ACT ACG ATG-3'

P = dU^{DPP}



P = dU^{TPP}



A similar list of oligonucleotides is provided as an A3 attachment at the back of the thesis. Herein the red colour illustrates diphenyl porphyrin, whilst the blue colour illustrates tetraphenyl porphyrin.

CHAPTER 1: INTRODUCTION

1.1 DNA in nanotechnology

As one of the most important discoveries in modern science, the Nobel prize winning elucidation of the deoxyribonucleic acid (DNA) double helix structure in 1953 by Watson, Crick, Wilkins and Franklin¹⁻³ has helped to understand the fundamental importance of DNA in life. It has also laid the foundation for 21st century nanotechnology research based on DNA. This thesis describes the preparation and characterisation of a new class of nano-materials based on modified DNA, namely porphyrin-DNA, which has potential use in future nano-architecture, using DNA as a supramolecular scaffold.

1.1.1 Structures of DNA

1.1.1.1 Basic components of DNA

DNA contains the genetic information of every living organism. It exists as polymers consisting of nucleotide monomers, each of which is made from three components: a heterocyclic base, a sugar and a phosphate ester.

The four heterocyclic bases found in DNA belong to two aromatic families of monocyclic pyrimidines and bicyclic purines.

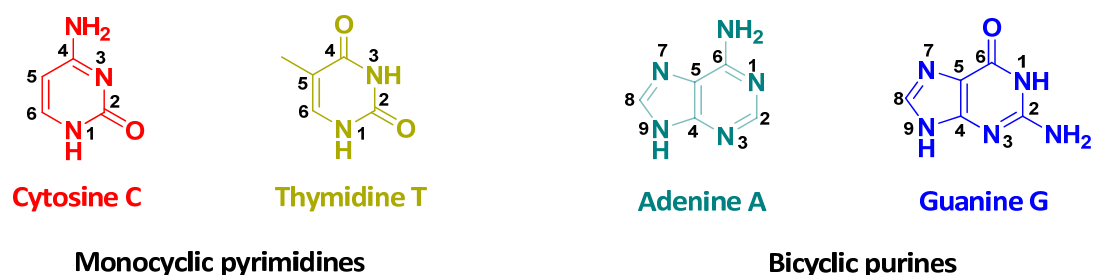


Figure 1.1: Molecular structures of heterocyclic bases in DNA.

Nucleotide is the collective term used to describe the base-sugar-phosphate unit, whereas a **nucleoside** is one which lacks a phosphate ester. The sugar is a ribose in

the case of RNA, and 2'-deoxy ribose in the case of DNA, hence the naming of ribonucleic acid and deoxyribonucleic acid. The nucleosides are connected *via* the phosphate diester from the 3'-OH to the 5'-OH groups. **Figure 1.2** shows the structure of a short DNA chain.⁴ By convention, a DNA chain is written in the order of 5' to 3'.

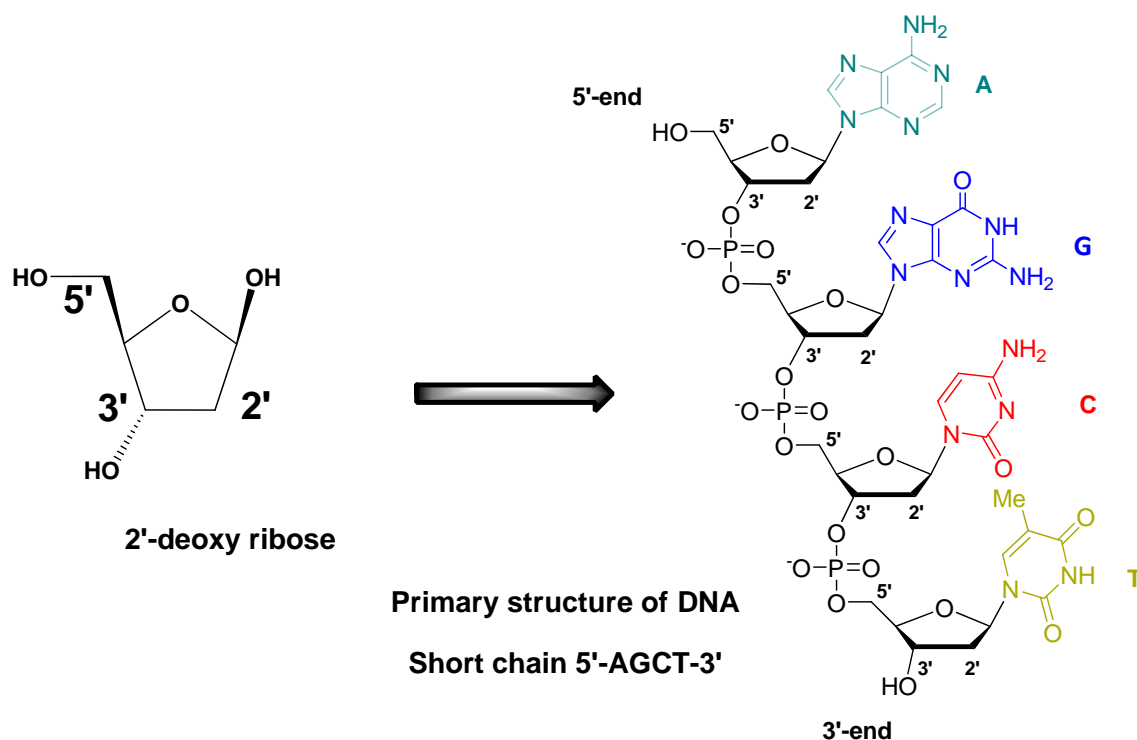


Figure 1.2: Structures of 2'-deoxy ribose sugar and 2'-Deoxyribo-Nucleic Acid.

1.1.1.2 Hydrogen-bonding in DNA

The existence of N-H groups, which are good hydrogen donors, and C=O or C=N-groups, which are good hydrogen acceptors in the heterocyclic bases enables hydrogen bonding between the bases, and hydrogen bonding results in adenine (A) pairing with thymidine (T) and guanine (G) pairing with cytosine (C) due to the matching donor-acceptor configuration (**Figure 1.3**). Along with factors such as base stacking and the chirality of the ribose, A-T and C-G base-pairings contribute to the double helical twists in DNA.⁵

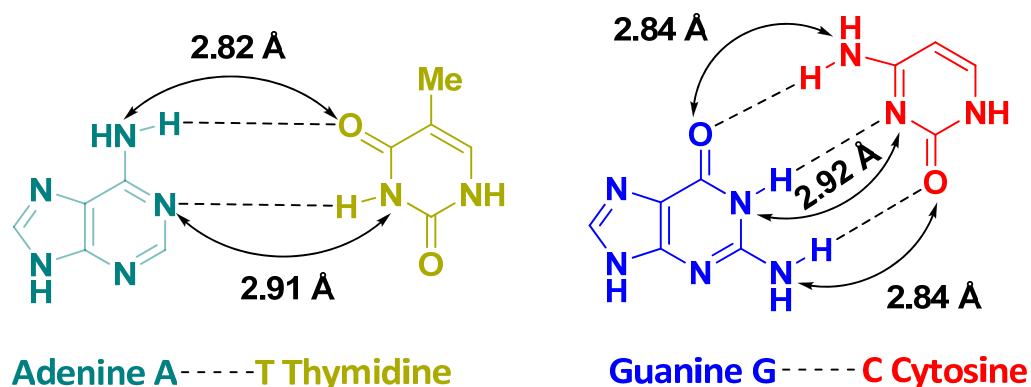


Figure 1.3: Base pairings through hydrogen bondings.⁶

1.1.1.3 Double helix DNA

Using the X-ray diffraction results of Franklin and Wilkins,⁷ Watson and Crick proposed the double stranded helix for with the two DNA strands being held together *via* A-T and C-G base-pairings. Also, as earlier suggested by Franklin, Watson and Crick proposed that the two strands must run in opposite directions to allow the phosphate groups to be exposed to water whilst the bases are held inside the helix. This means one strand runs from 5' to 3' whereas its complementary strand follows the 3' to 5' direction. DNA double helices are primarily *right-handed* helices, which exist in an A-form in high salt concentration (*i.e.* low humidity) and a B-form in low salt concentration (*i.e.* high humidity).⁷ Another Z-form of DNA is, however, *left-handed*. The A-form of the helix is also the predominant form of RNA duplexes.

B-DNA is by far the most common form of duplexes found in biological systems. Two important features of B-DNA are the minor and major grooves, which provide primary positions for DNA modification, binding sites for proteins, and surfaces for chemicals and drug interactions. **Figure 1.4** shows a presentation of an idealised B-type DNA double helix structure in solution. Each helical turn completes a 360° rotation, and the basic terminology and parameters of B-DNA in solution are illustrated in **Figure 1.4**. These are:

- *Residues per turn*: There are 10.5 base pairs in one complete helical rotation.
- *Axial rise*: The distance between adjacent base pairs is 3.4 Å.
- *Twist angle*: The angle between two adjacent base pairs is 34.3°.
- *Helix pitch*: The length of a complete duplex helical turn is 35.7 Å.
- *Diameter of the helix*: The width of the helix is 20 Å.⁶

In contrast to B-type DNA, the A-type conformation is found in less hydrophilic conditions (*i.e.* in dry DNA). The grooves in A-DNA are not as deep as in B-DNA, the base pairs are stacked more towards the outside of the helix and are more tilted relative to the axis of the helix. Each helical turn of A-DNA consists of 11 base pairs of 28 Å in length. The axial rise of 2.56 Å is shorter than in B-DNA, and the base is 4.5 Å away from the helical axis.

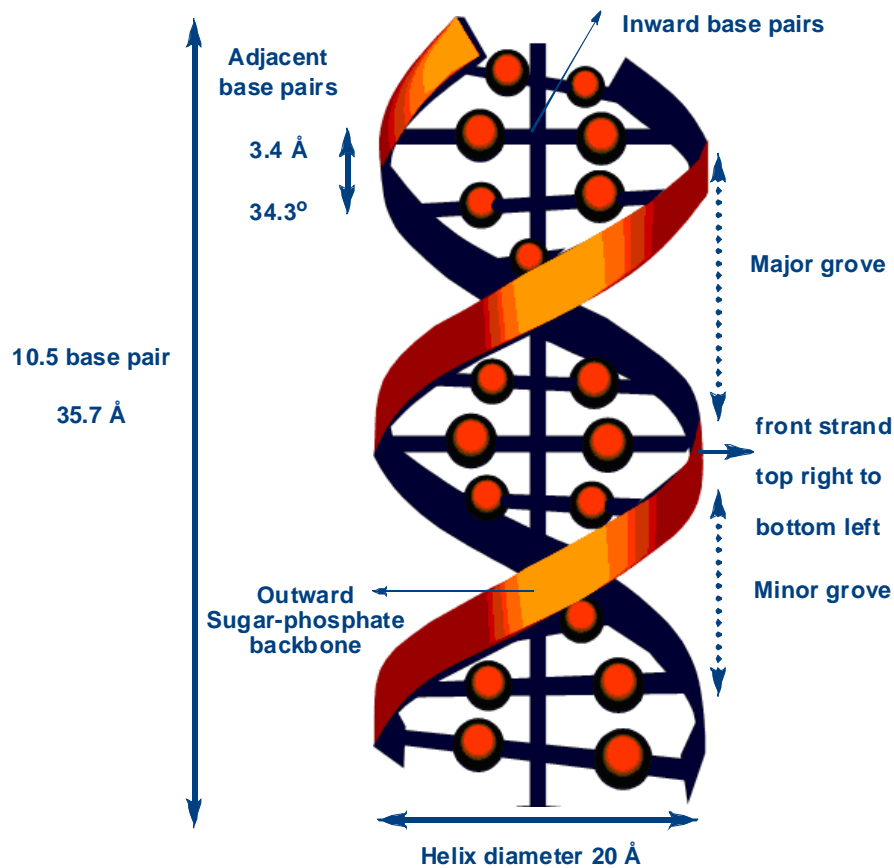


Figure 1.4: A diagrammatic representation of the B-type DNA double helix structure in solution.

In the presence of high salt concentration (*i.e.* 4 M NaCl),⁸ or in ethanol, DNA duplexes may change from the *right-handed* B-form to the *left-handed* Z-form DNA. Although the widely adopted Z-structure in alternating G-C sequences still has two anti-parallel strands with the base pairs governed by Watson-Crick hydrogen bonds, there are many structural differences between these two forms. Firstly, the name Z-DNA is derived from the zig-zag arrangement of the phosphate backbones, instead of a smooth curvature found in B-DNA. Secondly, the Z-helix diameter of 18 Å is shorter than in the B-helix. Thirdly, each Z helical turn consists of 12 base pairs compared to 10.5 in B-DNA. Finally, but importantly, the grooves in Z-DNA are of opposite order to those in B-DNA. Thus the minor groove is deep, but the major groove is much more shallow and is usually not a good target for bonding.^{6,7} The *right-handed* conformation of DNA means the strand which is at the front of the duplex coils from top right to bottom left direction (**Figure 1.5**), whereas the duplex

front strand coils from top left to bottom right in the *left-handed* conformation. Collectively, all of the A, B and Z-forms of DNA duplexes are known as the secondary structures of DNA.

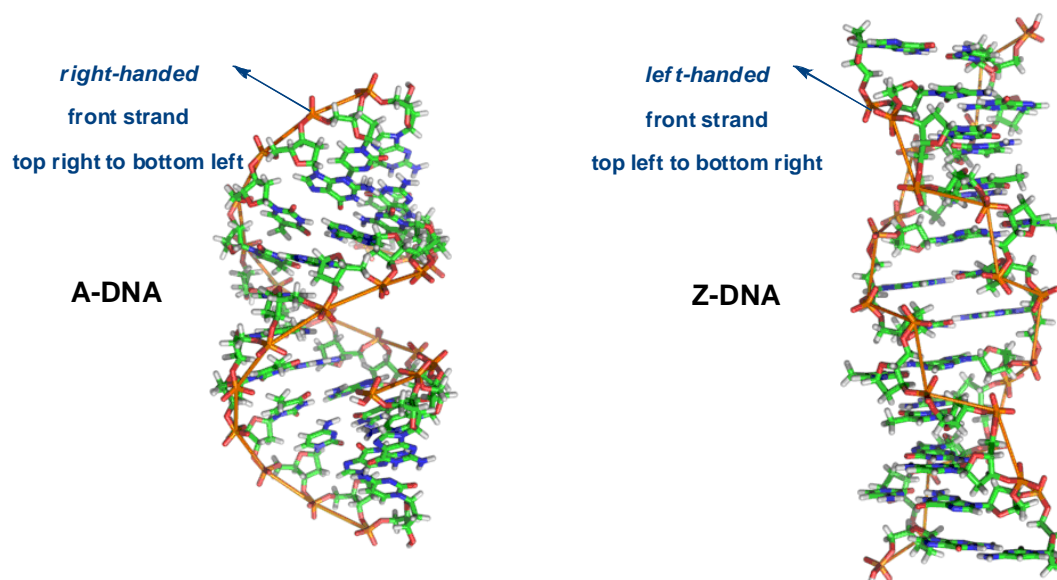


Figure 1.5: Representations of the A-form (left) and Z-form (right) of DNA duplexes.⁹

There are around three billions base pairs in every cell, and the natural twists of DNA into helical forms, together with further size reduction through formation of chromatin complexes with histones (protein-DNA complexes) to form chromosomes, improve their spatial arrangement efficiently to fit into a cell.¹⁰ Knowledge of the behaviour of DNA at the molecular level is important for understanding the origin of life, the molecular details that distinguish different forms of life, and the ability of different life forms to adapt to different environments.

1.1.2 Synthesis of DNA

1.1.2.1 Reactivity of DNA

The sequences of oligonucleotides that make up the primary structure of DNA (**Figure 1.2**) can be replicated synthetically in the lab. Using an automated solid-phase DNA synthesiser, the nucleosides are connected *via* phosphodiester

bridges which link the 3'-hydroxyl group that carries the phosphate derivative to the 5'-hydroxyl group of the neighbouring nucleoside to form an oligonucleotide. Unlike natural DNA synthesis which proceeds in a 5' to 3' direction, chemical synthesis of DNA is carried out in the opposite 3' to 5' direction.^{11, 12}

Both the 3'- and 5'-OH groups of riboses are active nucleophiles, so one must be protected to allow selective phosphorylation of the remaining group. Whilst one nucleotide has its 5'-OH site protected by dimethoxytrityl (DMT) (**Figure 1.6.**), the other is protected at its 3'-OH position, as in the example of the synthesis of a dinucleotide. Coupling between the 3' and 5' positions then joins these two nucleotide and nucleoside *via* the phosphodiester linkage to form a fully protected dinucleotide monophosphate.¹³ The 5'-DMT group in the dinucleotide is then cleaved to allow coupling to more nucleoside units.



Figure 1.6: Illustration of the DMT protecting group on the 3' and 5' positions of ribose sugars.

The phosphorus reactive species which is used for the coupling reaction is a phosphoramidite. This P(III) group is electrophilic and reacts with the 5'-OH, which is the nucleophile. The oxygen on the phosphoramidite needs to be protected in order to prevent side reactions, and protecting groups such as chlorophenyl derivatives or 2-cyanoethyl, are used to produce the corresponding protected phospho-triester or phosphate-triester (**Figure 1.7**) after oxidation to P(V). Also, H-phosphonate is sometimes used as a protected phosphate, since the proton on the backbone is inert.

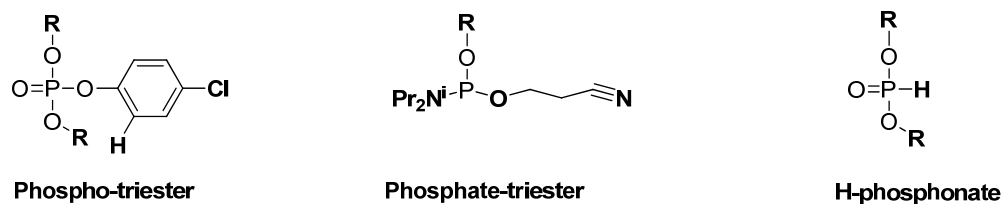


Figure 1.7: Examples of protected phosphate backbones in DNA synthesis.

With the exception of thymidine, the exocyclic amino groups on adenine, cytosine and guanine nucleobases are naturally nucleophilic. Therefore they need to be protected during DNA synthesis. Commonly, benzoyl protecting groups are chosen to protect the NH_2 on adenine and cytosine, whilst isobutyryl is used for guanine (Figure 1.8).

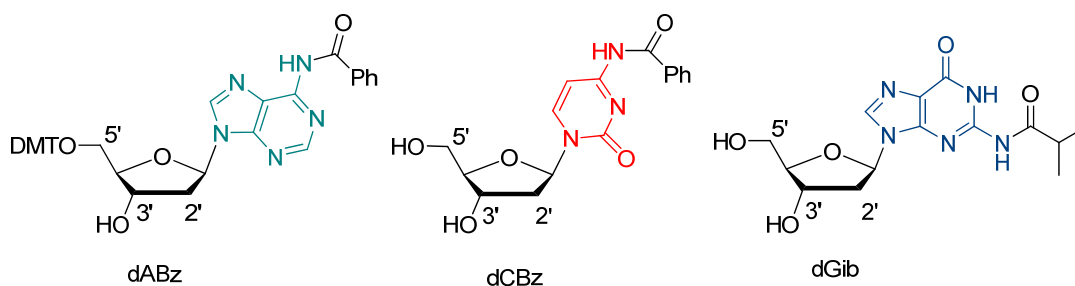


Figure 1.8: Protected nucleobases in DNA synthesis.

Generally, a nucleotide has many reactive sites, but the DNA is tolerable to many harsh conditions such as strong acid or base. However, the DNA can also degrade by long exposure to strong acids and bases, where depurination (loss of G or A nucleobase) or phosphodiester hydrolysis can occur.¹⁴ The reaction conditions must be tuned for use in DNA synthesis. These include alkaline and acid hydrolysis of nucleobase and phosphate protecting groups and of the DMT group, respectively, nucleophilic displacement during the coupling, and oxidation of P(III) to P(V). Although it is possible to synthesise DNA under these reaction conditions with manual coupling between 3'-phosphate and 5'-OH groups, the process is too labour intensive for routine use. Most notably, column chromatography is required for purification after every single coupling. Hence today this solution coupling method is simply impractical for synthesis of long chain DNA with more than 2-3

monomers, and current methods for oligonucleotide synthesis are optimised automatically by solid-phase synthesis, developed by Caruthers and Merrifield, for which Merrifield received the 1984 Chemistry Nobel prize.¹⁵

1.1.2.2 DNA automated solid-phase synthesis.¹⁵

Using an automated solid-phase synthesiser (**Figure 1.9**), it is now possible to create long oligonucleotide chains in a short time with little effort. The method uses a solid support to which nucleotides are bound firmly, and this is held inside a reaction column so that solvents and reagents can pass through and react efficiently. The support is made from insoluble particles of 50-100 microns diameter derived from materials such as controlled pore glass or polystyrene, and to which nucleotides are bound covalently with a base labile linker. The advantages of DNA automated solid-phase synthesis over solution synthesis are immense because:

- Reactions take place on solid resins so time is saved on purification. There is no remaining reagent or by-product after each monomer coupling step because all excess reagents and impurities are washed away from the reaction column.
- Excess amounts of reagents can be used to accelerate reactions.
- The method can be computer-controlled and automated for the production of designed DNA sequences.
- Because every step is automated, creating DNA chains requires little labour. It is also safer than manual syntheses, since reactions can be performed in a sealed and safe environment.



Figure 1.9: Expedite[™] automated solid-phase DNA synthesiser (left) and reaction column (right).

Further discussion of all the steps involved in DNA automated solid-phase synthesis are presented later in the **Chapter 2, Section 2.2.1**.

The synthesis and modification of DNA are of extremely high value to research in the life sciences, because the availability of particular oligonucleotide sequences enables scientists to study functions of nucleic acids in chemistry, biology, biomedical and forensic sciences. For example, AZT (zidovudine), one of the best-known anti-retroviral drugs used to suppress HIV replication, is a modified thymidine (*i.e.* 3'-azidothymidine, **Figure 1.10**). Combining AZT with a modified cytosine (*i.e.* lamivudine 3-TC, **Figure 1.10**),^{4,16} which is an anti-viral drug against AZT-resistant viruses, yielded success in AIDS therapy in the 1990s.

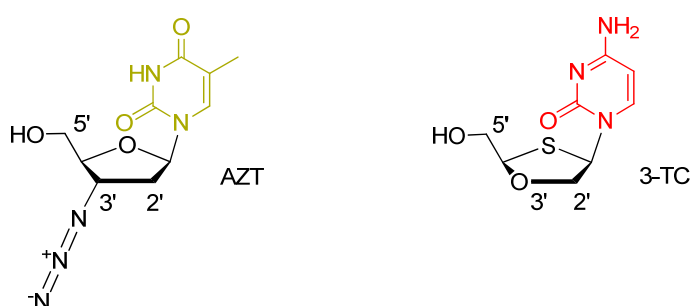


Figure 1.10: Examples of synthetic modified nucleosides with biomedical applications.

The developments in automated solid-phase synthesis of DNA have contributed towards designing novel oligonucleotides with new modifications to help open doors for studies in non-genetic related DNA applications. Thanks to the ease of making DNA strands on automated system in the last two decades, the idea of using DNA in nanotechnology has been extensively developed.

1.1.3 DNA as scaffold in supramolecular chemistry

Advances in DNA research mean that chemists can now make oligonucleotides with almost any desired modification, provided that the chemical reactions at the sites of modification are compatible with the chemistry of DNA synthesis. Strategies for DNA modifications vary, depending on the type of functional molecules attached but they mainly cover:

- (i) *Functionalisations at 3' and 5' termini* (e.g. **Figure 1.11**), which involves attaching a new functional group directly onto the 5' position of the ribose ring (Mokhir *et al.*)¹⁷ or *via* a phosphitylated entity that carries the functional group (Balaz *et al.*)¹⁸ Although less practical, modifications at the 3' terminus can be achieved with post-synthetic coupling at the phosphitylated 3' site (Mukae *et al.*)¹⁹ in addition to direct addition of functional groups, analogous to 5' methodology.²⁰

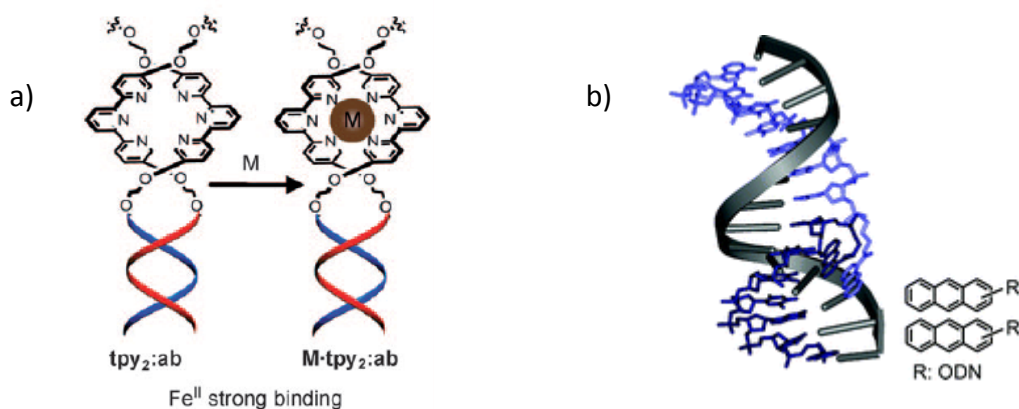


Figure 1.11: Examples of DNA end-modifications at a) 5' functionalisation with terpyridine²¹ and b) 3' functionalisation with anthracene.¹⁹

(ii) *Internal modification of DNA* is a methodology which involves changes within the base pairings stacked inside the duplex (e.g. **Figure 1.12**).

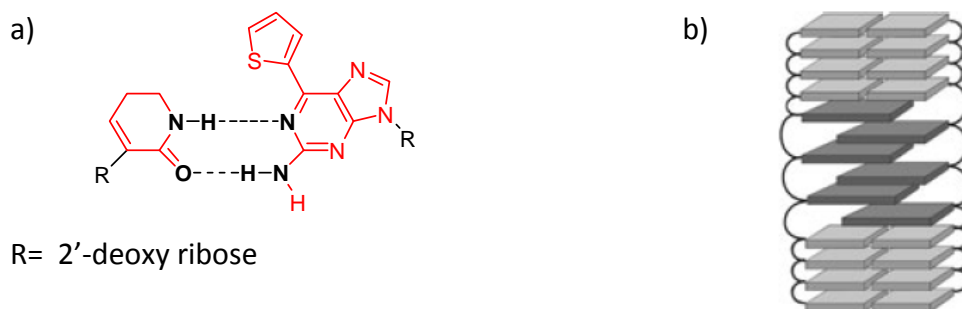


Figure 1.12: Internal modification with new nucleobases a) and zipper stacking between strands b).²²

Replacement of natural nucleobases by artificial moieties on the 1' site of the ribose ring can result in the formation of artificial base pairs with the availability to form non-covalent bonds between two single strands, and the corresponding nucleobases may stack on top of each other in a zipper manner.²³ In addition, self assembly of DNA duplexes with internally chelated metals has been reported.^{24, 25} Removal of a section of oligonucleotides and substitution with modifications is another example of how double strands can be functionalised internally.²⁶

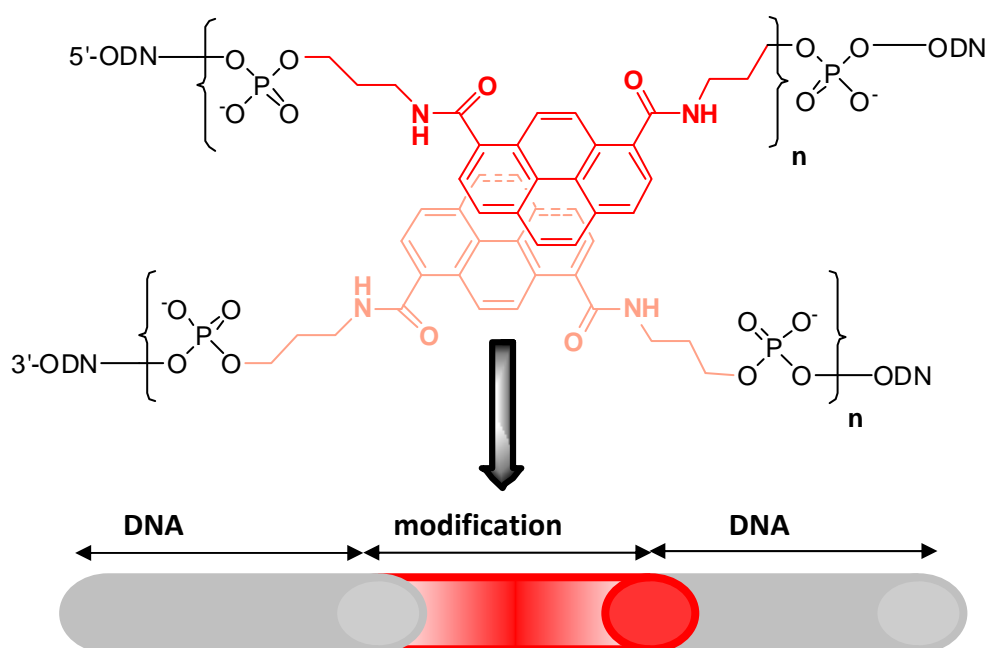


Figure 1.13: Example of DNA substituted with an internal modification.

(iii) *External modifications of DNA.* Functionalisation of nucleic acids can also occur on the outside of the helix,²⁰ and this strategy was applied in the present project. It takes advantages of the natural DNA grooves, which provide excellent attachment sites for a variety of compounds, such as porphyrins, pyrenes, bipyridines, terpyridines, etc. Usually the major groove is chosen as the location for external attachment of substituents, simply because of its larger size which can accommodate both small and bulky substituents. Often the modifications are attached to the thymidine T nucleoside prior to polymerisation on an automated solid-phase DNA synthesiser, because this particular nucleobase does not require protecting groups. Sonogashira cross-coupling with an alkynyl functionalised molecule²⁷ is commonly used for attaching functional molecules onto iodinated bases.²⁰

Choosing a specific position for modification on a nucleobase is an important synthetic strategy because of its effect on the DNA structure once it is incorporated into the duplex. For example, Vrabel *et al.*²⁸ showed that modification at the 7-position of a 7-deaza purine-5'-O-triphosphate is preferred over the 8-position (**Figure 1.14**). The latter provides a poor substrate for DNA polymerases due to enhanced steric hindrance in the DNA backbone: the substituent at the 8-position points directly into the phosphate diester group. This has very negative consequences for both PCR synthesis and duplex stability, which is avoided when the substituent is attached to the 7-position. Besides chelation of metals such as copper, mercury and iron to the duplex internally,^{24, 25, 29} metal complexes of $[\text{Ru}(\text{bpy})_3]^{2+}$ and $[\text{Os}(\text{bpy})_3]^{2+}$ can be attached externally through linkage to the nucleobase. Whilst C(7) is the favoured site for modification on bicyclic purines, C(5) is the preferred location for functionalised monocyclic pyrimidines.³⁰ The triphosphates of these modified nucleotides provide good substrates for enzymatic DNA synthesis *via* PCR.

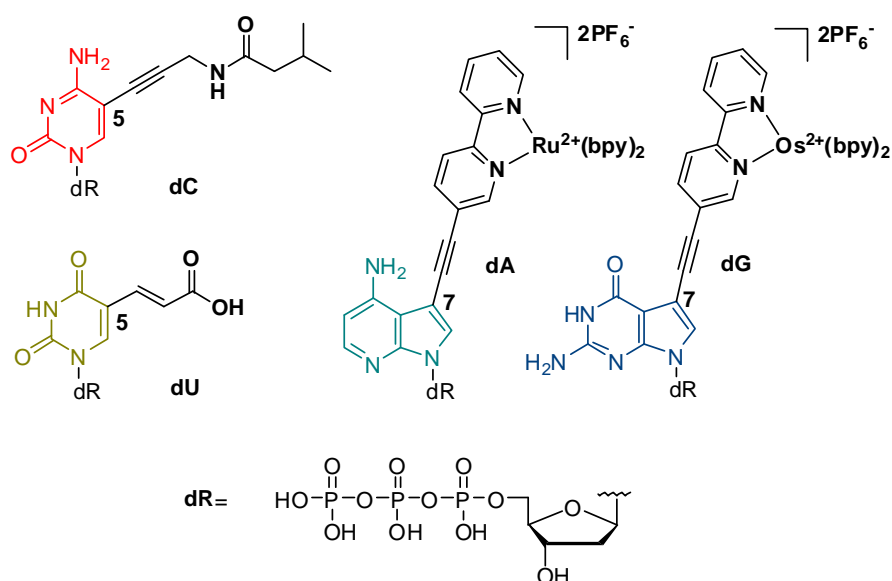


Figure 1.14: Functionalisation of A, C, G, T nucleobases on external DNA modifications.³⁰

Regarding the modification of nucleosides, Barbaric and Wagenknecht,³¹ Stulz *et al*,³² and Datta and Schuster³³ have shown that fluorophores can be covalently connected to DNA and aligned within the major groove to form a helical array of stacked chromophores (**Figure 1.15**). Again, the 5-position of thymidine³² or cytosine³¹ are the most commonly used sites for modifications. The stability of the resulting array depends on whether the chromophores are attached to one strand only, or to both complementary strands in an alternating fashion; the later leads to external zipper arrays. For example, zipper-like stacking of pyrenes does not greatly reduce the stability of duplexes, and has the advantage of maintaining the integrity of the system.³¹ Hydrophobic substituents such as porphyrins tend to destabilise the DNA duplex if attached to one strand only, despite evidence from CD spectroscopy and molecular modelling³⁴ that the structure is not greatly altered.

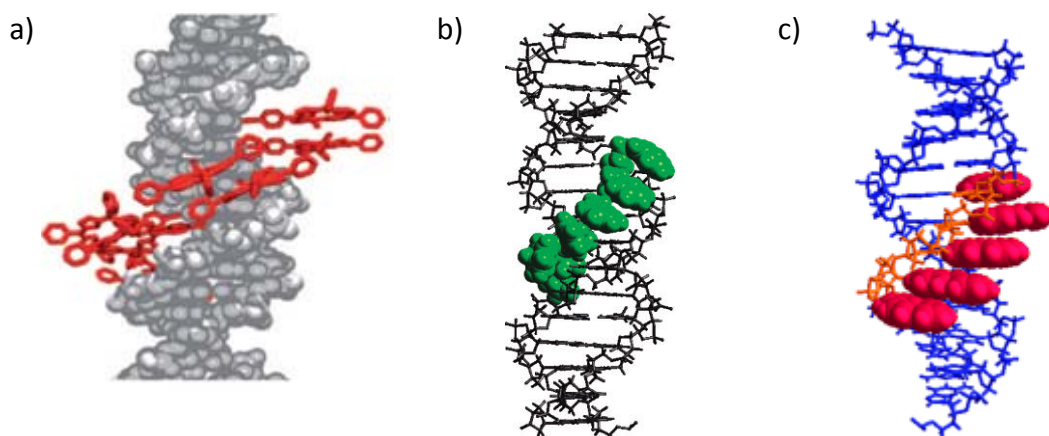


Figure 1.15: Calculated externally modified structures of a) porphyrin-DNA,³⁵ b) aniline-DNA³³ and c) pyrene-DNA.³⁶

The above DNA chemistry illustrates the diversity and versatility of these naturally existing molecules. Alterations of DNA structures are now highly sophisticated and double helical strands can be used to scaffold a variety of functional molecules. Thus DNA can be used as a novel template for supramolecular chemistry and nanoscience.

1.1.4 DNA: From supramolecular chemistry template to a scaffold for nanotechnology.

1.1.4.1 The origin of nanotechnology

Nanotechnology is an area of science that focuses on the design, characterisation and application of objects with dimensions on the nanometre scale (the length at which fingernails grow per second). Nano-materials can be in a variety of forms (nanocrystals, nanowires, nanotubes, *etc.*) that can self-assemble to create larger arrays. Attention to this concept was first drawn by Richard Feynman, whose famous quotation “*there is plenty of room at the bottom*”^{37,38} underlines the *top-down* (*i.e.* large-downward) approach, where larger components are used for the miniaturization of smaller objects (*e.g.* in using laser techniques to make microchips).^{39,40} The opposite approach, labelled as the *bottom-up* (*i.e.* small-upward) approach, is the study of items at the molecular level with atomic

precision that can then build up to become part of a bigger nanostructure, such as crystal growth.^{38,40} Thus, DNA can play a crucial role in *bottom-up* nanotechnology.⁴¹

Developments in nanotechnology have expanded rapidly with the arrival of sophisticated techniques for the characterisation and manipulation of molecules at the atomic level (*e.g.* STM, AFM and chemical synthesis). In addition to being used to construct devices such as nanowires and nanochips for the next generation of electronic gadgets, nanotechnology is now being used in many areas of science, such as energy and environment (*e.g.* water monitoring for quality control) and healthcare and life sciences (*e.g.* for drug delivery, gene therapy and point-of-care diagnostics). **Figure 1.16** shows examples of the impact of nanoscience on our daily life, with emphasis on silver nanotechnology.

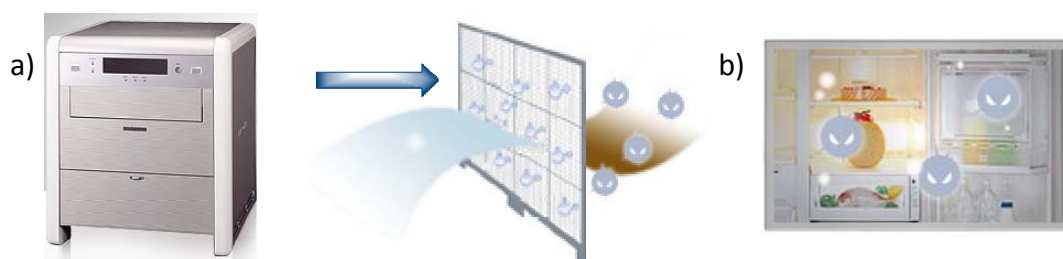


Figure 1.16: Ag^+ particles used in Samsung silver nanotechnology for a) air purifier to kill germs that pass through the silver ions filter and b) refrigerator to inhibit germ respiration on the compartment walls (figure courtesy of Samsung).

Nanotechnology research in the healthcare and life science area is currently attracting high levels of investment in the UK, particularly in diagnostic and therapeutic treatments, and there is increasing demand for systems which can assemble nanostructures for interdisciplinary applications. Since DNA is a naturally occurring biological template in which structures are measured in nanometres, it is an ideal candidate for such applications. Because of their fast automated solid-phase synthesis, DNA with versatile modifications to meet different needs can

be produced on a larger scale, and perhaps most importantly, its unique double helix structure can self-assemble into various nanostructures.

1.1.4.2 DNA: From building block of life to building block for nanostructures

DNA, often known as the building block of life, has been studied extensively at the molecular levels by scientists over the past decades as a future nanotechnology toolbox. These naturally existing molecules have been explored for uses in multidisciplinary areas, from curing diseases to the next class of electronic devices.

As proposed by Seeman,⁴¹ the DNA double helix structure (**Figure 1.17**) can, for example, be self-assembled into cages to hold molecules that are incorporated into the structure in a fixed orientation, thus having the same order as crystals. In addition, DNA can be used as a scaffold for chromophores, and therefore it has uses for molecular electronic devices, such as nanosensors, bio-molecular computers and other electronic devices with nanometre-scale precision. These devices could be used for parts of molecular robots to detect and cure diseases, creating electrically conductive narrow wires, forming crucial moving parts of nanomachines, and providing a template for new types of polymer.^{42, 43}

One of the most important elements which a system must possess for the construction of small scale products, is an ability to branch into three dimensions. The specificity of Watson-Crick DNA base-pairing, induced by hydrogen bonding, offers an excellent strategy to design specific sequences, so that they can be connected selectively through hybridisation to form extended DNA grids with 4 arm junctions. It is worth noting that branched DNA also exists in living cells and advances in DNA synthesis in the 21st century has enabled scientists to mimic design from nature to fashion artificial DNA networks. Seeman *et al.*⁴¹ first created a 2-D DNA crystal, which itself is a junction made from 4 duplexes, each attached with a sticky end (**Figure 1.17 a**). Each sticky end is a short single strand extended beyond the duplex and maybe programmed to complement to another sticky end on a neighbouring duplex, in order to interconnect different DNA junctions and thus form a DNA grid-like structure (**Figure 1.17 b**). Based on this principle of sticky end

self-assembly, construction of 3-D cube-like DNA, taking advantages of cyclic interlocking single strands, has become a reality (**Figure 1.17 c**).

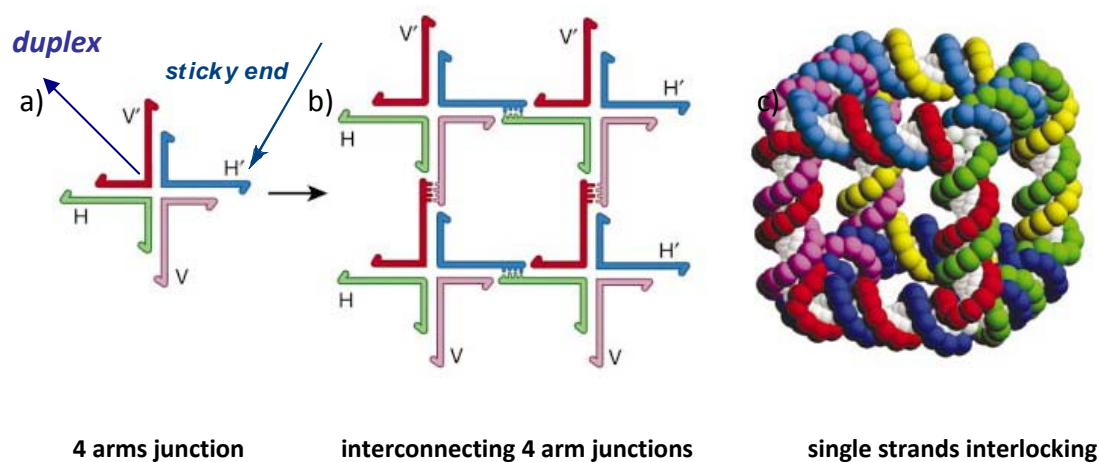


Figure 1.17: Self-assembly of DNA into a) and b) 2-D grid-like and c) 3-D cube-like structures.⁴¹

Major advances have now been made since the establishment of DNA self-assembly as a viable procedure. More complicated DNA networks have been built on the original 4 arms junction idea by the groups of Yan and Labean, who have reported nanofabrication of four 4 arm-branched junctions (*i.e.* 4 x 4 tiles) perpendicular to one another. Each of these 4 x 4 tiles contains 9 strands, in which one strand contributes to all four junctions (**Figure 1.18**). With the participation of sticky ends, these 4 x 4 DNA nanogrids can further interlink to form a more rigid DNA lattice, which could then be used as a scaffold to facilitate the self-assembly of other nano components. The cavity in the middle of the grid also has the potential to function as a drug binding site.⁴⁴

Being a key component in the bottom-up approach to nanotechnology, the application of DNA technology continues to surprise us with its ability to construct well-defined and elaborate macromolecular structures from a miniature model. Work by Liu *et al.*⁴⁵ illustrates how a complicated DNA nanotube can be designed from just a single DNA sequence.

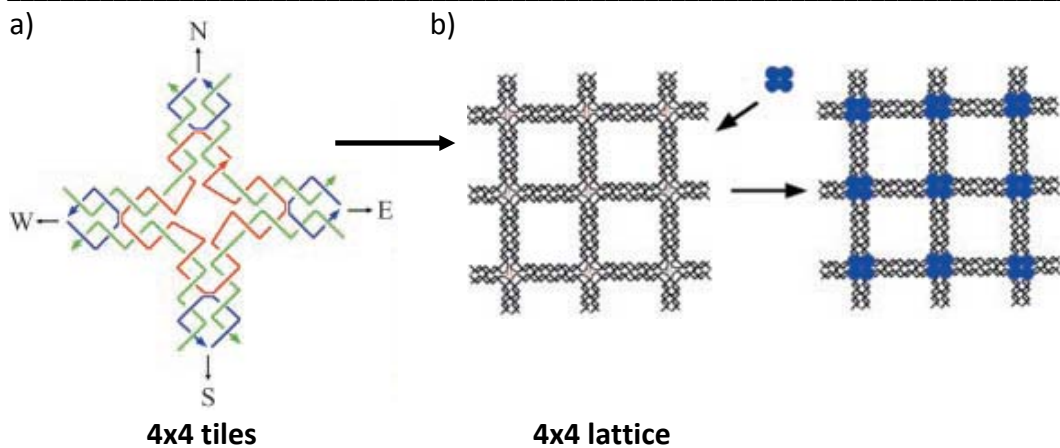


Figure 1.18: DNA self-assembly 2-D structures of a) four 4 x 4 tiles made from four 4 arm junctions, and b) a rigid 4 x 4 tile lattice.⁴⁴

By synthesising a 52-mer single strand, which is divided into four segments (each of which is a part-palindromic sequence and therefore can form duplexes with itself in well defined sections), it is possible to form larger building blocks based on double strand complexes (as shown in **Figure 1.19 b**) with sticky ends. As with other DNA self-assembled structures, these sticky ends control the associations of double strand complexes into a flexible 2-D lattice through hybridisation of these overhang single strands (**Figure 1.19 c**). Subsequently, the 2-D lattice folds over to form a 3-D DNA nanotube consisting of multiple interlocked strands. There is speculation that once a small section of the nanotube is hybridised, the rest just self-assembles to elongate the tube. The DNA nanotube (**Figure 1.19 d**) is of 20–45 nm in diameter and up to 60 μm long, which makes it suitable for nano-scaffolding.

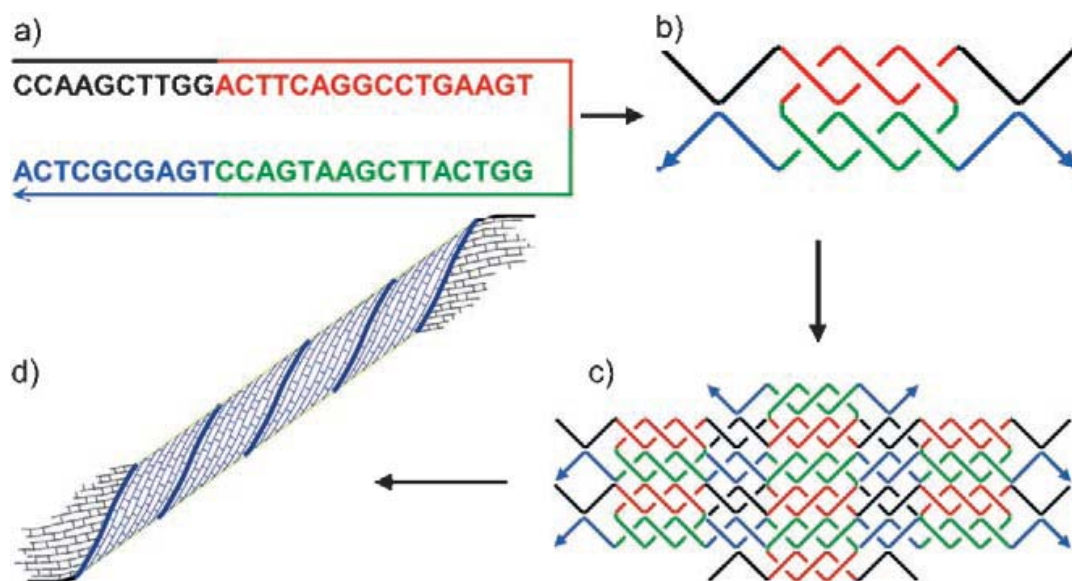


Figure 1.19: Self-assembly of DNA from a) self-complementary single strand to b) duplex complex with sticky ends to c) 2-D lattice to d) 3-D DNA nanotube.⁴⁵

Research on supramolecular fabrication from nano sized DNA is now referred to as DNA origami technology, an innovative research field that was voted by Chemistry World to be one of the six Chemistry cutting edges in 2009.⁴⁶ Most notable is the 3-D DNA crystal⁴⁷ X-ray crystallography data that revealed 3 duplexes hybridised into a 3-D tensegrity triangle. The sticky ends then linked each unit to other DNA triangles to construct a well-organised lattice. The result is a macromolecular crystal with dimensions of 0.25 mm (**Figure 1.20**).

Recent progress in DNA origami technology has helped to fulfil Seeman's 30-year-old dream of obtaining a crystalline DNA lattice. Thus the branching of DNA into nanotechnology is no longer just a vision, but a reality, which is expected to have major scientific impacts in the current century.^{41, 42}

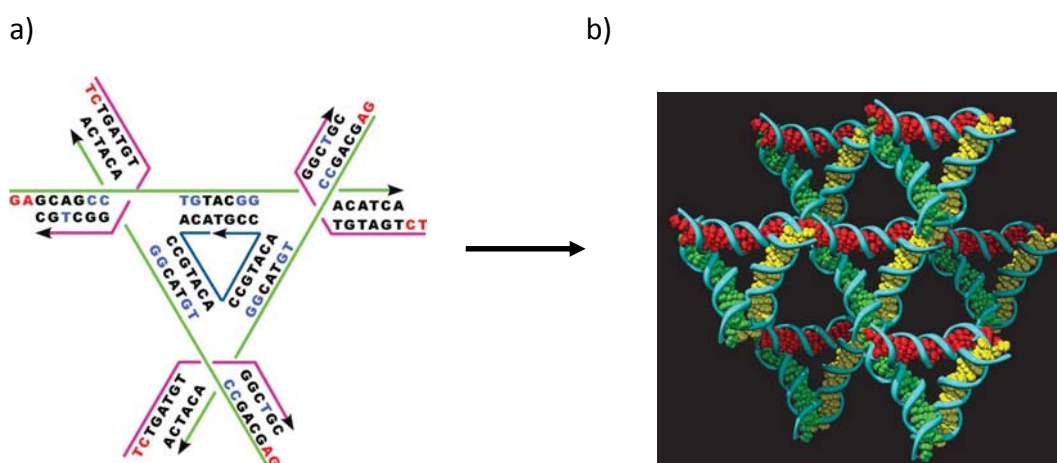


Figure 1.20: a) DNA tensegrity triangle self-hybridises to form b) a lattice of DNA tensegrity triangles.⁴⁷

1.1.4.3 Applications of DNA in nanotechnology

Products of the DNA self-assembly branching concept are reflected in numerous potential applications, ranging from DNA nano-sensors, drug delivery, cancer and genetic disease detection, forensic science through to the next generation of molecular computers, machines and nano-electronic components. These vast potentials for DNA nanotechnology have created new opportunities for commercial exploitation of DNA nanostructures.⁴⁸

In the field of materials and devices, Fischler *et al.*⁴⁹ have coupled nano gold particles onto DNA, and the high conductivity of these nano metallic particles may one day transform modified DNA chains into nanowires (**Figure 1.21 a**). In 2010, the first DNA rotaxane⁵⁰ was prepared from synthetically modified nucleotides to produce mechanically interlocking DNA with circular geometry, that could be used to make a new class of molecular switches for nanorobotics (**Figure 1.21 b**).

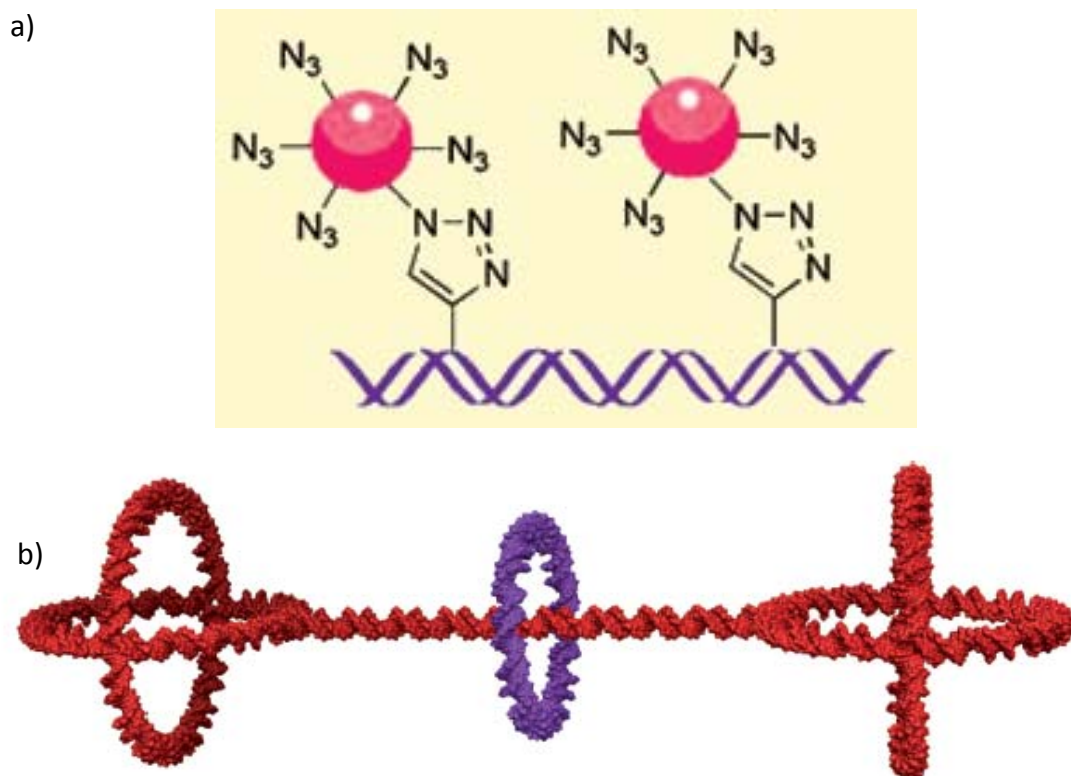


Figure 1.21: Illustration of the formation of a) Gold particles-DNA for nanowires⁵¹ and b) DNA-rotaxanes for molecular switches.⁵⁰

Anderson *et al.*⁵² have reported the formation of a DNA box by attaching complementary strands to areas of a single long circular DNA sequence made from folding six DNA origami sheets. By using the sticky-ends principle, a DNA dual lock-key system was created to open the lid of the box. The potential for a DNA box with a controllable open-close lid is huge, because the box may compute logic functions that may set the foundation for future DNA-based computers.⁵³

In addition to the production of nano materials and devices, DNA nanotechnology is being explored for use in medical diagnostics and disease treatments. The 3-D DNA box, for example, could be exploited for trapping viruses, and storing enzymes.⁵³

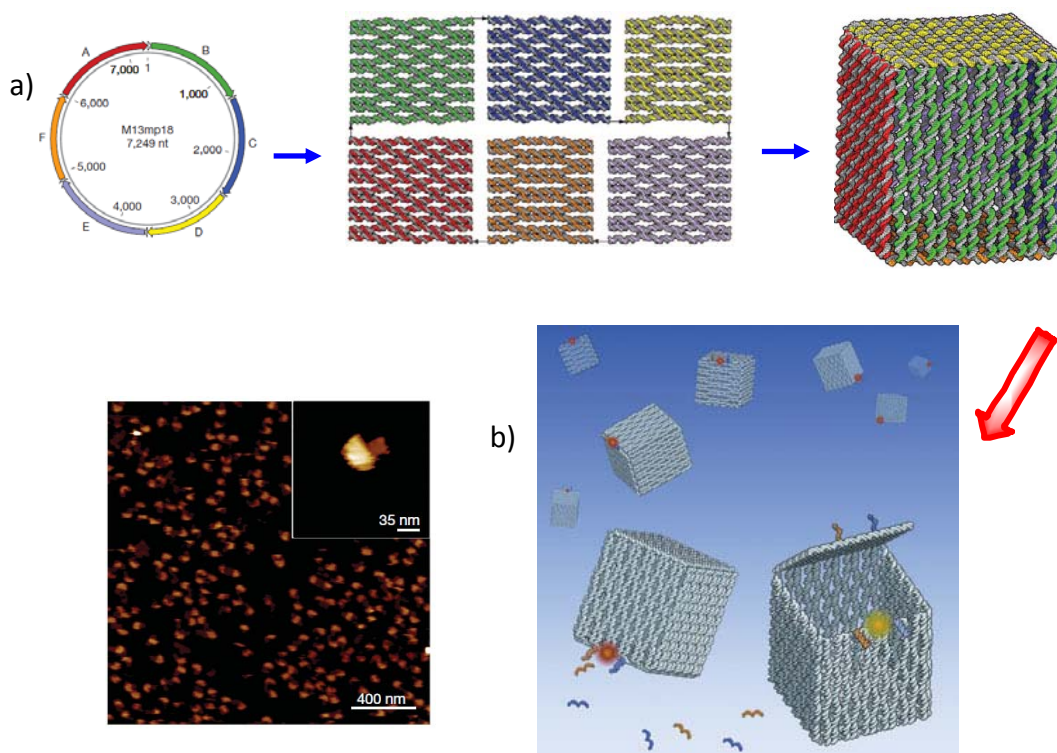


Figure 1.22: a) Circular single strand DNA combined with complementary strands to form a DNA box,⁵² and b) the opening and closing of a DNA box by a DNA lock and the recognised complementary key concept.⁵³

Deposition of nanoparticles on DNA is another developing area because of its direct applications in medicine. For example, Thaxton *et al.*⁵⁴ have shown that gold nanoparticles combined with DNA have the ability to detect recurring prostate cancer based on determining the prostate specific antigen (PSA), a protein associated with prostate cancer. DNA gold nanoparticles (Au NP) conjugate with PSA-specific antibodies, then bind to a MMP (magnetic microparticle probe) that is functionalised with antibodies to PSA and the PSA target protein (*i.e.* an antigen). A magnetic field is then applied, and the PSA-specific DNA strands are cleaved and detected (**Figure 1.23**).⁵⁵ The amount of PSA is proportional to the amount of DNA that is released, and the return of post-surgery cancer can be detected. This technique is about 300 times more sensitive than other tests that are currently available.

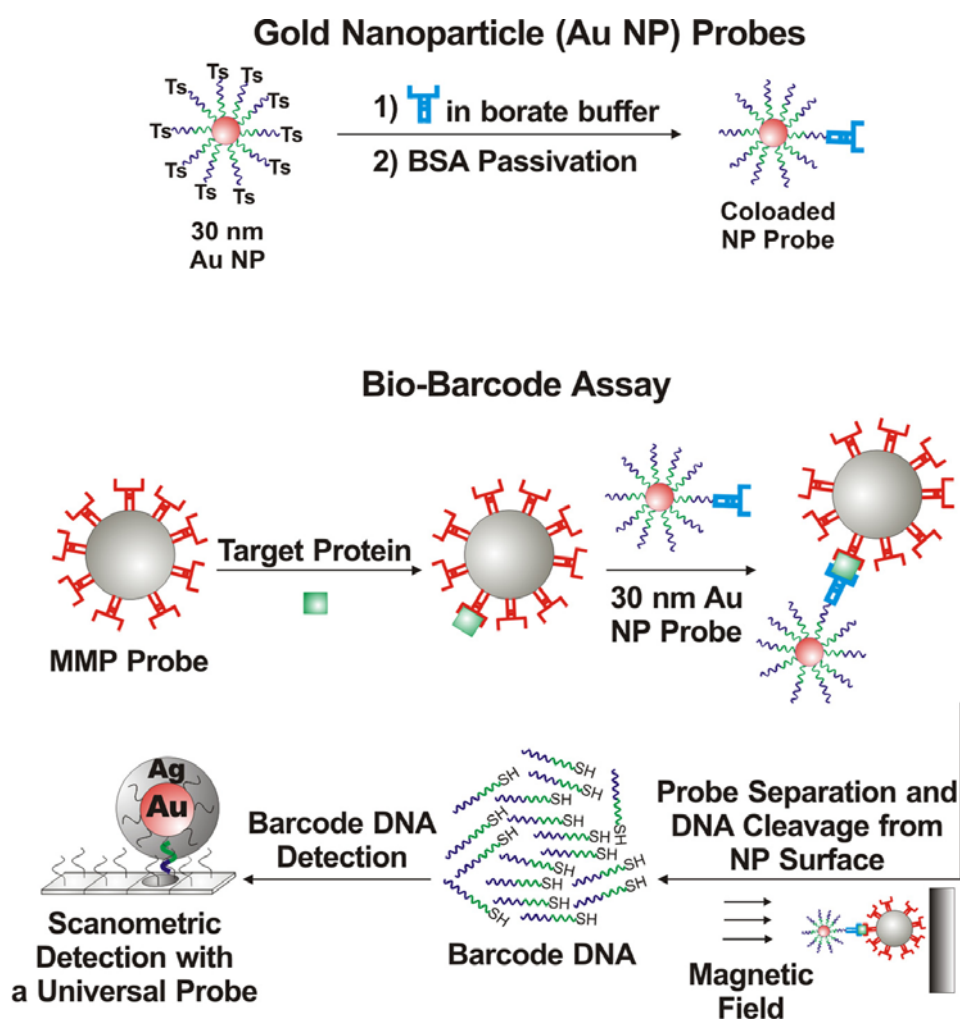


Figure 1.23: The principle of detection of prostate cancer by nanoparticles of gold and DNA.⁵⁴

The newest drug delivery system that DNA nanotechnology can offer relies not only on the self-assembly of DNA, but is also directed by transition metals. Lo *et al.*⁵⁶ have successfully built a DNA nanopod template (**Figure 1.24**), in which rigid triangular building blocks are linked vertically by DNA strands to form a nanotube. The new tube can encapsulate metals of a specific size, such as gold nanoparticles, which may have potential in biomedical applications.⁵⁷ On a similar basis to the 3-D DNA box, this DNA nanopod can trap nanoparticles that are 65 nm apart inside. Upon addition of eraser strands (*i.e.* strands that are complementary to sequences which hold the nanotube together), the DNA nanopod structure disassembles into single strands, thus liberating the nanoparticles. This represents the first instance of a host-guest 3-D DNA design that can control both the uptake and discharge of

nanoparticles.⁵⁸ Potentially, this DNA nanopod concept could assist cancer treatment by using gene-triggered selective delivery of drugs; a cancer protein may bind to the closing strands of the nanopod to open the cage and release gold or other drugs specifically at the cancer sites.

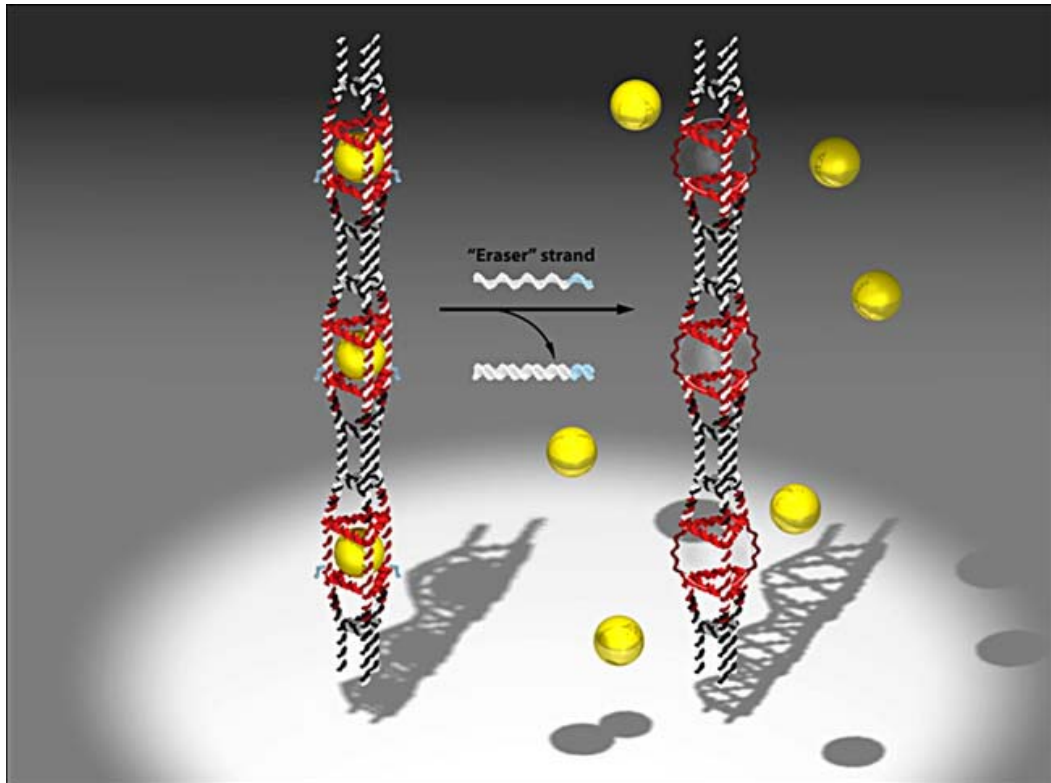


Figure 1.24: Formation of a DNA nanopod and the controllable release of encapsulated gold nanoparticles.⁵⁷

These are just a few selected examples of recent developments in DNA nanotechnology, which represent one of the most exciting and rapidly expanding areas of science at the present time.

1.2 Porphyrin-DNA as a scaffold for nanoarchitecture

The rapid development in DNA nanotechnology means there is a high demand for new structures of modified DNA. The availability of the synthetic DNA and its selectivity to form well-defined helical structures of DNA through base-pairing has recently been proposed as a method for specifically connecting different electrochemically and photophysically active molecules. Examples include porphyrins, amino acid derived side chains or pyrenes, which form multifunctional molecules on the nanometre scale.^{30, 34, 36} The well-established applications of porphyrins in the creation of optical electronic devices, photodynamic therapy, and molecular dyes make this class of material very attractive for fabrication in DNA nanoarchitecture.

1.2.1 Structures and properties of porphyrins

As with DNA, porphyrins are naturally occurring molecules that are key parts in essential biological processes. They are basic components of the photosynthetic system, which controls the conversion from sunlight energy to chemical energy, and haemoglobin which controls oxygen transport. Porphyrins have been studied extensively over many years. In 1926, the first porphyrin was synthesised by Hans Fischer, who is referred to as the father of contemporary porphyrins.⁵⁹ Others have subsequently designed further porphyrin synthetic strategies to optimise the functionalisations and the notoriously low yield of porphyrin synthesis.⁶⁰

Porphyrins are heterocyclic macrocycles derived from 4 pyrrole subunits linked on opposite sides through 4 methine bridges (=CH-).^{61, 62}

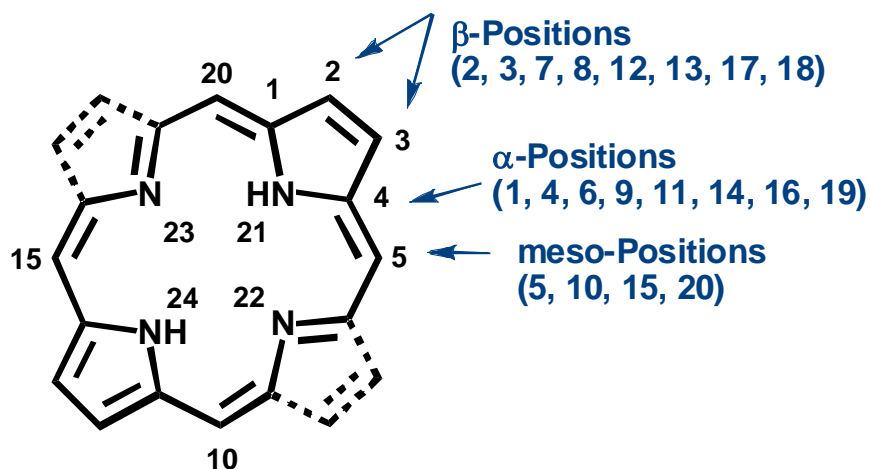


Figure 1.25: Structure of simplest porphyrin found in nature (*i.e.* porphine).

There are 9 double bonds around the periphery of the porphyrin ring (*i.e.* solid line in **Figure 1.25**), and 18 conjugated electrons out of possible 22 π electrons of total 11 double bonds. These 18 electrons obey the Hückel rule of $(4n + 2)$ and hence porphyrins are aromatic compounds.⁶³ The extensive conjugated system gives porphyrins their distinctive chromatic identity. In fact, the name *porphyrin* takes its origin from a Greek word meaning purple, which is the primary colour of these compounds.

Porphyrin bond distances vary depending on the substituents attached to the ring. The nitrogen-metal bonds, in the range of 1.90 – 2.10 Å, are especially influenced by the types of metals that bind to the porphyrin core. **Figure 1.26** shows structural parameters for the free-base (*i.e.* metal free) porphine. Furthermore, X-ray diffraction has confirmed that the 2 hydrogen atoms on the pyrrole groups must face each other in opposite direction.⁶⁴

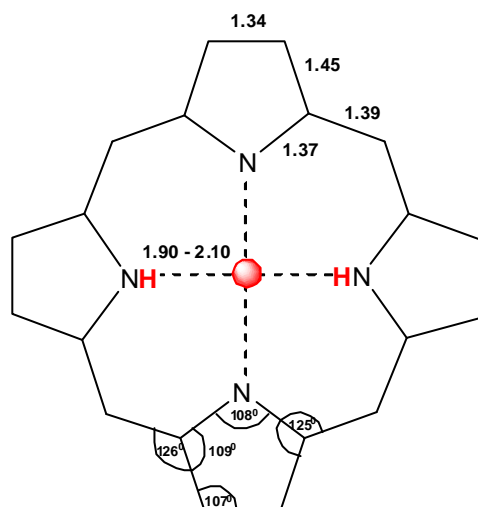


Figure 1.26: Structural data for a porphyrin ring.

Porphyrins have a strong affinity for a variety of transition metal ions including Fe(II), Fe(III), Co(II), Ni(II), Cu(II), Zn(II), Mn(III), Cr(III), *etc.* These metal ions may influence the electronic properties of the molecules, and thus the biological activities of metalloporphyrins.⁶⁵ For instance, the reactive part of haemoglobin binds Fe(II) to give the complex a strong blood red colour, whereas chlorophyll, with Mg(II) at its centre, is green (**Figure 1.27**). Simple monometallic porphyrins are often formed by reacting the free-base porphyrin with a metal salt, and the side product is the consequential acid. When a strong acid is added, the reaction equilibrium shifts in the opposite direction, and results in demetallation of the porphyrin. The steps involved in porphyrin metallation vary depending on the metal and its preferred coordination. With a divalent metal ion, such as Ni(II) which adopts a square-planar geometry, metallation proceeds *via* the deprotonation of the two hydrogen atoms in the equatorial plane (coloured red in **Figure 1.26**), accompanied by dissociation of the metal salt to produce the metal cation, which binds to the centre of the deprotonated porphinate dianion.⁶⁶ Although metalloporphyrins may possess square planar, square pyramidal, or distorted octahedral geometries, depending on the coordination numbers that the metals adapt, the majority of metalloporphyrins adapt a square planar geometry. Most of

the metals, including those discussed in this PhD project⁶⁴ are coordinated to the four nitrogens in the porphyrin centre.

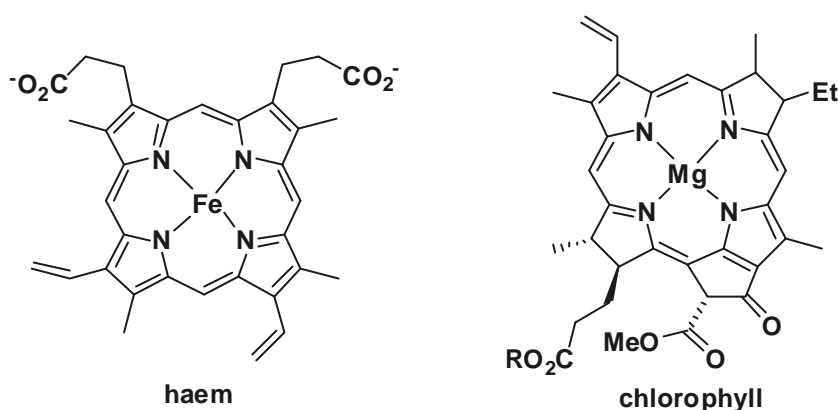


Figure 1.27: Porphyrin structures in two important biological complexes.

The extinction coefficients of porphyrin absorption bands are typically high and the intense absorbance at 380-420 nm, namely the Soret band or B-band, is a signature for the macrocyclic conjugation. Other absorbance bands, which are less intense, co-exist at 450-700 nm, and are known as the Q-bands.⁶⁷ Generally, free base and metalloporphyrins fluoresce in the range of 600-800 nm. Many porphyrins, especially in solution, are unstable to light, since they can undergo photoreduction to form free radicals.^{68, 69} Despite this problem with light sensitivity, the dual-abilities of porphyrins to both absorb and emit light efficiently are major strengths for the development of their uses. This property enables porphyrins to act as indicators of changes once they are incorporated into other compounds, and changes in the absorbance or emission reflect alterations in the surroundings and/or structures of host molecules. Porphyrin photophysical properties are further discussed in the **Chapter 3**. However, because of their distinctive chromatic identities, metal binding, relative ease of functionalisation, and sensitivity to light, porphyrins provide versatile building blocks for supramolecular chemistry.

1.2.2 Porphyrins in supramolecular chemistry

Supramolecular chemistry is a multidisciplinary field that links inorganic, organic and bio-chemistry. Known as “chemistry beyond the molecule”, the main principles are based on intermolecular forces rather than classical strong covalent interactions.⁷⁰ These non-covalent bondings help to assemble individual molecules into one reversible design, as illustrated through ion binding host-guest concepts, which were introduced by Cram *et al.*,⁷¹ Behr *et al.*⁷² and Pederson.⁷³ Their early work on the syntheses of spherands, cryptands and crown ethers, macrocycles which provide cages for non covalent cation binding (*e.g.* Na⁺, K⁺, Li⁺, *etc.*) built up the preorganisation principle and pioneered the beginning of supramolecular chemistry.⁷⁴

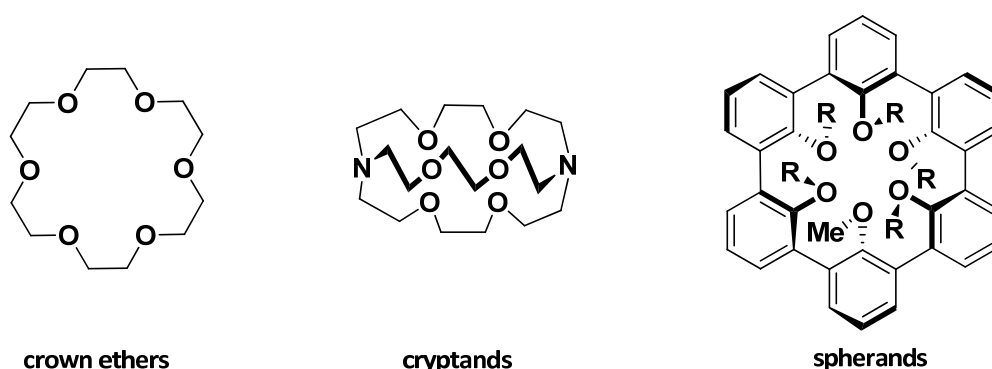


Figure 1.28: General structures of some early macrocycles in supramolecular chemistry.

Other supramolecular molecules that have been developed more recently include indolocarbazole-containing rotaxane,⁷⁵ carbazolylureas⁷⁶ and anthracene (**Figure 1.29**) that can be attached to DNA⁷⁷ for potential uses in anion receptors, sensors and molecular switches. Apart from its applications in functional architecture to create future molecular devices, supramolecular chemistry can also help to understand essential biological processes, as for example in the identification of non-covalent hydrogen bond interactions in the DNA double helix structure.⁵

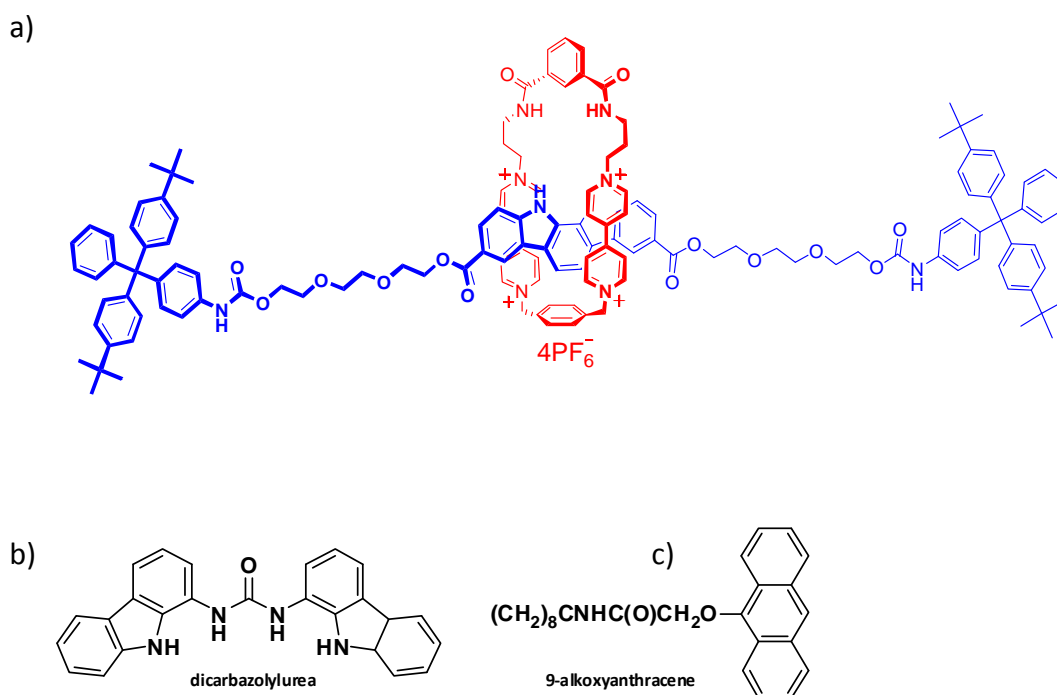


Figure 1.29: Examples of novel supramolecular molecules: a) rotaxane complexed with indolocarbazole,⁷⁵ b) carbazolylurea and c) anthracene for attachment to DNA.

Because of its electrostatic π - π interaction, the availability of various sites for functionalisation, and its affinity for metals, the porphyrin chemical family appears to be an ideal building block for supramolecular chemistry. Sophisticated self-assembled host-guest supramolecular macrocycles can be prepared with porphyrins, and pre-organised and well-defined pentaporphyrin cages have been synthesised for different metalloporphyrins and free-base porphyrins (**Figure 1.30 b**). Known for their intramolecular energy transfer property,⁶⁹ the quenching of the fluorescence of all individual porphyrins in this pentaporphyrin unit further illustrates their potential for the formation of light-harvesting systems.⁷⁸

Stulz *et al.*⁷⁹ have also shown that in addition to the preparation of large macrocyclic molecules, porphyrins can also self-assemble to form linear dimeric and trimeric arrays *via* ruthenium and rhodium porphyrins coordinated to phosphines, as shown in **Figure 1.30 a**.

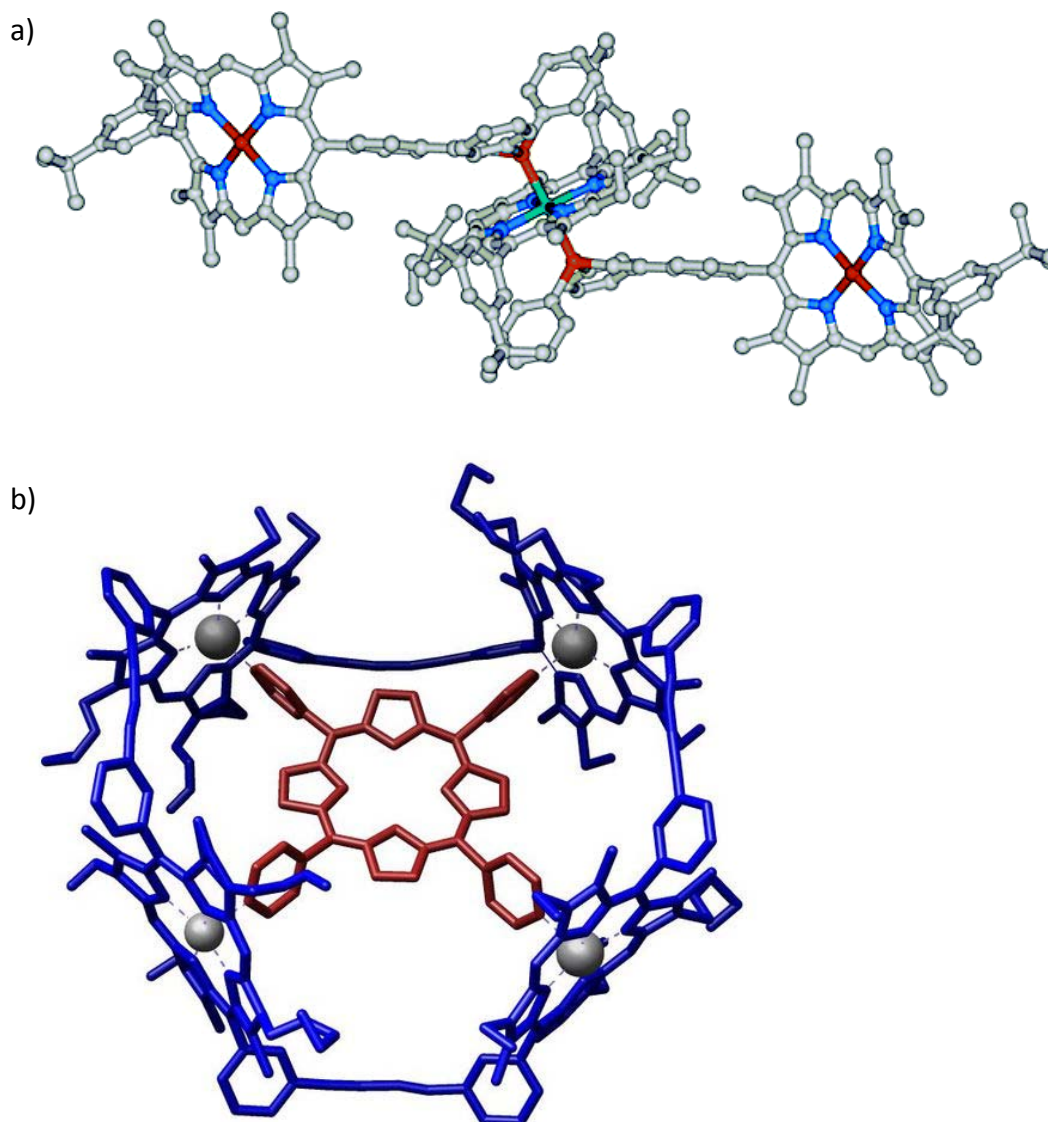


Figure 1.30: a) Trimer of Ni-Ru-Ni bisphosphin-substituted porphyrin array;⁷⁸ b) pentaporphyrin array.⁷⁸

The phosphine substituted porphyrins act as ligand donors whilst ruthenium and rhodium porphyrins are ligand acceptors. Together, they form donor-acceptor dimers and trimers, which could be used to transfer energy along the porphyrin array.⁷⁹

One of the latest ventures of porphyrin arrays for photofunctional design involves complexation with POM (polyoxometalates) to form hamburger-shaped porphyrin units. Yokoyama *et al.*⁸⁰ have reported two molybdenum diphenyl

metalloporphyrins, which changed the polyoxometalate redox property when two axial metal ions were coordinated to the centre of the POM. In addition, the π - π interactions of the porphyrins aid the self-stacking of the porphyrin “hamburgers” into a highly stable lattice containing sheets of metalloporphyrin-POMs (**Figure 1.31**).

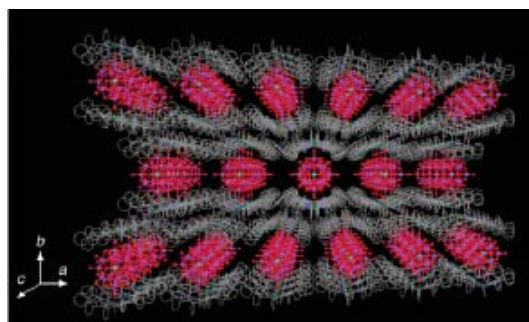
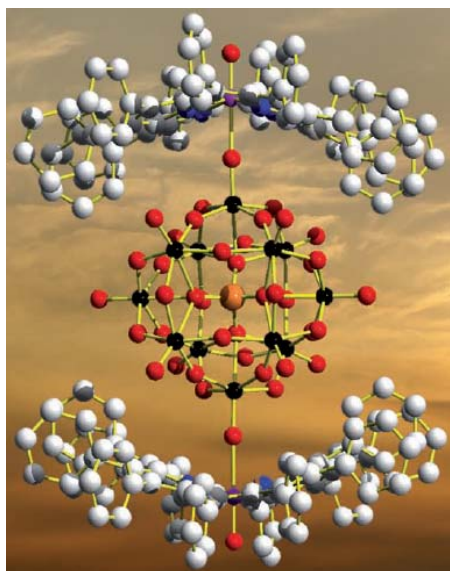


Figure 1.31: Diphenyl metalloporphyrins sandwiching a POM (left) and the corresponding 3-D porphyrin-POM lattice formed through porphyrin π - π interactions.⁸⁰

In addition to their utilisation in constructing light-induced photoactive complexes, porphyrins also possess nanoscale molecular-sensing properties. Cormode *et al.*⁸¹ showed the formation of a new assembly of disulfide-modified porphyrins surrounding gold nanoparticles with enhanced anion binding properties compared to free porphyrins in solutions (**Figure 1.32**). This is due to the pre-organised structure of porphyrins on the surface, helped by gold nanoparticle adsorbance.

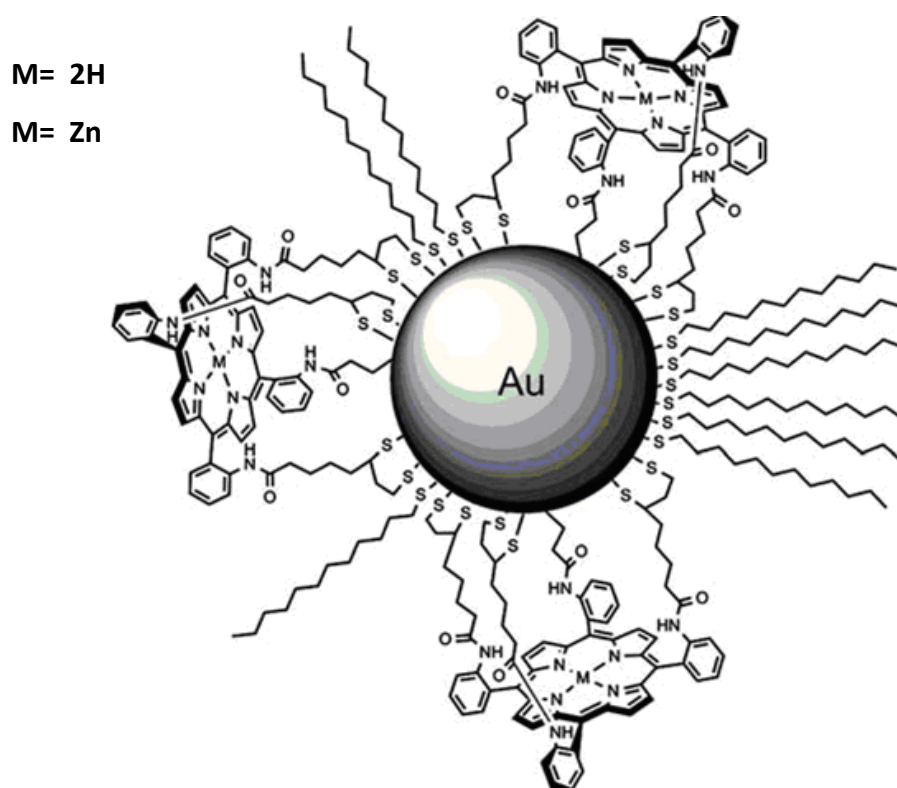


Figure 1.32: Disulfide porphyrin binding to gold nanoparticles for anion sensing.³¹

In general, the functionalisation of macrocyclic porphyrin arrays is well established, but within the limit of this thesis, only some examples are selected to represent advances made in the last two decades. However, from these selected publications, it can be seen that porphyrins represent excellent building blocks for supramolecular chemistry, and in nanotechnology for producing the next generation of optoelectrical devices and molecular sensors.

1.2.3 Porphyrin modified DNA in nanotechnology

The characteristic and tunable electronic properties, such as redox potential and photophysical properties, of molecules functionalised by porphyrins have been studied extensively. DNA, on the other hand has only recently been found to be a suitable supramolecular scaffold for the construction of functional molecules. Hence, it seems logical that combining the chemical properties of porphyrins and

DNA would open the door to the production of multiporphyrin arrays, using DNA as a scaffold to create a nanotechnology toolbox for the future.

The initial syntheses of chlorin and porphyrin covalently attached to DNA were reported by Boutorine *et al.*,⁸² Mestre *et al.*,⁸³ and Schuberta *et al.* (**Figure 1.33**).⁸⁴

Boutorine *et al.* showed that chlorin could be linked to oligonucleotides *via* coupling of the carboxylic acid and aldehyde functional groups on the chlorin to the 3'- amino activated phosphate end of DNA. Similarly, amide bond formation also connected different porphyrins to oligonucleotides through the coupling of the carboxylate arms of porphyrins and the 5'-aminoalkylated oligonucleotides, as shown by Mestre *et al.*, and Schuberta *et al.* The aim of these early syntheses of modified DNA with covalently attached porphyrins and chlorins was for potential therapeutic applications, such as killing tumors upon activation, which results in DNA cleavage.

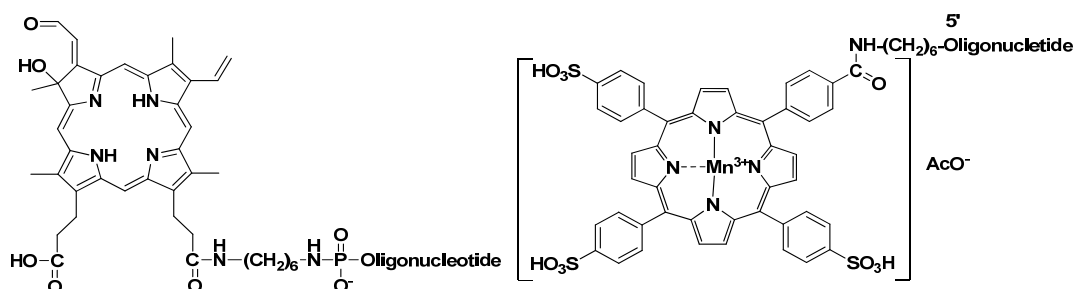


Figure 1.33: Chlorin (left) and porphyrin (right) modified DNA.

The molecular sensing property of porphyrin on DNA has been explored by Balaz *et al.*⁸⁵ By covalently attaching a 5'-end tetraphenyl porphyrin modified nucleotide to DNA (**Figure 1.34**), significant hypochromicity (*i.e.* decrease in UV-absorbance) was observed in both the oligonucleotide band and the porphyrin B-band. Changes in circular dichroism upon the addition of salts were also observed. These results confirm that porphyrins can be used as indicators of structural changes on oligonucleotides. Specifically in this case, the porphyrins revealed the transformation from the normal right-handed B-type double strands to the less common left-handed Z-type duplex.

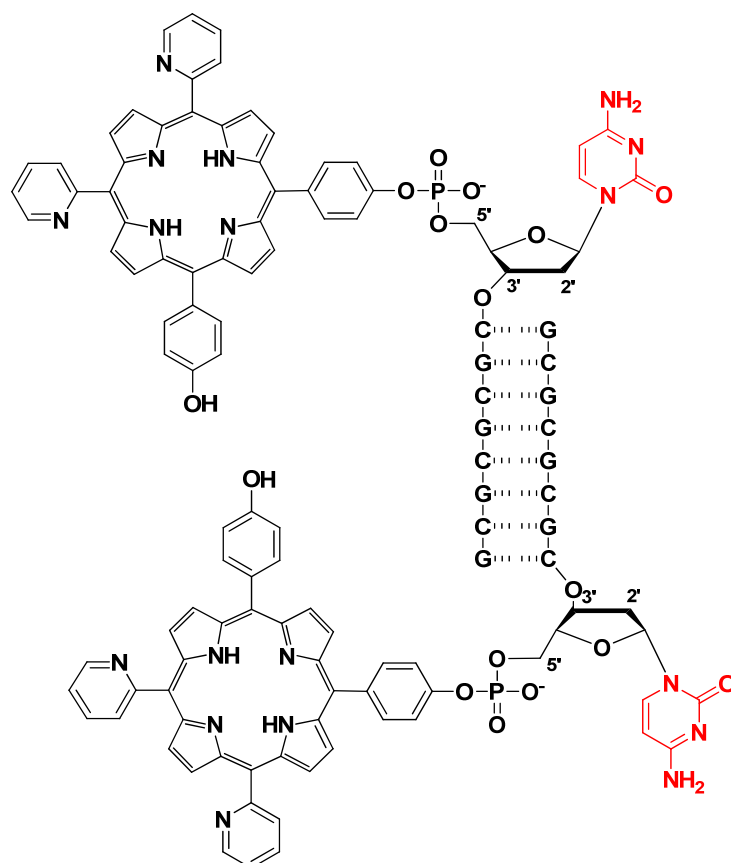


Figure 1.34: 5'-covalently modified porphyrin-DNA as a structural sensor.

Another strategy to efficiently assemble porphyrin-DNA structures was followed by Endo *et al.*^{86, 87} by conjugating a maleimide-substituted tetraphenyl porphyrin with four thiol functionalised DNA strands. Upon duplex formation with complementary strands, 4 double helices were assembled and used to create porphyrin diads, which showed good energy transfer from a Zn porphyrin to the freebase (**Figure 1.35 a**). Potentially, this DNA structure could accommodate a host-guest system within the co-facial porphyrin dimers.⁸⁶ This four-way-branched DNA was also used as a connector in a DNA tile system to build DNA nano-tubes.⁸⁷

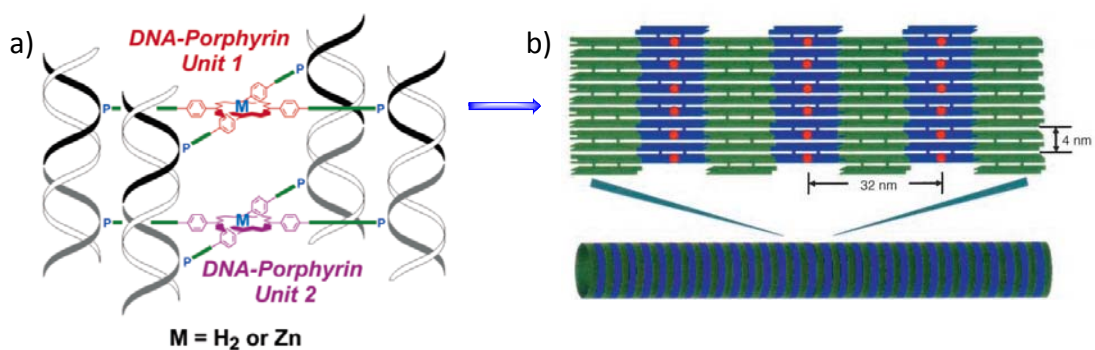


Figure 1.35: Construction of a 3-D DNA nano tube (b)⁸⁷ from the four-way-branched porphyrin-DNA double-helix assembled structure (a).⁸⁶

One property of porphyrins, which makes them robust in transmitting energy, is their high extinction coefficients ($\epsilon \sim 20\,000\text{ M}^{-1}\text{ cm}^{-1}$). Thus they absorb light efficiently around 400-500 nm, which is in the region of many emitting fluorophores. Mimicking the light harvesting antenna asset of this chemical family, Börjesson *et al.*⁸⁸ successfully created a porphyrin-DNA assembly that allows conversion of light into chemical energy for the lipid membrane.

The supramolecular assembly in **Figure 1.36** was designed by covalently connecting a zinc porphyrin to a short 14-mer DNA strand, followed by deposition onto a lipid membrane. When the lipophilic porphyrin entered the lipid membrane, the hydrophilic DNA remained on the outside, and was thus available for hybridising with a complementary strand that carries two fluorophores. Light was then emitted from the two fluoresceins, absorbed by the porphyrin, and then efficiently emitted into the lipid membrane, thus trapping light as chemical energy (**Figure 1.36**).

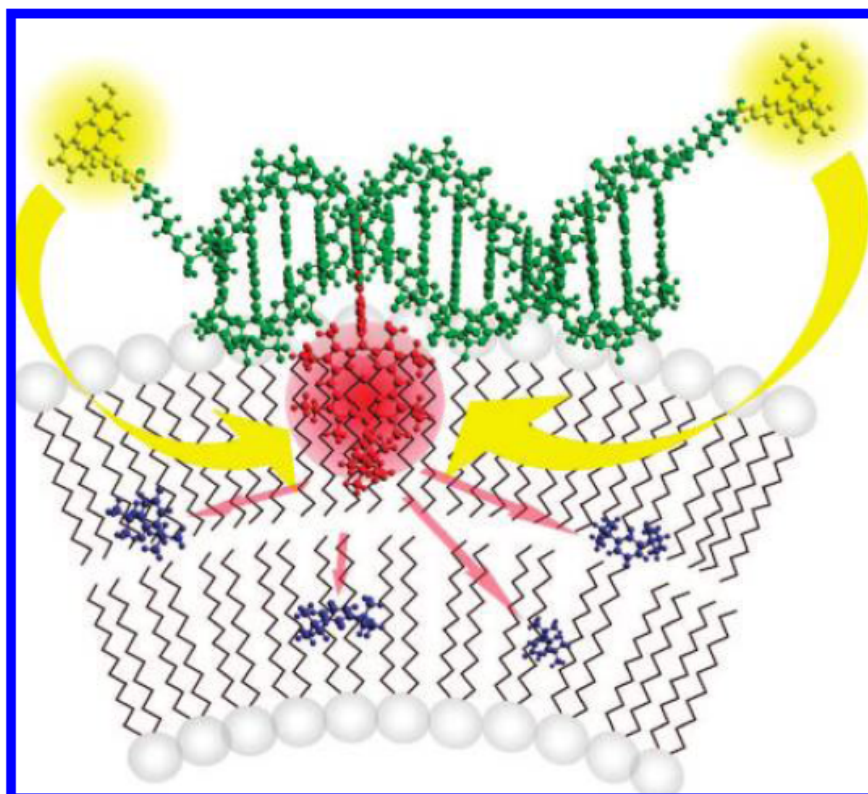


Figure 1.36: Porphyrin-DNA light conversion assembly for biological lipid membrane.⁸⁸

Collectively, these examples reinforce the idea that DNA, as a supramolecular scaffold, can provide an excellent array for externally and covalently linked functionalities. These examples showcase the high potentials of porphyrin-DNA for applications in all areas of nanotechnology, such as designing nano electrical gadgets (materials and devices), constructing nano light trapping (energy and environment), or converting light into chemical energy for use in biological and chemical processes inside lipid membranes. Bottom-up DNA and porphyrin chemistry are not just automated solid-phase synthesis and pyrrole polymerisation. Nevertheless, it is important to recognise the value of the early work on DNA and porphyrin structures, without which today nanotechnology applications could not have been achieved.

1.3 Project aims.

The objective of this project was to explore the potential of modified DNA in bio-nanotechnology, especially in electronic and biomedical applications. The initial aim was to produce and analyse multiporphyrin arrays, using DNA as a scaffold, and then to investigate their potential uses as electronic wires and therapeutic agents. The work described in this thesis forms part of the larger project on using DNA as a scaffold for the synthesis of new functional molecules on the nanometre scale. This is ultimately achieved by connecting molecules that have different electrochemical and photophysical properties to the nucleosides, and then using these for sequence specific incorporation into DNA (**Figure 1.37**).^{89, 90}

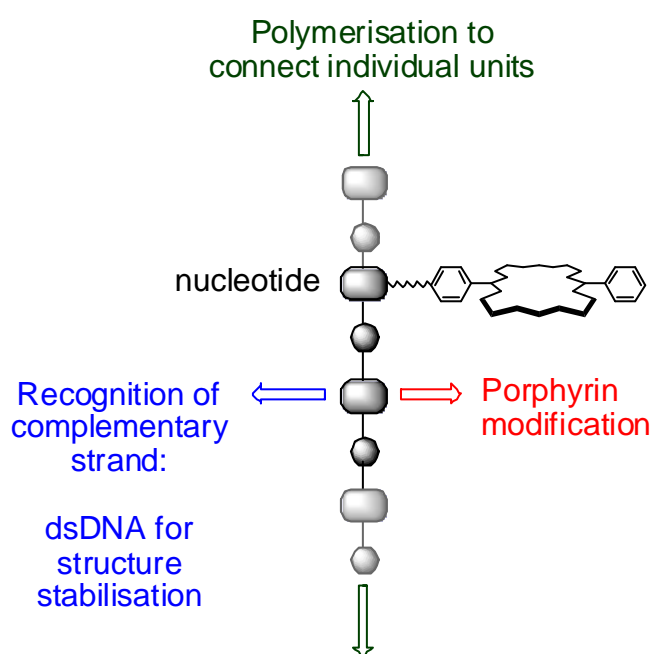


Figure 1.37: Strategy for connecting porphyrins to oligonucleotides to form porphyrin-DNA arrays.

Porphyrins, a class of naturally occurring materials (such as heme or chlorophyll)^{4, 91} were chosen for functionalising DNA on the basis of the extensive knowledge of their properties and their potential for creating novel optical electronic devices (**Figure 1.38**)

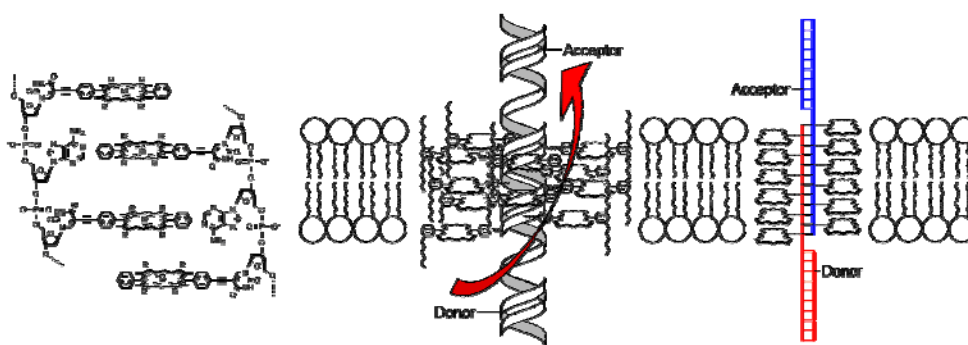


Figure 1.38: Schematic representation of cross-membrane electron transfer in porphyrin-DNA arrays.

Since porphyrins are also under clinical trials for photodynamic therapy of skin cancer,⁹² another part of the research focused on assessing the potential use of porphyrin-DNA in medical applications. This combined the therapeutic properties of porphyrins, with DNA, some sequences of which can enhance the efficacy of cancer treatments.⁹³

It is very difficult for charged molecules such as DNA to diffuse across the lipid bilayer of cell membranes, unless they can be taken up by cells *via* a different mechanism.⁹⁴ However, porphyrins are more lipophilic and their potential roles in aiding DNA to cross cell membranes were also investigated. Preliminary investigations have now shown successful porphyrin- skin cell transfections with a porphyrin that carries two negative charges (**Figure 1.39**). Hence future experiments plan to transfect into skin cells a porphyrin-modified dinucleotide with only one negative charge, before studying the permeability of long porphyrin-DNA arrays.

This project was an extension of that of Dr. Imenne Bouamaied's⁹⁵ and pursued the nanotechnology *bottom-up* approach. Novel diphenyl porphyrin modified DNA strands were synthesised (**Figure 1.40**), and their properties analysed in detail using UV-vis and fluorescence spectroscopy, CD spectroscopy, EPR spectroscopy, UV-melting, gel electrophoresis, and HPLC. Post-synthetic metallation with zinc and

copper had not previously been studied, and were investigated in order to obtain suitable systems for energy transfer or for EPR spectroscopic analysis.

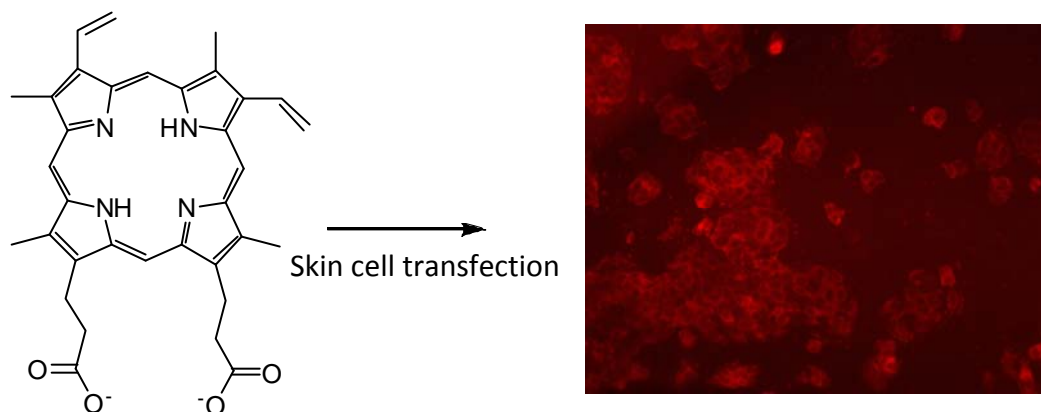
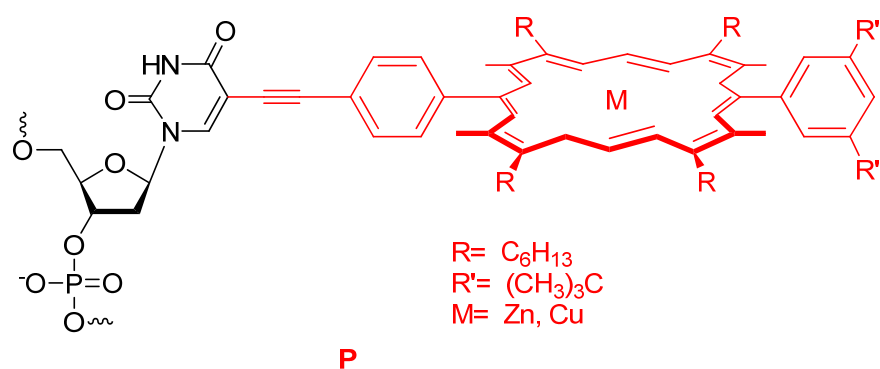


Figure 1.39: A successful charged porphyrin transfection into skin cells.



5'-CAT CGT AGT TTT **PAP** TTT TCC GTA CTC-3'

5'-CAT CGT AGT **APA PAP APA** TCC GTA CTC -3'

5'-GAG TAC GGP **APA** CCG TAC TC-3'

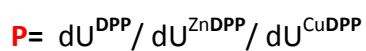


Figure 1.40: Building block **P** and representatives of porphyrins-DNA sequences.

The analytical studies described above were also applied to tetraphenyl porphyrin-DNA strands in order to draw parallels and contrasts with a different multi-porphyrin array.³⁵ However, the primary investigation focused on diphenyl porphyrin-DNA, because this molecule is thought to have a better π - π interaction than the bulkier tetraphenyl porphyrin, and to cause less steric hindrance in a supramolecular array. Comparisons between different porphyrin-DNA arrays are important because they provide useful feed-back to design potential nanowires from an optimal porphyrin-DNA array; one which needs to be robust and yet versatile for functionalisation

CHAPTER 2: SYNTHESIS AND CHARACTERISATIONS OF PORPHYRIN-DNA

The porphyrin syntheses and their couplings onto oligonucleotides in this project are continuations of the PhD work from Dr. Imenne Bouamaied,⁹⁶ whereas post synthetic metallations, purifications and analysis of porphyrin-DNA were initiated by myself. The synthesis of diphenyl porphyrin (**DPP**) **12**, its coupling to iodo-deoxy uridine and transformation to phosphoramidite monomer **1** therefore detail modifications of the original protocols in Bouamaied's thesis "DNA as Supramolecular Scaffold for Porphyrin Arrays", University of Basel. This chapter is divided into sections, with the first section detailing the making of the building block monomer **1**, followed by the second section describing the incorporation of the monomer into DNA by automated solid-phase synthesis and their purifications. Subsequent metallations of porphyrin-DNA are shown in **Section 2.3**, and **Section 2.4** illustrates RP-HPLC chromatograms of oligonucleotides.

2.1 Synthesis of the 5'-O-DMT-dU^{ZnDPP} phosphoramidite **1**⁹⁷

The first part of this project focused on the synthesis of the monomer 5'-O-DMT-dU^{ZnDPP} phosphoramidite **1** (**Figure 2.1**) before incorporation into DNA strands.

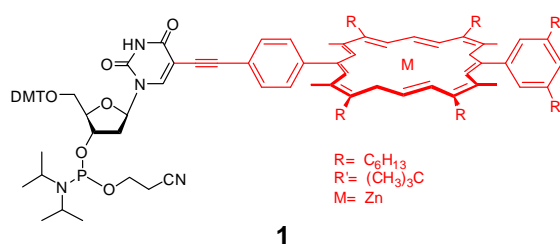
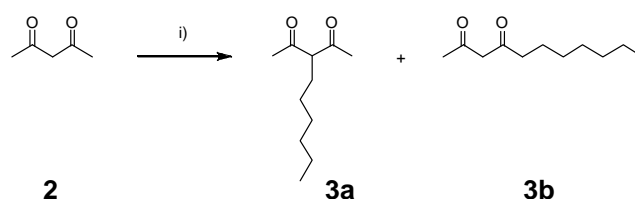


Figure 2.1: Structure of the porphyrin nucleotide building block **1**.

To synthesise the porphyrin monomer **1**, the dipyrromethane **7** (**Scheme 2.2**) had to be obtained first, as porphyrin synthesis is normally the result of pyrroles condensation. The dipyrromethane was synthesised from hexyl derivatised dione **2** (**Scheme 2.1**).

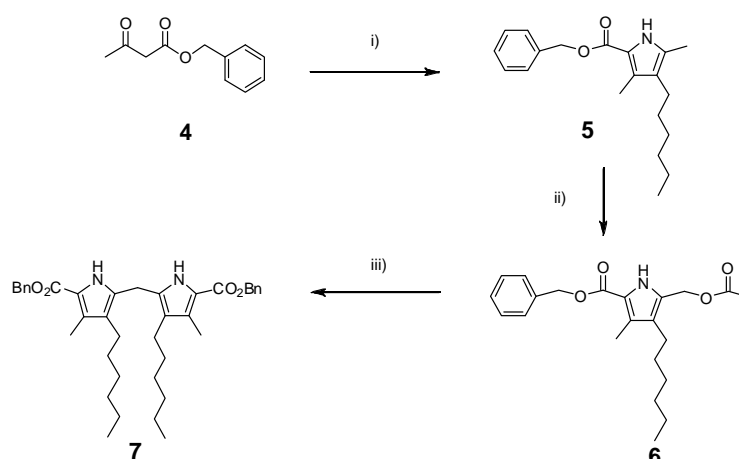
2.1.1 Synthesis of 3-hexylpentane-2,4-dione **3a**^{96, 98, 99}



Scheme 2.1: Reagents and conditions: i) 1-bromohexane/1-iodohexane, K_2CO_3 , acetone, 42 %.

Normally, the dione **3a** is obtained from 1-iodohexane and pentane-dione **2**. Due to the high cost of iodohexane, the use of the much cheaper (by a factor of > 10) bromohexane was investigated. Pentane-2,4-dione **2** reacted readily with 1-bromohexane under reflux for 24 h, but following purification by column chromatography only the side product **3b** was produced. The reaction was repeated for 48 h and produced two isomers **3a** and **3b** in a 2:1 ratio. Vacuum distillation was used for isomer separation, but the ratio of **3a** : **3b** did not change; thus the formation of 3-hexyl-pentane-2,4-dione **3a** was not favourable.⁹⁹ Shono *et al.*,⁹⁸ reported that the formation of single isomer 3-hexyl-pentane-2,4-dione **3a** with a hexyl chain at the meso position could only be achieved *via* an electroreduction method. Investigations on changing reaction conditions to make more of the main product **3a** than side product **3b** were attempted next.

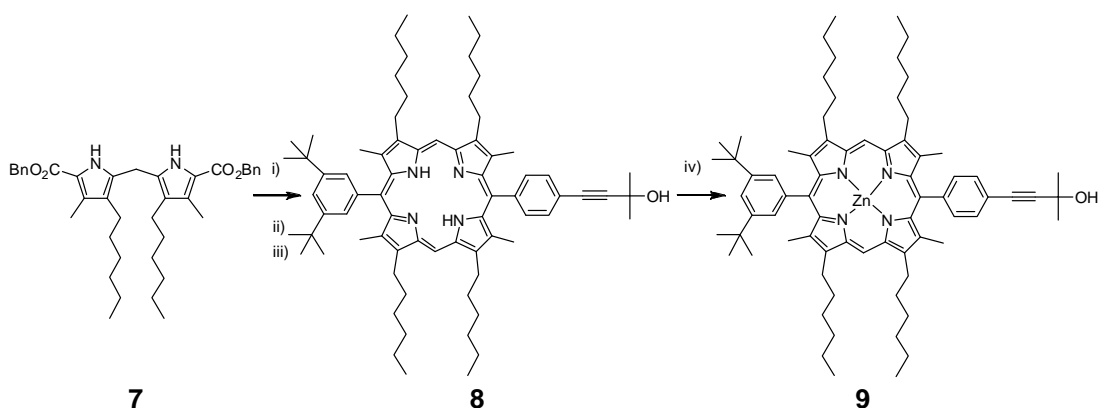
The synthesis was repeated with the addition of NaI, following the Finkelstein reaction.¹⁰⁰ The halogen exchange *via* S_N2 mechanism would replace 1-bromohexane by 1-iodohexane. In theory, this should accelerate nucleophilic substitution to form isomer 3-hexyl-pentane-2,4-dione **3a**. Vacuum distillation, however could not separate the isomers, as a mixture of **3a:3b** in a 2:1 ratio was still observed. 1-iodohexane was then used instead of 1-bromohexane as starting material and this immediately resulted in a significant decrease in the side product **3b**. The crude product was purified *via* vacuum distillation to provide a mixture of **3a:3b** in a good 20:1 ratio. This was still the most successful synthesis pathway and was used for making 3-hexyl-pentane-2,4-dione **3a** thereafter.

2.1.2 Synthesis of hexyl substituted dipyrromethane 7⁹⁶

Scheme 2.2: Reagents and conditions: i) NaNO_2 , H_2O , HOAc , Zn , HOAc , 3-hexyl-pentane-2,4-dione **3a**, 25 %; ii) PbOAc_4 , HOAc , MeOH , 140°C , 1 h, 41 %; iii) HCl , MeOH , 82°C , 10 h, 36 %.

Hexyl substituted pyrrole **5** was synthesised *via* the formation of an oxime, by nitration of benzyl acetoacetate **4**. Recrystallisation from ethanol was not successful, and the crude product was purified *via* column chromatography. The α -acetylation of **5** produced the expected α -acetyl hexyl substituted pyrrole **6** as a light grey solid, which was dried under high vacuum for a period of 22 h and kept in an inert atmosphere to prevent oxidation. **7** was synthesised by stirring **6** in MeOH and HCl under reflux conditions and ethanol was used to recrystallise the crude product (**Scheme 2.2**). ^1H NMR showed the expected peaks, but the crude product appeared as a dark brown solid instead of a white solid. The crude material was further purified by column chromatography (silica, 100:0.5 to 100:1 to 100:2 to 100:5 DCM/MeOH) to produce dipyrromethane **7** as a lighter yellow, needle-like crystalline solid. The TLC of this product showed only one spot, and the analytical data matched the literature data.^{96, 101}

2.1.3 Synthesis of protected zinc diphenyl-substituted porphyrin **9**⁹⁶



Scheme 2.3: Reagents and conditions: i) Pd/C, NEt_3 , THF, MeOH, H_2 ; ii) TFA, 4-(3-hydroxy-3-methyl-but-1-ynyl)-benzaldehyde, 3,5-Di-tert-butylbenzaldehyde; iii) DDQ; iv) $\text{Zn}(\text{OAc})_2 \cdot 2\text{H}_2\text{O}$, MeOH, CHCl_3 , DCM, 21 %.

Dipyrromethane **7** was deprotected with Pd/C in Et_3N , MeOH and hydrogenated for 2h. Addition of TFA for decarboxylation of **7**, followed by stirring in the dark with 4-(3-hydroxy-3-methyl-but-1-ynyl)-benzaldehyde and 3,5-di-tert-butylbenzaldehyde in MeOH, followed by overnight stirring with DDQ produced the crude product as a mixture of three different porphyrins. This mixture was metallated with an excess amount of zinc before purification *via* column chromatography to improve the separation of porphyrins (**Scheme 2.3**). The low yield (21 %) was due to formation of side-product porphyrins. The desired porphyrin **9** showed a strong pink fluorescence, which was observed in between side-products **10** and **11** on a TLC plate (**Figure 2.2**). Reactions on a 4.0 g scale of dipyrromethane resulted in a lower yield because of formation of more side products. Subsequent porphyrin syntheses were therefore reacted on a 2.0 g scale of starting material **7**.

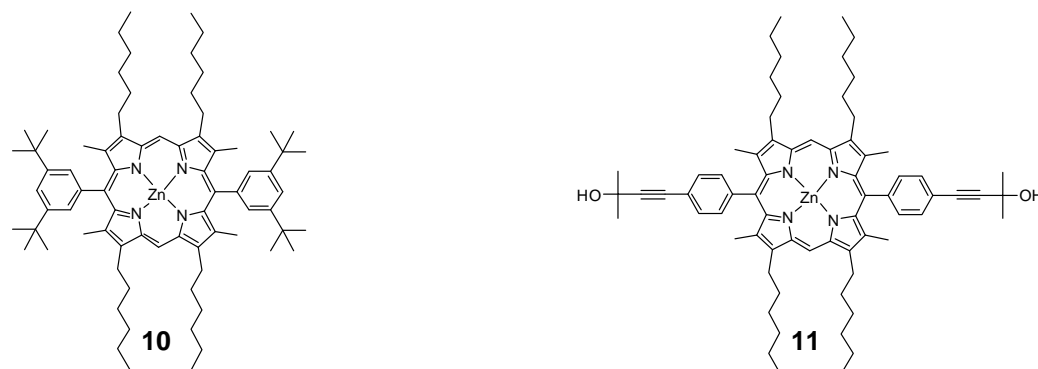
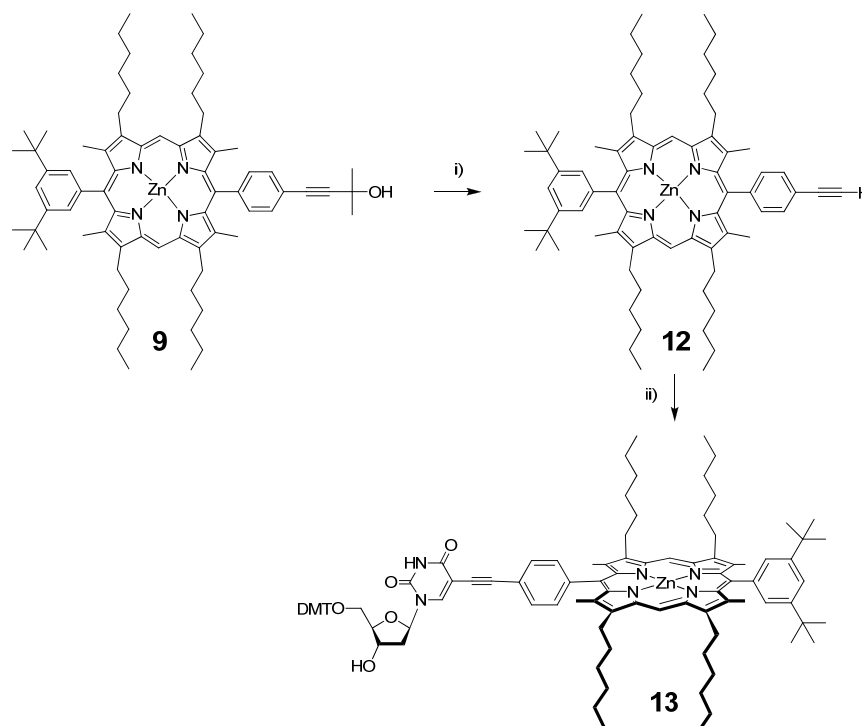


Figure 2.2: Side porphyrin products **10** and **11** in the synthesis of protected diphenylporphyrin **9**.

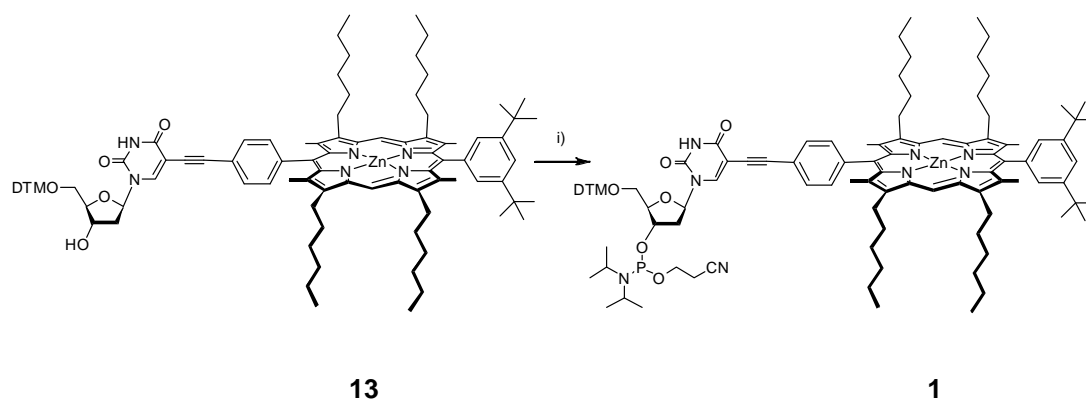
2.1.4 Synthesis of 5'-O-DMT-dU^{ZnDPP} **13** via formation of deprotected zinc diphenyl-substituted porphyrin **12**⁹⁶



Scheme 2.4: Reagents and conditions: i) NaOMe, toluene, Zn(OAc)₂·2H₂O, MeOH, DCM, 53 %; ii) CuI, 5'-O-DMT-iodouracil, DMF, Et₃N, tetrakis(triphenylphosphine)palladium, EtOAc, 47 %.

To couple the **DPP** to nucleoside dU, the alkylnyl group was first deprotected (**Scheme 2.4**) by reacting sodium methoxide and **9** under reflux conditions in dry toluene, followed by purification *via* column chromatography to produce **12**. **13** was synthesised *via* Sonogashira coupling of 5'-O-DMT-iodouracil and **12**. The crude product was purified *via* column chromatography (silica, 100:0.5 to 100:1 DCM/MeOH) to separate **13** from **12**, Another column chromatography in a more polar eluent (100:3 DCM/MeOH) was used to separate **13** from nucleoside 5'-O-DMT-iodouracil. It was important to increase the polarity of the eluent very gradually with small 0.5 % incremental steps of MeOH, because 5'-O-DMT-iodouracil and **13** had very small ΔR_f (≤ 0.07).

2.1.5 Synthesis of monomer 5'-O-DMT-dU^{ZnDPP} phosphoramidite **1**⁹⁰



Scheme 2.5: Reagents and conditions: i) diisopropylethylamine, cyanoethyldiisopropylchlorophosphoramidite, DCM, 2.5 h, 48 %.

The monomer **1** was synthesised under an inert atmosphere (**Scheme 2.5**), using standard phosphoramidite chemistry (chloro-cyanoethoxy-phosphoramidite, triethylamine in DCM) and purified *via* column chromatography (silica, 1:1 DCM/EtOAc, inert atmosphere). The product contained P(III) which readily oxidised to P(V), and it was therefore difficult to determine the molecular mass of **1**. The product peak found using MALDI-ToF MS was one that had been oxidised to give $C_{109}H_{137}N_8O_9PZn^+$ ($[M-O]^+$) = 1795.5. **1** was stored under an inert atmosphere prior to incorporation into oligonucleotides. Attempts to grow single crystals of **1** were not successful.

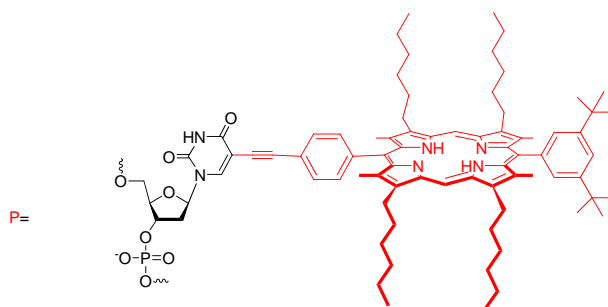
2.2 Incorporation of porphyrin building block onto DNA and purifications

This section describes the attachment of porphyrin-modified nucleotides onto DNA *via* automated solid-phase synthesis and purification of the products

5'-CAT CGT AGT TTT **PAP** TTT TCC GTA CTC-3' **ODN1**

5'-CAT CGT AGT **APA PAP APA** TCC GTA CTC -3' **ODN2**

5'-GAG TAC **GGP APA** CCG TAC TC-3' **ODN3**



This synthesis was first performed by Dr. Dorcas Brown (ATD Bio) on a 0.2 μmol scale of oligonucleotides using an ABI 394 automated solid-phase DNA synthesiser; zinc was spontaneously removed by the acids in the detritylation step of **1**. Subsequent porphyrin-modified DNA strands were synthesised on an Expedite synthesiser on the 1.0 μmol scale by myself with 5 - 10 min coupling time. The porphyrin-DNA strands were end-labelled with fluororous tag groups and purified *via* fluororous tagged column chromatography.

2.2.1 Automated solid-phase DNA synthesis¹⁰²

General principle

Because DNA is important in many areas of research, from molecular biology, molecular genetics, diagnostics, forensic science to nanotechnology, different sequences of oligonucleotides are made for studying their functions fully. In the phosphotriester method, nucleotides are linked together by coupling the 3'-phosphate of one monomer to the 5'-hydroxyl group on another monomer; the product is separated from the starting material *via* column chromatography on silica gel. The DMT group at one end of the protected nucleotide is then deprotected to couple to another monomer, purified and so on to build up a long sequence of oligonucleotides. Although this method is durable, it is very labour

intensive and the yield is not high, especially when long sequences are purified through many columns.¹⁵ The developments of phosphoramidite monomers and solid phase synthesis for oligonucleotides synthesis by Marvin Caruthers and Bruce Merrifield provided the solution to overcome these limits.¹⁵ All the steps involved in DNA solid phase synthesis are summarised in **Figure 2.3**.

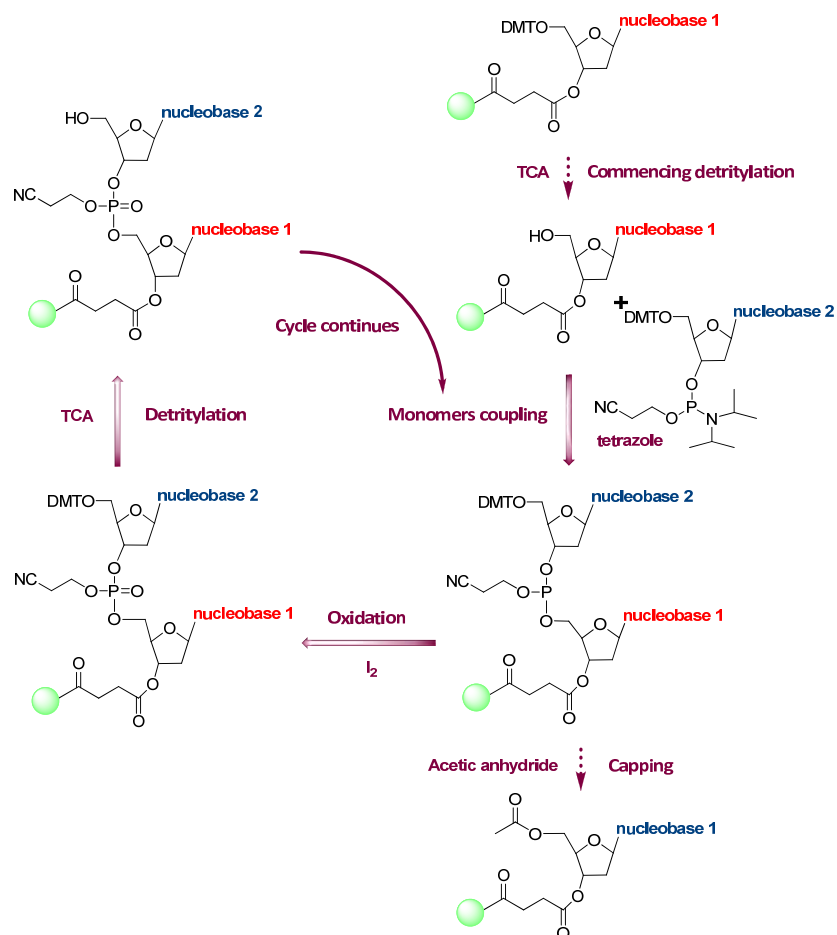


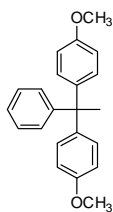
Figure 2.3: A complete cycle of DNA automated solid-phase synthesis.

Solid supports

These are resins made from insoluble particles such as silica gel, control pore glass (500 Å) or polystyrene to bind the oligonucleotides during the synthesis.

Commencing detritylation

The first monomer attached to the resin must have its 4,4-dimethoxytrityl (DMT) **14** (**Figure 2.4**) protecting group removed by the addition of an acid, to produce a 5'-hydroxyl group to couple to the 3'-phosphate group on the other monomer.

**14****Figure 2.4:** Protecting group 4,4-dimethoxytrityl (DMT) **14**

Coupling of monomers

An excess amount of nucleoside phosphoramidite in tetrazole and MeCN was added. The diisopropylamino group was protonated by tetrazole and displaced by nucleophilic attack of a 5'-hydroxyl group of the deprotected monomer to produce a phosphite triester.

Capping

Any unreacted 5'-hydroxyl monomer from the coupling was capped to prevent interference with the next monomer coupling, which could otherwise form a mixture of unwanted sequences. The 5'-hydroxyl group was acetylated in acetic anhydride and N-methylimidazole in tetrahydrofuran and pyridine. Uncontrolled detritylation by formation of acetic acid from mixing acetic anhydride with N-methylimidazole was a problem, but could be stopped by the addition of pyridine to maintain the basic conditions for the reactions.

Oxidation

The phosphite triester (P(III)) formed was unstable to acid, so iodine in water and pyridine were used to oxidise (P(III)) to (P(V)) to prevent further side reactions.

Detritylation

To enable the coupling of the next nucleotide phosphoramidite monomer, the 5'-DMT group was deprotected by trichloroacetic acid in DCM to start the cycle again. The DMT⁺ ions produced were orange in colour, and could be used as an indicator for the quality of the overall coupling reactions. The coupling of

monomers was started, followed by capping and oxidation, and the cycle then continued.

Cleavage and deprotection

The final full length DNA strands were treated with concentrated aqueous ammonia at 40 °C over night, to cleave the DNA from the solid support and to remove all the protecting groups from the nucleobases and phosphate groups.

2.2.2 Purification methods for oligonucleotides

2.2.2.1 Fluorous affinity purification of oligonucleotides^{103, 104}

To purify the crude porphyrin modified oligonucleotides attached with fluoros group after automated solid-phase synthesis, a protocol known as fluoros-tagged affinity purification was used. This method has many advantages, such as;

- Allowing one-pass loading without removing the ammonia from the cleavage and deprotection.
- Selective removal of failure sequences from the long oligonucleotides, because of the large difference in the retention of fluoros and non-fluorous materials.
- Higher recovery of DNA.
- Simple to use column.

More importantly, fluoros affinity purification is used in preference to reverse-phase (RP) DMT-on purification because:

- Premature removal of the product is limited due to a strong affinity of fluoros-tagged oligonucleotides for Fluoro-Pak adsorbent; thus higher yields.
- Ammonia does not inhibit the loading of fluoros tagged-on oligonucleotides to adsorbent as in DMT-on oligonucleotides.
- RP-phase DMT-on purification is only useful for short oligomers (≤ 40 -mers).

Principle of the column

The term “fluorous” is used to describe compounds that are both hydrophobic (insoluble in water) and lipophobic (insoluble in non-polar solvent) due to a high degree of fluorination, such as perfluorohexane. Fluorous-tagged molecules bind more strongly to the separation media in a Fluoro-Pak column. Attaching a fluorous ponytail-like perfluorohexane onto organic domains such as oligonucleotides enhances the separation of the fluorous-tagged desired oligonucleotides from other failure sequences and impurities. Information on how to use the Fluoro-Pak column for DNA purification is detailed in **Chapter 5, Section 5.3.3.1**.

2.2.2.2 Nap-5 purification of oligonucleotides

Nap-5 columns were used in this project to remove excess $\text{Zn}(\text{OAc})_2$ from porphyrin-DNA post-synthesis metallation and to desalt DNA. The principle of this purification relies on different molecular retention factors for various compounds. Larger molecules are not trapped in the pores of the matrix gel and hence elute first. Smaller molecules may be trapped in the matrix pores, so they flow through the gel at a slower rate and are eluted in later fractions.¹⁰⁵ Details of how the Nap-5 column was used to purify oligonucleotides is further discussed in **Chapter 5, Section 5.3.3.2**.

2.3 Post-synthetic metallations of porphyrin-DNA

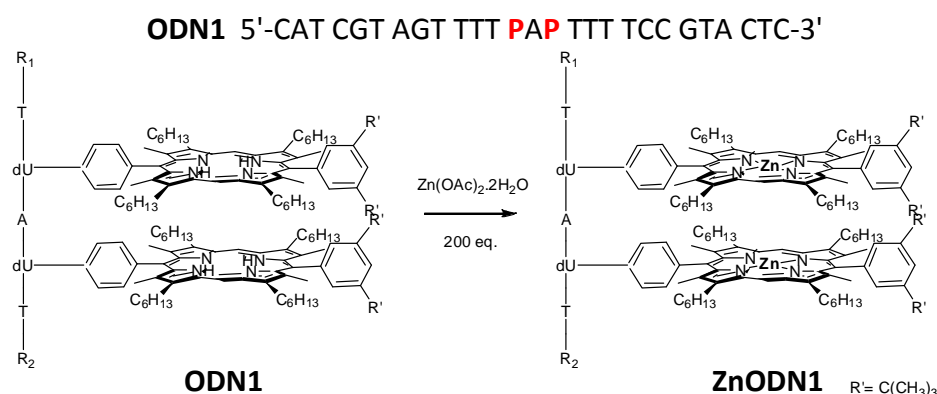
All metallations of porphyrin-DNA were performed after porphyrin attachments onto DNA, because zinc had been removed during automated solid-phase syntheses, and the DNA was always obtained as free base porphyrin-DNA.

2.3.1 Zinc metallation of porphyrin-DNA

Initially, zinc was used to metallate the porphyrins held on DNA for binding study.

Zinc was first chosen for the metallation because:

- $\text{Zn}(\text{OAc})_2 \cdot 2\text{H}_2\text{O}$ is available commercially.
- Zn has been shown to bind to porphyrin centres efficiently.⁸⁹
- Demetallation of zinc from porphyrins for retrieval of the original complexes is possible with the addition of HCl (conc.).



Scheme 2.6: Zinc metallation of example porphyrin-DNA strand **ODN1**.

100 equivalents of $\text{Zn}(\text{OAc})_2 \cdot 2\text{H}_2\text{O}$ were added to a solution of $10 \mu\text{M}$ porphyrin-DNA and the mixture was heated to $65 \text{ }^\circ\text{C}$ (**Scheme 2.6**). EDTA was used to quench the excess $\text{Zn}(\text{OAc})_2 \cdot 2\text{H}_2\text{O}$, and the crude product was purified *via* Nap-5 column. This method was, however thought to result in incomplete metallation of porphyrin-DNA, so 1000 – 2000 equivalents of $\text{Zn}(\text{OAc})_2 \cdot 2\text{H}_2\text{O}$ to **DPP** were added. A clear bathochromic shift from 409 nm to 413 nm and a hyperchromicity by 18 % (**Figure 2.5**) were thought to be the result of a better metallation.

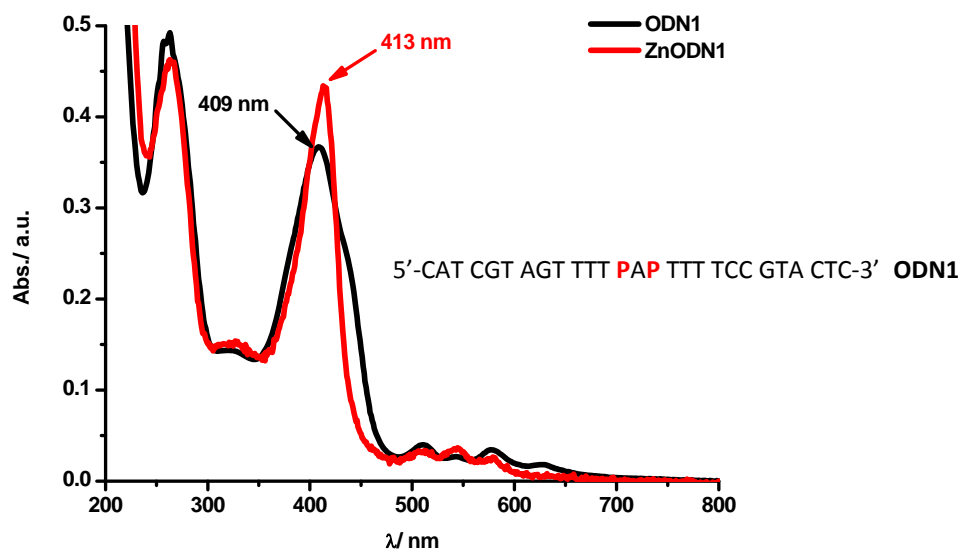


Figure 2.5: UV-vis spectra of porphyrin-DNA strand **ODN1** before and after zinc metallation. Spectra were acquired with 2 μM sample concentration and measured in water, 25 $^{\circ}\text{C}$.

The presence of three peaks in the Q-band, although two of them are shallow raises a question about the completion of metallation. The Q-bands of metallated porphyrins should show only two peaks.^{67, 106} The decrease in fluorescence emission of **ODN1** (**Figure 2.6**) is supporting evidence for the metallation of porphyrin-DNA, but the percentage of **ODN1** which has been successfully metallated cannot be determined based on these observations alone.

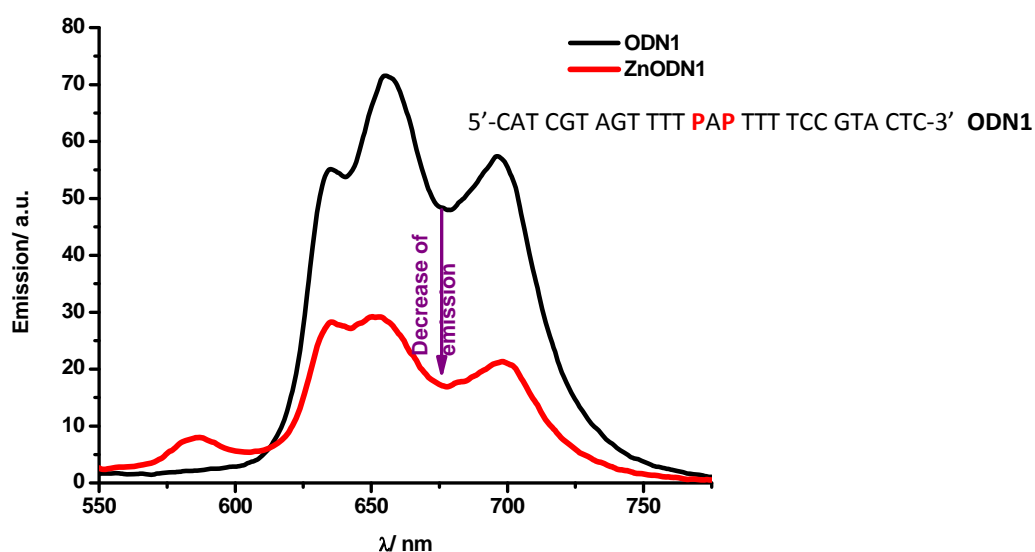
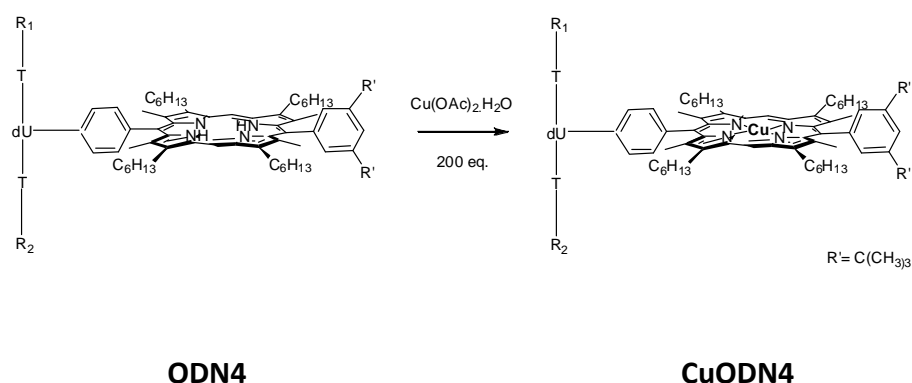


Figure 2.6: Emission spectra of porphyrin-DNA strand **ODN1** before and after zinc metallation. Spectra were acquired with 1 μM sample concentration and measured in buffer, 25 $^{\circ}\text{C}$.

It is important to note that evaluation of the fluorescence spectra of each sample in this project did not provide an absolute comparison. The emission was measured at the excitation wavelength of maximum UV-vis absorbance at the same concentration for each sample, and this wavelength value is not the same for different molecules. Instead, the relative intensities of peaks from the emission spectrum of a sample are considered. Absolute comparison of emission intensities can only be achieved when different samples are measured at an equal optical density (*i.e.* Abs.)

2.3.2 Copper metallation of porphyrin-DNA

ODN4 5'-TAC GAT TCG **TP**T CTA GCT AGC-3'



Scheme 2.7: Copper metallation of example porphyrin-DNA strand **ODN4**.

Following the metallation of porphyrin-modified oligonucleotides with zinc (**Scheme 2.6**), $\text{Cu(OAc)}_2 \cdot \text{H}_2\text{O}$ was used to metallate some porphyrin-DNA strands for characterisation by EPR spectroscopy (see **Chapter 4, Section 4.2.2**). Metallation of the simplest strand **ODN4** with only one porphyrin was investigated first in **Scheme 2.7**. With the EPR measurements to monitor successful metallation, 200 molar equivalents of $\text{Cu(OAc)}_2 \cdot \text{H}_2\text{O}$ per porphyrin were used to improve the metallation of **ODN4** from prior attempts with 1, 5, 10, 20, and 50 equivalents of Cu(II). An excess amount of EDTA (100 equiv. to $\text{Cu(OAc)}_2 \cdot \text{H}_2\text{O}$) was added to quench any Cu(II) remaining in solution, by forming CuEDTA. The sample was

purified *via* Glen-Pak cartridge to remove CuEDTA and to ensure that any EPR signal detected was due to Cu(II) bound inside the porphyrin, instead of free Cu(II) in solution. The usual Nap-5 column was replaced by Glen-Pak cartridge, which was essential for the complete removal of free Cu(II) in the reaction. The Glen-Pak cartridge is equivalent to reverse-phase chromatography, because it allows CuEDTA to elute in 0.1M TEAA prior to sample elution in MeCN (aq.) and can also desalt oligonucleotides. Although Glen-Pak cartridge does not purify as quickly as a Nap-5 column, which separates samples based on size exclusion principle, it is an ideal choice for the purification of metallated porphyrin-DNA.

In addition, EPR, UV-vis absorbance and fluorescence emission also indicated successful copper metallation of porphyrin-DNA.

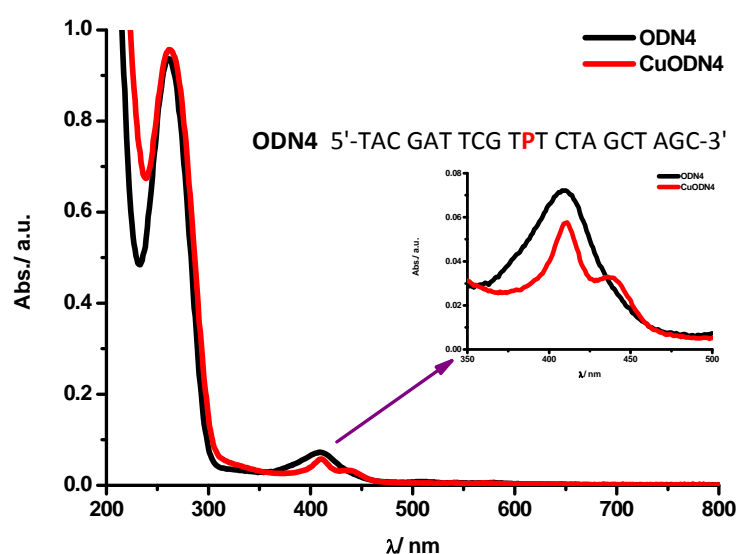


Figure 2.7: UV-vis spectra of porphyrin-DNA strand **ODN4** before and after copper metallation. Spectra were acquired with 5 μ M sample concentration and measured in water, 25 $^{\circ}$ C.

Figure 2.7 shows the porphyrin B-band absorption changes from a broad peak to shouldering (sh) peaks of smaller intensity upon heating the strand with Cu(II). This is indicative of a change in the electronic environment of the porphyrins, and so reinforces the view that Cu(II) has been bound to the porphyrin nitrogen ligands.

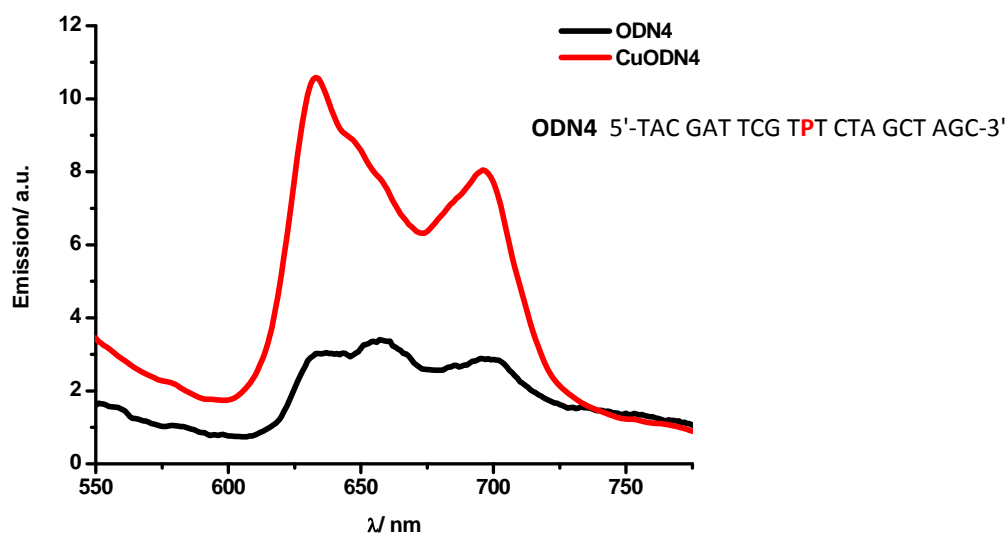


Figure 2.8: Emission spectra of porphyrin-DNA strand **ODN4** before and after copper metallation. Spectra were acquired with 5 μM sample concentration and measured in water, 25 $^{\circ}\text{C}$.

A change in the fluorescence emission intensity was also observed in strand **ODN4** before and after copper metallation (**Figure 2.8**). This also reflects a change in the electronic environment of porphyrins upon copper metallation. Both UV-vis and fluorescence emission spectra were used in conjunction with EPR to confirm the binding of copper to the nitrogens inside the porphyrin ring.

2.4 RP-HPLC analysis of oligonucleotides

Purification of some non-modified oligonucleotides, and diphenyl and tetraphenyl porphyrin modified oligonucleotides were attempted using RP-HPLC (reversed-phase high pressure liquid chromatography). The experimental details of RP-HPLC are described in **Chapter 5, Section 5.2.9**. To draw comparisons between non-modified and porphyrin-modified DNA, method A (35 minutes gradient) was used to purify oligonucleotides **ODN2, ODN6, ODN10, ODN18, ODN16** and **ODN17** were analysed by method B (60 minutes gradient). Both methods consist of 8.6 mM TEA/100 mM HFIP (hexafluoroisopropanol) buffer at pH 8.3, and MeCN. All chromatograms were monitored at 260 nm, at 260 nm and 410/420 nm for non-modified and porphyrin-modified oligonucleotides respectively.

Figure 2.9 a shows the RP-HPLC purification of non-modified single strand **ODN6**. The DNA major peak at 5-5.5 min (method A) was collected and re-injected to produce one sharp peak at 5.5 min retention time (**Figure 2.9 b**).

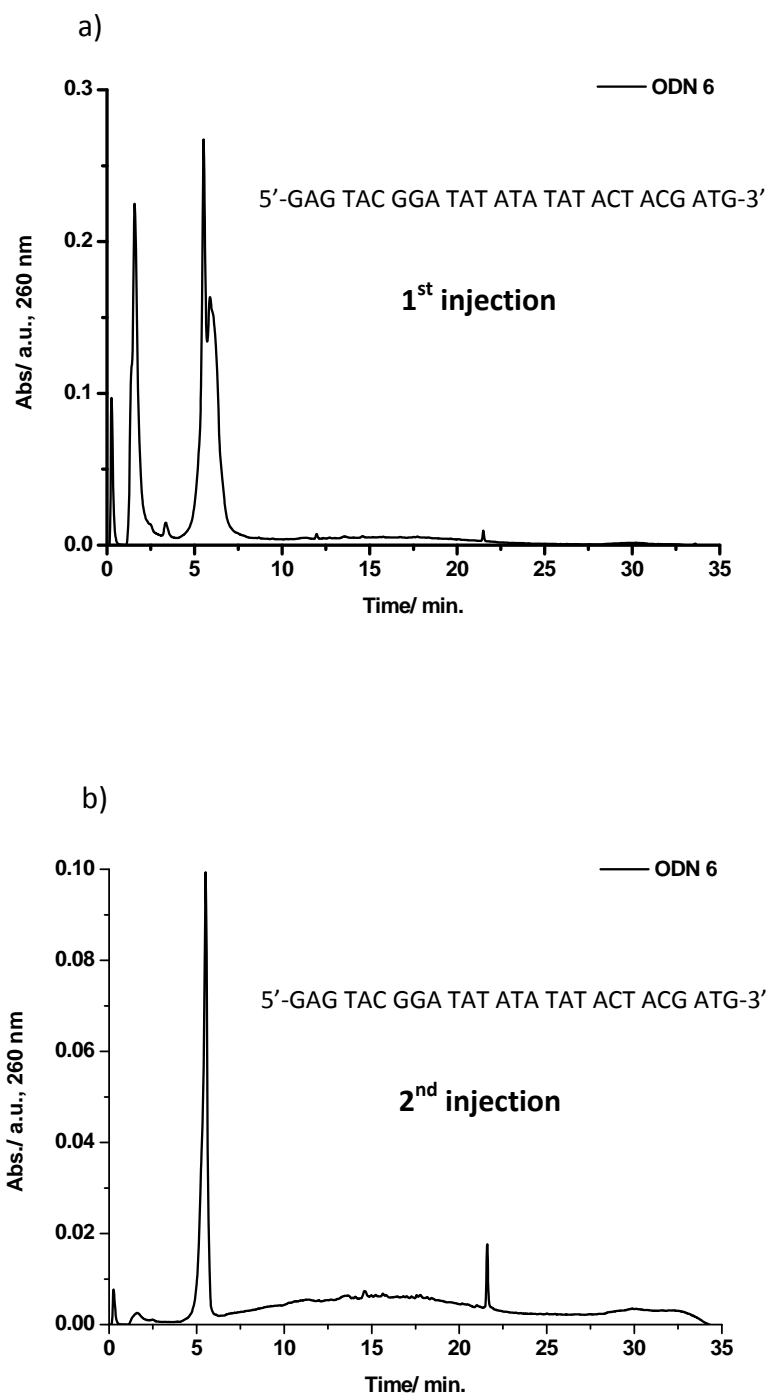


Figure 2.9: Analytical RP-HPLC chromatograms of non-modified single strand **ODN6**.

Interestingly, when the DNA major peak at 5-6 min retention time of **ODN10** (Figure 2.10 a) in the 1st RP-HPLC chromatogram was re-injected, a sharp peak at 2.5 min was obtained, as shown in Figure 2.10 b. However, MS analysis (Figure 2.11) showed the expected product peak at 8342.2.

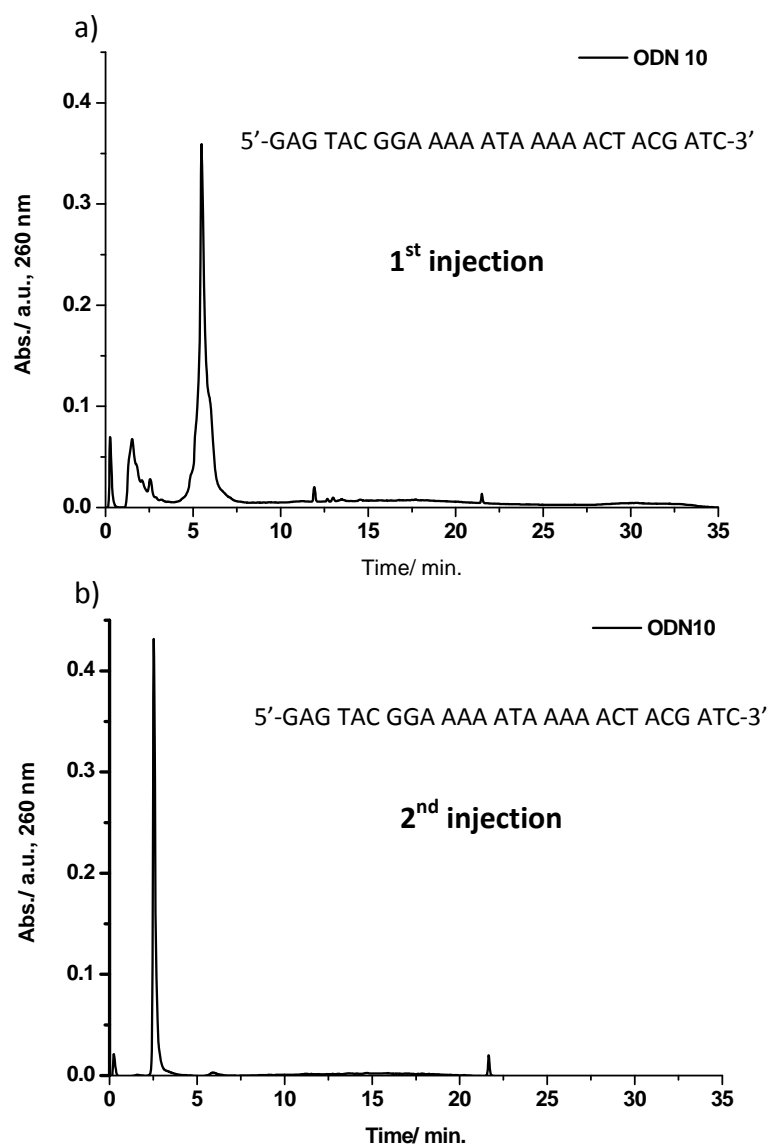


Figure 2.10: Analytical RP-HPLC chromatograms of non-modified single strand **ODN10**.

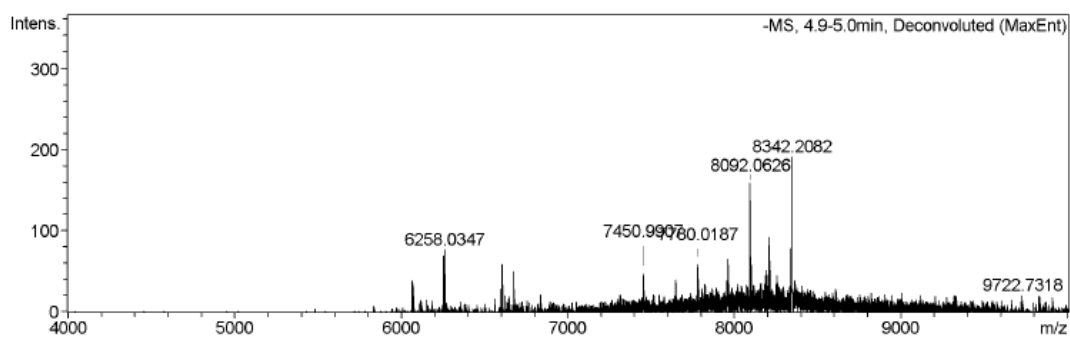


Figure 2.11: MS analysis of **ODN10** after 2nd HPLC injection.

RP-HPLC purification of diphenyl porphyrin-modified single strand **ODN2** (**Figure 2.12 a**) gave a **DPP-DNA** major peak at 20-22 min, which on re-analysis produced a single broad peak at 20 min retention time in **Figure 2.12 b**.

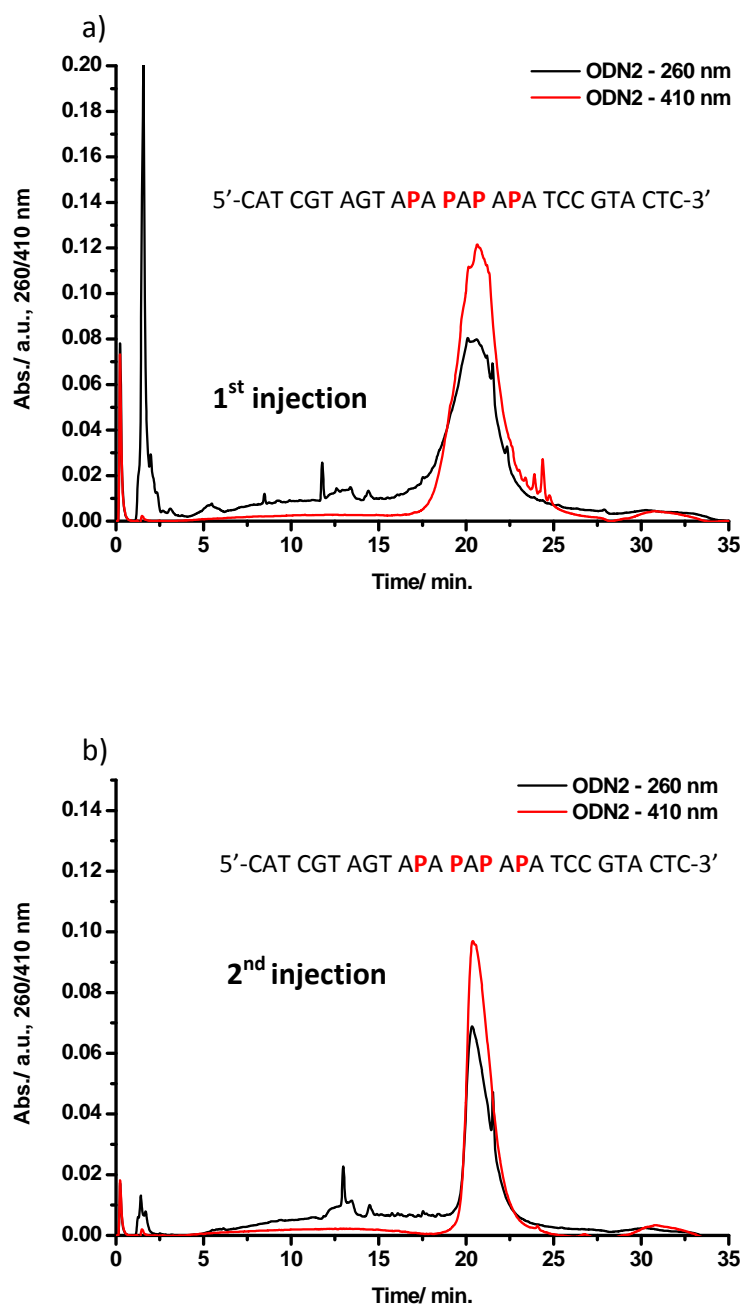


Figure 2.12: Analytical RP-HPLC chromatograms of diphenyl porphyrin-modified single strand **ODN2**.

When tetraphenyl porphyrin-modified single strand **ODN18** was purified on the same method as **DPP-DNA ODN2**, the most intense peak at 15-15.5 min (Figure 2.13 a) produced a single peak at 14.5 min retention time (Figure 2.13 b) when re-injected into the column.

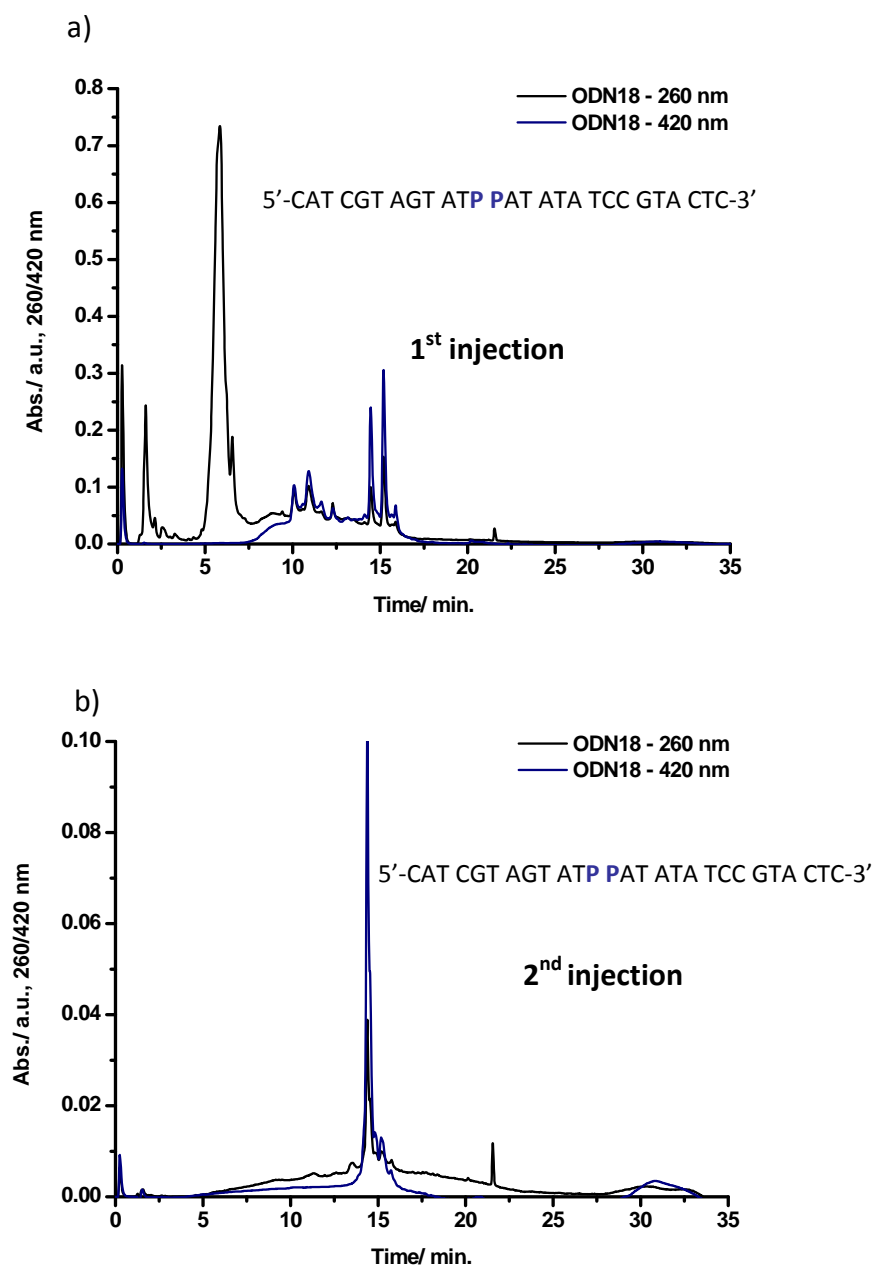
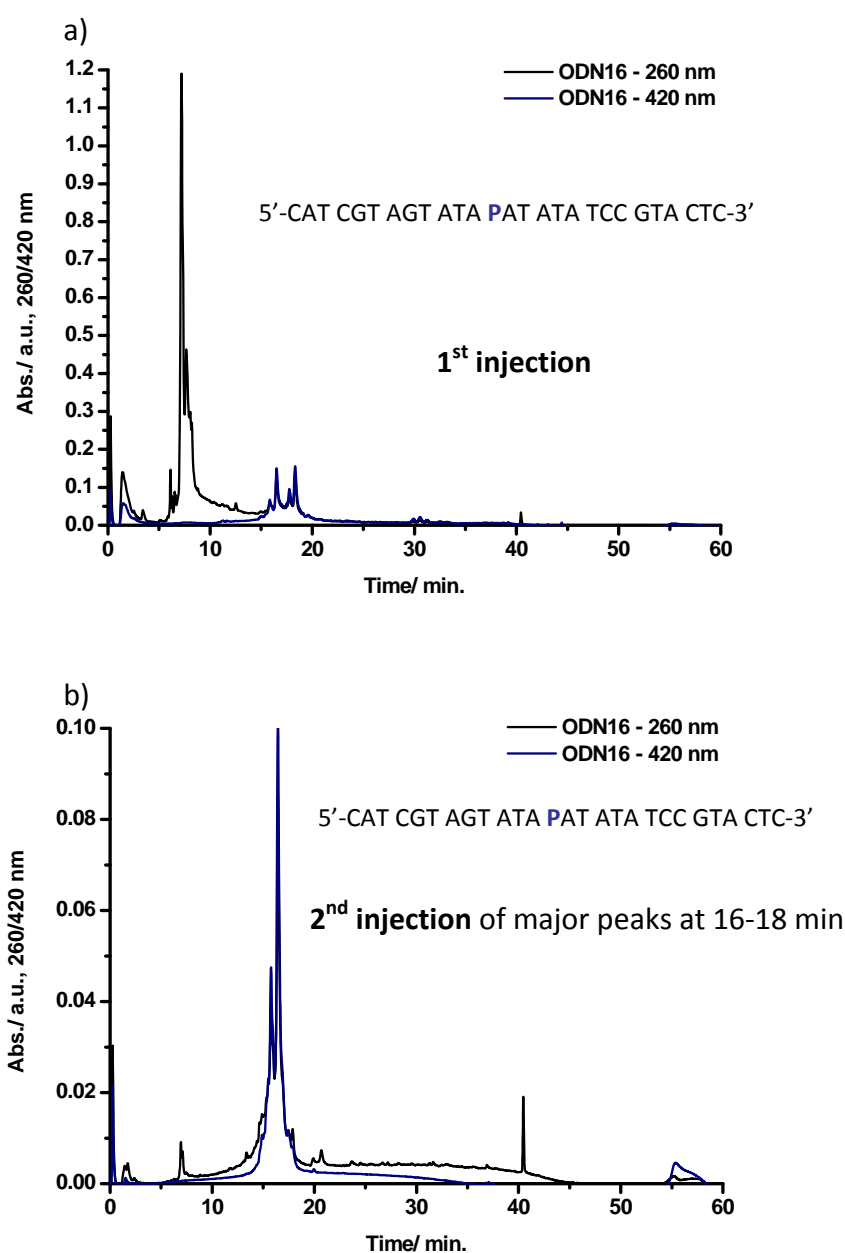


Figure 2.13: Analytical RP-HPLC chromatograms of tetraphenyl porphyrin-modified single strand **ODN18**.

Method B was used for purification of tetraphenyl porphyrin-modified **ODN16** single strand. The 1st RP-HPLC chromatogram of **ODN16** revealed intense peaks from **TPP-DNA** at 16-18 min and 18-20 min retention time (**Figure 2.14 a**). The 16-18 min fraction was re-injected and the dominant peak at 16-17 min from this 2nd injection (**Figure 2.14 b**) was further purified to obtain a clean peak at 16 min retention time (**Figure 2.14 c**). The major **TPP-DNA** peak at 18-20 min from the 1st HPLC chromatogram was also re-injected for a 2nd purification, and it also gave an intense peak at 16.5 min retention time (**Figure 2.14 d**).



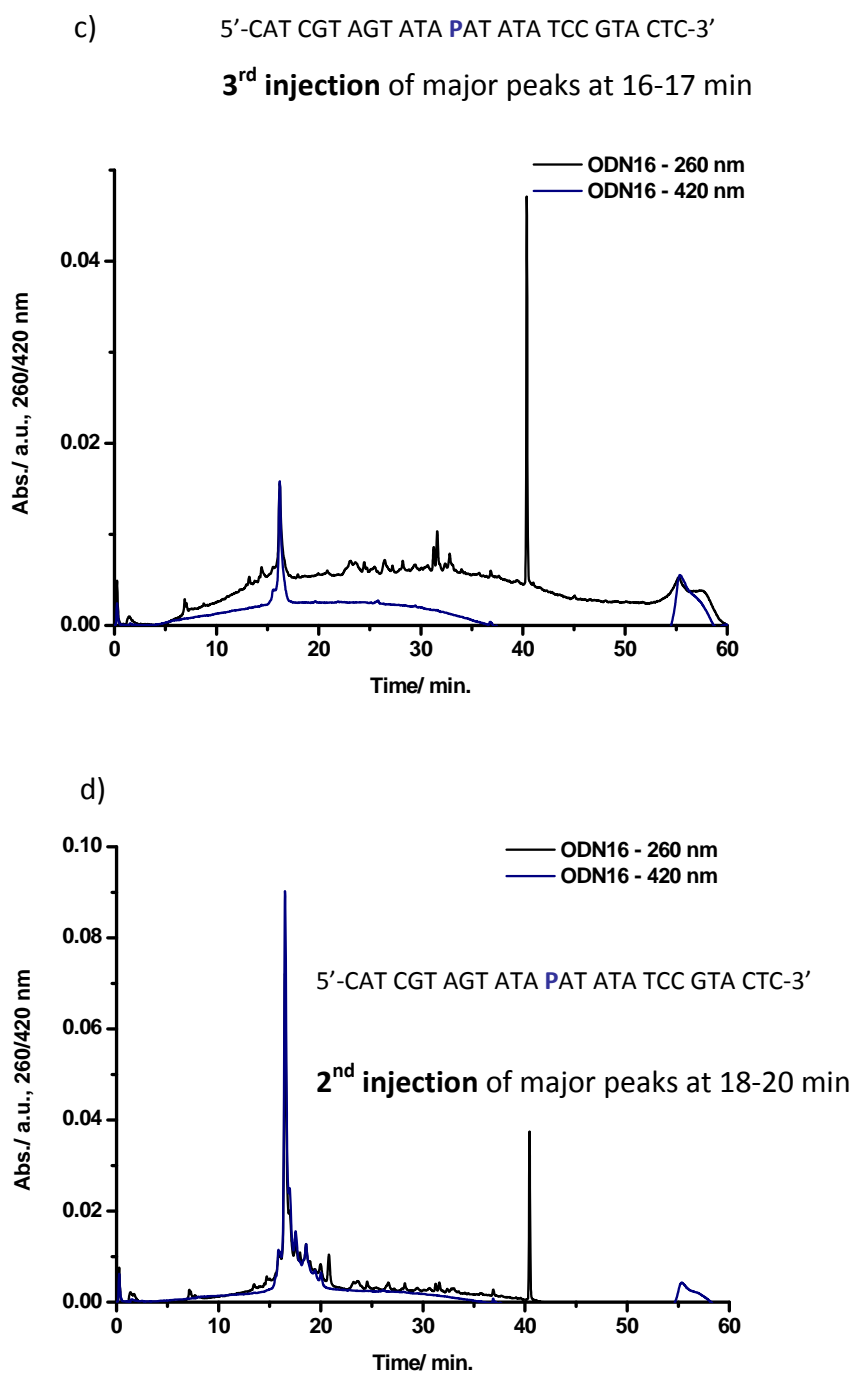


Figure 2.14: Analytical RP-HPLC chromatograms of tetraphenyl porphyrin modified single strand ODN16.

TPP-modified ODN17 was also purified by method B, and the TPP-DNA major peak at 41.5–42 min (Figure 2.15 a) was re-injected to produce a sharp single peak at 41 min retention time (Figure 2.15 b).

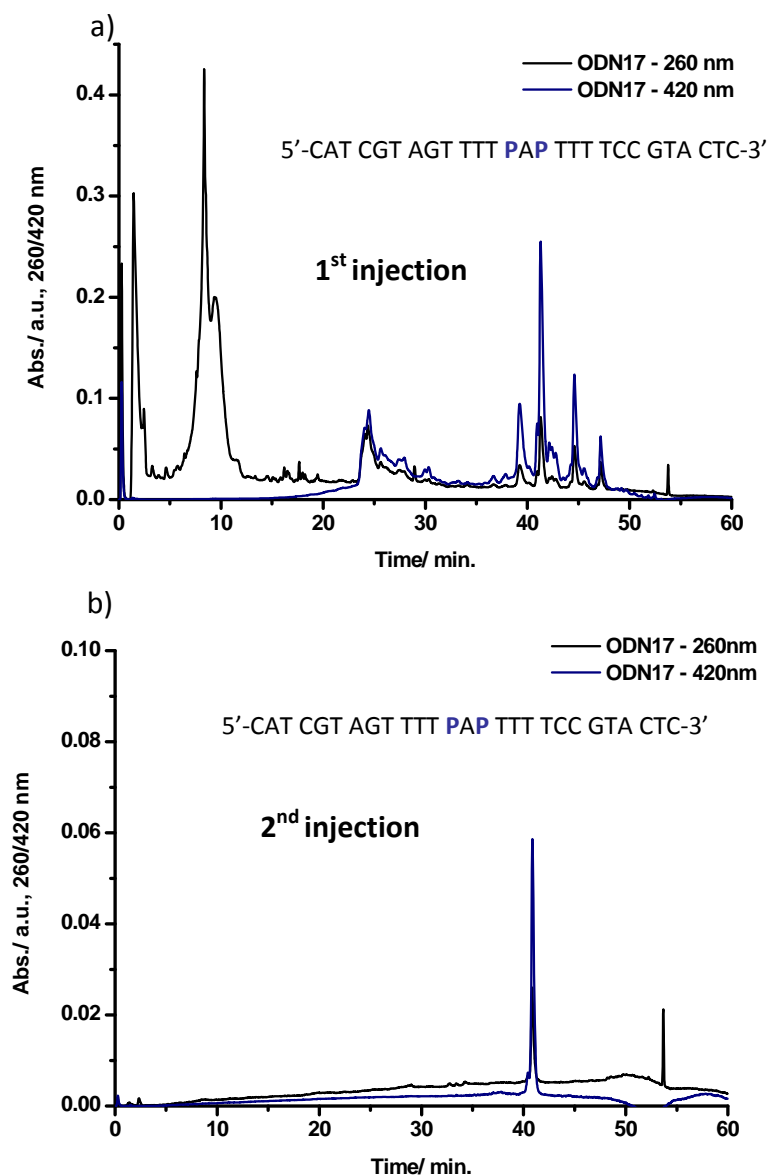


Figure 2.15: Analytical RP-HPLC chromatograms of tetraphenyl porphyrin modified single strand ODN17.

Copper(II) metallated porphyrin-DNA could not be purified using the same RP-HPLC methods, and DNA decomposition may be responsible for the production of multiple peaks in the chromatogram of copper porphyrin-DNA. It has been reported, that although transition metals (*e.g.* copper) binding to phosphate

backbone stabilise oligonucleotides, an excess amount can destabilise DNA.¹⁰⁷ However, this is not the situation with the porphyrin-DNA systems in the present work, because the EPR measurements show that the Cu(II) is chelated *inside* the porphyrin ring (**Chapter 4, Section 4.2.2.5**). Nevertheless, Cu(II) cations¹⁰⁸ and Cu(II) complexes with nitrogen-containing ligands (*e.g.* copper-phenanthroline,¹⁰⁹ copper-lysine¹¹⁰) are known to induce DNA damage. DNA decomposition in copper porphyrin-DNA proceeds *via* a redox process which leads to the reduction of Cu(II) to Cu(I) and free radical formation at the nucleobase is considered to be the more appropriate mechanism; this is further discussed in **Chapter 4, Section 4.4, Figure 4.36**. It is also worth noting that the repetitive extreme temperature changes (*i.e.* 120 K – 290 K) used in the EPR study may contribute to the lower stability of copper porphyrin-DNA compared to free base porphyrin-DNA.

Attempts to obtain mass spectrometric analyses of these HPLC purified porphyrin-DNA samples are still ongoing. However, previous standard MS analyses of these modified oligonucleotides (*i.e.* MALDI-ToF MS, ESI-MS) were not successful.

2.5 Conclusion

The UV-vis, fluorescence emission spectra, RP-HPLC chromatograms from this chapter, and other analytical data (see **Chapter 3**) provide strong supporting evidence for the successful incorporation of porphyrin monomers into oligonucleotides. Furthermore, it was possible to purify porphyrin-modified DNA by RP-HPLC. Ageing DNA samples produced significant differences in the chromatograms. Large non-modified DNA peaks and multiple porphyrin-DNA peaks at different retention times in the chromatograms of porphyrin-modified **ODN2, ODN16, ODN17, ODN18** suggest decompositions of DNA over time. The chromatograms also show the presence of failure sequences, including non-modified DNA. Therefore purification by HPLC is essential for the analysis, and the system described here is suitable for purifying porphyrin-DNA. It should be noted that the use of TEAA as buffer is not efficient in separating the DNA strands because the porphyrins induce immense streaking, thus making separation impossible. There remains a question as to whether the multiple peaks in the chromatograms are impurities that were present after the syntheses, or are the consequence of sample decomposition over time. This cannot be resolved at present, because the strands could not be measured immediately after syntheses due to limitations in the early methods. However, it should be noted that other porphyrin-modified DNA purified by members of the Stulz group showed clean traces for samples that were analysed by RP-HPLC immediately after syntheses. Although purification of copper porphyrin-DNA could not be achieved using RP-HPLC, these metallated oligonucleotides were analysed by EPR in **Chapter 4, Section 4.2.2**, to check for the presence of any paramagnetic impurities.

CHAPTER 3: PHYSICOCHEMICAL ANALYSES OF PORPHYRIN-DNA

Following the synthesis of diphenyl porphyrin **1**, its attachment to DNA and post-synthetic metallation of porphyrin-DNA, this section describes studies on porphyrin-modified oligonucleotides through the use of common analytical techniques, such as UV-visible, fluorescence and circular dichroism spectroscopies, as well as UV-vis and fluorescence melting studies. The general aims were to probe the electronic interaction between porphyrins held on DNA and how they influence the stability and structure of the DNA backbone.

3.1 UV-vis measurements of porphyrin-DNA

3.1.1 Theory of UV-vis spectroscopy

Ultraviolet-visible absorption spectroscopy is a physical analytical technique, where nearly monochromatic radiation is passed through a solution of sample and monitored as it is swept over a range of frequencies.¹¹¹ The spectrophotometer is named UV-vis (*i.e.* Ultraviolet-visible) spectrometer because it measures both the ultraviolet (190 nm – 420 nm) and visible (420 nm – 700 nm) regions of electromagnetic radiation.¹¹² The absorption is a measurement of the ratio of transmitted light over incident light, referred to as the transmittance **T**.

$$T = \frac{I}{I_0}$$

Equation 3.1¹¹¹

T= transmittance

I= transmitted intensity

I₀= incident intensity

The Beer-Lambert law governs the light transmittance, which is dependent on the concentration and pathlength of the sample (see **Chapter 5, Section 5.2.3**).¹¹¹

Herein, UV-vis spectroscopy is used to provide information on the electronic interaction within porphyrins held on DNA and to calculate the concentration of the DNA sample.

While oligonucleotides absorb in the ultraviolet region at 260 nm,¹¹³ porphyrin absorption spectra are dominated by π -electrons and have two main absorption regions: B-band or Soret band (380 - 420 nm) and Q-bands or red bands (450 – 700 nm). The B-band is more intense but less well resolved than the Q-bands, which appear as two pairs of peaks. The most red-shifted pair has the lower intensity, and both pairs become only two peaks at around 550 nm in metalloporphyrins.^{67, 106} The observation of these absorption bands in all the UV-vis spectra (**Figure 3.1**) helped to confirm that automated solid-phase synthesis had successfully combined the porphyrin and DNA units.

3.1.2 UV-vis spectra of porphyrin-DNA

Four conditions were investigated for the UV-vis absorption of porphyrin-DNA. They are (i) single strands and (ii) double strands at 15 °C, and (iii) single strands and (iv) double strands at 80 °C, with focus on the B-band absorbance of porphyrins. B-band absorption maxima are quantified to $\log \epsilon$ and presented in **Table 3.1** with other data. Unlike **ODN1** and **ODN2**, **ODN3** does not exist as a single strand, but as a self-complementary duplex. The temperature was raised progressively from 15 °C to 80 °C to ensure it passed the point where duplexes usually dissociate into single strands. Measurements of the different strands were performed using the same experimental settings to enable accurate comparisons.

Analogous to literature reports,³⁴ the changes in B-band extinction coefficients upon the hybridisation of **ODN1** and **ODN2** single strands to duplexes show that placement of the porphyrins in DNA grooves affects their electronic environments. The extents of these changes differ for different amounts of porphyrins attached to DNA. In the presence of non-modified complementary DNA strands, a decrease in extinction coefficients of **ODN1** is observed, whilst an increase is recorded for **ODN2**, which has twice the amount of porphyrins.

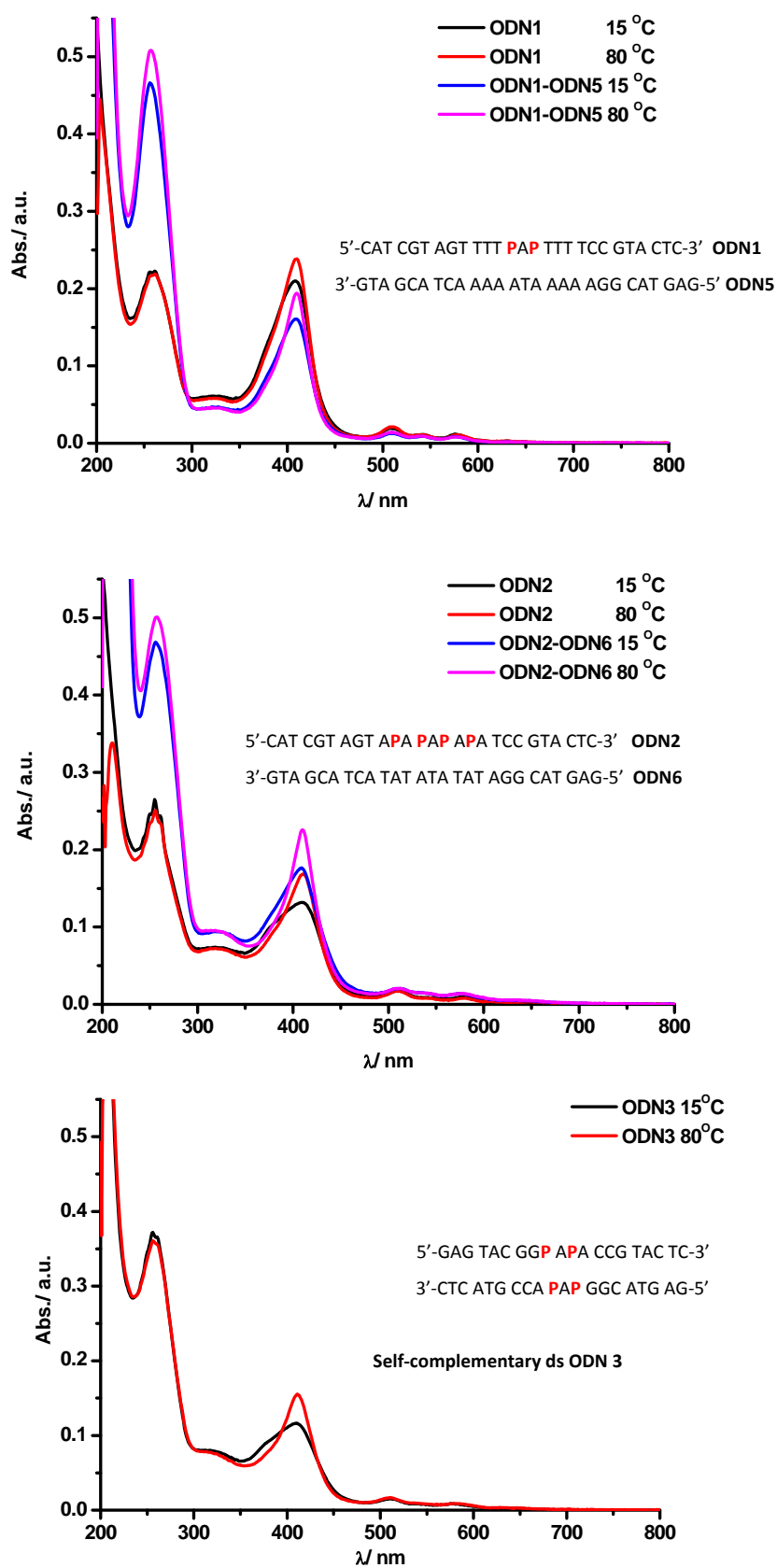


Figure 3.1: UV-vis spectra of porphyrin-DNA measured in water, at 1 μ M concentration of single and double strands at different temperatures.

In the four porphyrin array **ODN2** single strand, the B-band extinction coefficients are smaller than in the two porphyrin array **ODN1** at both temperatures, which contrast the observations for tetraphenyl porphyrin-DNA (**TPP-DNA**).³⁴ The opposite trend is observed in duplexes of **ODN2**, which have higher extinction coefficients than duplexes of **ODN1**. For the self-complementary duplex **ODN3** with zipper porphyrin stacking, the B-band extinction coefficients are lower than expected, although they have the same number of porphyrins as duplexes of **ODN2**. The interactions between chromophores results in B-band broadening in strands which have more than two **DPP** (e.g. **ODN2** and **ODN3**) at 15 °C. These electronic interactions are not very strong, because the second peak appears in a shoulder form, instead of as a distinct absorbance. The B-bands of **DPP-DNA** are also less broad than the B-bands of **TPP-DNA**.³⁴ All of these observations indicate that the type, the amount and the stacking of porphyrins influence the interactions between porphyrins attached to DNA.

Diphenyl porphyrin-DNA (**DPP-DNA**) single strands and double strands show significant increases in their B-band absorption maxima upon heating. The peaks also sharpen, and are comparable to observations in Bouamaied's work.^{34, 114} This hyperchromicity is higher in duplexes of **ODN1** than in their single strands (i.e. 21 % compared to 14 %). At 80 °C, the unstacking of porphyrins due to DNA denaturing results in the enhancement of porphyrin absorbance intensity. When exposed to higher temperature, DNA double helical arrays first dissociate into single strands and the arrangement of diphenyl porphyrins gets disrupted, analogous to tetraphenyl porphyrin-DNA.³⁴ Although UV-vis spectra are good indicators of the π - π interactions between porphyrins attached to DNA, this technique alone is not sufficient to understand the effect of porphyrin unstacking on the structure and stability of the DNA. UV-vis melting studies are therefore required (see **Section 3.3**).

Table 3.1: UV-vis data for porphyrin-DNA single and double strands at 15 °C and 80 °C.

Porphyrin-DNA	Temp. (°C)	Ratio P — bases	B-band Abs. maxima [nm (lgε)]	Abs. intensity (a.u.)	Intensity increases (%)
ss ODN1 (PAP)	15	0.07:1	408 (5.32)	0.210	0 ↓
ss ODN1 (PAP)	80	0.07:1	410 (5.38)	0.239	+ 14 %
ds ODN1 (PAP)	15	0.04:1	409 (5.21)	0.161	0 ↓
ds ODN1 (PAP)	80	0.04:1	410 (5.29)	0.194	+ 21 %
ss ODN2 (PAPAPAP)	15	0.15:1	380 (sh) 409 (5.12)	0.132	0 ↓
ss ODN2 (PAPAPAP)	80	0.15:1	410 (5.23)	0.169	+ 28 %
ds ODN2 (PAPAPAP)	15	0.07:1	380 (sh) 409 (5.25)	0.177	0 ↓
ds ODN2 (PAPAPAP)	80	0.07:1	410 (5.35)	0.226	+ 28 %
ds ODN3 (PAP)	15	0.10:1	380 (sh) 409 (5.07)	0.117	0 ↓
ds ODN3 (PAP)	80	0.10:1	411 (5.19)	0.155	+ 33 %

3.2 Fluorescence emission measurements of porphyrin-DNA as a complementary tool to UV-vis spectroscopy

The study of porphyrin-DNA arrays for their potentials in material science, and possibly in biological science, needs technically reliable and biologically safe methodologies. Fluorescence emission spectroscopy is one technique that satisfies these requirements, because:

- The emission can be detected at very low concentrations, making it an ideal technique when the solubility of large supramolecules is an issue.
- The radiation is not toxic to cells, so fluorescence spectroscopies can be studied in biological systems.
- It is sensitive to the microenvironment of fluorophores.¹¹⁵

For the investigation of multiporphyrin arrays based on a DNA scaffold, fluorescence emission spectroscopy is as important an analytical tool as UV-vis spectroscopy, because porphyrins both absorb and emit light.^{106, 116} Fluorescence emission spectroscopy is, therefore, used to obtain more information on the physicochemical properties of porphyrin-DNA arrays, in particular the factors which influence the electronic interaction between chromophores.

3.2.1 Theory of fluorescence emission spectroscopy

In fluorescence emission spectroscopy, molecules are first excited to a high electronic energy level E_1 by absorption of electromagnetic radiation, after which they then relax to a lower vibrational energy level E_2 before emitting a photon during decay back to the ground electronic state. The energy of the released photon is expressed in **Equation 3.2**.

$$h\nu = E_1 - E_2$$

Equation 3.2¹¹²

h = planck constant (J s)

ν = frequency of radiation emitted (Hz)

E = energy state (J)

The steps involved in the fluorescence emission are depicted in **Figure 3.2**. After absorbing light, the upper vibrational states perform radiationless decay and the excess energy is given to surrounding molecules. The transition from vibrational ground state of the upper electronic state then occurs to produce radiation, commonly known as fluorescence.¹¹²

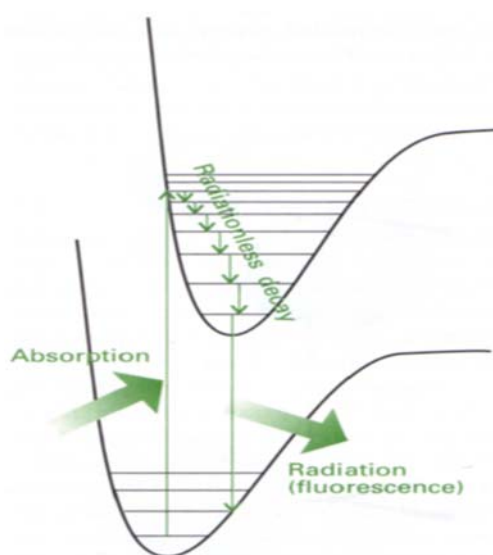


Figure 3.2: The steps involved in fluorescence emission.¹¹²

The energy levels involved in the transitions that result in emission are better illustrated by an energy level diagram (**Figure 3.3**). According to Kasha's rule,^{67, 117} after being excited to a higher energy level, the excited molecules need to relax to S_1 and T_1 states before showing emission (*i.e.* fluorescence or phosphorescence). The $S_0 \rightarrow S_1$ transition results in Q-bands in the absorption spectra of porphyrins. The $S_1 \rightarrow S_0$ transition is a radiative and spin-allowed transition that leads to fluorescence emission. In contrast, $T_1 \rightarrow S_0$ is a radiative spin-forbidden transition which is commonly known as phosphorescence emission, and lasts longer than the spin-allowed fluorescence. Besides these radiative transitions, other non-radiative transitions also occur in the system, such as intersystem crossing from $S_1 \rightarrow T_1$. Because fluorescence emission can only occur from a spin-allowed $S_1 \rightarrow S_0$ transition, the emission wavelengths of molecules are thus independent of the excitation wavelengths.⁶⁷

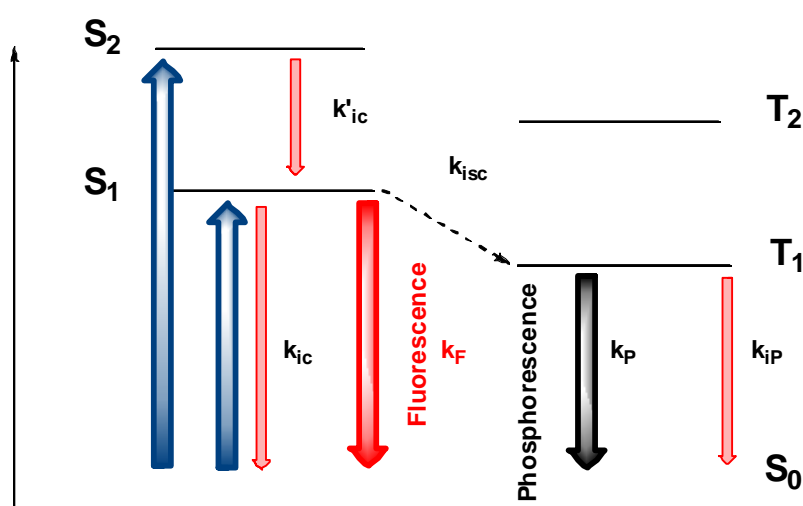


Figure 3.3: Energy level diagram of electronic transitions for a diamagnetic molecule.

The energy loss from excitation to emission is inevitable for fluorescent molecules in solution, (*e.g.* porphyrin-DNA strands in water). The emitted photon has less energy, hence longer wavelength (lower frequency) than the absorbed photon which has shorter wavelength (higher frequency). This energy difference is described by the shift in wavelength between the absorption and emission maxima, and is often referred to as the Stokes shift (**Figure 3.4**).¹¹⁸ For diphenyl porphyrin-DNA, the absorption maxima of porphyrins are around 410 nm, whilst their emission maxima are beyond 600 nm.

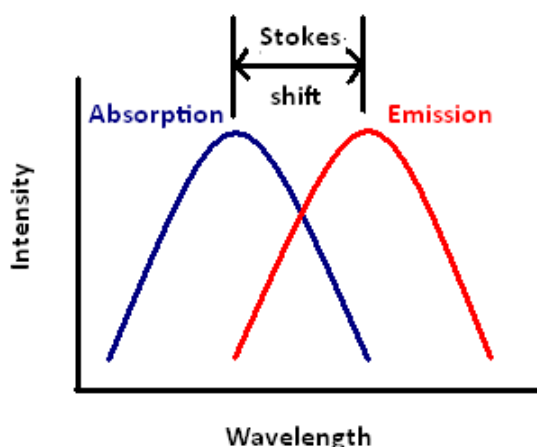


Figure 3.4: Stokes shift

Fluorescence emission spectroscopy is used as a complementary analytical technique to UV-vis absorption spectroscopy for the analyses of porphyrin-DNA.

3.2.2 Fluorescence emission spectra of porphyrin-DNA

The single and double strands of **ODN1**, **ODN2** and **ODN3** were measured at the same concentration as those recorded on the UV-vis spectrophotometer, and their analyses are quantified in **Table 3.2**. Herein, "sh" denotes shouldering peaks and the emission maxima are expressed in relative intensities. Both percentage of intensity decrease and the relative intensity (rel. int.) are calculated relative to the highest emission maximum. All porphyrin-modified DNA show different spectral shapes (**Figure 3.5**) to the fluorescence emission of free-base diphenyl porphyrin building block **2HDPP** (**Figure 3.6**), which was measured by Dr. Stulz.³² The shapes of **DPP**-DNA are also different from those of **TPP**-DNA arrays. There are three emission maxima in the spectra of **DPP**-DNA, whilst **TPP**-DNA has only two.³⁴ These findings indicate a distinctively different form of electronic interaction within diphenyl porphyrins connected to DNA, compared to the free-base porphyrin, and they are also different from **TPP**-DNA.

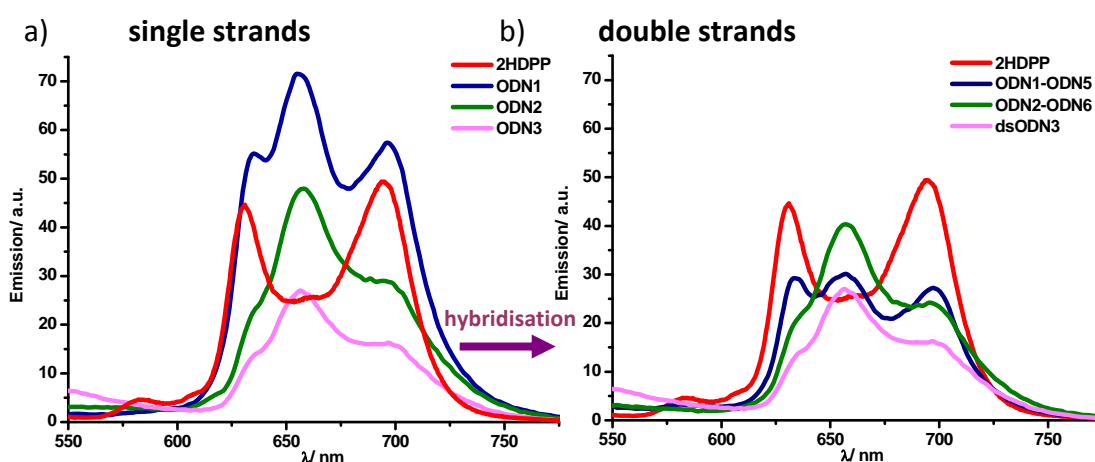


Figure 3.5: Fluorescence emission spectra of 1 μ M porphyrin-DNA single and double strands measured in buffer, and of porphyrin building block.

As reported by Stulz *et al.*,³⁴ the changes in emission spectra of diphenyl porphyrin-DNA help to reinforce the presence of porphyrin-DNA stacked arrays in single and double strands. As the number of porphyrins increases in single strands, a steady decrease in emission intensity is observed. Upon hybridisation to complementary non-modified DNA sequences, the shapes of spectra remain intact (**Figure 3.7**), but their emission intensities decrease significantly for all diphenyl

porphyrin-DNA. This finding is opposite to that for tetraphenyl porphyrin-DNAs, which have their luminescence enhanced when duplexes are formed.³⁴ A precise explanation is not yet known, but the larger steric hindrance of bulkier tetraphenyl porphyrins is assumed to be responsible for the smaller electronic interaction of chromophores. The same effect is most profound in **ODN1**, where hybridisation reduces the emission intensity by 58 %, compared to only a 16 % decrease in **ODN2**. The **ODN1-ODN5** emission intensity decrease is also in line with the diminishing of its duplex B-band absorbance. The smaller reduction in emission intensity of **ODN2-ODN6** compared to the **ODN1-ODN5** array is thought to be the result of a larger steric hindrance in the former duplex, which has twice the number of porphyrins. Most notable is the significantly smaller emission maxima of **ODN3** (Figure 3.5 b), where self-complementary existence of the duplex can cause the porphyrins to stack in a zipper manner. It seems that the π - π interaction of porphyrins is enhanced on a zipper array, which can place the chromophores closer than expected, thus increases their stacking.

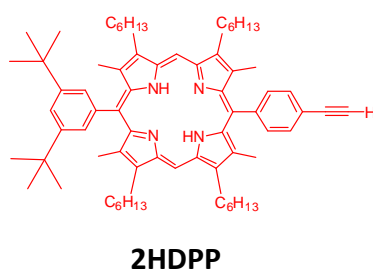


Figure 3.6: Porphyrin building block **2HDPP**.

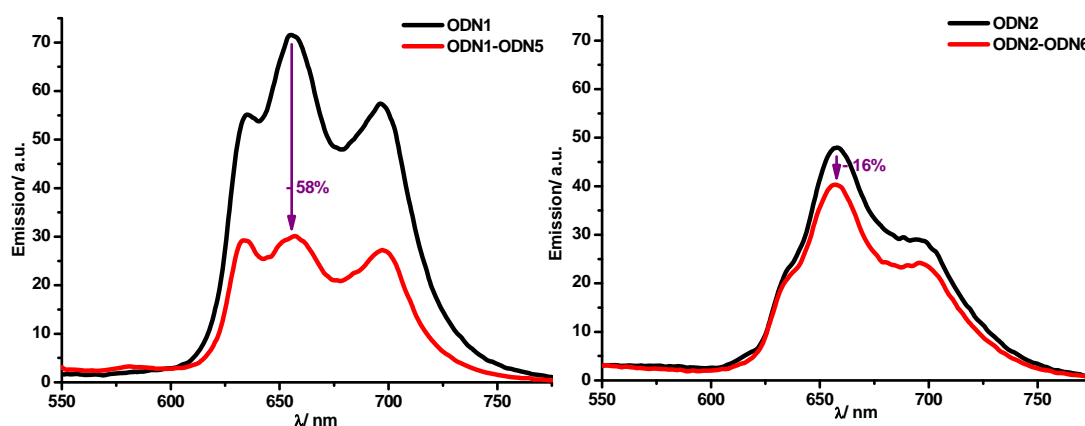


Figure 3.7: Decrease in emission intensity upon hybridisation of 1 μ M porphyrin-DNA single strands measured in buffer.

The emission intensity is not only dependent on the stacking of porphyrins, but also on the sample concentration. A decrease in luminescence is steadily detected across all porphyrin-DNA strands with decreasing sample concentration. These results also show that at a concentration up to 1 μM , porphyrin-DNA does not aggregate, because the fluorescence emission patterns of all sequences remain unaltered from 0.1 – 1 μM (**Figure 3.8**).

Table 3.2: Fluorescence emission data of porphyrin-DNA single and double strands.

Porphyrin-DNA	Ratio P — bases	Emission maxima [nm (rel. int.)]	Intensity decrease
ss ODN1 (PAP)	0.07:1	635 (0.77), 655 (1.00), 697 (0.80)	0 ↓
ds ODN1 (PAP)	0.04:1	634 (0.97), 657 (1.00), 698 (0.90)	- 58 %
ss ODN2 (PAPAPAP)	0.15:1	636 (sh), 658 (1.00), 695 (sh)	0 ↓
ds ODN2 (PAPAPAP)	0.07:1	636 (sh), 657 (1.00), 696 (0.60)	- 16 %
ds ODN3 (PAP)	0.10:1	636 (sh), 657 (1.00), 697 (sh)	

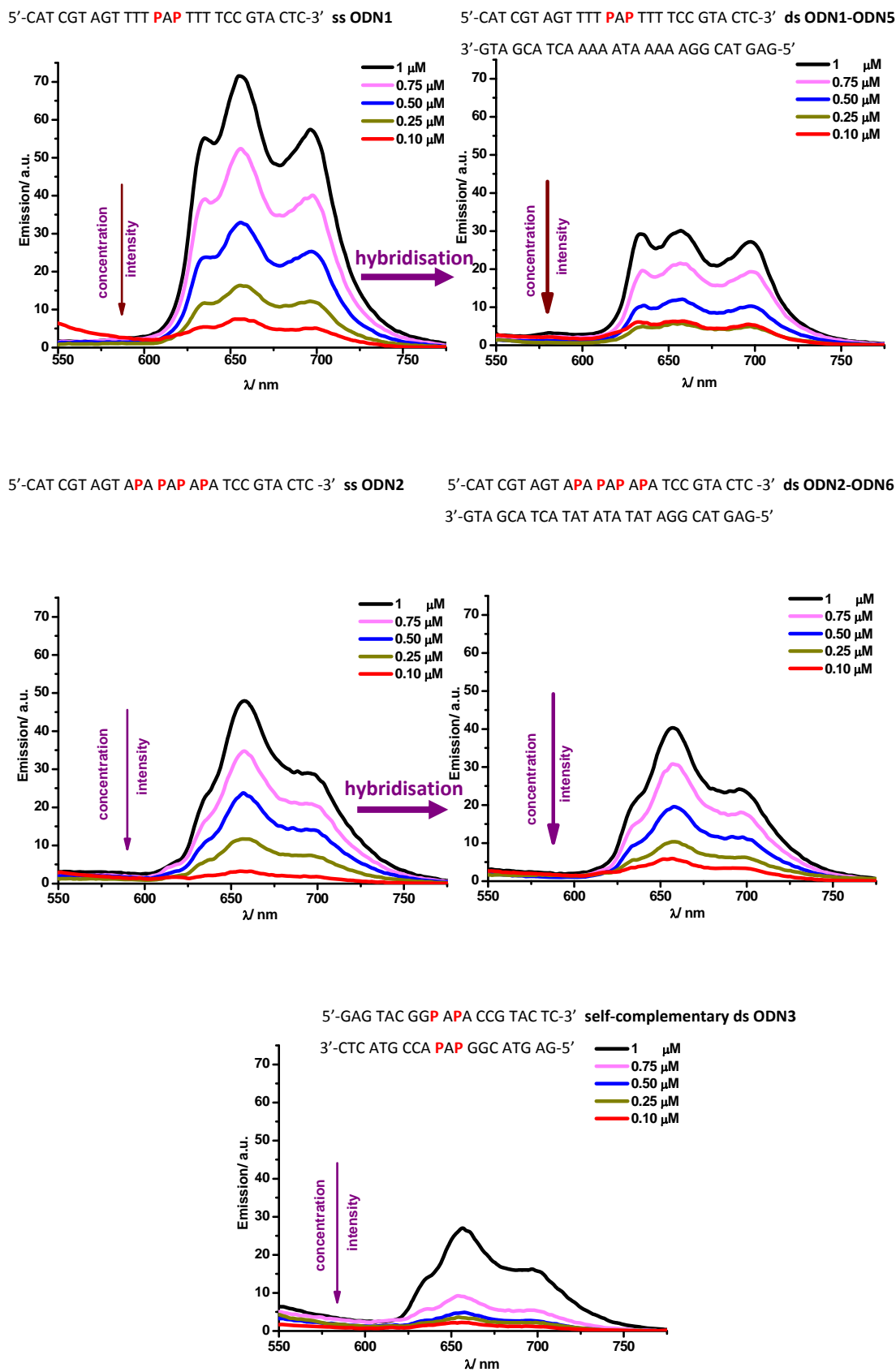


Figure 3.8: Fluorescence emission of DPP-DNA at different concentrations measured in buffer.

The intensity of emission maxima of the oligonucleotides were plotted against sample concentrations (**Figure 3.9**). A linear relationship is observed, which shows that the decrease in luminescence at lower concentrations is purely a dilution factor. Diphenyl porphyrin-DNA thus does not seem to aggregate and there is no intermolecular interaction of porphyrins attached to DNA up to 1 μM concentration.

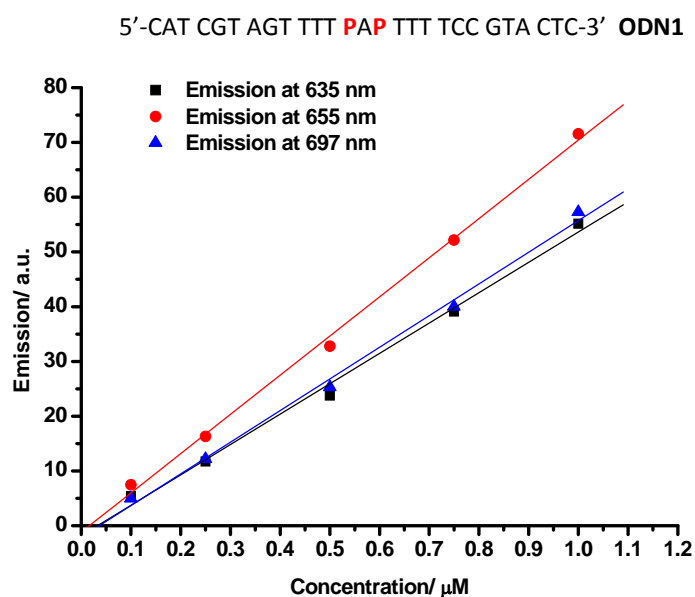


Figure 3.9: Linear relationship between emission maxima and concentrations of ODN1.

In summary, both UV-vis and fluorescence emission spectroscopies show that the arrangement and interactions of porphyrins are influenced by DNA. Details of energy transfer and in depth understanding of the electronic interaction within porphyrins held on DNA lie beyond the scope of this thesis. However, further analyses into the relation between these chromophores attached to the DNA backbone are discussed in the EPR study in **Chapter 4**.

3.3 UV-vis temperature and melting profiles of porphyrin-DNA arrays

Whilst UV-vis and fluorescence emission spectroscopies provide information on the electronic interactions of porphyrins attached to DNA, other techniques such as UV-vis and fluorescence melting studies are required to analyse the stability of DNA. UV-vis melting experiments were conducted in buffers, because they have been widely used for the melting studies of DNA.⁵ Buffers are known to stabilise the DNA duplexes better than pure water. The experiments were performed as close to physiological conditions as possible, so the buffer of 100 mM NaCl, 50 mM KH_2PO_4 , pH 7.0 was used throughout for consistency, and also because this was the buffer reported in Stulz and Bouamaied's publications.^{32,34} Sample concentrations of 1 - 2 μM were kept similar to those in UV-vis and fluorescence measurements.

The understanding of oligonucleotide stability is enhanced by the thermodynamic UV-vis melting study. Melting temperature T_m is the most important information deduced from the melting profile of DNA,

By definition, DNA melting temperature, denoted as T_m , is the temperature at which half of the DNA double strands have dissociated into single strands with the "random-coil" structure.¹¹⁹

In the following measurements, T_m is the turning point in the derivative of a UV-vis melting curve. Details of the instrument set-up are written in **Chapter 5, Section 5.2.4**.

3.3.1 UV-vis temperature profiles of porphyrin-DNA single strands

At first, the temperature profiles of single strands **ODN1** and **ODN2** were monitored at 410 nm absorption wavelength, where porphyrins on **DPP**-DNA absorb light (**Figure 3.10**). The curves reveal a similar inflection point, averaged at $T_p = 43^\circ\text{C}$ for both diphenyl porphyrin-modified single strands. These observations, which are comparable to those of tetraphenyl-porphyrin DNA reported by Stulz *et al.*³² suggest a form of single strand structural stabilisation in **DPP**-DNA.

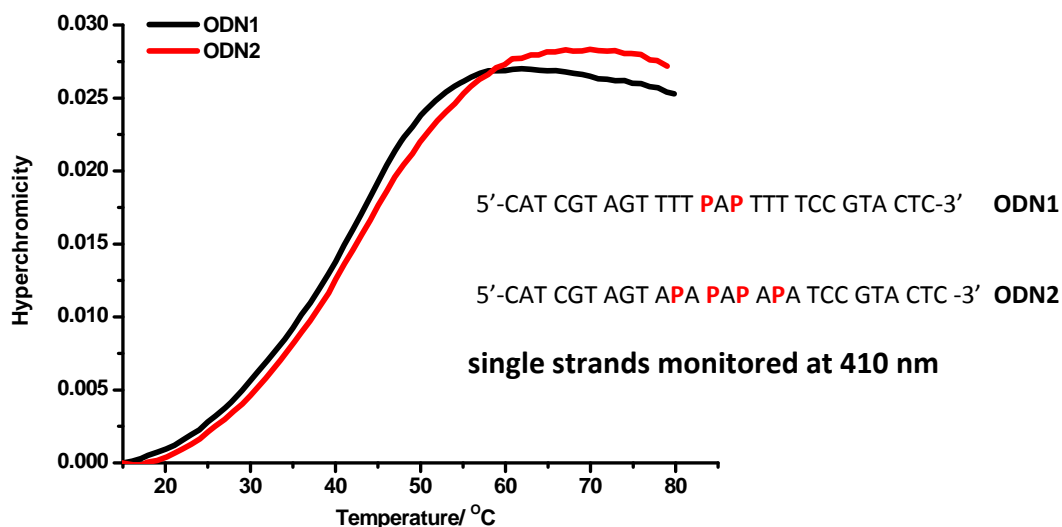


Figure 3.10: UV-vis temperature profiles of 1 μ M single strand **DPP**-DNA in buffer and monitored at 410 nm.

3.3.2 UV-vis melting profiles of porphyrin-DNA double strands

Following the recording of the temperature profiles of their single strands, **ODN1** and **ODN2** were hybridised with non-modified complementary strands **ODN5** and **ODN6**, respectively. The UV-vis melting measurements of **ODN1-ODN5** and **ODN2-ODN6**, along with **ODN3** and its equivalent non-modified duplex **ODN7** were first monitored at 260 nm, as shown in **Figure 3.11**.

The melting curve of non-modified self-complementary double strand **ODN7** recorded at 260 nm shows $T_m = 72$ °C, whilst its porphyrin modified analogue **ODN3** shows $T_m = 62$ °C. The melting profile of the equivalent non-modified duplex of porphyrin-DNA **ODN2-ODN6**, recorded by Dr. Stulz,³² shows a much higher $T_m = 65$ °C compared to its porphyrin modified analogue **ODN2-ODN6** for which $T_m = 37$ °C. This demonstrates a destabilisation effect induced by porphyrin modifications. Since **ODN3** and **ODN2-ODN6** both have four porphyrins, structural destabilisation of their double strands could therefore depend on the stacking of porphyrins on DNA. The melting curve of double strand **ODN1-ODN5**, however,

could not be obtained at 260 nm despite many repeated measurements, which raised questions about the sample purity or stability of the duplex.

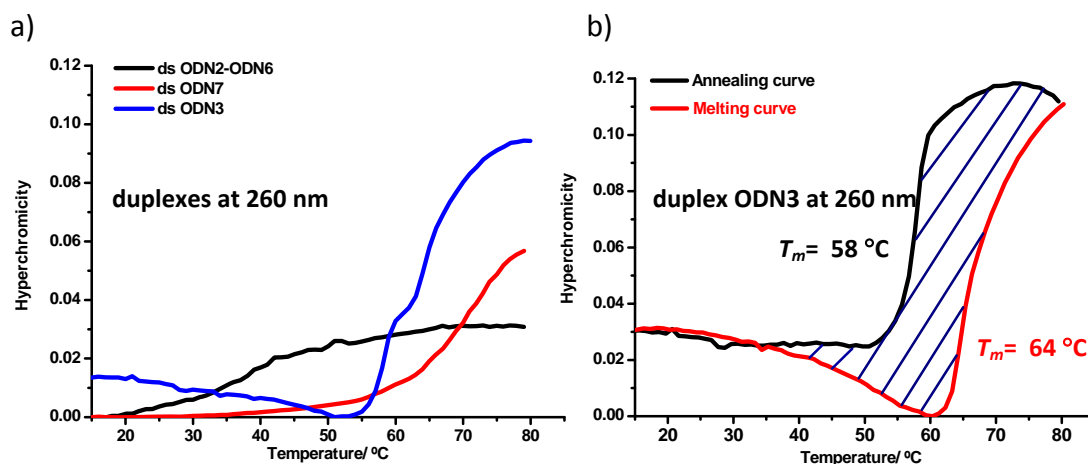


Figure 3.11: UV-vis melting profiles, measured at 1 μM concentration, in buffer and monitored at 260 nm of a) different duplexes and b) annealing and melting curves of duplex **ODN3**.

Furthermore, the melting profile of the self-complementary duplex **ODN3** shows a destabilisation per porphyrin of $\Delta T_m/\text{porphyrin} = 2.5\text{ }^\circ\text{C}$, which is much less than the value $\Delta T_m/\text{porphyrin} = 7\text{ }^\circ\text{C}$ in **ODN2-ODN6**. This suggests an interlocking system of porphyrins in a self-complementary duplex (**Figure 3.12**), where porphyrins stack in a zipper fashion, resulting in a lower destabilisation effect on the DNA double strands.

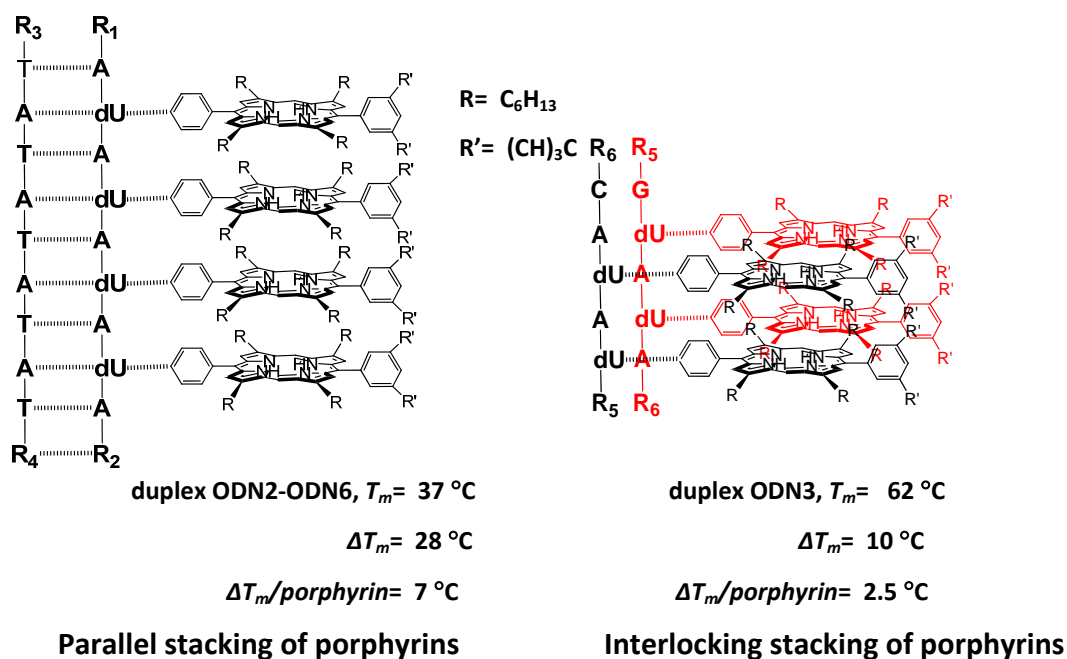


Figure 3.12: Effects of porphyrin stacking on DNA duplex stability.

Most notable is a large hysteresis, $\Delta T_m = 6\text{ }^\circ\text{C}$ (**Figure 3.11 b**), between the annealing and the melting curves of the **ODN3** duplex, which indicates different kinetics between the two processes. Certainly, a deviation observed from 15 - 60 $^\circ\text{C}$ in the melting curve of **ODN3** indicates that something happens to the duplex before it starts denaturing.

Data from the temperature profiles and melting profiles of different strands monitored at different absorption wavelengths are summarised in **Table 3.3**.

Table 3.3: T_p and T_m of single strands and double strands monitored at different wavelengths.

Strands	T_m or $T_p/^\circ\text{C}$ at 260 nm	T_m or $T_p/^\circ\text{C}$ at 410 nm
ss ODN1 (PAP)	N/A	43
ds ODN1-ODN5 (PAP)	N/A	44
ss ODN2 (PAPAPAP)	N/A	43
ds ODN2-ODN6 (PAPAPAP)	37	44
ds ODN3 (PAP)	62	44
ds ODN7 (no P modification)	72	N/A

UV-vis melting studies of duplexes **ODN1-ODN5**, **ODN2-ODN6** and **ODN3** at 410 nm, which is the absorption wavelength of porphyrins, all show an average turning point of $T_m = 44\text{ }^\circ\text{C}$. This number is very close to the average turning point $T_p = 43\text{ }^\circ\text{C}$ of single strands **ODN1** and **ODN2** (**Figure 3.10**). Duplex **ODN7** does not have a turning point at 410 nm because it has no porphyrin.

The fact that $T_m(410\text{ nm}) \neq T_m(260\text{ nm})$ for modified duplexes could indicate that dissociation in the porphyrin region is different from the DNA region at high temperature. In theory, an identical UV-vis absorbance for single strands and duplexes of modified oligonucleotides at 80 $^\circ\text{C}$ would confirm complete denaturing of the duplexes.³⁴ However, this is not the case for all diphenyl porphyrin-DNA, as shown in **Figure 3.1**. Some degree of diphenyl porphyrin stacking may still be

preserved upon DNA denaturing, just as observed for tetraphenyl porphyrin stacking in the literature.³⁴ Nevertheless, the observations from UV-vis and UV-vis melting studies alone are not enough for a complete proof. Circular dichroism spectroscopy is needed and will be discussed later in **Section 3.5**.

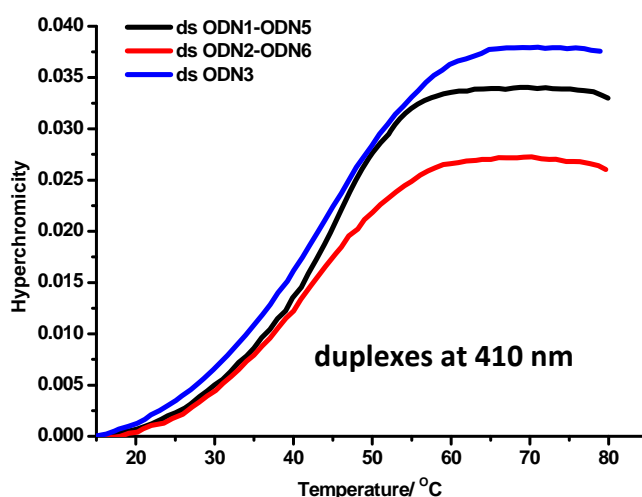
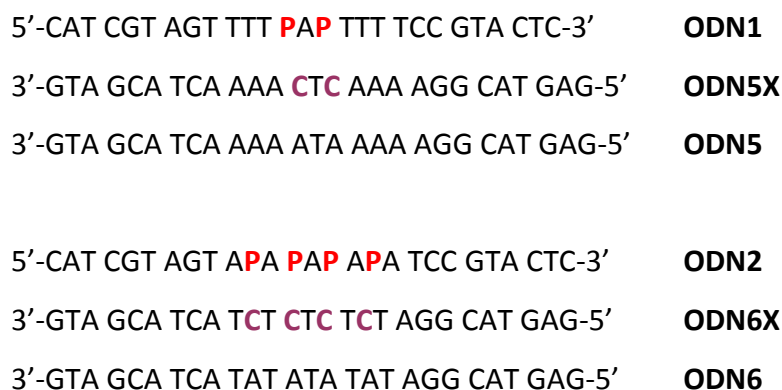


Figure 3.13: UV-vis melting profiles, measured at 1 μ M concentration, in buffer and monitored at 410 nm of different DPP-DNA duplexes.

3.3.3 UV-vis melting profiles of porphyrin-DNA mismatched double strands

For a control experiment of UV-melting studies at 260 nm absorption wavelength, DPP-DNA **ODN1** and **ODN2** were hybridised to **ODN5X** and **ODN6X**. They were equivalent to the precursors **ODN5** and **ODN6**, but with **C** replacing **A** nucleobases instead at the complementary porphyrin-binding positions. The aim was to test for a decrease in thermal stability of DNA duplexes as a result of the mismatched base pairings, and to determine if the modified **T** are involved in base pairings.



The melting curve of **ODN1-ODN5X** could not be obtained, as was the situation with its precursor **ODN1-ODN5**, which then raised questions about the purity of the samples. Umemoto and Wada¹²⁰ have reported alkylation on the thymidine nucleobase by acrylonitrile (**Figure 3.14**). Thus, since acrylonitrile was formed as a side product of the deprotection of a 2-cyanoethyl phosphate protecting group, alteration in the thymidine nucleobase may affect its base pairing with the complementary adenine, and thereby disrupt the base stacking. The **ODN1** duplex stability maybe reduced as a consequence of multi adjacent **T** in the sequence. However, this would not explain why other strands did not show similar alkylation. The lack of a UV melting curve could also arise as a result of low duplex stability, or the absence of changes in UV absorbance upon melting, as shown by Davis *et. al.*¹²¹

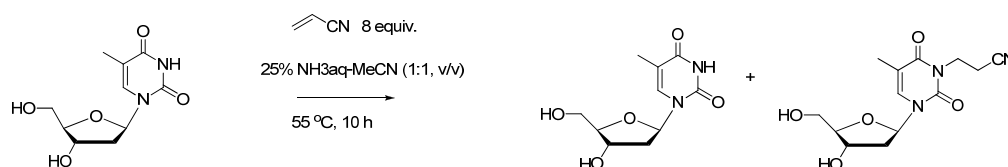


Figure 3.14: Representation of 2-cyanoethylation of thymidine.

In contrast, the UV-melting profile of **ODN2-ODN6X** exhibits a lower $T_m = 29$ °C, compared to $T_m = 39$ °C in non-mismatched **ODN2-ODN6** double strand (**Figure 3.15**). This finding indicates that the modified **T** does have an influence on base pairings, because replacing **T** with **C** did result in destabilisation of **DPP-DNA** duplexes.

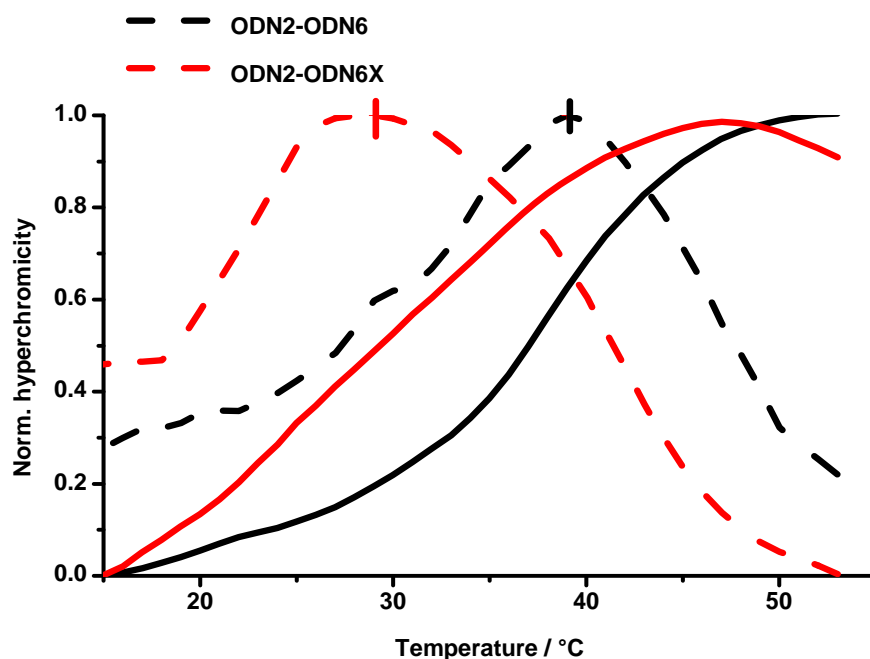


Figure 3.15: UV-melting curves (solid) and derivatives (dash) of 1 μ M **ODN2-ODN6** and mismatched **ODN2-ODN6X** duplexes measured in buffer and monitored at 260 nm.

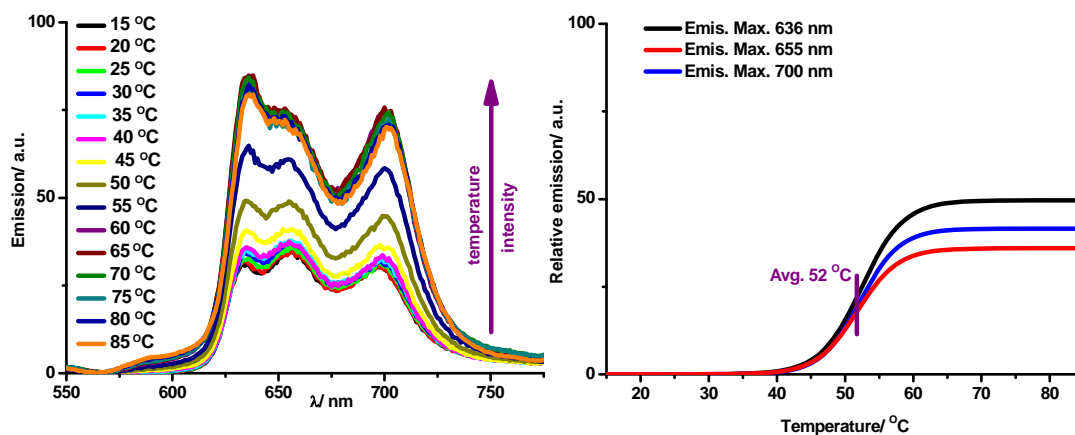
UV melting studies of mixed diphenyl porphyrin-DNA and tetraphenyl porphyrin-DNA duplexes of **ODN1** and **ODN2** were also attempted. The data were however disappointingly inconsistent, possibly due to decomposition of the old samples (*i.e.* > 2 years old) of tetraphenyl porphyrin-DNA. The extent of decompositions in old tetraphenyl porphyrin-DNA samples, which were prepared by Dr. Stulz and Dr. Bouamaied is not covered in this thesis.

3.4 Fluorescence temperature and melting profiles of porphyrin-DNA arrays

DPP-DNA single and double strand concentrations were kept at 1 μM in buffer to be consistent with previous analytical studies. Excitation wavelengths were chosen from 408 - 410 nm, depending on where each specific **DPP**-DNA strand absorbed light in the porphyrin B-band. The temperature and melting profiles were plotted with the emission intensities of different emission maxima against temperatures, then standardised so that the emission intensity started from 0 at 15 $^{\circ}\text{C}$ (**Figure 3.16**). The temperatures were increased manually from 15 $^{\circ}\text{C}$ – 85 $^{\circ}\text{C}$ and the spectra were recorded at every 5 $^{\circ}\text{C}$ increment. It was not possible to set up these temperature varying experiments on automatic mode as was used for UV-vis melting studies, due to instrumental limitations. Hence, fluorescence temperature and melting profiles provide qualitative supporting evidence for the electronic interactions of porphyrins, rather than the derivation of an accurate T_m or T_p . Analogous to UV-vis melting curves, the intensity of emission increases steadily when temperatures are raised (**Figure 3.16**). This is indicative of electronic interactions between porphyrins on DNA and porphyrin unstacking at high temperatures.

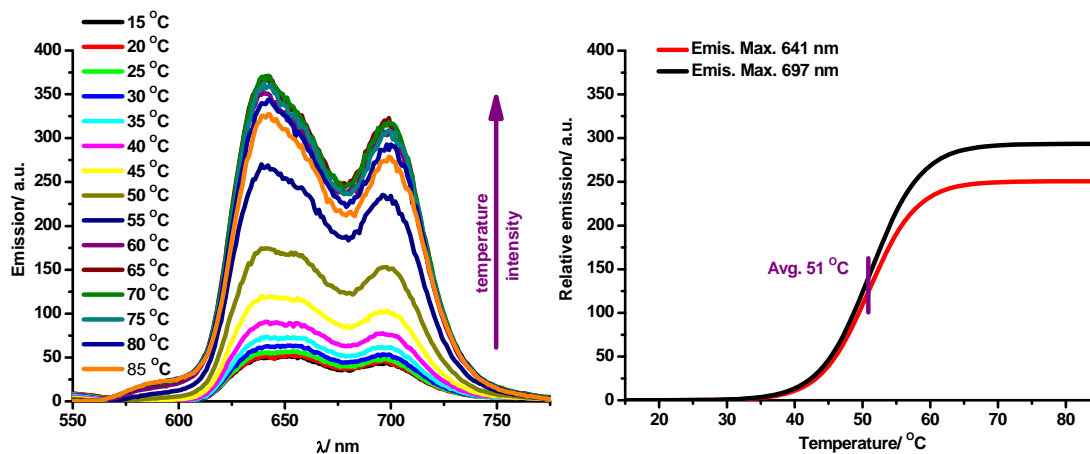
The qualitative average turning point obtained from the derivatives of **ODN3** (55 $^{\circ}\text{C}$) fluorescence melting curves is higher than **ODN2-ODN6** (47 $^{\circ}\text{C}$). This higher turning point is comparable to UV-vis melting results and indicates that a zipper stacking of diphenyl porphyrins enhances modified DNA duplex stability more than the parallel stacking mode of **DPP** on DNA.

5'-CAT CGT AGT TTT **PAP** TTT TCC GTA CTC-3' ODN1



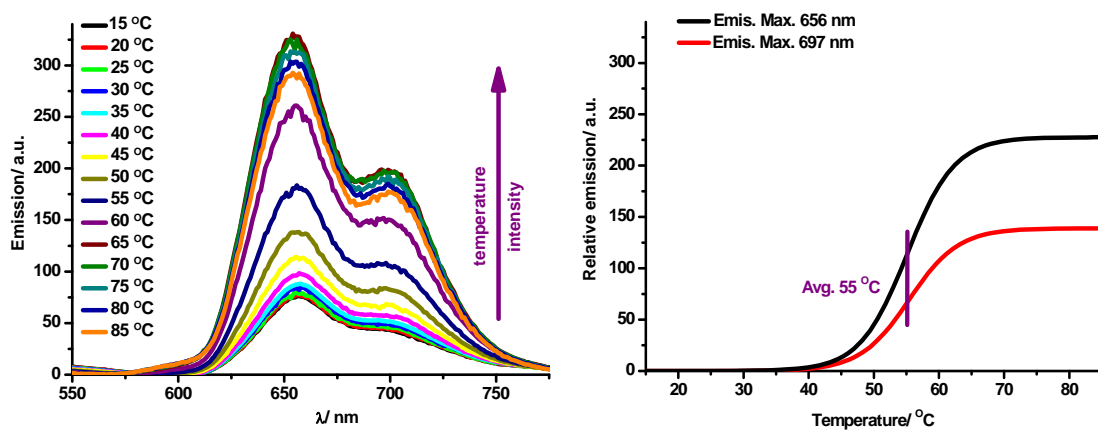
5'-CAT CGT AGT TTT **PAP** TTT TCC GTA CTC-3' ODN1

3'-GTA GCA TCA AAA ATA AAA AGG CAT GAG-5' ODN5



5'-GAG TAC GGP **APA** CCG TAC TC-3' self-complementary ODN3

3'- CTC ATG CCA **PAP** GGC ATG AG-5'



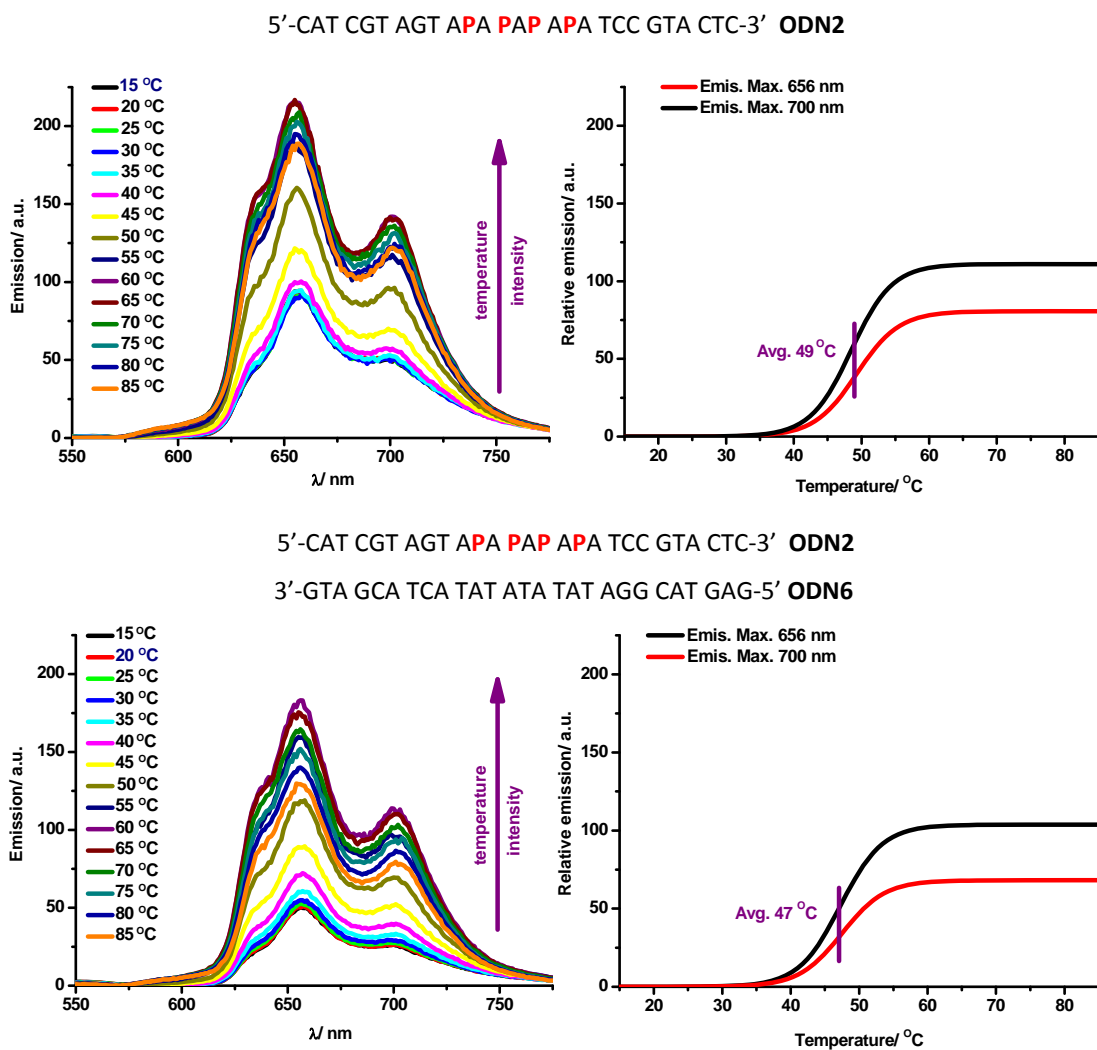


Figure 3.16: Fluorescence temperature and melting profiles of 1 μ M porphyrin-DNA in buffer at 408 - 410 nm excitation.

3.5 Circular Dichroism (CD) analysis of porphyrin-DNA

3.5.1 Theory of circular dichroism spectroscopy

Since UV-vis and fluorescence emission spectroscopies only outline the interaction within neighbouring porphyrins and their impact on DNA stability, there is a need for another method to quantify any structural change induced by covalently attached substituents to oligonucleotides. Originally developed by Biot, Fresnel and Cotton in the 19th century,¹²² circular dichroism (CD) spectroscopy has been used for determining the conformations of molecules, including ones of biological origin, such as proteins and DNA (*i.e.* A and B-type helix secondary conformation, random coil structure).

The light used in a CD spectrophotometer is electromagnetic radiation which consists of oscillating electric and magnetic fields. These fields are vectors, and therefore directionally dependent when they oscillate perpendicularly to each other and to the direction of propagation. Electromagnetic radiation is circularly polarised, which means that the electric field vector oscillates in the same magnitude but in a helical path while propagating through space at the same time (**Figure 3.17**). When the electric field vector rotates clockwise then a right circularly polarised light is produced. Conversely, an anti-clockwise rotating electric field vector would produce a left circularly polarised light.¹²³

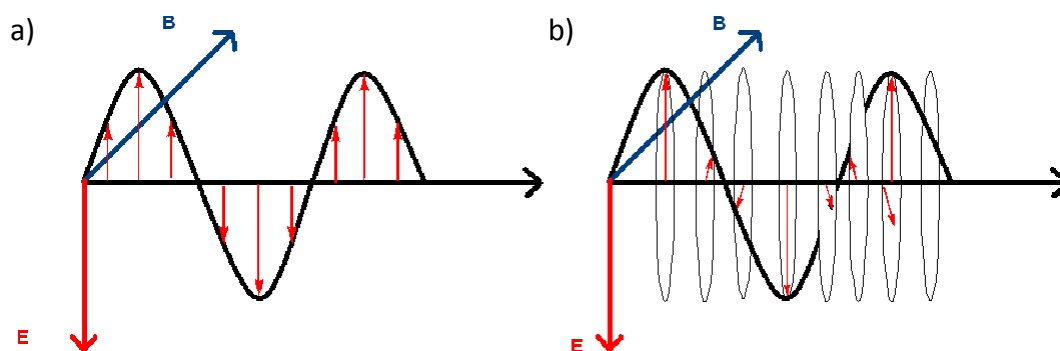


Figure 3.17: a) Oscillating electric field (red arrow) in plane polarised light and b) Right circularly polarised light.

In a CD spectrophotometer, an equal mixture of left and right circularly polarised light is passed through the sample, and these are absorbed in different ratios by chiral, and hence optically active samples. Circular dichroism is the measurement of the *difference* between absorbed clockwise and anti-clockwise circularly polarised light, as a function of wavelength, and the CD spectrum for a compound can be expressed as:

$$\Delta\epsilon = \epsilon_L - \epsilon_R = \frac{A_L - A_R}{lC}$$

Equation 3.3¹¹¹

A_L = absorbance of left circularly polarised light

A_R = absorbance of right circularly polarised light

l = sample path length (cm)

C = sample concentration (mol L⁻¹)

ϵ = molar extinction coefficient (M⁻¹ cm⁻¹)

CD spectra are often presented as molar ellipticity [θ], with units of deg M⁻¹ cm⁻¹ x 100, and they are therefore a function of wavelength. The molar extinction coefficient and molar ellipticity can be interconverted *via* **Equation 3.4**.

$$[\theta] = 3298 \times \Delta\epsilon$$

Equation 3.4¹²⁴

[θ] = molar ellipticity (deg M⁻¹ cm⁻¹ x 100)

$\Delta\epsilon$ = molar extinction coefficient (M⁻¹ cm⁻¹)

All CD spectra presented in this thesis are expressed in units of $\Delta\epsilon$, with respect to the sample concentration, and in some cases expressed as per base or per base-pair. Information on the calculation of $\Delta\epsilon$ from θ is written in **Chapter 5, Section 5.2.7**.

The spectra of DNA are derived from individual chiral nucleotide monomers and the overall helical structure of the strand.¹¹¹ For this research, CD spectroscopy is a useful analytical method, because not only can it probe information on the individual porphyrin-modified nucleotide, but it also gives insight into the overall DNA structure.

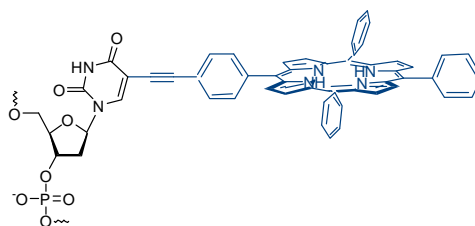
3.5.2 Circular dichroism spectra of porphyrin-DNA

CD measurements of the porphyrin modified DNA were investigated in two different spectrophotometers. Initially, all samples were measured using a Chirascan CD spectrophotometer with a long scan range (600 – 200 nm) to examine $\Delta\epsilon$ of both the porphyrin B-band and DNA. Thereafter, the experiments were conducted using an Olis DSM20 CD spectrophotometer with a narrow scan range (180 – 330 nm) to focus on $\Delta\epsilon$ of the oligonucleotides only, in order to further understand the DNA structural changes induced by the covalently attached porphyrins. The following samples of tetraphenyl porphyrin-DNA, prepared by I. Bouamaied and E. Stulz, were also examined to draw comparisons with diphenyl porphyrin-DNA arrays.

ODN8 5'-CAT CGT AGP **APA PAP APA PCC** GTA CTC-3'

ODN9 5'-GAG TAC GGA **PAP APA PAP** ACT ACG ATG-3'

P: Tetraphenyl porphyrin



3.5.2.1 CD spectroscopy of porphyrin-DNA measured with the Chirascan spectrophotometer

The instrumental set up and experimental conditions are described in **Chapter 5, Section 5.2.7**. All samples recorded on the Chirascan spectrophotometer were in the same buffer used in the UV-vis absorbance and fluorescence emission studies, to ensure experimental uniformity. Most samples were measured at a 5 μM optimum concentration, but for a limited number of samples, a 2 μM concentration was sufficient to obtain spectra.

In the last two decades, porphyrins have been classified as ideal CD reporter groups for other substrates, such as porphyrin assemblies and biomolecules.⁶² Many common CD chromophores (*e.g.* esters and amides)¹²⁵ absorb in the 230-310 nm

region; hence they overlap with the absorption maxima of oligonucleotides.¹²⁶

Porphyrins prevent spectral complications because their B-band (*i.e.* 410 nm) is red-shifted from the absorbance of DNA (*i.e.* 260 nm). The symmetric diphenyl porphyrin **2HDPP** (**Figure 3.6**) does not produce any CD signal. However, upon forming the building block **P** the nucleoside induced a negative CD signal on the porphyrin, as reported by Bouamaied *et al.*^{114, 127} Also, it should be noted that non-modified DNA single³⁴ and double strands (**Figure 3.18 b**) show no signal around 400 nm wavelength in their CD spectra. Thus the observation of a negative signal in the B-band region, as shown in **Figure 3.18** provides supporting evidences for the successful attachment of porphyrins to DNA.

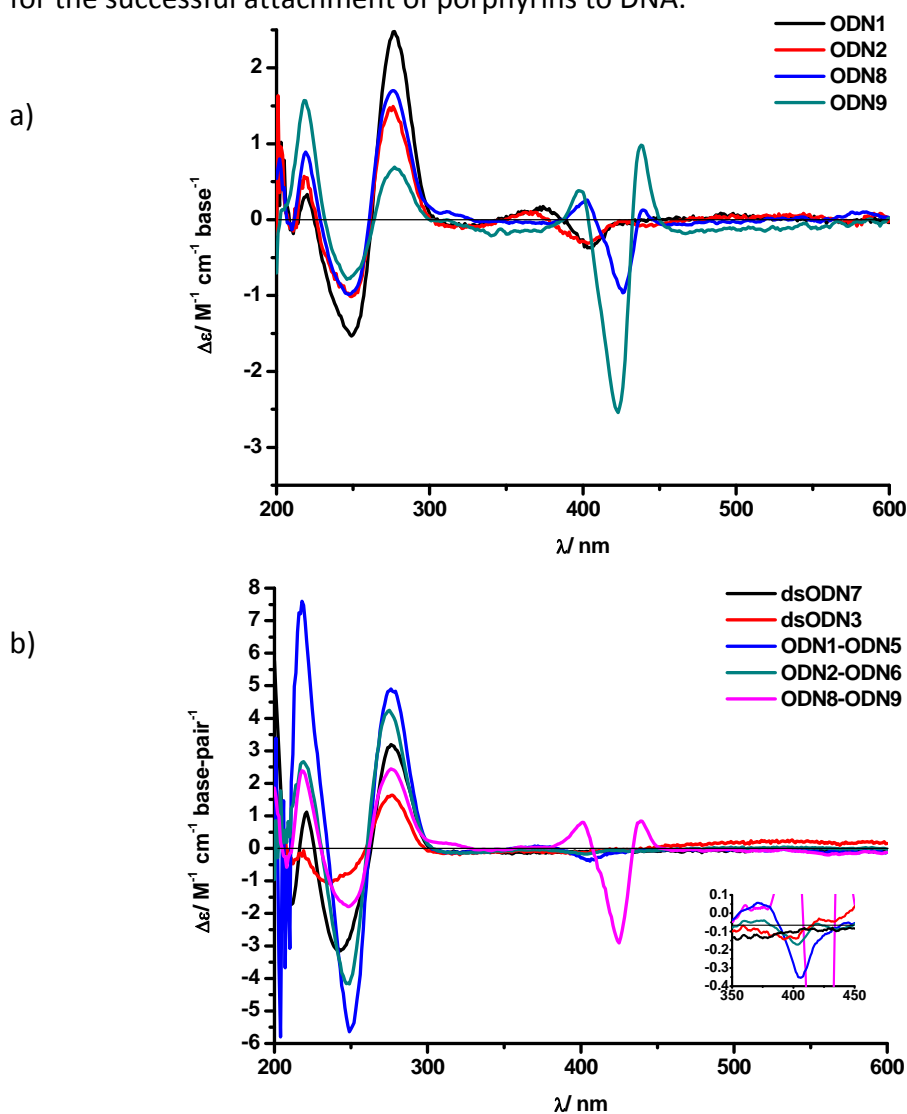


Figure 3.18: Circular dichroism spectra of diphenyl porphyrin and tetraphenyl porphyrin modified DNA single strands (a) and double strands (b) measured in buffer at 20 °C. The inset in b) shows an expansion of the porphyrin absorbance region.

In the CD spectra of porphyrin-DNA double strands (**Figure 3.18 b**), the induced signal in the porphyrin absorption region is dominated by a negative signal at 404 nm for **DPP**-DNA and at 425 nm for **TPP**-DNA. Whilst an induced positive CD signal in the Soret region indicates the external binding of porphyrins,¹²⁸ Bejune *et al.*¹²⁹ and Pasternack *et al.*¹³⁰ have suggested the intercalation of cationic porphyrins in the B-type duplex is associated with the induced negative signal, especially in G-C rich sequences. This porphyrin intercalation model nevertheless raises questions as to whether it could be applied to the porphyrin-DNA systems. The porphyrins reported here are covalently attached to oligonucleotides, and intercalation would imply flipping of the complementary bases to accommodate the chromophores. Also, the long acetylene linker would point the porphyrin outside the base-pair region, and would prevent stable stacking with the nucleobases without severely disrupting the B-type DNA structure. Therefore, the induced negative Cotton effect is thought to be an intrinsic property of porphyrin-DNA arrays.³⁴ The external stacking of tetraphenyl porphyrins and large diphenyl porphyrins on DNA is favoured over intercalation and minor groove binding.¹³¹ The calculated force-field minimised structure of the **DPP**-DNA **ODN1-ODN5** duplex (**Figure 3.19**)³² using MacroModel software (Amber force field) supports the theory of external stacking of porphyrins in the DNA major groove. However, it seems that CD spectroscopy cannot conclude the binding mode of porphyrins on oligonucleotides. It is recommended, therefore, that a linear dichroism study should be performed in order to determine the stacking of porphyrins.

Compared to the CD spectra of short porphyrin-tetranucleotide arrays,⁹⁷ the induced negative Cotton effects on > 20 mers porphyrin-DNA (**Figure 3.20 and Figure 3.21**) are broader. Their DNA regions (218 – 277 nm) show more resolved features, which reflect a more ordered structure for the oligonucleotide backbone.⁹⁷ Whilst the diphenyl porphyrins appear as broad bisignate features at +370/-403 nm, which are below their UV-vis absorption maxima (*e.g.* 410 nm), the tetraphenyl porphyrins show more red-shifted and sharper trisignate signals at +397/-423/+438 nm. A wavelength shift in the Soret region is often related to an effect on the π - π^* absorption.¹²⁸ In agreement with the UV-vis data of tetraphenyl

porphyrin-DNA,³⁴ these observed differences in the feature and wavelength of the negative Cotton effect suggest that not only is the induced chiral perturbation on the **DPP** by the oligonucleotides different from **TPP**, but also their electronic interactions are not the same. The extent of the differences in electronic interactions between these chromophores is not discussed here, because it lies beyond the scope of this work and the amount of information that can be extracted from the spectroscopic data. Nevertheless, the EPR study will further explore these porphyrin interactions in **Chapter 4**.

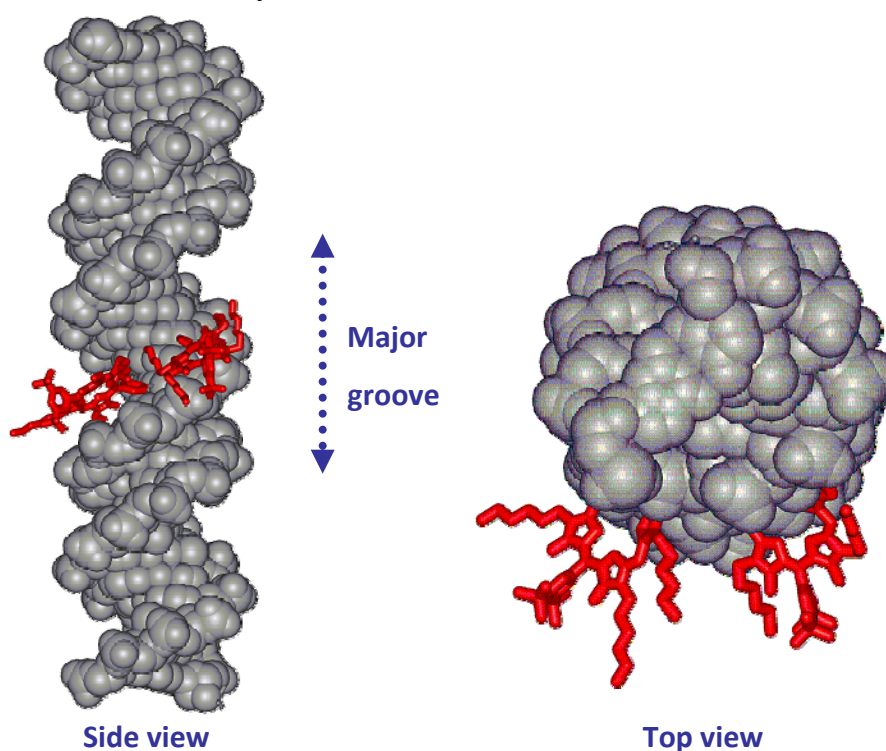


Figure 3.19: Force-field minimised structure of diphenyl porphyrin-DNA **ODN1** duplex.

The UV part of the CD spectra of the non-modified self-complementary **ODN7** duplex (**Figure 3.21 a**) displays a clear bisignate profile at -243/+276 nm. These numbers match the classic B-form DNA configuration in the literature,^{6,132} which shows a negative peak at ~250 nm and a positive peak at ~270-280 nm. Together with its UV-vis melting profile and temperature $T_m = 72$ °C (**Figure 3.11**), they support the conclusion that **ODN7** exists as a B-type duplex at ambient temperatures. All duplexes of **ODN1-ODN5**, **ODN2-ODN6**, **ODN3**, **ODN8-ODN9** (**Figure 3.20** and **Figure 3.21**) show similar bisignate profiles in the DNA region compared to **ODN7**, thus indicating that porphyrin-DNA double strands persist a

B-form configuration.⁸⁵ Modifying oligonucleotides with porphyrins does not seem to greatly alter their natural structure. Relative to the duplexes, a similar B-form bisignate profile, but with reduced intensities is displayed across all the porphyrin-DNA single strands, which is indicative of an incomplete helical denaturing conformation disruption. UV-vis melting experiments monitored at 410 nm of the single strands **ODN1** and **ODN2** also showed a reflection point $T_p = 43$ °C. These observations suggest the presence of a stabilised helical structure on **DPP**-DNA single strands, analogous to that reported for **TPP**-DNA single strands.³² The negative Cotton effect seems to be induced by the porphyrins, because the UV bisignate profile of a non-modified DNA single strand in literature is very different from those of the porphyrin DNA complexes.³⁴

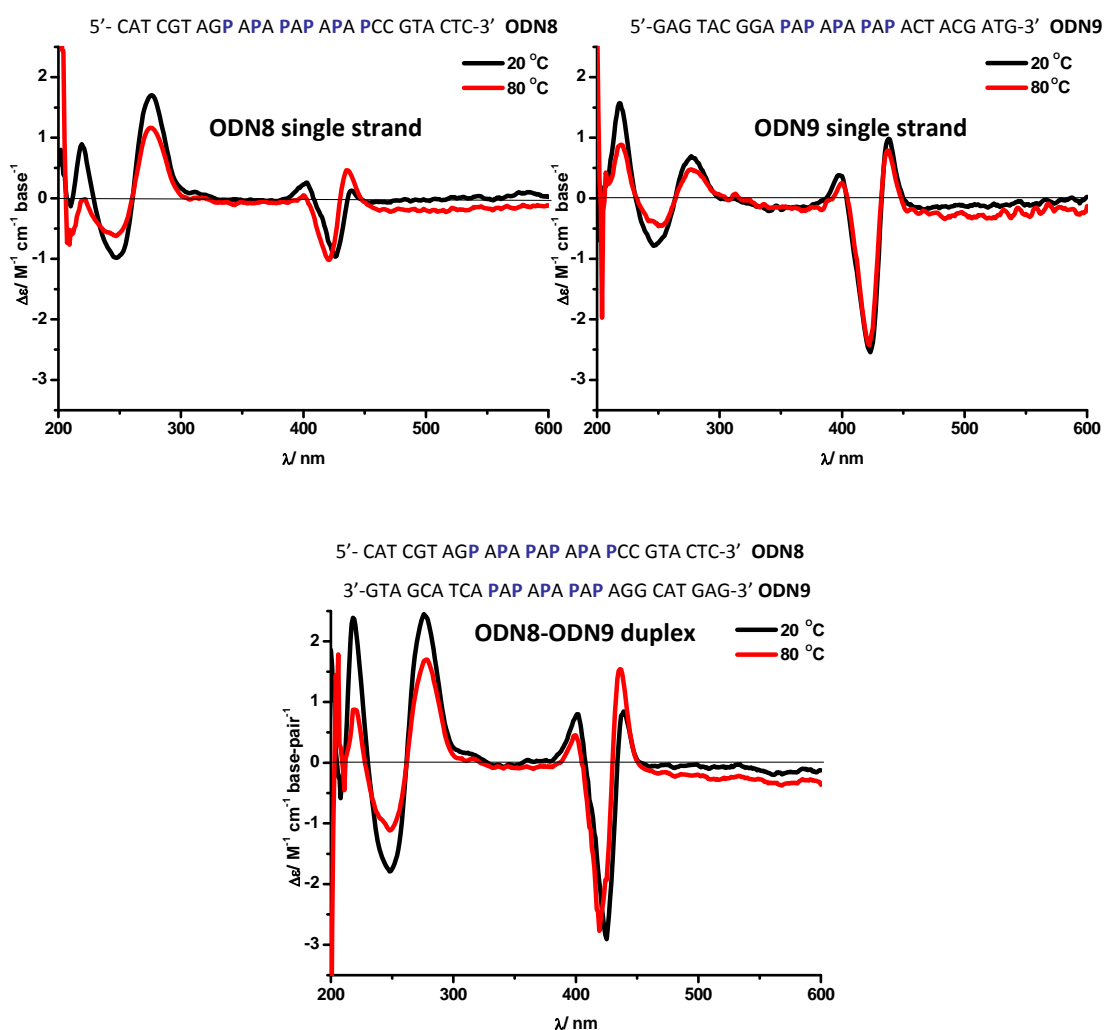


Figure 3.20: Circular dichroism spectra of tetraphenyl porphyrin-DNA single strands (above) and double strand (below), measured in buffer at 20 °C and 80 °C.

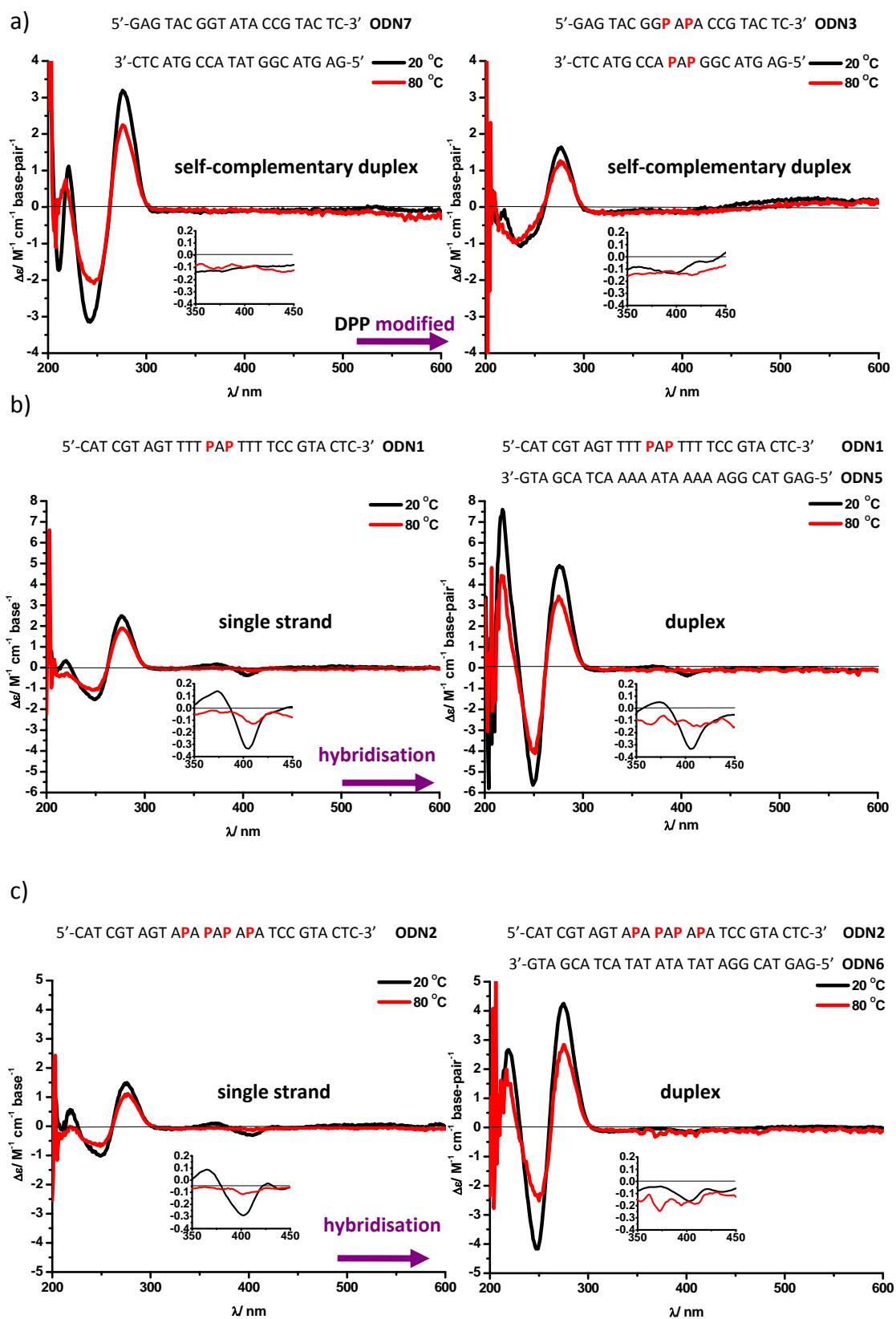


Figure 3.21: Circular dichroism spectra of diphenyl porphyrin-DNA single strands (left) and double strands (right), measured in buffer at 20 °C and 80 °C.

Upon heating to 80 °C, a shift in the absorption wavelength (**Table 3.4**) is observed for the porphyrin region of **TPP**-DNA arrays (**Figure 3.20**), and the induced negative Cotton effect in the CD spectra of **DPP**-DNA arrays (**Figure 3.21**) decreases in intensity (**Table 3.5**) and also broadens.

Table 3.4: Quantitative bisignate profiles of tetraphenyl porphyrin-DNA and the percentage of change in $\Delta\epsilon$ upon heating.

Porphyrin-DNA	Temp (°C)	DNA maxima [nm ($\Delta\epsilon$)]	Signal change (%)	Porphyrin maxima [nm ($\Delta\epsilon$)]	Signal change (%)
ss ODN8 (PAPAPAPAP)	15	247 (-0.98)	0	403 (+0.26)	0
		276 (+1.70)	0	426 (-0.96)	0
				439 (+0.13)	
ss ODN8 (PAPAPAPAP)	80	247 (-0.62)	-37 %	400 (+0.05)	-81 %
		275 (+1.16)	-32 %	421 (-1.02)	+6 %
				435 (0.460)	+254 %
ss ODN9 (PAPAPAPAP)	15	246 (-0.79)	0	397 (+0.38)	0
		277 (+0.69)	0	423 (-2.54)	0
				438 (+0.98)	
ss ODN9 (PAPAPAPAP)	80	250 (-0.46)	-42 %	400 (+0.25)	-34 %
		277 (+0.48)	-30 %	422 (-2.42)	-4.7 %
				437 (+0.79)	-19 %
ds ODN8-ODN9 (PAPAPAPAP) (PAPAPAPAP)	15	248 (-1.79)	0	401 (+0.80)	0
		276 (+2.45)	0	425 (-2.91)	0
				439 (+0.85)	
ds ODN8-ODN9 (PAPAPAPAP) (PAPAPAPAP)	80	248 (-1.12)	-37 %	399 (+0.45)	-44 %
		278 (+1.70)	-31 %	419 (-2.77)	-5 %
				436 (+1.54)	+81 %

In agreement with the sharpening of the diphenyl porphyrin UV-vis absorption maxima (**Figure 3.1**), and the increase in their emission maxima at 80 °C (**Figure 3.16**), the changes in their negative Cotton effect also suggest a different electronic interaction within porphyrins at high temperature, as a result of porphyrin unstacking. These alterations are analogous to the spectral changes reported for tetraphenyl porphyrin-DNA.^{34, 35, 133} Heating also resulted in a decline in $\Delta\epsilon$ at the DNA region for all the strands (**Figure 3.20 and Figure 3.21**). In duplexes of **ODN2-ODN6**, **ODN3** and **ODN7**, the changes in CD spectra and UV-vis melting profiles are associated with duplex denaturing that induces changes to the DNA configuration. However, some CD characteristics of a B-type DNA are still preserved at 80 °C on both single and double strands.

Although features of the B-form DNA are retained upon modifying oligonucleotides with porphyrins, the decrease in $\Delta\epsilon$ observed for **DPP-DNA duplex ODN3** relative to its non-modified duplex **ODN7** (**Figure 3.21 a**), raises questions about the duplex formation of porphyrin-DNA, or the exact nature of the duplex, which could deviate significantly from the ideal B-type DNA to give a different CD spectrum. To monitor the duplex formation of oligonucleotides, electrophoresis on some strands will be described in **Section 3.6**.

Table 3.5: Quantitative bisignate profiles of diphenyl porphyrin-DNA and percentage of decreases in $\Delta\epsilon$ upon heating.

Porphyrin-DNA	Temp (°C)	DNA maxima [nm ($\Delta\epsilon$)]	Intensity Decrease (%)	Porphyrin maxima [nm ($\Delta\epsilon$)]	Intensity decrease (%)
ss ODN1 (PAP)	15	249 (-1.53)	0	373 (+0.14)	0
		277 (+2.48)	0	405 (-0.33)	0
ss ODN1 (PAP)	80	247 (-1.08)	-29 %	373 (-0.03)	-121 %
		276 (+1.89)	-24 %	409 (-0.13)	-61 %
ds ODN1 (PAP)	15	249 (-5.64)	0	373 (+0.05)	0
		276 (4.90)	0	405 (-0.34)	0
ds ODN1 (PAP)	80	251 (-4.11)	-27 %	373 (-0.08)	-260 %
		275 (+3.43)	-30 %	405 (-0.13)	-62 %
ss ODN2 (PAPAPAP)	15	249 (-1.02)	0	365 (+0.09)	0
		276 (+1.49)	0	402 (-0.29)	0
ss ODN2 (PAPAPAP)	80	249 (-0.69)	-32 %	365 (-0.06)	-167 %
		277 (+1.11)	-26 %	402 (-0.12)	-59 %
ds ODN2 (PAPAPAP)	15	249 (-4.16)	0	373 (-0.04)	0
		275 (+4.25)	0	403 (-0.16)	0
ds ODN2 (PAPAPAP)	80	250 (-2.52)	-39 %	373 (-0.24)	-500 %
		275 (+2.84)	-33 %	403 (-0.17)	-6 %
ds ODN3 (PAP)	15	236 (-1.08)	0	365 (-0.09)	0
		277 (+1.64)	0	398 (-0.14)	0
ds ODN3 (PAP)	80	231 (-0.99)	-8 %	365 (-0.15)	-67 %
		276 (+1.26)	-23 %	398 (-0.14)	0 %
ds ODN7 (no P)	15	243 (-3.15)	0	N/A	N/A
		276 (3.20)	0		
ds ODN7 (no P)	80	247 (-2.09)	-34 %	N/A	N/A
		276 (+2.25)	-30 %		

3.5.2.2 CD spectra of porphyrin-DNA measured with the Olis DSM20 spectrophotometer

The CD spectra of all porphyrin-DNA arrays measured on the Chirascan spectrophotometer displayed similar features in the DNA region, but different values of $\Delta\epsilon$ for different strands. To understand the variation in $\Delta\epsilon$, porphyrin-DNA samples were analysed on an Olis DSM20 CD spectrophotometer attached to a beamline of a synchrotron radiation source. The measurements, in collaboration with Dr. Giuliano Siligardi, Dr. Rohanah Hussain and Dr. Daniel Myatt at Beamline 23, Diamond Light Source, were at 180 – 330 nm, the most sensitive range for this instrument.

The samples recorded on the Olis DSM20 instrument were measured in special designed circular cells that can hold each sample in a minimum volume of 160 μL at 0.05 cm pathlength (**Figure 3.22**). This is an advantage that Olis DSM20 has over Chirascan spectrophotometer: limited amount of compounds, such as porphyrin-DNA, can be examined in small quantities. The spectra of all samples were recorded in water, because buffers show some absorption below 230 nm.



Figure 3.22: Sample in a circular cell (top) measured in Olis DSM20 CD spectrophotometer (bottom).

The following additional **DPP**-DNA arrays were synthesised for the investigation on the Olis DSM20 CD spectrophotometer.

5'-GAG TAC GGA AAA **APA** AAA ACT ACG ATC-3' **ODN13**

5'-GAT CGT AGT TTT **PAP** TTT TCC GTA CTC-3' **ODN14**

5'-GCT AGC TAG **PPP** CGA ATC GTA-3' **ODN15**

At first, the spectra of **DPP**-DNA single and double strands were compared with their equivalent non-modified oligonucleotides.

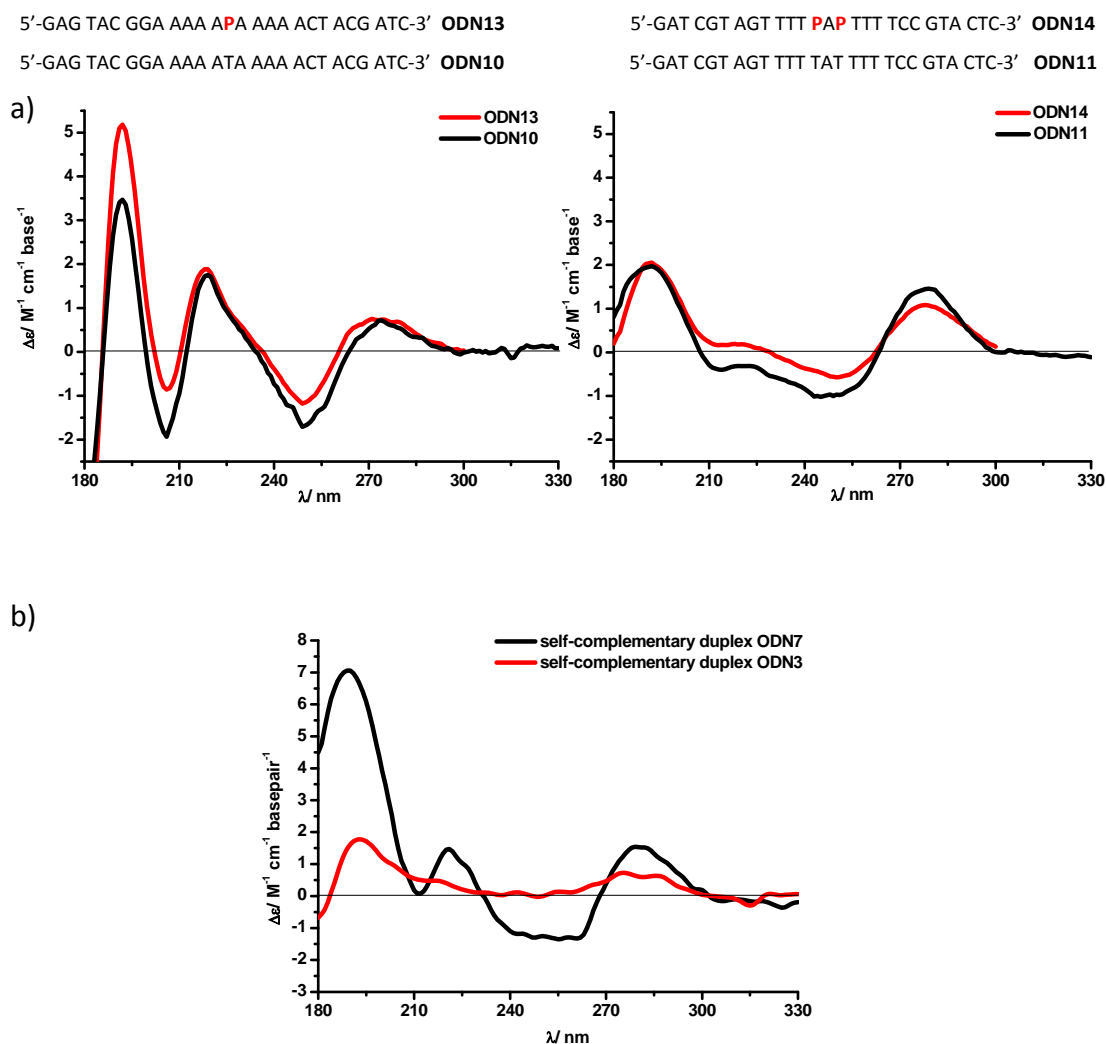


Figure 3.23: CD spectra of non-modified and **DPP**-modified oligonucleotides measured in water.

The examples of single strands **ODN13** and **ODN14** show induced changes in the CD spectra of non-modified oligonucleotides caused by porphyrin modifications (**Figure 3.23 a**). Compared to its equivalent non-modified single strand **ODN10**, the attachment of one porphyrin in **ODN13** reduces the intensity of the peak at -249 nm by 31 %. Attachment of two porphyrins in **ODN14**, however, not only reduces the peak at -250 nm of **ODN11** by 41 %, but also decreases $\Delta\epsilon$ at +276 nm by 24 %. Nevertheless, the overall shape of the spectra was not altered to a large extent. Addition of porphyrins to DNA duplexes (**Figure 3.23 b**) also results in decreases in $\Delta\epsilon$ of the characteristic B-form bisignate features, where the absorbance at -250 nm is almost lost. Thus porphyrins do induce changes in the natural structures of oligonucleotides. More features below 200 nm were also revealed on this instrument compared to the Chirascan spectrophotometer.

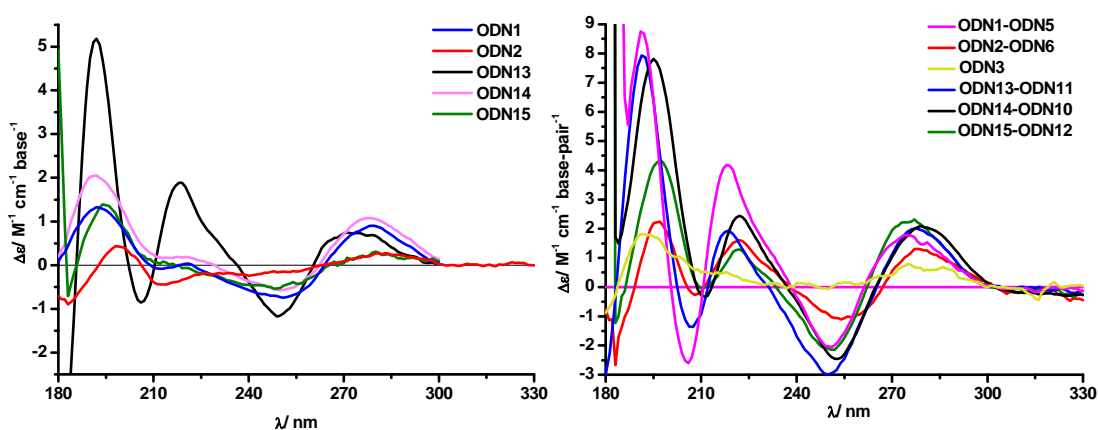


Figure 3.24: CD spectra of DPP-DNA single and double strands measured in water.

Generally, the CD signal intensities of all porphyrin-DNA arrays at -250 nm decrease with increasing number of porphyrin modifications (**Figure 3.24**). Most notable is the significant decrease in $\Delta\epsilon$ in the single strand **ODN2** and duplex **ODN3**, where the attachment of four diphenyl porphyrins results in an almost complete loss of CD features. Although these observations are indicative of a larger disruption to the original configuration of natural DNA with greater amount of porphyrins (**Table 3.6**), an absolute comparison cannot be made because these DPP-DNA arrays do not have the same DNA sequence. Analyses of non-modified strands on the Olis DSM20 spectrophotometer also show effects of the nucleobase composition on CD profiles.

Table 3.6: Amount of diphenyl porphyrin and the relative effects on the CD spectra.

Strands	Number of DPP (Diphenyl porphyrin)	DNA maxima [nm ($\Delta\epsilon$)]	Signal change (%)
ODN13	1	249 (-1.18)	0
		271 (+0.76)	0
ODN14	2	250 (-0.58)	-51 %
		278 (+1.08)	+42 %
ODN1	2	251 (-0.74)	-37 %
		279 (+0.91)	+20 %
ODN15	3	248 (-0.54)	-54 %
		280 (+0.31)	-59 %
ODN2	4	249 (-0.16)	-86 %
		283 (+0.27)	-65 %
ODN3	4	250 (-0.07)	-94 %
		275 (+0.79)	+4 %

Non-modified single strands **ODN5**, **ODN6**, **ODN10**, **ODN11** were measured to examine the effects of the nucleobases on CD profiles. Of these, **ODN5** was compared with **ODN6**, whilst **ODN10** was compared with **ODN11**, because they had similar sequence length and amounts of G and C (**Table 3.7**).

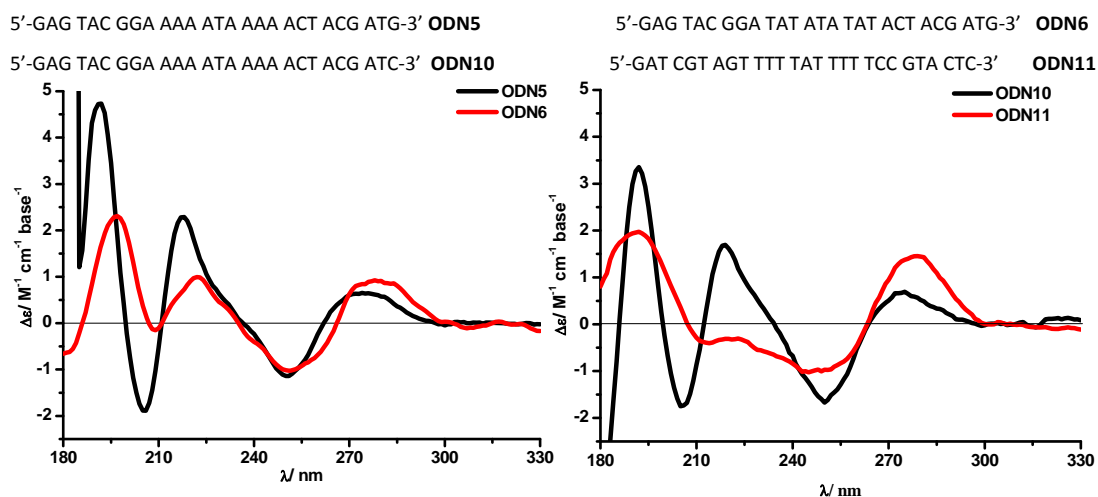
**Figure 3.25.** CD spectra of non-modified DNA single strands measured in water.

Table 3.7: Amount of nucleobases in different non-modified DNA single strands.

Non-modified single strands	Number of T	Number of A	Number of G	Number of C
ODN5	4	14	6	3
ODN6	8	10	6	3
ODN10	4	14	5	4
ODN11	14	4	4	4

Compared to **ODN5** and **ODN10**, **ODN6** and **ODN11** respectively display lower intensities in the spectra (**Figure 3.25**), and they also consist a higher number of T. It seems that varying the nucleobase composition does have an effect on the spectral features, and hence the configuration of the oligonucleotides. Although these primary data are indicators of factors which could alter the structure of the DNA, more non-modified strands need to be synthesised to understand these results further. A new set of non-modified DNA single strands from a similar sequence but with different amounts of T were synthesised and recorded on the Olis DSM20 spectrophotometer. The study is still under investigation, but early data analysed by Thomas J. Bandy¹³⁴ suggest that a high number of T could account for the reduced intensities in the DNA spectra.

3.5.3 Circular dichroism of DNA as a function of time

Irradiating DNA samples on the beamline over a long period of time may decompose the molecules, since it is known that UV-irradiation in the form of UV-A (400 - 315 nm), UV-B (315 - 280 nm) and UV-C (280 - 100 nm) can damage DNA.¹³⁵ Dimerisation of T^{136, 137} or degradation of G¹³⁸ by UV-B can be causes of mutations after exposure to sunlight.^{139, 140} Hence, it was important to investigate the stability of oligonucleotides as a function of time, so that adjustments of the DNA exposure time to light could be made, if necessary, to minimise the risk of decomposition. Non-modified duplex **ODN7** was selected for the test due to its simple synthesis. A clean mass spectrum of the sample also confirmed the authenticity of the strand.

The ellipticity of **ODN7** duplex at 190 nm was measured on the Olis DSM20 for 60 minutes, using the following settings:

Scan range: 0 min to 60 min.

Slit width: 0.5 mm

Integration time: 2 s

Pathlength: 0.05 cm to 0.1 cm

Solvent: water

Sample concentration: 11 μM

To be consistent, the CD intensity of **ODN7** was also converted to $\Delta\epsilon$

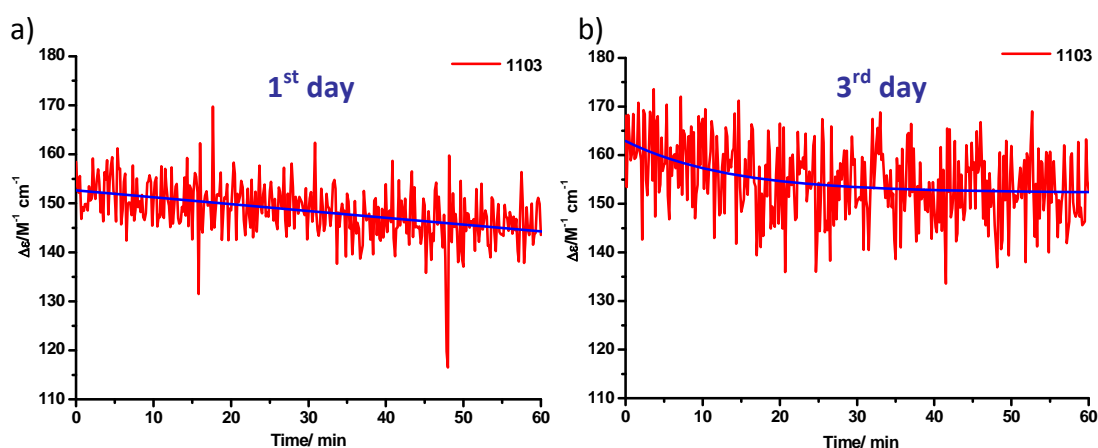


Figure 3.26: Molar ellipticity of **ODN7** at 190 nm as a function of time.

The ellipticity of **ODN7** recorded on the first day (**Figure 3.26 a**) shows a decrease in $\Delta\epsilon$ by 5 % over 60 minutes, indicating that the DNA duplex was not denatured by the beamline light during spectral recording to a large extent. Subsequent analyses of other strands were thus kept ≤ 60 minutes to minimise the risk of denaturing oligonucleotides. A spectrum of this **ODN7** sample in a 180 nm – 300 nm scan range was also re-recorded after storage in a refrigerator for two days. The ellipticity observed on the third day showed some initial decrease in $\Delta\epsilon$, but it stabilised after five minutes (**Figure 3.26 b**). Thus although the synchrotron light does have an effect on the DNA, there is no evidence for extreme structural change (*i.e.* DNA duplex denaturing).

3.6 Native PAGE of oligonucleotides

To provide additional supporting evidences for duplex formations of oligonucleotides, some samples were further analysed on native PAGE (polyacrylamide gel electrophoresis). Unlike denaturing PAGE, the native PAGE does not disrupt the secondary structure of oligonucleotides.¹⁴¹

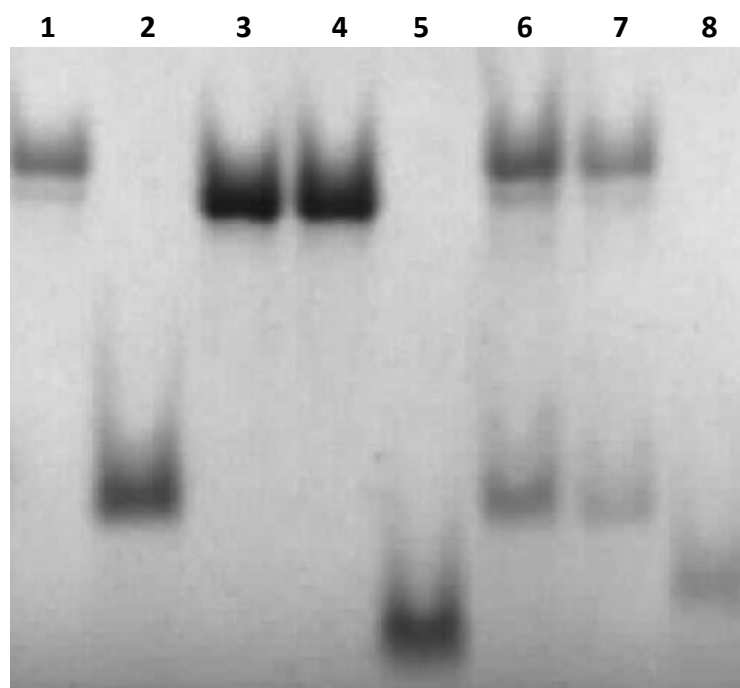


Figure 3.27: Native PAGE of non-porphyrin-modified DNA. Lane 1: **ODN19-ODN20** 1:1, lane 2: **ODN19**, lane 3: **ODN6-ODN19** 1:1, lane 4: **ODN6-ODN19** 1:1, lane 5: **ODN6**, lane 6: **ODN19-ODN20** 2:1, lane 7: **ODN19-ODN20** 2:1, lane 8: **ODN20**. 12 % polyacrylamide gel at constant voltage (120 V) for 15 h, using 0.09 M Tris-borate-EDTA buffer (pH 8.2).

ODN6 5'-GAG TAC GGA TAT ATA TAT ACT ACG ATG-3'

ODN19 5'-CAT CGT AGT ATA TAT ATA TCC GTA CTC -3'

ODN20 5'-**FAM**GAG TAC GGA TAT ATA TAT ACT ACG ATG-3'

Non-modified and **FAM** (carboxyfluorescein)-modified DNA in this native PAGE investigation were synthesised and purified by ATDBio, then used as supplied. The bands separation (**Figure 3.27**) confirms duplex formations of **ODN6-ODN19** (lane 3, 4), **ODN19-ODN20** (lane 1, 6, 7). Single strands **ODN6** (lane 5), **ODN19** (lane 2), **ODN20** (lane 8) migrate faster than their duplexes.

Diphenyl porphyrin-modified **ODN2**, however, shows no migration on the native gel (**Figure 3.28**, lane 1, 2). This gel penetration retardation is comparable to observations from Stephenson¹⁴² and Stulz *et. al.*³⁴ Explanations for the unexpected retardation of **DPP**-DNA on denaturing gel penetration compared to **TPP**-DNA (**Figure 3.29**, lane 1) are not yet fully understood, but can most likely be attributed to the hydrophobicity of the porphyrins. Because of sample limitation for porphyrin-DNA **ODN2**, only 44 pmol of **ODN20** was used for hybridisation with an excess amount of **ODN2**. However, it should be noted that from previous native PAGE experiments, an amount of 44 pmol of **ODN20** was enough for visualisation, even without staining. The absence of **ODN20** traces in lane 2 and 3 in **Figure 3.28**, compared to lane 4 shows that **ODN20** does not migrate in the gel in the presence of porphyrin-DNA **ODN2**. This may indicate a duplex formation of **ODN20** with **ODN2** and hence prevent the DNA from entering the gel.

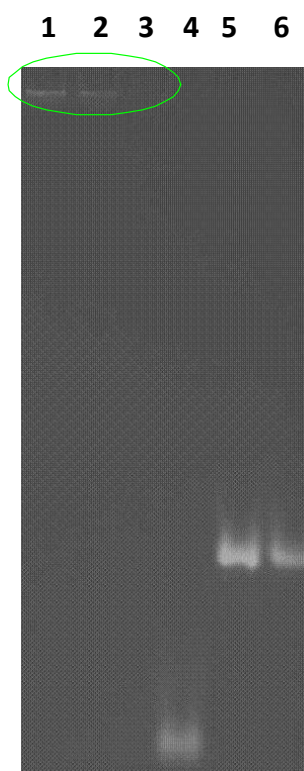


Figure 3.28: Native PAGE of **FAM**-modified and diphenyl porphyrin-modified DNA.

Lane 1: **ODN2** (1 nmol), lane 2: **ODN2-ODN20** (440: 44 pmol), lane 3: **ODN2-ODN20** (132:44 pmol), lane 4: **ODN20** (2 nmol), lane 5: **ODN19-ODN20** (2:2 nmol), lane 6: **ODN19-ODN20** (3:1 nmol).

12 % polyacrylamide gel at constant voltage (120 V) for 13 h, using 0.09 M Tris-borate-EDTA buffer (pH 8.2).

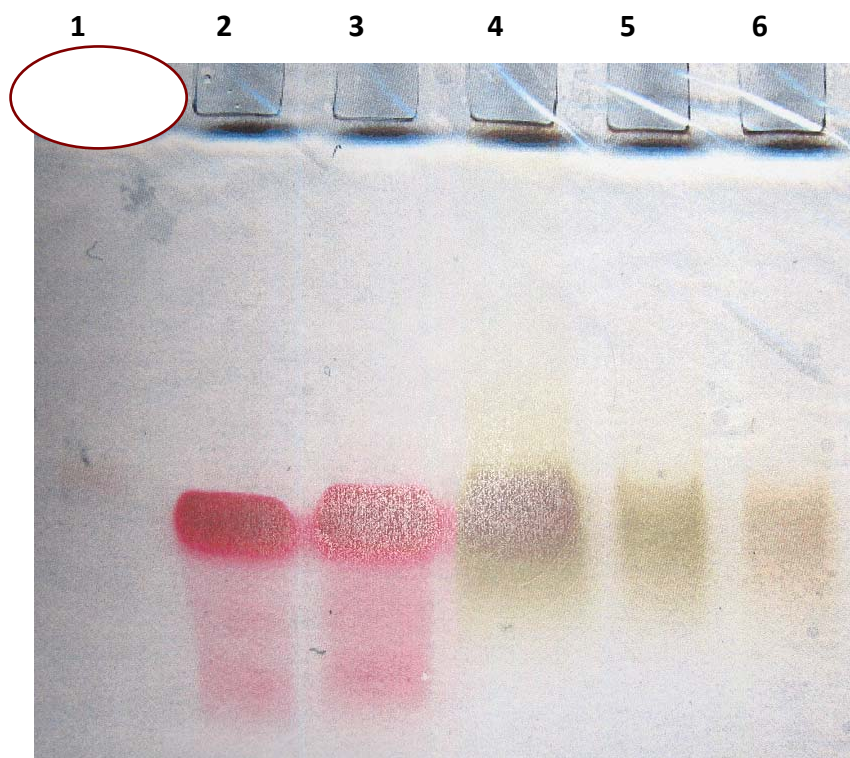


Figure 3.29: Denaturing PAGE of zinc metallated **DPP**-DNA and **TPP**-DNA by Stulz *et al.*¹⁴³

Lane 1: **DPP**-DNA, lane 2, 3: control strands, lane 4-6: **TPP**-DNA. 17 % polyacrylamide gel with urea at constant voltage (400 V), using 0.09 M Tris-borate-EDTA buffer (pH 8.2).

3.7 Conclusion

The preliminary analytical examinations of diphenyl porphyrin-DNA reveal that UV-vis and fluorescence emission spectroscopies are capable of more than just probing the electronic interactions within molecules. Besides showing the influence of the number of chromophores attached to DNA on diphenyl porphyrin π - π stacking, they also confirm post-synthetic metallation of porphyrin-DNA, with for example zinc and copper. The percentages of successful metallation in the strand, however, cannot be determined by either technique.

UV-vis and fluorescence emission melting experiments indicate increasing trends in the absorbance and emission intensities upon heating. The UV-vis melting studies of **DPP**-DNA double and single strands suggest the melting processes occur in two stages with $T_m \neq T_p$. T_m denotes the temperature at which DNA duplexes denature and T_p is the unwinding temperature of single strand porphyrin-DNA (**Figure 3.30**). T_p is independent of the ratio of porphyrin:nucleobases, and a similar T_p of 43 °C suggests an induced secondary structure on single strands by the porphyrins. The DNA B-form features from CD spectra of porphyrin-DNA single strands further support the presence of an induced stabilised helical structure. Just as DNA structures can influence the interaction within attached arrays of chromophores, the stacking of porphyrins can determine DNA stability. It was found in this work that interlocking stacking of porphyrins helps to stabilise **DPP**-DNA, compared to their parallel stacking.

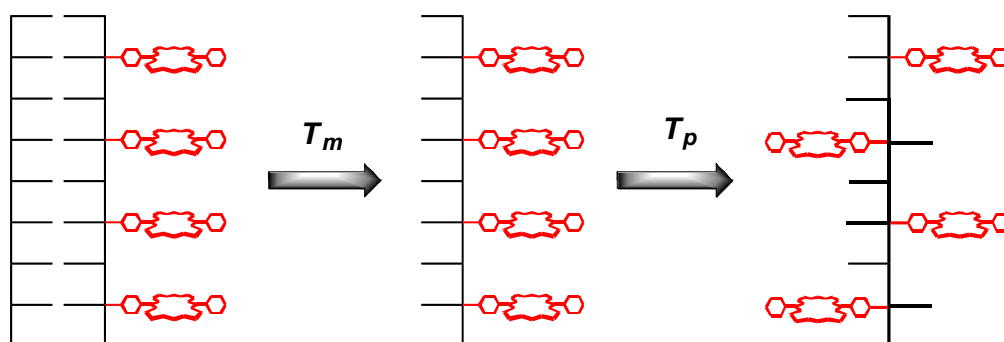


Figure 3.30: Two stages melting process of porphyrin-DNA and disruptions in **DPP** arrangements.

The circular dichroism study indicates the amount of porphyrins and the nature of nucleobases could possibly affect the overall structure of porphyrin-DNA arrays. Investigations on the effect of a particular base on DNA structure are under evaluation. To reinforce the above observations and to investigate the electronic interactions in porphyrin-modified DNA arrays in detail, more **DPP**-DNA needs to be synthesised and analysed by similar procedures. It is also a good idea to check for porphyrin interactions on a wider selection of base separations. The estimated distance between **DPP** could be varied from 5 – 30 Å and the arrays monitored at every 5 Å successive increment. This is useful to reveal a design that possesses the strongest porphyrin interaction, in order to optimise the electron cross-membrane transfer for making future nanowires and nanochips. It is, however highly recommended that the initial research is performed on DNA modified with well-known tetraphenyl porphyrins, because their syntheses have been optimised to proceed in fewer steps and also produce higher yields than diphenyl porphyrin-DNA.

CHAPTER 4: ELECTRON PARAMAGNETIC RESONANCE (EPR)

INVESTIGATION OF PORPHYRIN-DNA COMPLEXES

4.1 Introduction to EPR

Atoms or molecules have discrete energy levels and spectroscopic techniques involve monitoring transitions between them as a result of absorption or emission of electromagnetic radiation (**Figure 4.1**).¹¹¹

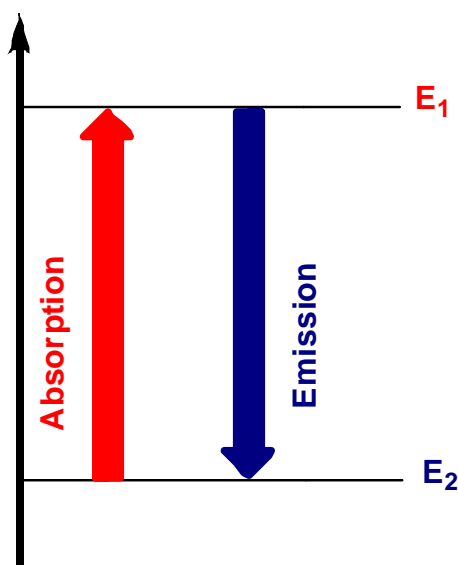


Figure 4.1: Absorption and emission of photons between energy levels.

Electron paramagnetic resonance (EPR), also known as ESR (electron spin resonance) involves transitions between electron spin states, and is the electron analogue of NMR spectroscopy. The electron spin quantum number, S , can have values m_s of $\pm 1/2$, and an EPR spectrum represents transitions between electron spin states, as illustrated in **Figure 4.2**.

Since the formation of chemical bonds involves the pairing of electrons and a net spin $S = 0$, it is only molecules and ions with *unpaired* electrons that exhibit EPR.¹¹² EPR was first observed by Zavoisky in 1944,¹⁴⁴ and much of the theoretical principles were subsequently made at Oxford University (Abragam, Bleaney *et al.*).¹⁴⁵ Over the past six decades EPR has been demonstrated to be a powerful technique for the production of bonding and structural information in free radicals

and other molecules with *unpaired* electrons. In favourable situations, it can determine the delocalisation of an *unpaired* electron over metal ions and their surrounding ligands.¹⁴⁶

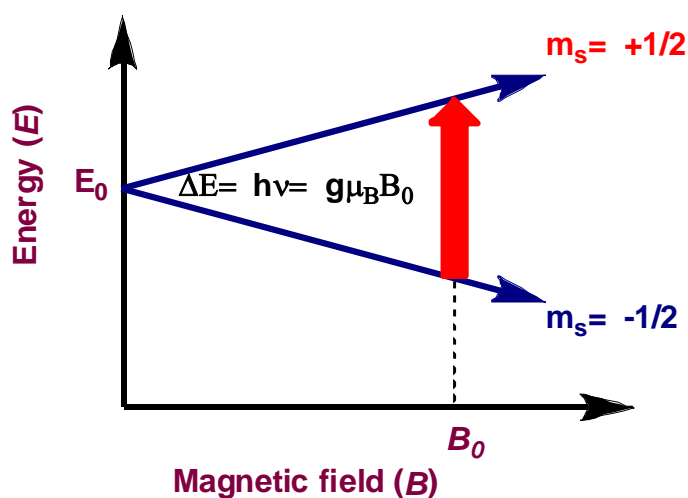


Figure 4.2: Illustration of the transition between the electron energy levels in applied magnetic field.

4.1.1 Basic principles of EPR

This section describes briefly the background of EPR spectroscopy, the origin of the principal spectral parameters (the g and A values) from the relative energies and symmetries of molecular orbitals, and the interactions between electron and nuclear spins. In addition, the basic components of a spectrometer are also presented.

In the absence of a magnetic field, the two spin states m_s of an electron are of equal energy and hence equally populated. However, an *unpaired* electron also has a magnetic moment μ , and when it experiences a magnetic field, B_0 , the magnetic moment of the electron can either align with or against the field, resulting in states of lower energy or higher energy, respectively. This interaction between an *unpaired* electron and a magnetic field is called the Zeeman effect.¹⁴⁷ The difference in energy of the electron spin states is given by **Equation 4.1**.

$$\Delta E = h\nu = g\mu_B B_0$$

Equation 4.1¹⁴⁶

where **h**: Planck's constant

μ_B : the Bohr magneton

g: is a constant known as the
g-value

Thus the magnetic field and frequency of the electromagnetic radiation, ν , are variables that can be adjusted to find the resonance condition. Since ν is in the microwave region of the electromagnetic spectrum for magnetic fields that are conveniently obtained with electromagnets, an EPR spectrum is usually obtained by varying the magnetic field whilst the frequency of the microwaves is kept constant.

For instrumental reasons, EPR spectra are usually acquired as first derivatives of the microwave absorption rather than the absorption itself, and sometimes second derivatives are used in order to enhance resolution and discrimination between peaks with different linewidths. In the 1st derivative spectrum, the zero point crossing the baseline correlates to the maximum peak of absorption spectrum and minimum peak of 2nd derivative spectrum (**Figure 4.3**).¹⁴⁸ The linewidth is the peak to trough distance of the signal, as depicted in 1st derivative spectrum in **Figure 4.3**. This is close to the full width at half maximum of the absorption peak.

The signal intensity, which is directly proportional to the number of *unpaired* electrons in a sample, is the integral of the absorption or the double integral of the 1st derivative of the absorption.¹⁴⁹ Also, because dipolar interactions between electron spins on neighbouring molecules result in spectral broadening, it is common for EPR spectroscopists to dilute their samples in diamagnetic matrices or solvents (*e.g.* DCM, DMSO, toluene, *etc.*) in order to optimise spectral resolution.

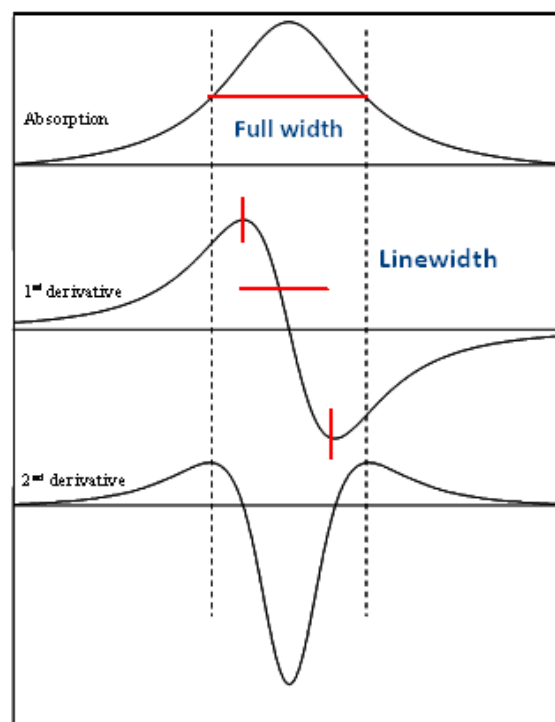


Figure 4.3: Absorption, 1st and 2nd derivative Lorentzian lineshapes. The dashed lines indicate full width at half maximum of the absorption peak.

Because each electron has a magnetic moment, μ , it can interact with other atomic or molecular species which also possess magnetic moments. The two most important interactions in EPR are:

- (i) Interaction of electron spins with other *unpaired* electrons.
- (ii) Interaction of electron spins with the spins of nuclei that are involved in the molecular orbital containing the *unpaired* electron.

if a compound which has a single *unpaired* electron is in a dilute solution then (i) can be neglected. In (ii) the energy states of the *unpaired* electron are split as a result of a local magnetic field \mathbf{B}_l produced by the magnetic moments of nuclei with non-zero spin. This interaction, which is known as the *hyperfine interaction* can be used as a “fingerprint” for the presence of some elements; it also provides information on their contribution to the molecular orbital containing the *unpaired* electron.

Interactions between *unpaired* electron and nuclear spins result in the splitting of the spectra into $2I+1$ components for each nucleus (where I is the nuclear spin); the resonance condition is given by **Equation 4.2**, and illustrated in **Figure 4.4** for a single nucleus with $I = 1/2$:

$$h\nu = g\mu_B(B_0 + Am_I)$$

where **A**: hyperfine coupling
constant

m_I: nuclear spin quantum

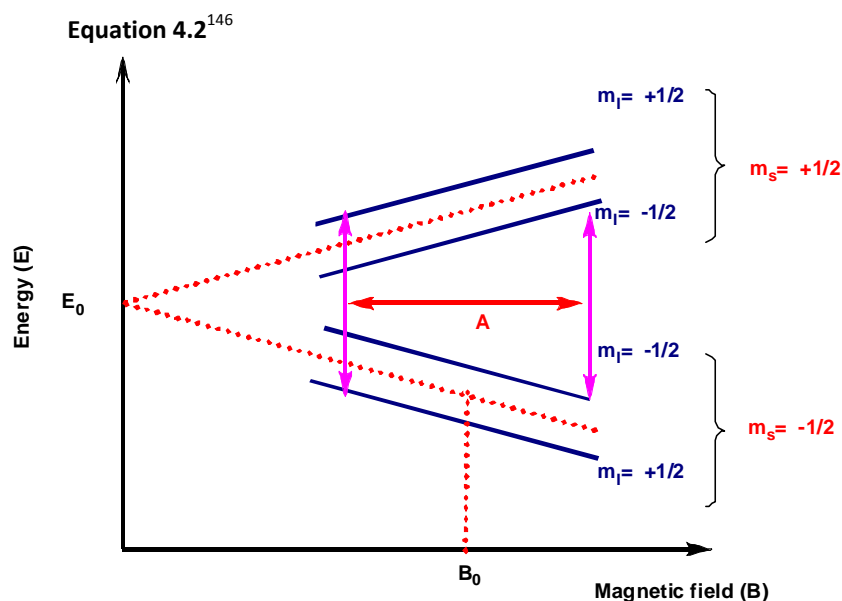


Figure 4.4: Energy levels of an electron in a magnetic field upon interaction with a spin $\frac{1}{2}$ nucleus.

The separation between peaks is known as the hyperfine coupling constant, **A**, and is usually expressed in Gauss or mT, though sometimes it is converted to wavenumbers or MegaHertz.¹⁴⁵ The arrows show allowed transitions for which $|\Delta m_I| = 0$ and $|\Delta m_s| = 1$. In transition metal EPR, the term *hyperfine structure* is associated with interaction of the *unpaired* electron with the metal nucleus and the term *superhyperfine structure* is used for structure arising from ligand nuclei.

When there is > 1 equivalent nucleus contributing to the hyperfine structure, the relative intensities of the peaks are given by a Pascal triangle and two equivalent spin $1/2$ nuclei produce hyperfine structure with relative intensities of 1:2:1. In the present work, hyperfine structure arises from the $^{63,65}\text{Cu}$ (both of which have $I = 3/2$) and ^{14}N ($I = 1$); the major isotopes of C, O have $I = 0$, and hence produce no hyperfine structure. For example, the theoretical relative intensities for a nonet

derived from interaction of the *unpaired* electron with 4 equivalent ^{14}N (total $I=4$), therefore are 1:4:10:16:19:16:10:4:1.

4.1.2 EPR parameters

This section attempts to provide a basic explanation for the origins of the **g**- and **A**-values, which are necessary for understanding the interpretation of EPR results that are discussed in **Section 4.2**.

g-value: It is related to the coupling between the electron spin and orbital angular momenta.

A-value: The hyperfine coupling constant (units in Gauss or mT), the magnitude of which corresponds to the *unpaired* electron density on that nucleus.

Generally in transition metals, *unpaired* electrons occupy d-orbitals, and the magnitudes of **g** and **A** are dependent on the orientation of the molecular orbital relative to the magnetic field.¹⁵⁰ Also, since Cu(II) porphyrins have the *unpaired* electron in a $d_{x^2-y^2}$ orbital and square planar geometry,¹⁵¹ it is necessary only to discuss axial symmetry for the present work. For axial symmetry, there are two principal **g**-values, namely $g_{//}$ and g_{\perp} ,¹⁵² which can be determined for an EPR spectrum, provide information on molecular symmetry and the energy separation between the orbital containing the *unpaired* electron and those with which it can mix *via* spin-orbit coupling.

$g_{//}$: The observed g-value, when the principal axis of the orbital is parallel to the direction of the magnetic field.

g_{\perp} : The observed g-value, when the principal axis of the orbital is perpendicular to the direction of the magnetic field.

The hyperfine coupling constants (**A**-values) provide a measure of the probability of the *unpaired* electron being on the magnetic nucleus that produces the hyperfine splitting. Thus in the case of the highly conjugated copper(II) porphyrin ring, the

A-values can show the extent to which the *unpaired* electron density is localised on the Cu(II) ion or is delocalised to the four surrounding nitrogen nuclei. As with **g**-values, **A**-values are orientation dependent (anisotropic), and for molecules with axial symmetry, EPR spectra produce two principal parameters, **A**_{//} and **A**_⊥. In analysing the spectra in the present work, it is assumed that the **g**- and **A**-values are co-axial, although this is not necessarily the case.

When spectra are recorded for samples in fluid solution, average values for **g** and **A** are obtained provided molecules are tumbling rapidly. With single crystal samples, the individual values are obtained for each orientation, and in powder or frozen solutions, all orientations are present simultaneously and a spectrum consists of a sum of the spectra for all orientations weighted by their probabilities. However, in solutions of large molecules (*e.g.* porphyrin-DNA complexes) or when using viscous solvents, tumbling rates may be slow compared to the timescale of the EPR transition, and spectra then resemble those of frozen solutions. Powder and frozen solution EPR spectra are by far more commonly measured than single crystals.

For rapidly tumbling molecules, the relationships between the spectral parameters determined for fluid and frozen solutions are:

$$g_{\text{iso}} = \frac{1}{3} (g_{//} + 2g_{\perp}) \quad A_{\text{iso}} = \frac{1}{3} (A_{//} + 2A_{\perp})$$

Equation 4.3

An alternative description of the hyperfine coupling constants, **A**_{//} and **A**_⊥, is by use of the parameters **A**_{iso} and **A**_{aniso} where **A**_{iso} is constant and **A**_{aniso} is orientation dependent. For the Cu(II) ion, the values determined for **A**_{aniso} provide a direct measure of the d-orbital electron density. For axial symmetry with the *unpaired* electron in a **d**_{x²-y²} orbital, such as occurs in copper porphyrins, the **g**_{//} and **g**_⊥ values are given by the following expressions:¹⁵³

$$g_{\parallel} = 2.0023 + 8\lambda/\Delta E (d_{x^2-y^2} - d_{xy})\alpha$$

$$g_{\perp} = 2.0023 + 2\lambda/\Delta E (d_{x^2-y^2} - d_{xz,yz})\alpha$$

Equation 4.4

where λ is the spin-orbit coupling constant.

ΔE is the energy separations between the $d_{x^2-y^2}$ orbital and orbitals with which it can mix *via* spin-orbit coupling.

α is the fractional occupancy of the $d_{x^2-y^2}$ orbital in the molecular orbital.

The positive sign + is because spin orbit coupling occurs between the molecular orbital and occupied orbitals.¹⁵⁴

Theoretical EPR spectra for frozen solutions of paramagnetic species with axial and rhombic symmetry, but without hyperfine structure, are shown **Figure 4.5**.



Figure 4.5: Simulated anisotropic spectra for (top) axial symmetry, (middle) small and (bottom) large rhombic distortions for molecules without hyperfine structure.

Although axial symmetry is assumed for all spectra analysed in this thesis, it is important to recognise the effects of lower symmetry on spectral line shapes, since this is in principle possible for the Cu porphyrin-DNA complexes.

4.1.3 “Forbidden” transitions in EPR

In EPR, allowed transitions satisfy the condition $|\Delta m_l| = 0$ and $|\Delta m_s| = 1$. However, when two $S = \frac{1}{2}$ centres are close to one another they can interact to produce a singlet $S = 0$ and a triplet $S = 1$ state, the latter having m_s values of +1, 0 and -1. In this case, the transition probability of normally forbidden transitions between $m_s = +1$ and $m_s = -1$ states can become non-zero and an absorption occurs at half of the magnetic field required for allowed transitions (**Figure 4.6**). For this reason it is sometimes referred to as a **Half-Field** transition.¹⁵⁵ The half-field transition can be used to determine the distance between two *unpaired* electron spins,¹⁵⁶ and could therefore potentially be used to elucidate the distance between Cu(II) ions in porphyrins attached to DNA in **Section 4.2.2.6**.

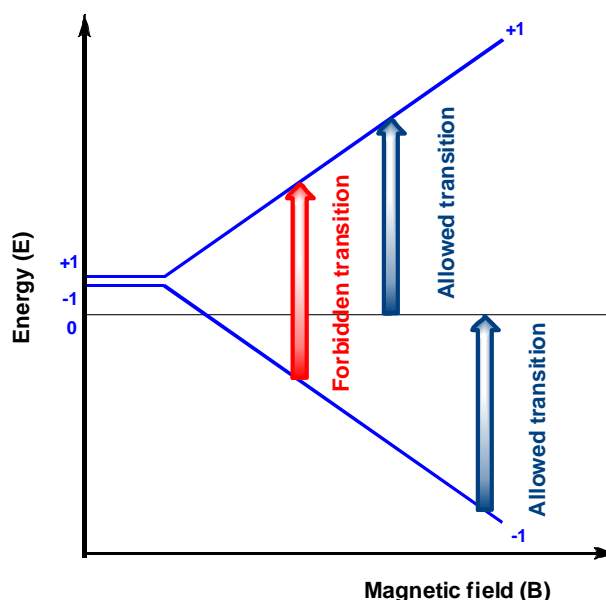


Figure 4.6: Forbidden transition observed for $|\Delta m_s| = 2$.

4.1.4 Components of EPR spectrometer

EPR is performed in a microwave cavity that is held inside an electromagnet and connected to a microwave bridge, which supplies electromagnetic radiation and also functions as a signal detector (**Figure 4.7**). In modern spectrometers, all operations and spectral acquisition parameters are controlled by computer. For frozen solution measurements, the cavity is connected to variable temperature attachment which uses liquid nitrogen to achieve temperatures from 90 K upwards, and liquid helium for lower temperatures (down to 4.2 K).



Figure 4.7: Basic components of a Bruker X-band EPR spectrometer.

Because of its ability to provide information on the distribution of *unpaired* electron density in free radicals and paramagnetic transition metal complexes, EPR spectroscopy has applications in a wide range of scientific subjects, including the life, materials and environmental sciences, as well as more basic applications in physics, chemistry and biochemistry. Furthermore, EPR spectra of DNA duplexes with Cu(II) centres stacked internally between complementary strands²⁹ have indicated the existence of connectivity along metal arrays self-assembled by the DNA matrix, thus suggesting use for EPR in constructing new functionalised DNA arrays in the preparation of nanowires.

Finally, EPR spectroscopy is non-destructive and non-invasive, and thus is ideal for studying nano-materials such as porphyrin-modified DNA, which can only be produced on a small scale. In addition, EPR is a sensitive technique, and considerable information can be obtained with a few mgs of solid sample, or μM concentrations in volume of a few hundred μL . The technique provides information specifically on paramagnetic components in a sample. Cu(II) with nine 3d electrons (one short of a filled shell) is excellent for EPR studies, but Cu(I) is diamagnetic and hence EPR silent. Natural copper contains two isotopes (^{63}Cu and ^{65}Cu), both of which have good properties for EPR spectroscopy, and EPR spectra consist of a superimposition of the spectra from the individual isotopes.

4.2 EPR results and discussion

There is extensive literature on EPR of Cu(II) porphyrins and related complexes, which in combination with the report of Cu(II)-DNA intercalation from Tanaka *et al.*¹⁵⁷ was a major consideration in choosing copper over other metals for the present investigations. Since the EPR spectral parameters are related to the symmetry at the copper site, and provide information on the *unpaired* electron density on both the copper nucleus and nitrogen atoms in the ligands, it is potentially valuable for determining whether the Cu porphyrin structure has been maintained in the DNA complexes.¹⁵⁸

Previously, applications of EPR to nanotechnology of DNA were performed only on duplexes with internal metal stacking. In this thesis, however, such applications have been extended to include both DNA double strands and single strands using EPR active chromophores (*i.e.* copper(II) porphyrin) externally stacked on DNA. This research was performed with the aim of enhancing the understanding of porphyrin-DNA structure by combining the ability of DNA to form self-assembling functional molecules and the optoelectronic activity of porphyrins. These experiments reinforce the utility of porphyrin-DNA as a scaffold for nanoarchitecture, and represent an ideal bottom-up approach for the design of functional nanosystems.

This chapter displays all the EPR spectra measured for copper porphyrin building blocks and porphyrin-DNA strands, followed by data interpretations. All the experimental spectra are presented in their original forms unless otherwise stated, and any numbers labelled on the experimental spectra are for indicative purposes only. The accurate EPR parameters can only be deduced from the simulated EPR spectra and their quantitative values are tabulated in **Section 4.2.1.5**. EPR spectral measurements, simulations and discussion were done in collaboration with Dr. Ruth Edge, Prof. David Collison, Prof. Eric McInnes at the EPSRC EPR National Service, University of Manchester and Prof. Bernard A. Goodman of Guangxi University, China.

4.2.1 EPR study of copper porphyrin building blocks

Most EPR spectra of copper porphyrin building blocks were recorded on a Bruker EMX Micro spectrometer operating at X-band frequencies and equipped with a super high sensitivity rectangular X-band cavity. Reflection of continuous microwaves generated from a microwave bridge onto the sample was measured by a built-in frequency counter. Samples recorded on the Bruker EMX Micro X-band spectrometer were measured in 3 mm i.d. (internal diameter) quartz sample tubes. Spectra were recorded in 2048 points using 100 kHz modulation frequency, either as 1st or 2nd derivatives of the microwave absorption.

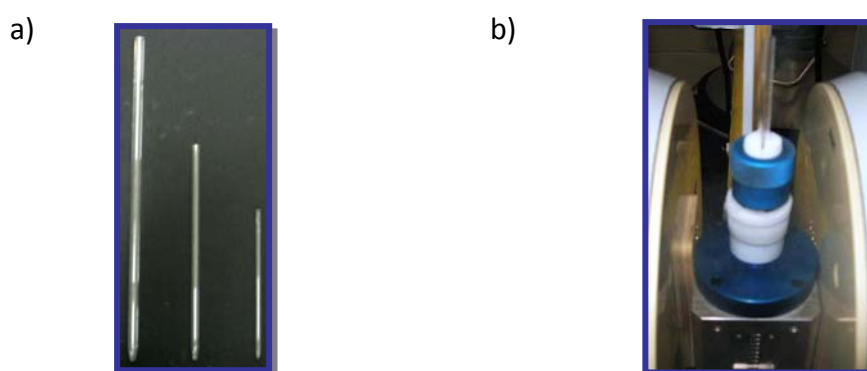


Figure 4.8: a) EPR tubes used in X-band (3 mm i.d.), K-band (2 mm i.d.) and Q-band (1 mm i.d.) (left to right) spectrometers and b) Bruker EMX Micro X-band cavity.

In order to optimise the spectral resolution and signal-to-noise (S/N) ratio, it is important to carefully control the two most critical parameters, namely:

- (i) Microwave power, measured in milliWatt (mW).
- (ii) Modulation amplitude, measured in Gauss (G).

This is because in the absence of saturation, the signal intensity is proportional to the square root of the microwave power. When a very high microwave power is applied, the rate of excitation of electrons to the excited state can exceed the rate of relaxation back to the ground state, and the signal intensity is no longer proportional to the square root of the microwave power. This is then known as saturation of signal and can be avoided by using a low microwave power, to enable accurate measurements of parameters from spectra such as linewidths, hyperfine

coupling constants. Spectroscopists can check for the absence of signal saturation by decreasing microwave power and plotting a graph to verify that the signal intensity falls by the square root of microwave power.^{147, 150} In practice, however weak spectra are often recorded under conditions of partial saturation in order to maximise the signal-to-noise ratio. Signal broadening also occurs but only becomes important for extreme saturation.

Also, the spectral resolution is dependent on the modulation amplitude. Spectral broadening (hence loss of resolution) occurs when the modulation amplitude approaches or exceeds the spectral linewidth. The signal intensity is proportional to the modulation amplitude, which is the reason for using as high a value for modulation amplitude as possible without causing significant spectral broadening. For all of the EPR measurements of porphyrin building blocks, the modulation amplitude was chosen to be less than the peak-to-trough widths of the narrowest line of 1st derivative spectra, in order to minimise any broadening, hence loss of resolution effect.

The microwave power and modulation amplitude selected for initial measurements of copper porphyrin building blocks in this work were 4 mW and 2 G respectively, so that any saturation or distortion of signal would be negligible. 5 G modulation amplitude was later used to enhance signal-to-noise.

4.2.1.1 Copper porphyrin building blocks preparation for EPR

At first, samples of copper(II) di-tert-butyl diphenyl porphyrin **CuDPP 15** (~ 1 mg) were investigated under three separate conditions:

- (i) As pure solid powder at 120 Kelvin (K) and 290 K.
- (i) In fluid solution in DCM (0.20 mL) at 290 K.
- (iii) In frozen solutions of DCM/Toluene 10:1 (0.20 mL) at 120 K.

The above experiments were chosen because solid state samples produce anisotropic spectra. On the other hand, fluid samples average the anisotropic terms and can therefore record sharper peaks, which maybe better for determining the nuclear environment of copper.^{150, 154} These experiments of **CuDPP** building blocks should therefore acquire enough parameters for subsequent comparisons to EPR of copper porphyrin-DNA. Samples of copper(II) acetylene tetraphenyl porphyrin **CuTPP 16**, which were prepared by Jonathan R. Burns, University of Southampton were also investigated, following conditions used for **CuDPP**. The aim was to draw comparisons between the two porphyrins that are used in the Stulz group to create porphyrin-DNA assemblies.

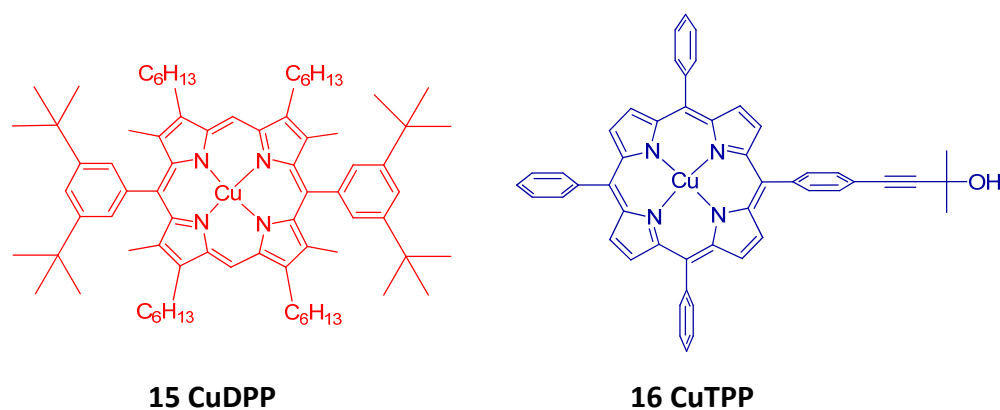


Figure 4.9: Copper porphyrin building blocks for EPR spectroscopy.

4.2.1.2 Fine powder measurements of CuDPP and CuTPP

X-band EPR spectra of a fine powder of dry **CuDPP 15** (~ 1 mg) were first acquired for a short scan (2200 G – 3700 G) at room temperature 290 K, followed by 120 K. These 1st derivative results were similar to those reported in the literature.¹⁵⁹ Measurements were then expanded to the 1100 G – 3700 G field range to check for any spin forbidden transition that arises at ~1600-1700 gauss (see **Section 4.1.3** for reference on half-field signal); and for any discrepancy at different temperatures. **Figure 4.10** shows the X-band EPR spectra of **CuDPP 15** measured in fine powder form.

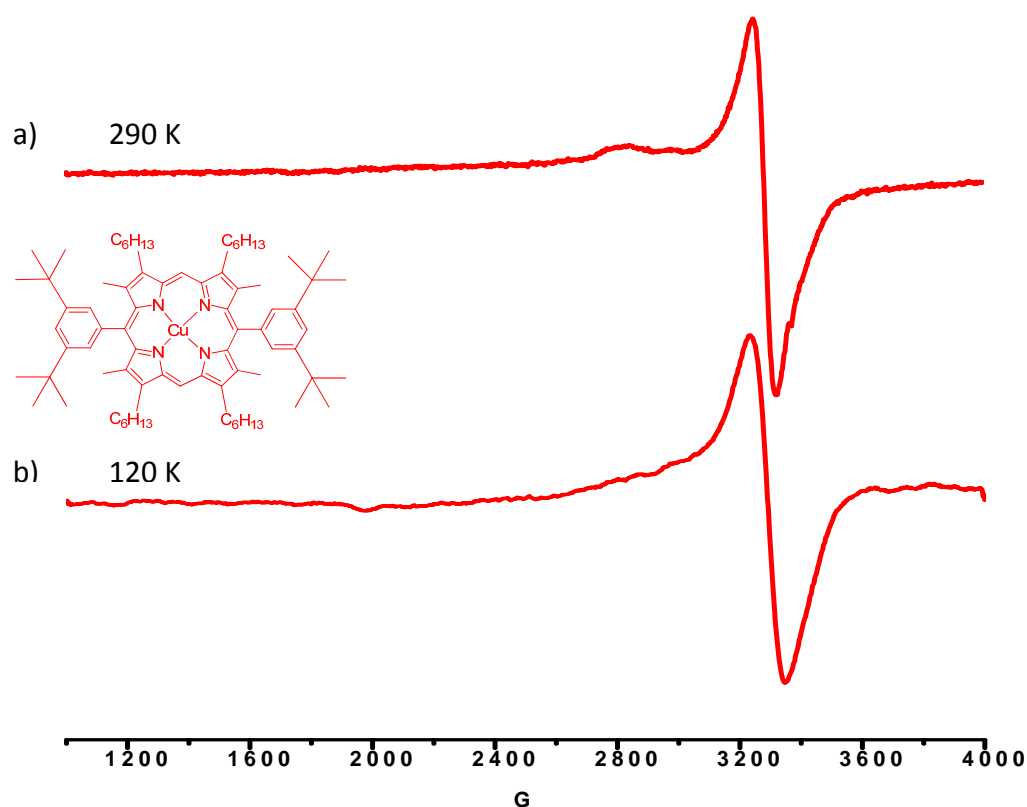


Figure 4.10: 1st derivative EPR spectra of powder sample of copper(II) di-tert-butyl diphenyl porphyrin **CuDPP 15** at a) 290 K and b) 120 K. Spectra were acquired with 3.99 mW microwave power, 2 Gauss modulation amplitude, and approx. 9.4 GHz microwave frequency.

The 1st derivative EPR spectra of the pure powders of **CuDPP 15** at 290 K and 120 K consist of essentially single peak resonances (**Figure 4.10**). These spectra produce broad single peaks because of exchange coupling, which is due to the individual Cu(II) ions in the samples being sufficiently close for rapid electron exchange to occur between neighbouring paramagnetic centres. When this electron exchange frequency approaches the magnitude of the hyperfine structure (measured in frequency units), the hyperfine lines start to broaden and move towards the centre of the spectrum, thus form a single broad peak. This process is known as *exchange broadening* and is observed in this case. It seems also that this process is temperature independent. On the other hand, *exchange narrowing* occurs when the electron exchange frequency is greater than the hyperfine structure, resulting in peaks getting narrower.

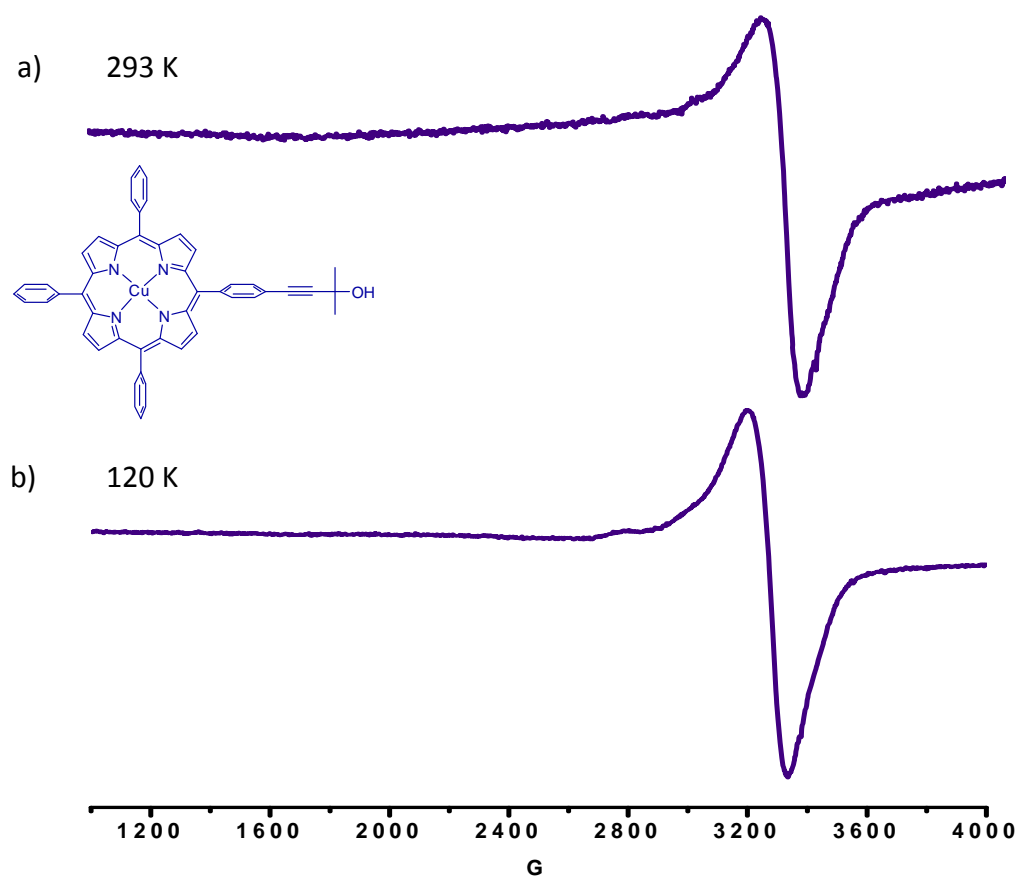


Figure 4.11: 1st derivative EPR spectra of powder sample of copper(II) acetylene tetraphenyl porphyrin **CuTPP 16** at a) 293 K and b) 120 K. Spectra were acquired with 3.99 mW microwave power, 2 Gauss modulation amplitude, and approx. 9.4 GHz microwave frequency.

Similarly, EPR spectra of **CuTPP 16** (**Figure 4.11**) consist of broad single peaks due to the same exchange coupling effect. These observations suggest that the interaction between individual Cu(II) ions remains the same at different temperatures for fine powder of copper porphyrin. Also this interaction is independent of the functional groups attached to the porphyrin. Half-field signals were not observed in these measurements.

4.2.1.3 Fluid solution measurements of CuDPP and CuTPP

Figure 4.12 depicts 1st derivative EPR spectra of a solution of **CuDPP 15** in different solvent mixtures. Unlike the fine powder which produces only one broad signal, more peaks can be observed in fluid solution spectra. These peaks arise from the interactions of the *unpaired* electron with copper and nitrogen nuclei. Because the Cu(OAc)₂ reagent used to metallate the porphyrins is a mixture of isotopes, this interaction is due to ⁶³Cu and ⁶⁵Cu nuclei. Both isotopes are spin active ($I = 3/2$), so they generate hyperfine splitting into $(2I + 1)$ components. ⁶³Cu and ⁶⁵Cu make up 69 % and 31 % natural abundances and their magnetic moments of 2.2206 and 2.3790 nuclear Bohr magnetons are not sufficiently different for all the peaks to be resolved in 1st derivative spectra.¹⁵⁸ Theoretically, there should be 4 peaks observed as a result of $(2I + 1)$ splitting by copper nuclei ($I = 3/2$). The presence of the 1st peak is, however, can only just about be seen in **Figure 4.12 d**.

There is a considerable linewidth variation in the individual copper peaks with the width increasing progressively at lower fields because the rate of tumbling of molecules is not sufficiently rapid to completely average the spectral anisotropy.¹⁵⁴ The overlapping of different lines is mostly responsible for the incompletely resolved spectra.

Although the overlapping of mixed isotopes ⁶³Cu and ⁶⁵Cu splittings is another contributing factor to poorly resolved copper peaks, this effect is of smaller significance. Simulations of fluid solutions EPR measurement of porphyrin building blocks were tried to resolve spectra. These simulations are based on single Cu isotope and four equivalent ¹⁴N. As a consequence, the separations between four copper peaks are more clearly resolved in simulated spectra and splittings can also be observed in 3rd copper peak, as shown in **Figure 4.13**.

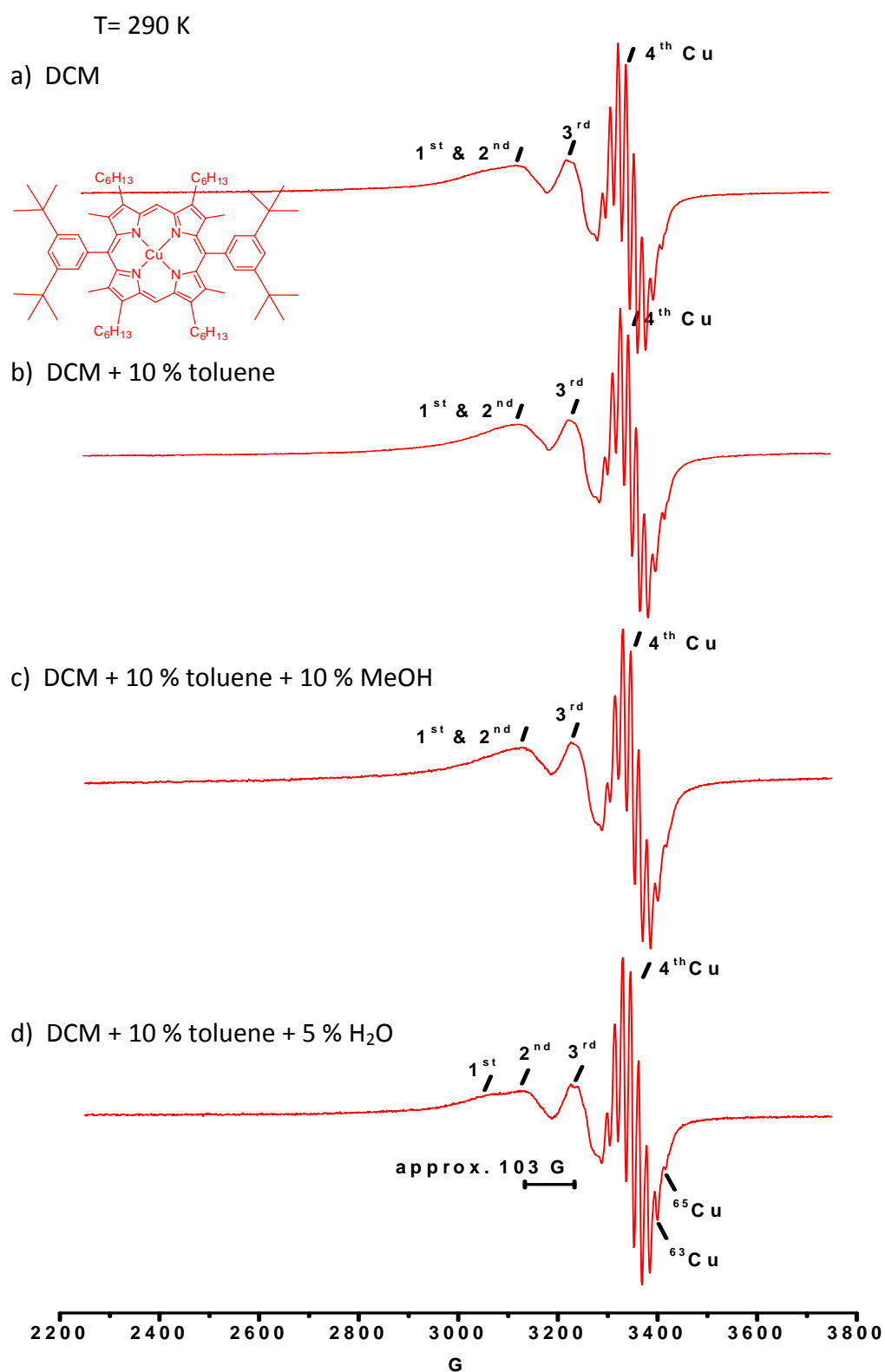


Figure 4.12: 1st derivative spectra of solution of **CuDPP 15** in a) DCM; b) DCM + 10 % toluene; c) DCM + 10 % toluene + 10 % MeOH; d) DCM + 10 % toluene + 5 % H₂O, 290 K. Spectra were acquired with 3.99 mW microwave power, 2-5 Gauss modulation amplitude and approx. 9.4 GHz microwave frequency.

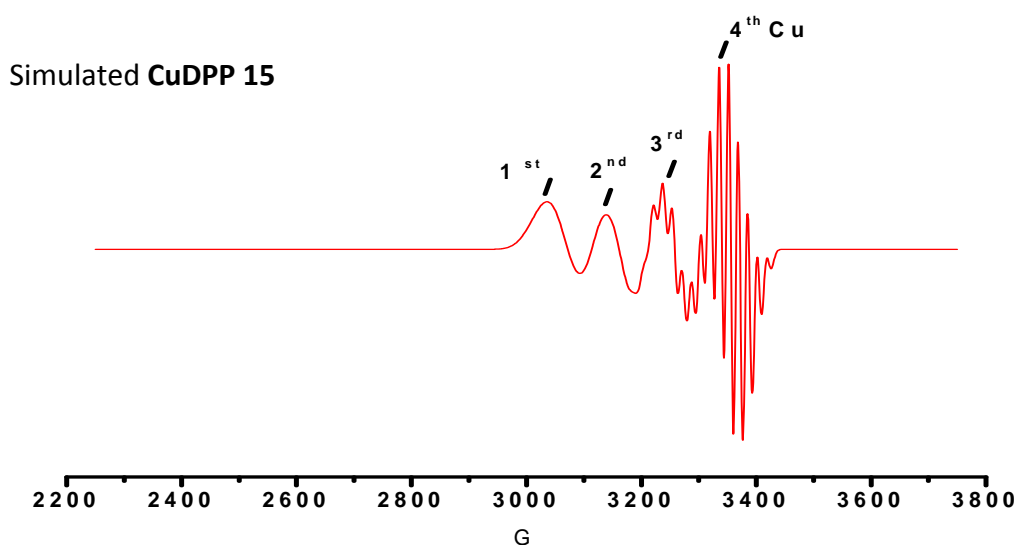


Figure 4.13: Simulation of 1st derivative solution spectrum of **CuDPP 15**, ⁶³Cu (100 %) in DCM have $g_{\text{iso}} = 2.095$, $A_{\text{iso}}(^{63}\text{Cu}) = 90$ Gauss, $A_{\text{iso}}(^{14}\text{N}) = 16$ gauss, Lorentzian/Gaussian lineshape = 1, $L/W = a + bm + cm^2$, $a = 20$ G, $b = 10$ G, $c = 3$ G.

Simulation of the 1st derivative solution spectrum of **CuDPP 15** is achieved using Simfonia software to resolve copper peaks. In an isotropic environment where molecules spin equally in all directions (*i.e.* spinning football scenario), the tumbling of molecules would be faster than the microwave frequency (GHz) to enable the complete isotropic averaging to give 4 nonets for 4 copper peaks. Each nonet is derived from the coupling of the *unpaired* electron to four equivalent ¹⁴N ($I = 1$). However as **CuDPP 15** does not have perfect symmetry (*i.e.* spinning dinner plate scenario), it is therefore important to include the tumbling effect in simulations, which requires setting 100 % natural abundance for ⁶³Cu single isotopes in the program. More details on simulations are described in **Section 4.2.1.5** and in **Chapter 5, Section 5.2.2**.

The first spectrum was recorded in DCM for X-band as **CuDPP 15** was most soluble in DCM. 10 % of toluene was then added to see if this would improve spectral resolution as toluene/DCM had been used to enhance glass formation for frozen EPR samples. Nevertheless, the spectral resolution remained unaltered upon addition of toluene. 10 % of MeOH and a small amount of 5 % of H₂O (as these porphyrins were hydrophobic) were added to check for the binding of MeOH and

H₂O to porphyrins. This investigation is important, because the initial results provide valuable comparisons with the possible binding of porphyrin-DNA to solvent at the porphyrin sites, which may affect DNA stability and duplex formation. As there is negligible discrepancy between these 1st derivative spectra, it is thus concluded that **CuDPP 15** does not form octahedral complexes with either MeOH or H₂O in fluid solution at room temperature.

Besides copper hyperfine structures, some superhyperfine structures from interactions of the *unpaired* electron with ¹⁴N are observed in **CuDPP 15** fluid solution EPR spectra, most notably on the highest field copper peak. The superhyperfine structure (shfs) follows a (2nI + 1) pattern, consisting of 9 peaks arising from 4 equivalent neighbouring ¹⁴N nuclei, each has I = 1, therefore giving a total nI = 4. The nitrogen shfs is seen more clearly in 2nd derivative recordings.

Figure 4.14 a shows apparent shfs as a nonet following intensity ratio 1:4:10:16:19:16:10:4:1. Despite a clear nonet shfs observed in the 4th copper peak, the other copper peaks in **CuDPP 15** are still not narrow enough for this structure to be resolved. Hence simulation was carried out (**Figure 4.14 b**).

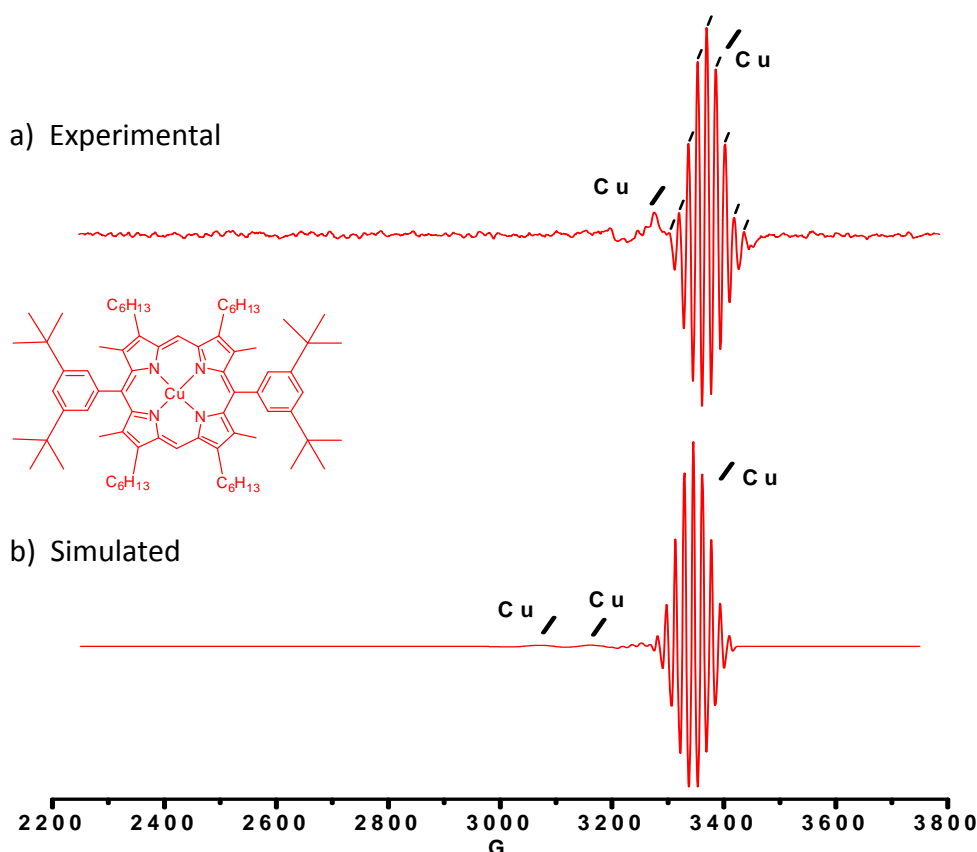


Figure 4.14: 2nd derivative fluid solution EPR spectra of **CuDPP 15** in DCM, 290 K of a) experimental spectrum acquired with 3.99 mW microwave power, 5 Gauss modulation amplitude and approx. 9.4 GHz microwave frequency; b) simulated spectrum ⁶³Cu (100 %) having $g_{\text{iso}} = 2.095$, $A_{\text{iso}}(^{63}\text{Cu}) = 90$ G, $A_{\text{iso}}(^{14}\text{N}) = 16$ G, L/G lineshape = 1, L/W = $a + bm + cm^2$, $a = 40$ G, $b = 18.5$ G, $c = 0.1$ G.

A fluid solution EPR spectrum was also recorded for copper(II) acetylene tetraphenyl porphyrin **CuTPP 16** (Figure 4.15). Herein, the four peaks due to *unpaired* electron split by copper nuclei are observed more clearly compared to spectra of **CuDPP 15**, and some shfs can even be seen in the lowest field copper peak. More splittings in 3rd copper peak could be associated with different molecular tumbling rates between **CuTPP** and **CuDPP**.¹⁶⁰ The faster the isotropic tumbling, the better the spectra get resolved. Visible splitting in 3rd copper peak is a result of a faster **CuTPP** tumbling rate than for **CuDPP**, probably because of the difference in molecular bulk (*i.e.* number of atoms and their overall shape). Otherwise, 1st derivative fluid solution EPR spectra of **CuTPP 16** look quite similar to spectra of **CuDPP 15** measured at room temperature. Simulation of **CuTPP** shows a slightly smaller $A_{\text{iso}}(^{63}\text{Cu})$ compared to **CuDPP** (*i.e.* 88 G instead of 90 G).

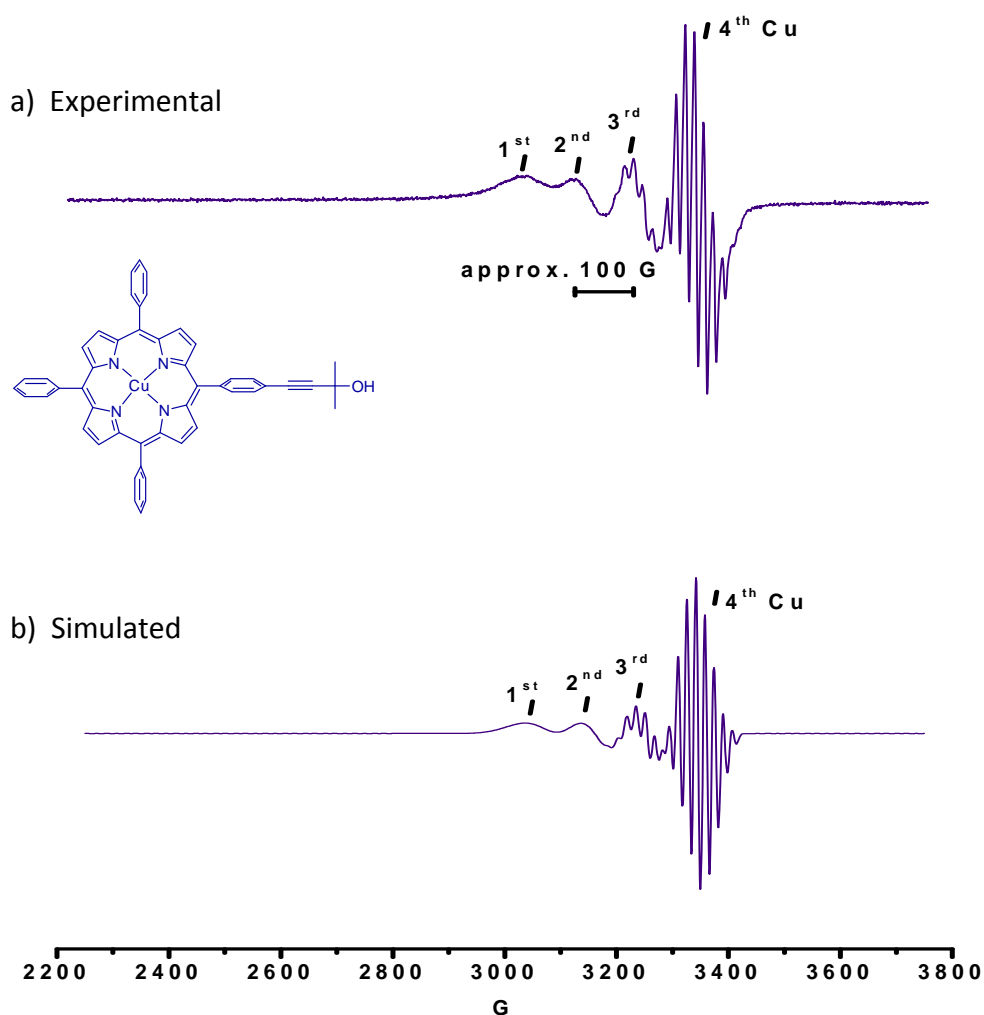


Figure 4.15: 1st derivative fluid solution EPR spectra of **CuTPP 16** in DCM + 10 % toluene, 293 K of a) experimental spectrum was acquired with 3.99 mW microwave power, 1 Gauss modulation amplitude, approx. 9.4 GHz microwave frequency; b) simulated spectrum ⁶³Cu (100 %) having $g_{\text{iso}} = 2.095$, $A_{\text{iso}}(^{63}\text{Cu}) = 88$ G, $A_{\text{iso}}(^{14}\text{N}) = 15.8$ G, L/G lineshape = 1, $L/W = a + bm + cm^2$, $a = 23$ G, $b = 21$ G, $c = 8$ G.

In order to study the differences in EPR spectra between **CuDPP** and **CuTPP** at the molecular level, one needs to perform EPR slow motion lineshape calculations. This produces values for molecular tumbling rates, and therefore provides a better understanding of the structures of molecules. Initial work for this project has been carried out in collaboration with Dr. Par Hakansson at the University of Southampton.

4.2.1.4 Frozen solution measurements of CuDPP and CuTPP

In order to derive anisotropic values, copper(II) di-tert-butyl diphenyl porphyrin **CuDPP 15** spectra were acquired from frozen solutions at 120 K. The 1st derivative spectrum in DCM solution is presented in **Figure 4.16 a**. It shows features corresponding to $g_{//}$ and some ^{14}N shfs on the g_{\perp} features, which can be resolved better in 2nd derivative. Although these features are apparent, the peaks are relatively broad and the quality of spectra is unsatisfactory. It is difficult to determine the $A_{//}(^{14}\text{N})$ values, because of the large linewidth, to which the presence of the two Cu isotopes is a contributing factor. However, as in the fine powder spectra, electron exchange interactions are largely responsible for this spectral broadening. This occurs because of segregation of the solvent and solute that results in the poor glassing in a frozen sample. Hence, 10 % of toluene by volume was added into DCM solution to improve the glass formation.¹⁶⁰

Upon addition of toluene, the frozen sample was seen to form better glassing inside the EPR tube and the quality of spectra improved greatly. All **Figure 4.16 b, c and d** show clearer features of ^{14}N shfs on the 4th copper peak, and some narrow shfs on the g_{\perp} features. Similarly to fluid solution spectra, adding MeOH or H₂O has little effect on the frozen EPR spectra of **CuDPP 15**, suggesting that neither in fluid solutions or frozen solutions do **CuDPP 15** form octahedral complexes with either MeOH or H₂O.

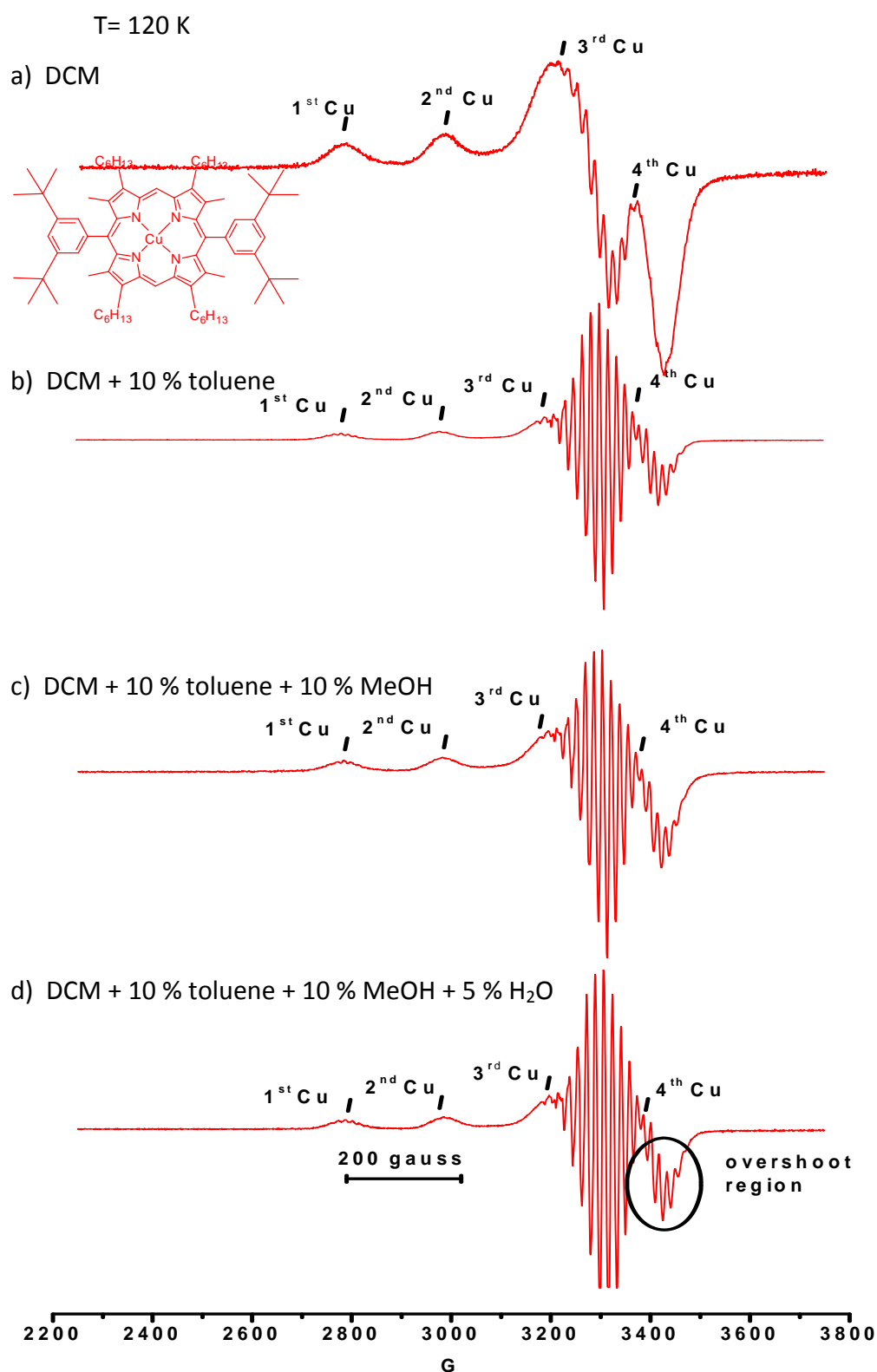


Figure 4.16: 1st derivative EPR spectra of frozen solution of **CuDPP 15** in a) DCM; b) DCM + 10 % toluene; c) DCM + 10 % toluene + 10 % MeOH; d) DCM + 10 % toluene + 5 % H₂O, 120 K. Spectra were acquired with 3.99 mW microwave power, 2 Gauss modulation amplitude and approx. 9.4 GHz microwave frequency.

Good glassing of the frozen solutions upon addition of toluene also improves the quality of 2nd derivative spectra, as seen in **Figure 4.17 a** and **b**, with higher resolution of shfs than measured in DCM alone. Although the ¹⁴N shfs can be better resolved in 2nd derivative compared to 1st derivative recordings, the nonet of intensity ratio 1:4:10:16:19:16:10:4:1 cannot be resolved completely, due to the overlapping of high field copper hyperfine peaks, in addition to an overshoot effect observed at the highest field.¹⁵²

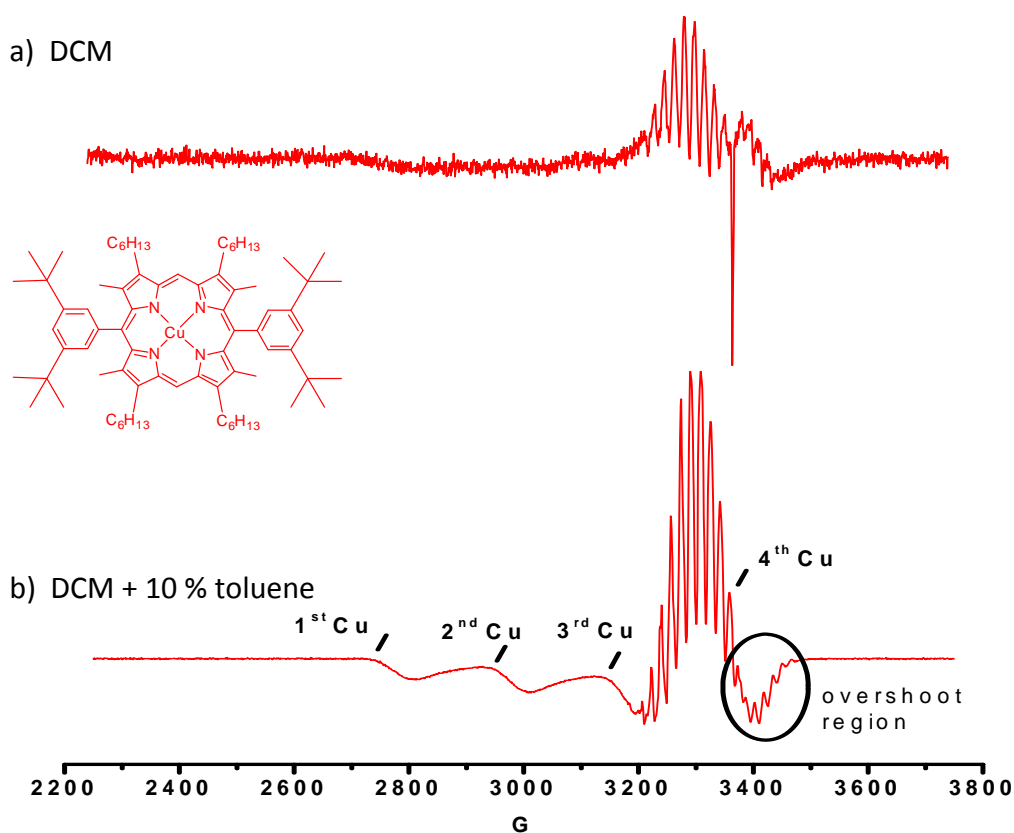


Figure 4.17: 2nd derivative EPR spectra of frozen solution of **CuDPP 15** in a) DCM; b) DCM + 10 % toluene, 120 K. Spectra were acquired with 3.99 mW microwave power, 2 Gauss modulation amplitude and approx. 9.4 GHz microwave frequency.

For the purpose of providing evidence to support the authenticity of compounds by confirming successful copper metallation of porphyrins, the above spectra are considered adequate, especially in addition to proof from mass-spectrometry of **CuDPP 15** (see **Chapter 5, Section 5.4**).

Frozen solution EPR spectra of copper(II) acetylene tetraphenyl porphyrin **CuTPP 16** were also recorded, and **Figure 4.18** shows that there is negligible difference between the spectra of **CuTPP 16** and **CuDPP 15**. This is because both molecules are static at 120 K and hence no difference in rotation rates. The 2nd derivative EPR spectrum of frozen **CuTPP 16** is still not completely resolved due to the overlap of the g_{\perp} feature with the 3rd and 4th copper peaks of the g_{\parallel} feature.

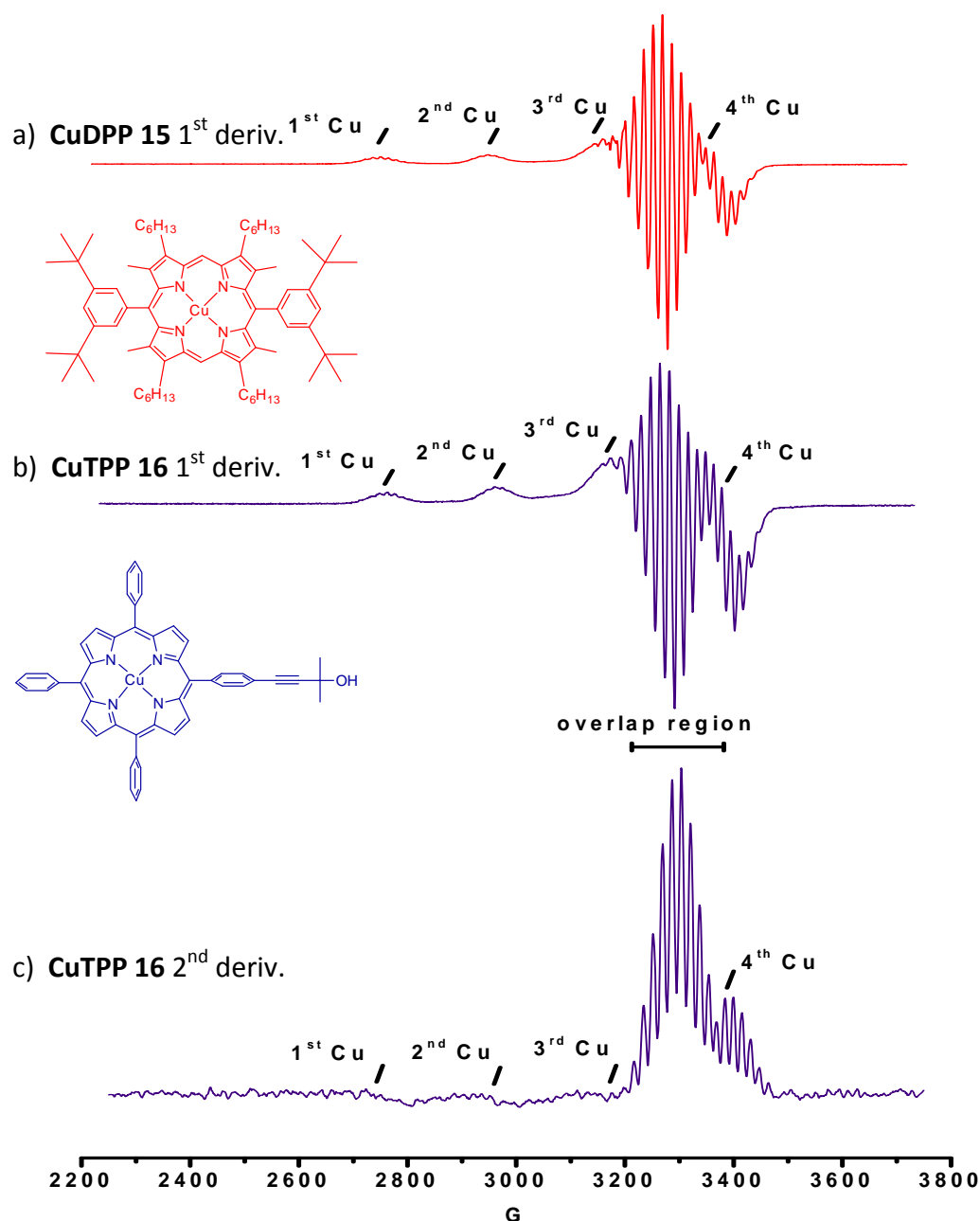


Figure 4.18: 1st derivative EPR spectra of frozen solution in DCM + 10 % toluene, 120 K of a) **CuDPP 15** from **Figure 4.16**.; b) **CuTPP 16**, c) 2nd derivative of **CuTPP 16**. Spectra were acquired with 3.99 mW microwave power, 1-2 Gauss modulation amplitude and approx. 9.4 GHz microwave frequency.

4.2.1.5 Spectral simulations of frozen solution CuDPP and CuTPP

Four-coordinate metalloporphyrins are typically square planar¹⁵¹ so it is sufficient to assume axial symmetry in simulating their frozen solution spectra. Simulations enabled the ¹⁴N shfs on the low field copper peak to be seen more clearly than in the experimental spectra (**Figure 4.19**). Γ_{\perp} and Γ_{\parallel} denote the linewidths used in simulations.

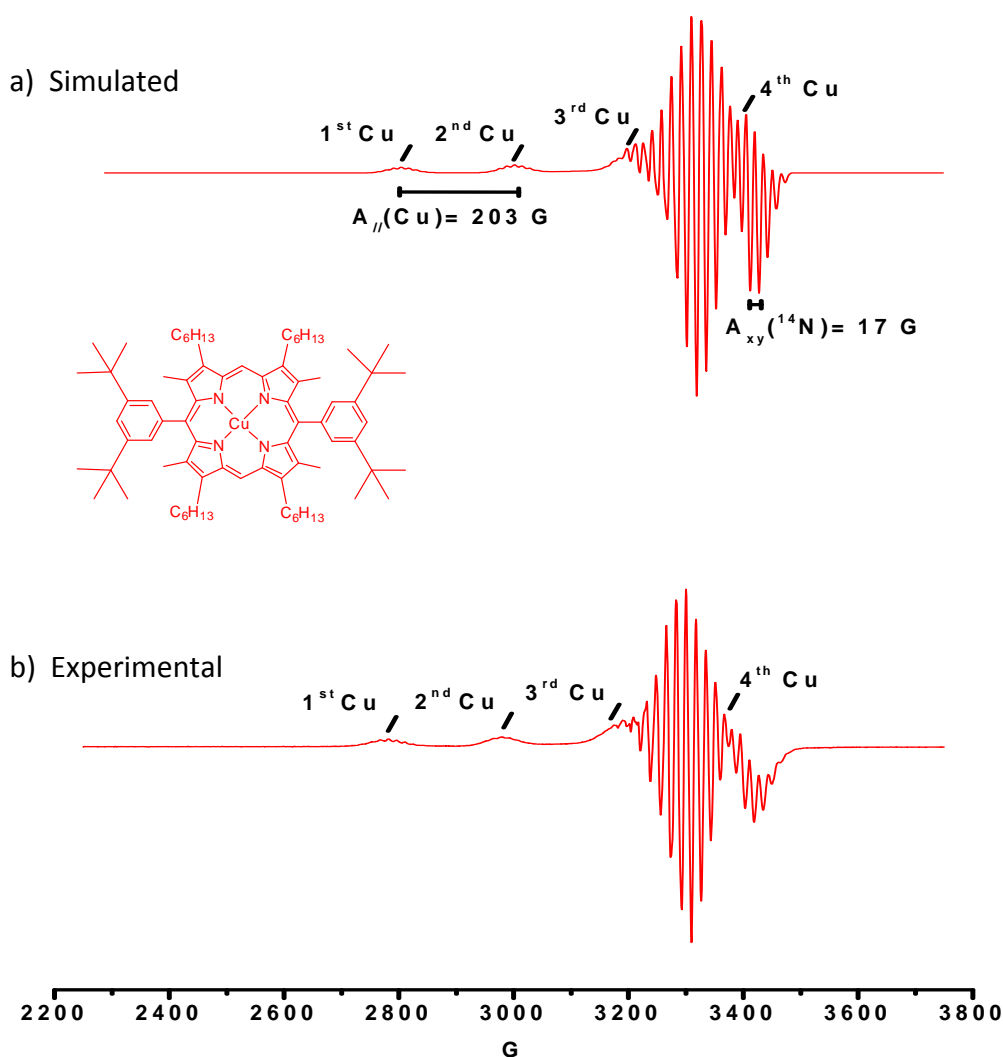


Figure 4.19: a) Simulation of 1st derivative frozen solution EPR spectrum of **CuDPP 15** having $g_{\perp} = 2.0445$, $g_{\parallel} = 2.183$, $A_{\perp}(\text{Cu}) = 33.5$ Gauss, $A_{\parallel}(\text{Cu}) = 203$ Gauss, $A_{\perp}(^{14}\text{N}) = 17$ Gauss, $A_{\parallel}(^{14}\text{N}) = 13.5$ Gauss, Lorentzian/Gaussian lineshape = 1, $\Gamma_{\perp} = 7$ gauss, $\Gamma_{\parallel} = 10$ Gauss against b) experimental spectrum from **Figure 4.16 b**.

First, approximate values for g and A were measured using WinEPR, and these parameters were then adjusted using Bruker Simfonia software to obtain a good fit to the experimental spectra. It should be noted that the experimental spectra contain a mixture of copper isotopes, ^{63}Cu and ^{65}Cu , whilst the simulation is based on the spectrum of the main isotope only. However, due to the cost of copper single isotopes, and the fact that the main purpose of this work was to compare the EPR of copper porphyrin building blocks with copper porphyrin-DNA to further understand DNA structure and stability, it was considered adequate to use the mixed isotopes at this stage.

The 1st derivative frozen solution EPR spectrum of **CuTPP 16** was also simulated and its parameters are compared with those of **CuDPP 15** in **Tables 4.1** and **4.2**.

Table 4.1: g and A values from simulated EPR spectra of fluid solutions of copper porphyrins.

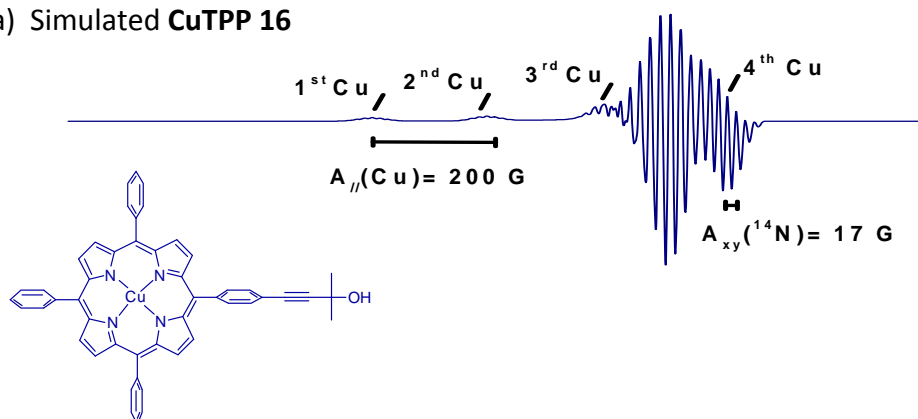
Complex	g_{iso}	$A_{\text{iso}}(^{63}\text{Cu})/\text{G}$	$A_{\text{iso}}(^{14}\text{N})/\text{G}$
CuDPP 15	2.095	90.0	16.0
CuTPP 16	2.095	88.0	15.8

Table 4.2: g and A values from simulated EPR spectra of frozen solutions of copper porphyrins.

Complex	g_{\perp}	g_{\parallel}	$A_{\perp}(\text{Cu})/\text{G}$	$A_{\parallel}(\text{Cu})/\text{G}$	$A_{\perp}(^{14}\text{N})/\text{G}$	$A_{\parallel}(^{14}\text{N})/\text{G}$
CuDPP 15	2.0445	2.183	33.5	203	17.0	13.5
CuTPP 16	2.0560	2.187	32.0	200	17.0	13.5

The differences are small ($\leq 1.3\%$ in $A_{\parallel}(\text{Cu})$) and hence the *unpaired* electrons are in similar environments in both complexes. Thus the structure and the geometry of porphyrins remain intact upon addition of different functional groups.

a) Simulated CuTPP 16



b) Simulated CuDPP 15

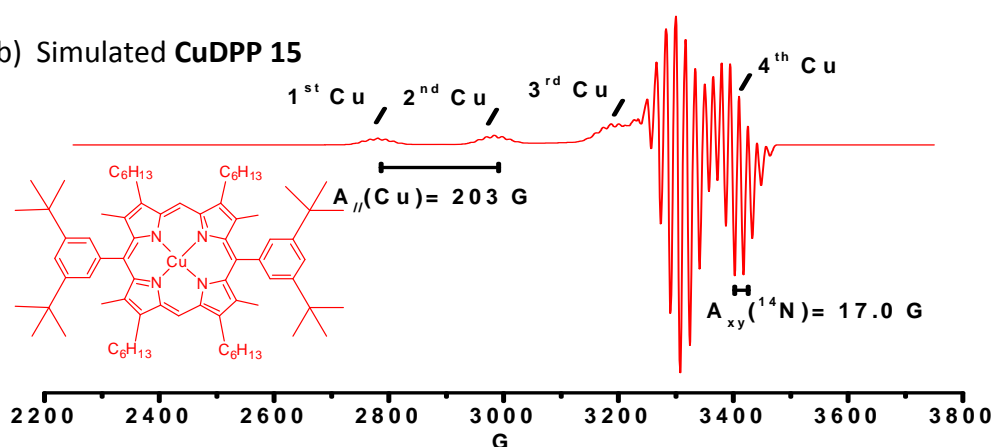


Figure 4.20: a) Simulation of 1st derivative frozen solution EPR spectrum of CuTPP 16 having $g_{\perp} = 2.056$, $g_{\parallel} = 2.187$, $A_{\perp}(\text{Cu}) = 32.0$ Gauss, $A_{\parallel}(\text{Cu}) = 200$ Gauss, $A_{\perp}({}^{14}\text{N}) = 17.0$ Gauss, $A_{\parallel}({}^{14}\text{N}) = 13.5$ Gauss, Lorentzian/Gaussian lineshape = 1, $\Gamma_{\perp} = 7$ gauss, $\Gamma_{\parallel} = 10$ Gauss against b) simulated spectrum of CuDPP 15 from Figure 4.19.

4.2.1.6 Interpretation of EPR spectra of copper porphyrins

The Cu(II) ion contains nine 3d electrons, a configuration that can be treated as a single electron hole in a filled 3d shell. When the *unpaired* electron lies in $d_{x^2-y^2}$ and in axial symmetry, the g-values are given by these expressions:¹⁵³

$$g_{\parallel} = 2.0023 + 8\lambda/\Delta E(d_{x^2-y^2} - d_{xy})\alpha$$

$$g_{\perp} = 2.0023 + 2\lambda/\Delta E(d_{x^2-y^2} - d_{xz,yz})\alpha$$

Equation 4.5

If alternatively, the *unpaired* electron was in d_z^2 then the following equations would apply:

$$g_{//} = 2.0023$$

$$g_{\perp} = 2.0023 + 6\lambda/\Delta E(d_z^2 - d_{xz,yz})$$

Equation 4.6

Thus the *unpaired* electron does not lie in d_z^2 orbitals of **CuDPP 15** or **CuTPP 16** molecules because they both have $g_{//} \neq 2.0023$. On the contrary, the *unpaired* electron is located in a molecular orbital where copper contributions are $d_x^2 - y^2$ in character, because both porphyrins have $g_{//} > g_{\perp} > 2$. The copper $A_{//}$ values (*i.e.* ~ 200 G) lie in the range normally found for *unpaired* electron in $d_x^2 - y^2$ orbital. Shfs from ^{14}N indicates that the molecular orbital contains appreciable ligand contributions.¹⁵³

By checking with the parameters derived from simulated spectra, the following relationships (assuming axial symmetry, *i.e.* $g_x = g_y$ and $A_x = A_y$):

$$g_{\text{iso}} = 1/3(g_x + g_y + g_z)$$

$$A_{\text{iso}} = 1/3(A_x + A_y + A_z)$$

Equation 4.7

are verified reasonably well in the results for the present complexes and indicate that the interpretations of fluid solution spectra, besides frozen spectra have both been consistent. It should also be noted that the value of $A_{\perp}(\text{Cu})$, which was later used to simulate frozen solution spectra of **CuDPP** was first calculated from the simulated solution spectrum of **CuDPP** by using the 2nd expression in **Equation 4.7**.

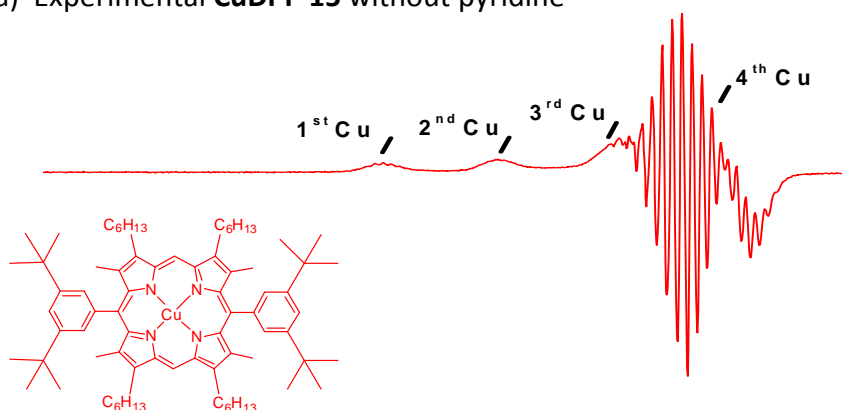
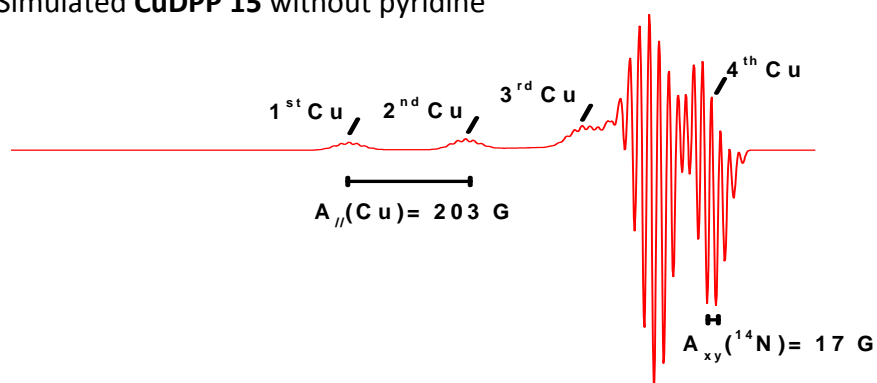
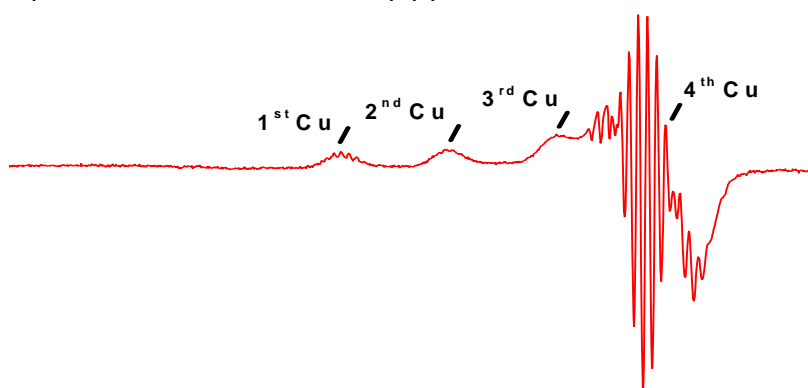
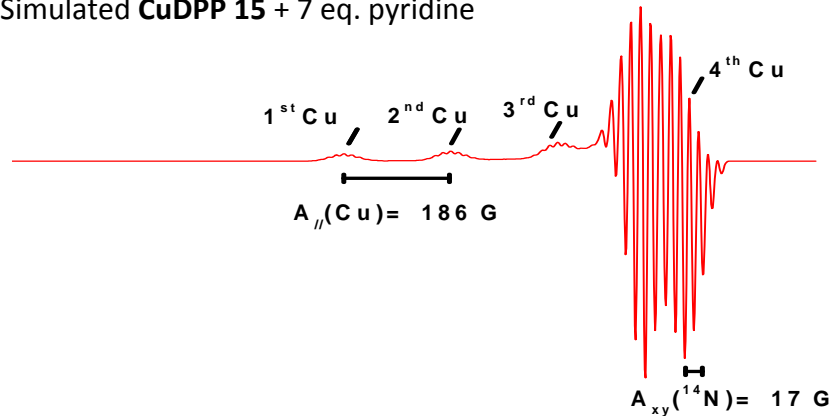
The above EPR spectra and parameters show that the symmetry and ligand molecular orbital contributions of different porphyrins are quite similar. The different functional groups on porphyrins do not alter their EPR spectra

significantly. EPR has also been used to confirm the porphyrin stability, and the spectra of both **CuDPP 15** and **CuTPP 16** show no change after one month in DCM solution, similarly to the literature.^{161, 162}

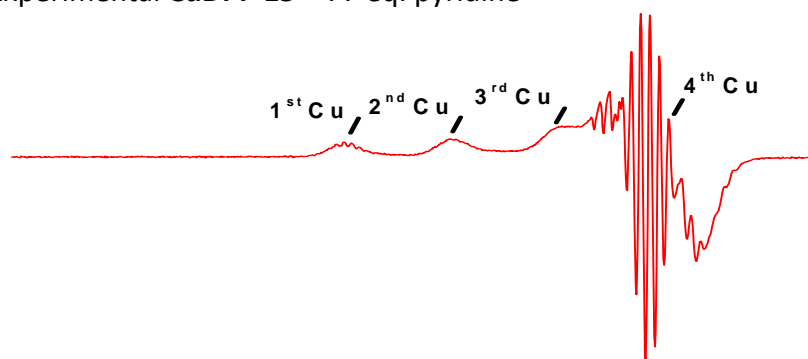
4.2.1.7 EPR binding study of CuDPP

EPR measurements of **CuDPP 15** in different solvent mixtures showed no binding affinity of copper porphyrins to either toluene, MeOH or H₂O. Further measurements were then made using pyridine, a well known binding reagent in order to investigate possible disruptions of the dipolar interaction between square planar copper porphyrins, especially along z-axis. The aim of this investigation was to enhance the understanding of porphyrin-stacking on DNA, which is thought to have a strong interaction in the direction of the z-axis.

To a solution of **CuDPP 15** in DCM + 10 % toluene, 7 molar equivalents of pyridine, followed by a large excess (77 molar equivalents) of pyridine were added and the spectra were recorded at 120 K. Due to the maintenance of Bruker EMX Micro spectrometer, all EPR binding study spectra were recorded on Bruker EMX X-band with the same cavity at 3.95-4.00 mW microwave power, 2 Gauss modulation amplitude and approximately 9.5 GHz microwave frequency. Simulations of these experimental EPR spectra were then attempted (**Figure 4.21**).

a) Experimental **CuDPP 15** without pyridineSimulated **CuDPP 15** without pyridineb) Experimental **CuDPP 15** + 7 eq. pyridineSimulated **CuDPP 15** + 7 eq. pyridine

c) Experimental **CuDPP 15** + 77 eq. pyridine



Simulated **CuDPP 15** + 77 eq. pyridine

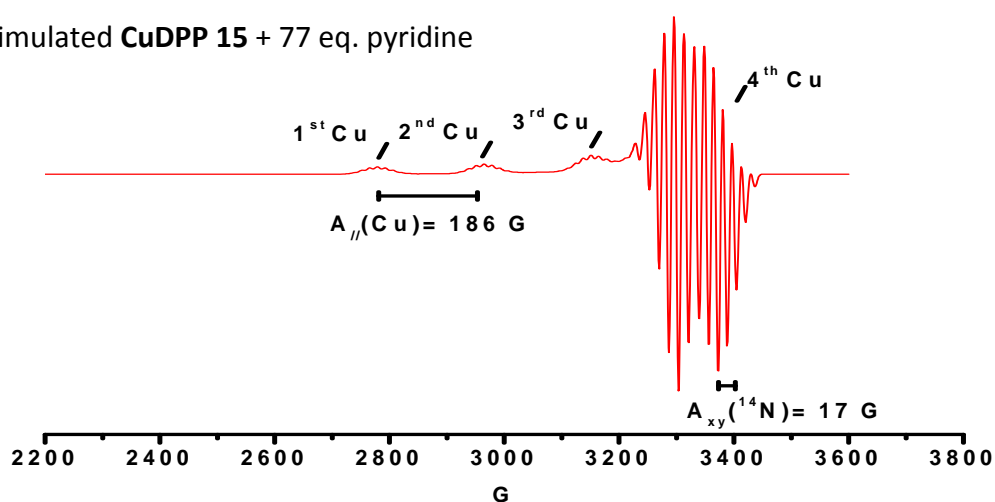


Figure 4.21: Experimental and simulations of 1st derivative frozen solution EPR spectra using Lorentzian/Gaussian lineshape= 1, Γ_{\perp} = 7.50 Gauss, Γ_{\parallel} = 10 Gauss of a) **CuDPP 15** having g_{\perp} = 2.042, g_{\parallel} = 2.183, $A_{\perp}(\text{Cu})$ = N/D, $A_{\parallel}(\text{Cu})$ = 203 Gauss, $A_{\perp}(^{14}\text{N})$ = 17 Gauss, $A_{\parallel}(^{14}\text{N})$ = 13.5 Gauss; b) **CuDPP 15** + 7 equiv. pyridine having g_{\perp} = 2.050, g_{\parallel} = 2.208, $A_{\perp}(\text{Cu})$ = N/D Gauss, $A_{\parallel}(\text{Cu})$ = 186 Gauss, $A_{\perp}(^{14}\text{N})$ = 17 Gauss, $A_{\parallel}(^{14}\text{N})$ = 13.5 Gauss; c) **CuDPP 15** + 77 equiv. pyridine having g_{\perp} = 2.050, g_{\parallel} = 2.208, $A_{\perp}(\text{Cu})$ = N/D Gauss, $A_{\parallel}(\text{Cu})$ = 186 Gauss, $A_{\perp}(^{14}\text{N})$ = 17 Gauss, $A_{\parallel}(^{14}\text{N})$ = 13.5 Gauss.

Table 4.3 below summarises all the parameters obtained from simulated spectra.

Table 4.3: g and A values from simulated EPR spectra in a binding study of **CuDPP 15** with pyridine.

Complex	g_{\perp}	$g_{//}$	$A_{\perp}(\text{Cu})$	$A_{//}(\text{Cu})$	$A_{\perp}(^{14}\text{N})$	$A_{//}(^{14}\text{N})$
			G	G	G	G
CuDPP	2.042	2.183	N/D	203	17	13.5
CuDPP + 7 eq. Pyridine	2.050	2.208	N/D	186	17	13.5
CuDPP + 77 eq. Pyridine	2.050	2.208	N/D	186	17	13.5

Upon additions of pyridine, the EPR spectra shifted to lower field with increasing magnitudes of g-values, particularly in $g_{//}$. It seems that pyridine has induced a change in the copper environment consistent with coordination of 1 or 2 molecules along the z-axis. Introducing pyridine has decreased the $A_{//}$ value and thus the *unpaired* electron density on copper. The *unpaired* electron density has delocalised to ^{14}N pyridine from its own parent Cu(II) nuclei. In contrast, this *unpaired* electron density distribution on four equivalent neighbouring ^{14}N in the porphyrin ring remains unchanged, because the $A_{\perp}(^{14}\text{N})$ shfs is unchanged. These findings correspond to changes in z-axis (*i.e.* significant changes in parallel parameters).

Changes in both the $g_{//}$ and $A_{//}$ values confirm that copper porphyrins have a strong affinity for pyridine binding. 7 molar equivalents of pyridine were enough to enable binding, as there was no other change measured after a further excess of 77 molar equivalents of pyridine were added. To conclude whether one pyridine is bound above or below the porphyrin ring, or both by two pyridine molecules, future spectral analyses, either by EPR (*i.e.* fluid solution measurement to determine all A values, including $A_{\perp}(\text{Cu})$), UV-vis or both will be required. For the purpose of comparing with possible binding of solvents to porphyrin-DNA, however this EPR binding study was concluded at this point.

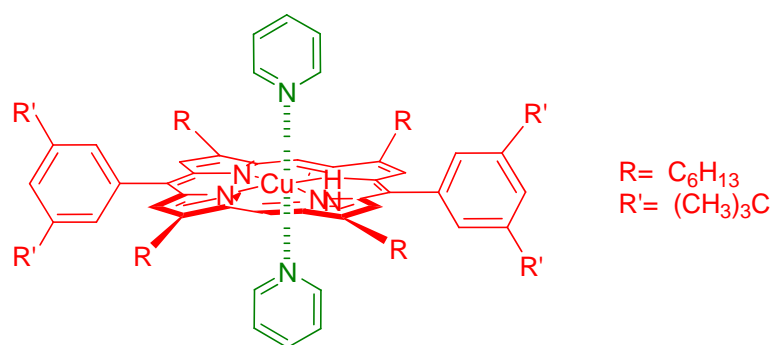


Figure 4.22: 2D illustration of possible pyridine binding above and below a porphyrin ring.

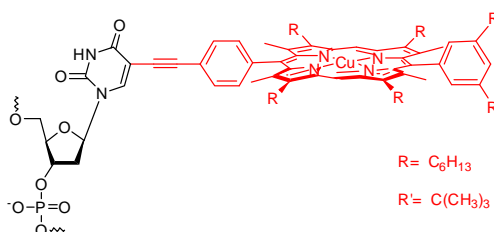
4.2.2 EPR study of porphyrin-DNA

As EPR measurements of copper porphyrin building blocks produced good quality spectra and considerable information, the next step was to try recording EPR of porphyrins attached to DNA. Single and double strands of the following porphyrin-DNA were investigated.

CuODN1 5'-CAT CGT AGT TTT **PAP** TTT TCC GTA CTC-3'

CuODN4 5'-TAC GAT TCG **TPT** CTA GCT AGC-3'

P: Diphenyl porphyrin



CuODN16 5'-CAT CGT AGT ATA **PAT** ATA TCC GTA CTC-3'

CuODN17 5'-CAT CGT AGT TTT **PAP** TTT TCC GTA CTC-3'

CuODN18 5'-CAT CGT AGT ATP **PAT** ATA TCC GTA CTC-3'

P: Tetraphenyl porphyrin

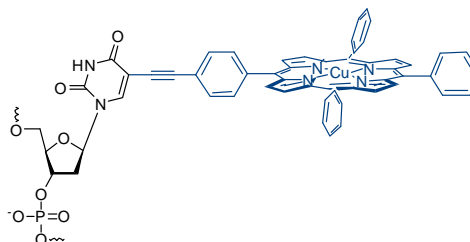


Figure 4.23: CuDPP-DNA and CuTPP-DNA for EPR investigations.

Currently, there is a lot of interest in using FRET (fluorescence resonance energy transfer) as a molecular ruler to determine the distance between chromophores attached on DNA.^{163, 164} FRET efficiency relies on the energy transfer between chromophores, which is then dependent on the distance and the orientations of dipole moments between donor and acceptor molecules. Many of these works are still in the pipeline, because obtaining sufficient energy transfer across porphyrins held on DNA is challenging.¹⁶⁵ The aim of the present investigation was to try using EPR to provide a more reliable method for distance calculation between chromophores attached to DNA, starting with diphenyl porphyrin-DNA.

4.2.2.1 Early EPR study and synthesis of CuDPP-DNA

Few EPR studies have been done on DNA modified with transition metals, apart from EPR of self-assembled metal arrays in DNA duplex, which were synthesised by Carrel and Shionoya *et al.*²⁴ Together, they showed a new concept to efficiently combine metal ions in DNA. Early work on EPR of DNA done by Schiemann¹⁶⁶ and Kato¹⁵⁷ eventually led to a possible calculation of the distance between metals bound inside DNA duplex. In particular, the distance between Cu^{2+} - Cu^{2+} ions stacked internally on adjacent base-pairs inside a DNA duplex cage was estimated to be 3.7 Å.

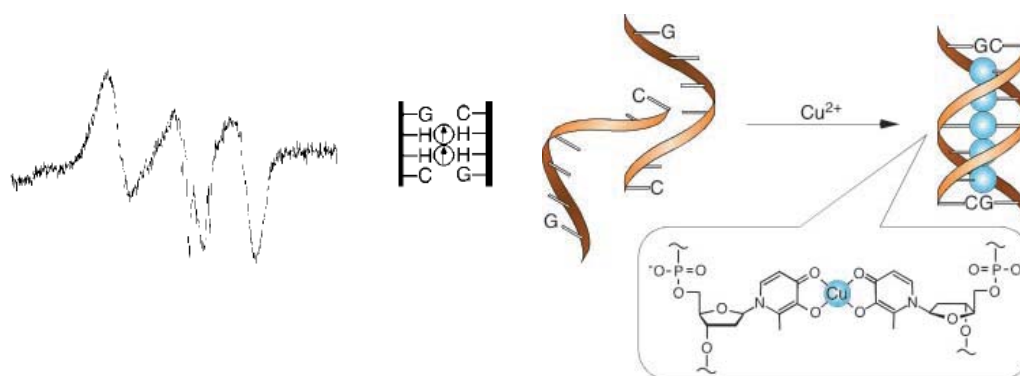


Figure 4.24: EPR spectrum of discrete copper self-assembled metal array in artificial DNA duplex.¹⁵⁷

There is limited knowledge for the synthesis of external self-assembled metals on DNA and their EPR spectra. The first challenges of this chapter were to find an efficient metallation of porphyrin-DNA, and then subsequently to set up experimental procedures to obtain their EPR spectra. This investigation marks the

first EPR measurements of transition metals (*i.e.* copper) that are covalently and externally attached to DNA, not just in duplexes but also in single strands. In this case, the EPR hfs and shfs can indicate successful post-synthetic copper metallation of porphyrin-DNA; just as the complete copper metallation of porphyrin building blocks can be proven by this technique.

The first frozen solution EPR spectra of copper metallated diphenyl porphyrin-DNA (**CuDPP-DNA**) were however, disappointing. A concentration of 34 μM was insufficient for good resolution, and the spectrum was essentially dominated by a broad peak at ~ 3100 G, which looked like that of fine powder **CuDPP** (**Figure 4.25**), and thus hindered confirmation of sample authenticity.

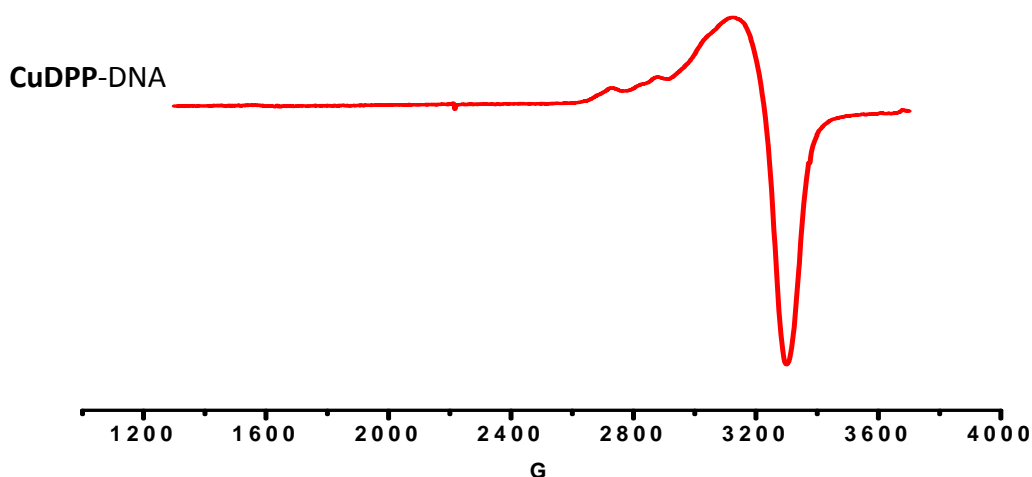


Figure 4.25: 1st derivative EPR spectrum of frozen solution of 34 μM copper diphenyl porphyrin-DNA in water, 120 K. Spectrum was acquired with 3.99 mW microwave power, 5 Gauss modulation amplitude and approx. 9.4 GHz microwave frequency.

Initially, this broad copper peak was thought to be of free Cu(II) ions in solution from the use of excess $\text{Cu}(\text{OAc})_2$ (1000 equiv. to **CuDPP-DNA**). Purification through Nap-5 column[®] in the synthesis (see **Chapter 5, Section 5.3.3.2**) did not remove all $\text{Cu}(\text{OAc})_2$. However, $\text{Cu}(\text{OAc})_2$ exists as a strongly magnetically coupled dimer ($S=1$), and its EPR spectrum observed over a wide magnetic field range (0-8000 G at X-band frequency), does not match that of **CuDPP-DNA**. Thus excess $\text{Cu}(\text{OAc})_2$ was unlikely to be responsible for the broadening, and this then led to various hypotheses:

1. Some excess $\text{Cu}(\text{OAc})_2$ was present and was bound to the copper porphyrin-DNA.
2. Excess EDTA (1000 equiv.) scavenged the remaining $\text{Cu}(\text{OAc})_2$, and the broad signal was essentially due to CuEDTA.
3. The formation of CuEDTA upon addition of EDTA to $\text{Cu}(\text{OAc})_2$ resulted in some CuEDTA binding to **CuDPP**-DNA.
4. The partial scavenging of EDTA meant interactions of $\text{Cu}(\text{OAc})_2$ and CuEDTA.

A series of elimination experiments to ascertain the factors responsible for this broadening effect in frozen **CuDPP**-DNA spectra were tried. This also helped to provide a feed-back loop to redesign the post-synthetic metallation of porphyrin-DNA. EPR measurements of $\text{Cu}(\text{OAc})_2$ and CuEDTA additions to a non-modified DNA strand were carried out to verify the above hypotheses. 20 molar equivalents $\text{Cu}(\text{OAc})_2$ were added to a non-modified DNA strand and the EPR spectrum at 120 K showed a similar broad peak. From this comparison, it looks like the broadening of EPR spectra of **CuDPP**-DNA was caused by an excess $\text{Cu}(\text{OAc})_2$ binding to DNA, possibly through the phosphate backbones. Hence the synthesis was revised and a smaller amount of $\text{Cu}(\text{OAc})_2$ (50 molar equivalents to DNA instead of 1000) was added to metallate **DPP**-DNA, followed by an increase in EDTA to completely scavenge any remaining $\text{Cu}(\text{OAc})_2$. The new set of **CuDPP**-DNA spectra recorded at 100 μM then showed a decrease in the spectral broadening. Extra peaks at 2600–3100 G were also observed, besides an appearance of a half-field signal at 1600 G.

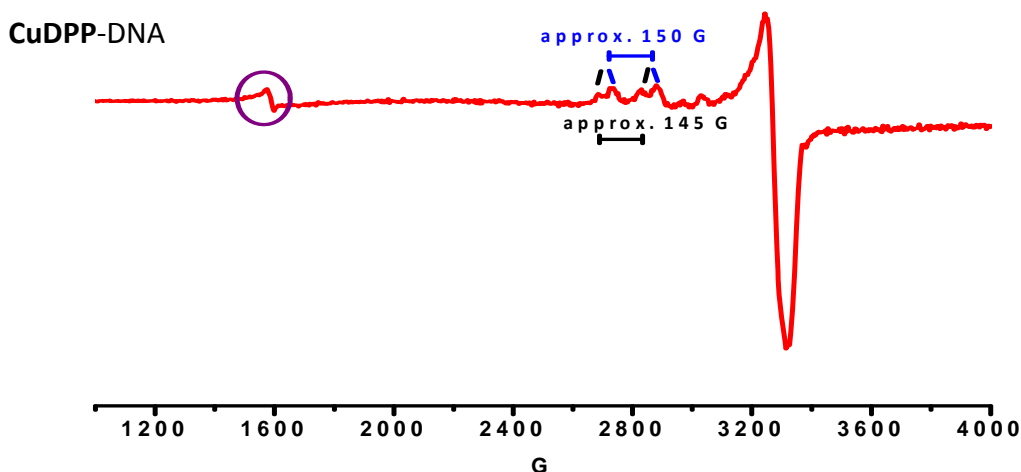


Figure 4.26: 1st derivative EPR spectrum of frozen solution of 100 μM **CuODN4** in water, 120 K. Spectrum was acquired with 3.99 mW microwave power, 5 Gauss modulation amplitude and approx. 9.4 GHz microwave frequency.

From the above experimental EPR data, it can be seen that any nitrogen shfs are very small, so one is forced to conclude that the chemical environment of this Cu(II) is quite different from that in the copper porphyrin building block, and the two sets of low field peaks are definitely not the consequence of the two Cu isotopes. The $g_{//}$ of 2.425 for **CuODN4** is quite close to that of uncomplexed Cu(II), although the considerable high $A_{//}$ value eliminates the free ion as being responsible for the spectrum.¹⁶⁷ The appearance of the peak at 1600 G ($g= 4.3$) indicates the formation of a triplet state as could be found in dimetallic species.¹⁶⁸ The contribution of this half field peak to the spectrum is relatively small however. Most of the spectral intensity is centred around $g= 2$, and thus corresponds to single (isolated) electrons.

These observations led to the conclusions that these EPR signals do not arise from copper complexes with porphyrin, and the large $g_{//}$ value suggests that there is some oxygen in the Cu coordination sphere. The possibility of copper porphyrin DNA complexing with EDTA was tested by performing a set of EPR titrations where CuEDTA was titrated into a non-modified DNA single strand at increasing concentrations. The spectra of non-modified DNA + CuEDTA produced the same

features around $g = 2$ as in **Figure 4.26**, with the absence of a half-field peak, and thus demonstrated that excess CuEDTA was responsible for the spectral intensity at $g \sim 2$.

The synthesis of copper porphyrin DNA was then reviewed and a change in the purification step was adopted to help remove any excess CuEDTA. This modification involved replacement of the Nap-5 column[®] by Glen-Pak[®] (see **Chapter 5, Section 5.3.3.4**) in the final purification. Thereafter, traces of CuEDTA were not observed. After much trial and error, and measurements at both X and Q band frequencies, besides seeking external advice;^{150, 169, 170} we began to see hfs and shfs for copper diphenyl porphyrin DNA. The initial concentration was kept at 300 μM in 36-45 μL water volume inside an X-band EPR tube.

4.2.2.2 EPR study of porphyrin-DNA single strands

In addition to measurements with diphenyl porphyrins on DNA, EPR spectra of copper(II) acetylene tetraphenyl porphyrin-DNA (**CuTPP-DNA**) complexes were also recorded (**Figure 4.27**) to see if EPR could be used to compare the electronic interactions between these two types of porphyrin on a DNA scaffold.

In the porphyrin-DNA system, the $\Delta m_s = 2$ transition in a triplet state is responsible for the appearance of the a half-field peak. This normally forbidden transition, however, can be produced by the coupling of the *unpaired* electrons on two paramagnetic centres in close proximity to one another.

All strands show very similar EPR parameters (**Table 4.4**); simulations were not performed because of low resolution of the experimental spectra, and all parameters are thus approximate. The relative intensities of spectral components were calculated as *the ratio of the height of half-field peak at $g = 4.3$ to the height of main field peak $g = 2$* ; integrated intensities were not used because of the possibility of very large errors from broad background signals.

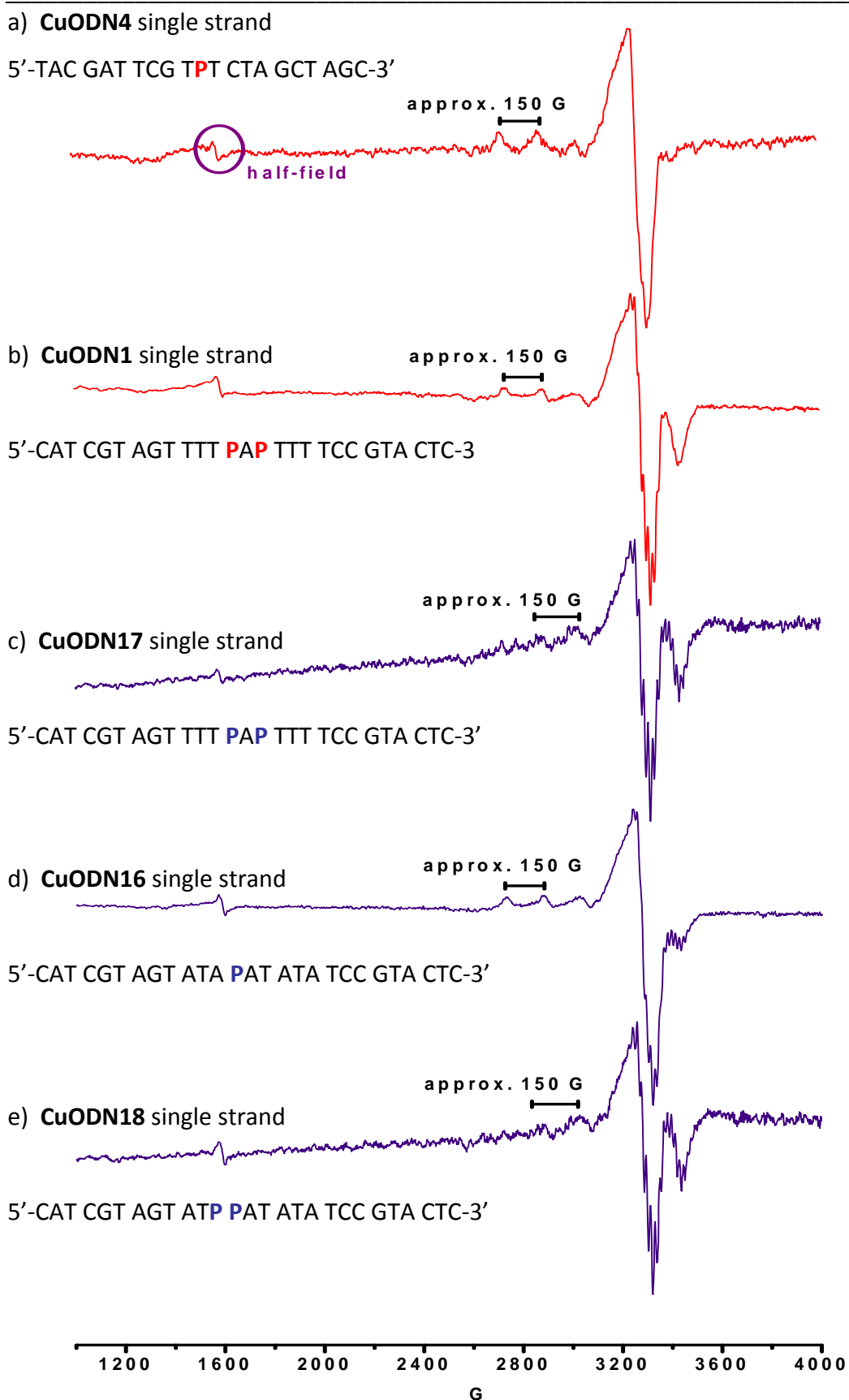


Figure 4.27: 1st derivative frozen solution EPR spectra of 300 μ M porphyrin-DNA single strands in water at 120 K. Spectra were acquired with 3.99 mW microwave power, 5 Gauss modulation amplitude and approx. 9.4 GHz microwave frequency.

Table 4.4: Approximate parameters from experimental EPR data of porphyrin-DNA single strands.

The relative intensity is the ratio of height of half-field peak at $g= 4.3$:height of main field peak $g= 2$.

Porphyrin-DNA Single strands	$g_{//}$	g_{\perp}	$A_{//}(\text{Cu})/\text{G}$	$A_{\perp}(\text{N})/\text{G}$	Relative intensity
CuODN4 (TPT)	2.29	2.04	148	N/D	0.08:1
CuODN1 (PAP)	2.29	2.05	150	17	0.06:1
CuODN17 (PAP)	2.28	2.05	150	17	0.10:1
CuODN16 (APA)	2.28	2.05	148	17	0.08:1
CuODN18 (PP)	2.27	2.05	150	17	0.12:1
CuDPP 15	2.183	2.045	203	17	N/D
CuTPP 16	2.187	2.056	200	17	N/D

While $A_{\perp}({}^{14}\text{N})$ of all porphyrin-DNA strands are comparable to the corresponding copper porphyrin building blocks, a significant decrease by around 50 Gauss is observed in $A_{//}(\text{Cu})$ values. Similarly, while g_{\perp} remains the same upon attachments of porphyrins onto DNA, the magnitude of $g_{//}$ increases and shifts to lower field. It seems that single strand DNA is accountable for a change in the interaction along the z-axis of the porphyrins. The constant $A_{\perp}({}^{14}\text{N})$ value is indicative of no change in the bonding between ${}^{14}\text{N}$ and Cu, but the differences in $g_{//}$ values indicate a change in the energy separation between molecular orbitals in the \mathbf{d}_{xy} and $\mathbf{d}_{x^2-y^2}$ orbitals.

In addition to the expected intra-molecular interactions between porphyrins on the same DNA molecule, the presence of a half-field signal in a strand which has only one porphyrin chromophore indicates the co-existence of inter-molecular interactions between porphyrins on different strands. Despite having the same DNA sequence, **CuODN18** has twice as many porphyrin moieties as **CuODN16** and a larger relative intensity of half-field against main field signals. Thus, adding more porphyrins per strand increases their intra- and inter-molecular interactions. These EPR results also show stronger interspin transition for **TPP** than **DPP**. This is reflected through a larger relative intensity for the half field peak in **CuODN17** compared to **CuODN1** (Table 4.4).

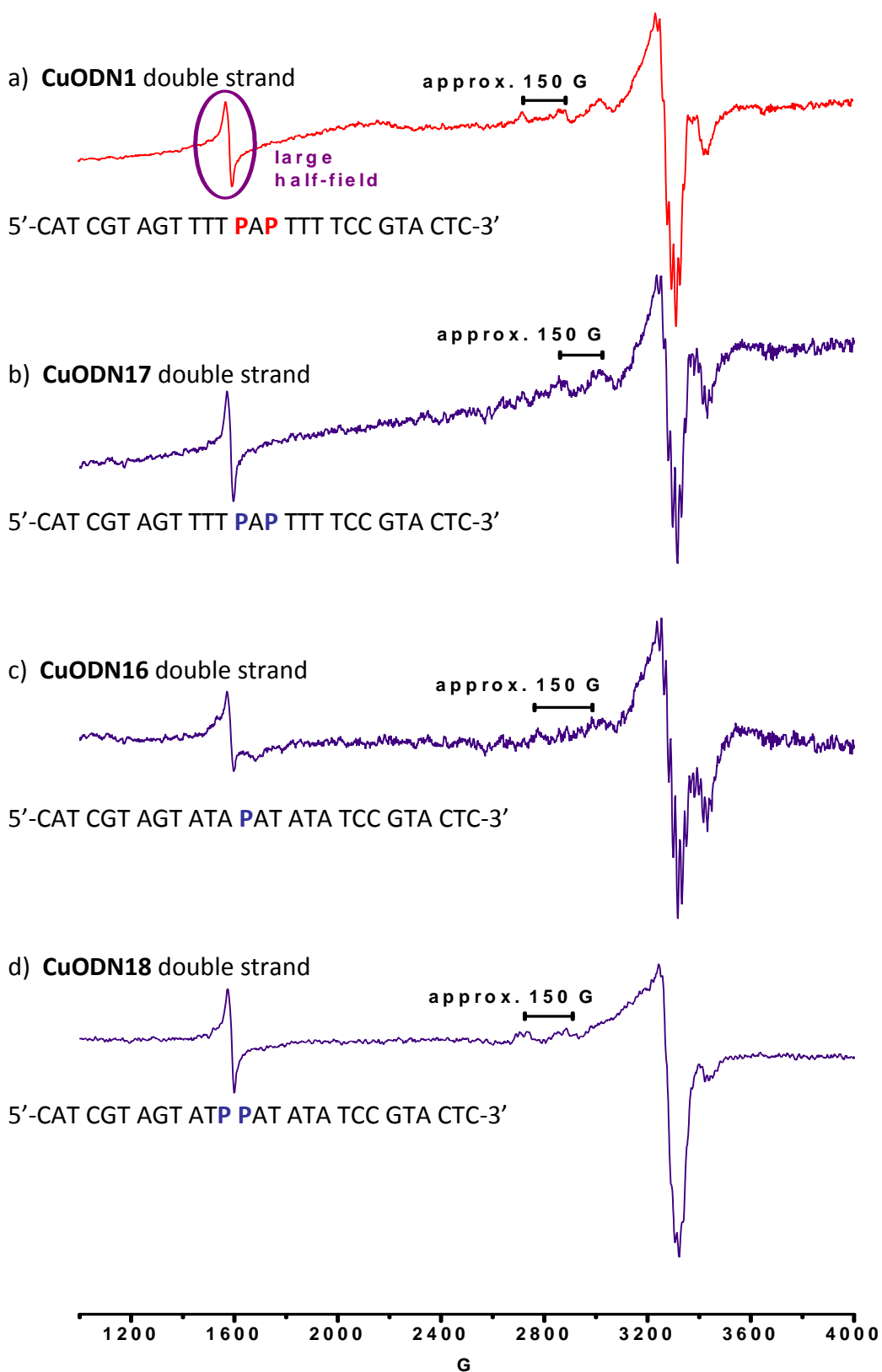
4.2.2.3 EPR study of porphyrin-DNA double strands

Figure 4.28: 1st derivative frozen solution EPR spectra of 300 μ M Porphyrin-DNA double strands in water at 120 K. Spectra were acquired with 3.99 mW microwave power, 5 Gauss modulation amplitude and approx. 9.4 GHz microwave frequency.

Non-modified complementary DNA strands were annealed with the above porphyrin-DNA single strands, and EPR spectra of all corresponding duplexes were then measured using the same spectral parameters as previously (**Figure 4.28**). The EPR of duplex **CuODN4**, however, could not be obtained due to limited sample and the denaturing of DNA after this strand had been measured many times.

Table 4.5: Approximate parameters derived from EPR data of porphyrin-DNA double strands. The relative intensity is the ratio of height of half-field peak $g = 4.3$:height of main field peak at $g = 2$.

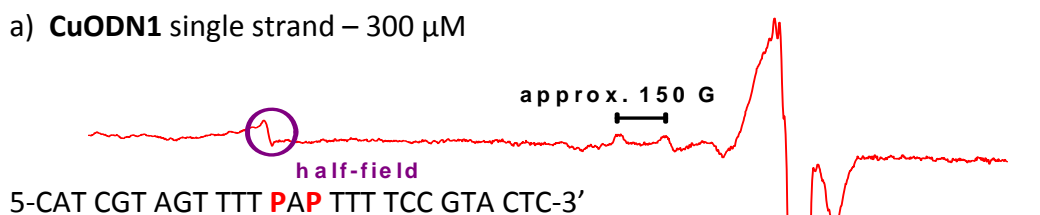
Porphyrin-DNA Double strands	$g_{//}$	g_{\perp}	$A_{//}(\text{Cu})/\text{G}$	$A_{\perp}({}^{14}\text{N})/\text{G}$	Relative intensity
CuODN1 (PAP)	2.27	2.05	150	17	0.28:1
CuODN17 (PAP)	2.30	2.05	150	17	0.37:1
CuODN16 (APA)	2.30	2.05	148	17	0.24:1
CuODN18 (PP)	2.30	2.04	150	17	0.37:1
CuDPP 15	2.183	2.045	203	17	N/D
CuTPP 16	2.187	2.056	200	17	N/D

All the approximate $g_{//}$, g_{\perp} , $A_{//}(\text{Cu})$, $A_{\perp}({}^{14}\text{N})$ values derived manually from the EPR spectra of porphyrin-DNA duplexes in **Table 4.5** are very similar to those observed in the corresponding single strands, except for the relative intensities. The ratios of intensities between half-field to main field signals of all porphyrin-DNA double strands are significantly greater than those found in their corresponding single strands. A larger relative intensity calculated for duplex **CuODN17** compared to duplex **CuODN1** (**Table 4.5**), both of which have the same DNA sequence, suggests stronger interspin transitions between tetraphenyl porphyrins than between diphenyl porphyrins, as found in single strands (**Table 4.4**).

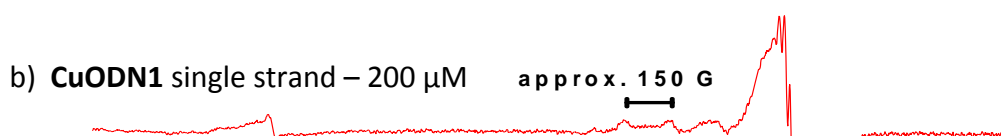
4.2.2.4 EPR study of porphyrin-DNA dilutions

To further understand the interaction which gives rise to a signal at half-field $g = 4.3$, EPR dilution experiments were investigated. All porphyrin-DNA single and double strands were diluted from the original 300 μM concentration to 200 μM and 100 μM in 45 μL to 135 μL of water. **Figures 4.29** and **4.30** show representative examples of EPR dilution study through the single and double strands of **CuODN1**

a) **CuODN1** single strand – 300 μM



b) **CuODN1** single strand – 200 μM



c) **CuODN1** single strand – 100 μM

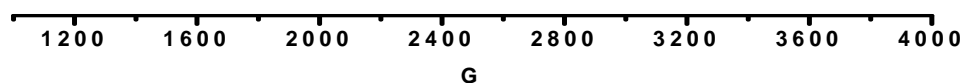
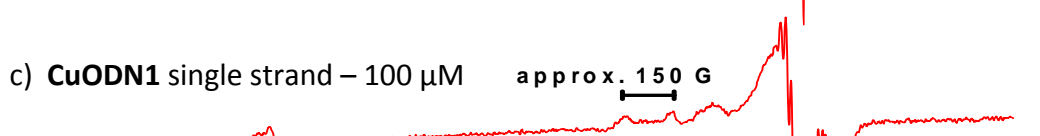
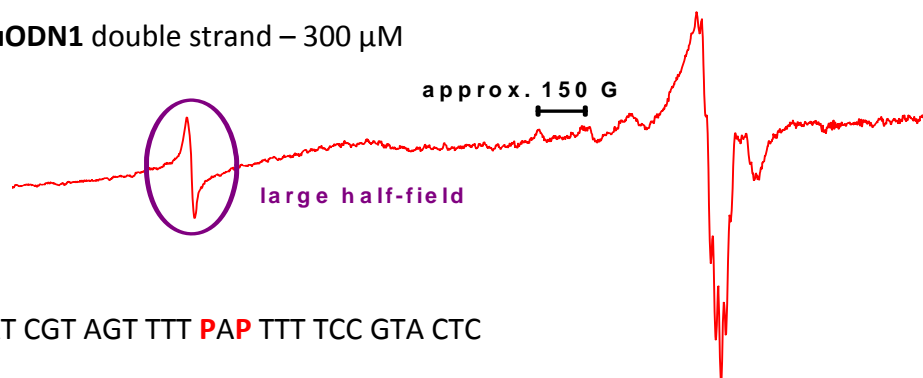


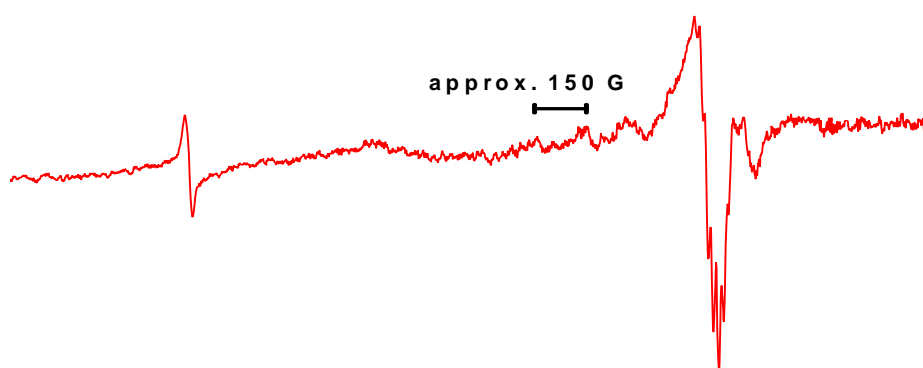
Figure 4.29: 1st derivative frozen solution EPR spectra of single strand diphenyl porphyrin-DNA **CuODN1** in water at 120 K at different concentrations. Spectra were acquired with 3.99 mW microwave power, 5 Gauss modulation amplitude and approx. 9.4 GHz microwave frequency.

Generally, the relative intensity increases upon dilution with water for porphyrin-DNA single strands, perhaps due to the hydrophobic interactions between porphyrins.

a) **CuODN1** double strand – 300 μM



b) **CuODN1** double strand – 200 μM



c) **CuODN1** double strand – 100 μM

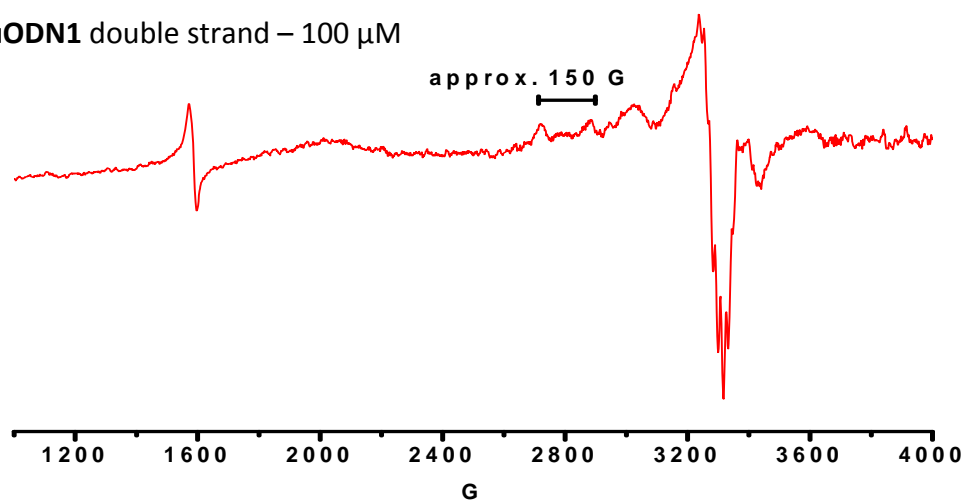


Figure 4.30: 1st derivative frozen solution EPR spectra of double strand diphenyl porphyrin-DNA **CuODN1** in water at 120 K at different concentrations. Spectra were acquired with 3.99 mW microwave power, 5 Gauss modulation amplitude and approx. 9.4 GHz microwave frequency.

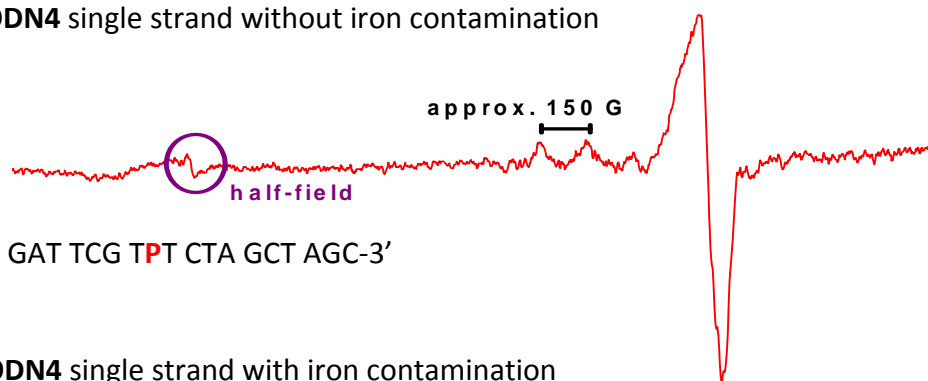
Similar to porphyrin-DNA single strands, the relative intensities of their double strands also increase upon dilution. Nevertheless, this change is of a smaller degree than in single strands. Spectral resolution of porphyrin-DNA duplexes was also improved compared to single strands. It seems that increasing the number of oligonucleotides, through the addition of a non-modified complementary strand also increases the quality of sample glass. **Table 4.7** in **Section 4.2.2.5** displays the relative intensity of all other strands in EPR dilution experiments.

4.2.2.5 EPR spectral interpretation of porphyrin DNA

Since literature¹⁷¹ reports no half-field signal associated with $|\Delta m_s| = 2$ in porphyrins measured in water, and the control experiments of non-modified DNA with CuEDTA, Cu(OAc)₂ also show only the presence of main-field peak, the half-field signal is an intrinsic property that is only observed when copper porphyrins are attached onto DNA. The appearance of this half-field signal opens many discussions, including the formation of triplet states, as could occur in dimeric species, interactions between neighbouring metal centre, or π - π interactions; all of which suggest structural changes in the z-axis orientation of porphyrins stacked on DNA. However, this half-field signal at $g = 4.3$ can only be a small part of the story, because much of the spectral intensity is still centred around $g = 2$. Therefore a single, isolated *unpaired* electron still dominates these EPR signals.

The possibility of an iron impurity being responsible for the half-field signal at $g = 4.3$ was also considered,¹⁷² since a large half-field peak (*i.e.* larger than main field peak) was observed in the early measurements that contained a trace of iron impurity (**Figure 4.31**) prior to the optimisation of the metallation and purification of copper porphyrin-DNA. After eliminating contacts with metals in the revised syntheses, the EPR spectra then showed much smaller half-field peaks. With more reproducible copper porphyrin-DNA EPR spectra obtained after the optimisation of syntheses, the speculation of half-field signal derived from iron impurity was thus ruled out.

a) **CuODN4** single strand without iron contamination



5'-TAC GAT TCG TPT CTA GCT AGC-3'

b) **CuODN4** single strand with iron contamination

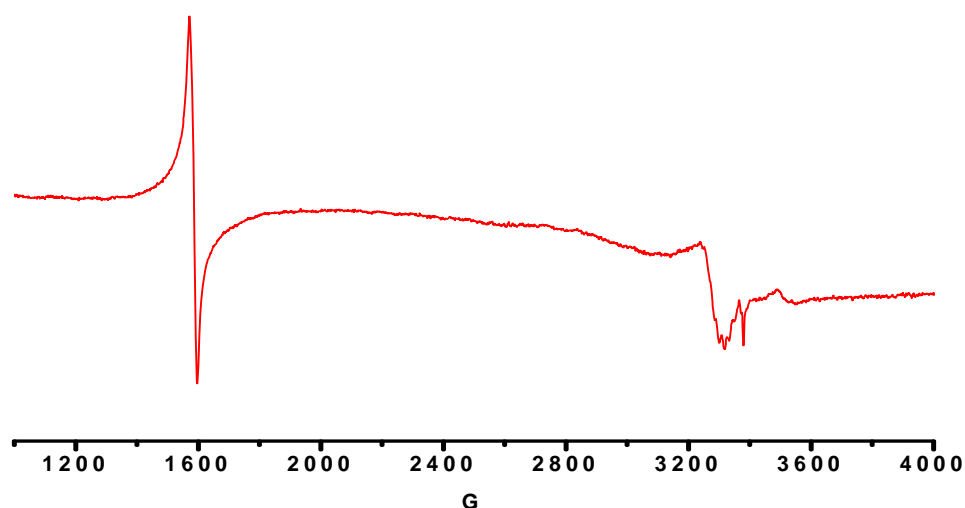


Figure 4.31: 1st derivative frozen solution EPR spectra of single strand diphenyl porphyrin-DNA **CuODN4** with and without iron contamination in water at 120 K at 300 μ M concentrations. Spectra were acquired with 3.99 mW microwave power, 5 Gauss modulation amplitude and approx. 9.4 GHz microwave frequency.

A close-up analysis of main-field splittings helps rationalise the half-field signal. The values of g_{\perp} and $A_{\perp}(^{14}\text{N})$ of copper porphyrins remain the same upon attachment to DNA, which indicate no major structural change of porphyrins in the xy plane. The lack of change in the $A_{\perp}(^{14}\text{N})$ shfs also supports the conclusion that there is little change in the Cu-N bonding. However, the substantial increase in g_{\parallel} and decrease $A_{\parallel}(\text{Cu})$ (**Table 4.4, 4.5**) for both porphyrin-DNA single and double strands indicates some degree of structural alteration along the z direction of the Cu porphyrin complexes.

It is important to remember that the half-field signal is not a consequence of porphyrins measured in water,¹⁷¹ and thus it is not an intrinsic property of porphyrins. The theory that DNA must have induced a change in the stacking of porphyrins along the z-axis, which subsequently gives rise to a half-field signal is then considered. A significant decrease of $A_{//}(\text{Cu})$ from 200 Gauss in copper porphyrin building blocks to approximately 150 Gauss in porphyrin-DNA suggests a decrease in the *unpaired* electron density at Cu(II). It seems that the natural helical structure of DNA has induced a change in the *unpaired* electron density on copper porphyrin, and encourages interspin transitions. This may indicate porphyrins are closer to each other on DNA than previously assumed, and the interactions between *unpaired* electrons on Cu(II)-Cu(II) centres along z-axis are greater than expected (**Figure 4.32**). This interspin transition is distance dependent, because the relative intensity (taken as the ratio of half-field against main-field peak heights) is larger when the two copper porphyrins are adjacent to each other in **CuODN18**, compared to when they are placed further apart by a non-modified base in **CuODN17** (**Table 4.4**). Both **CuODN18** and **CuODN17** have the same DNA sequence.

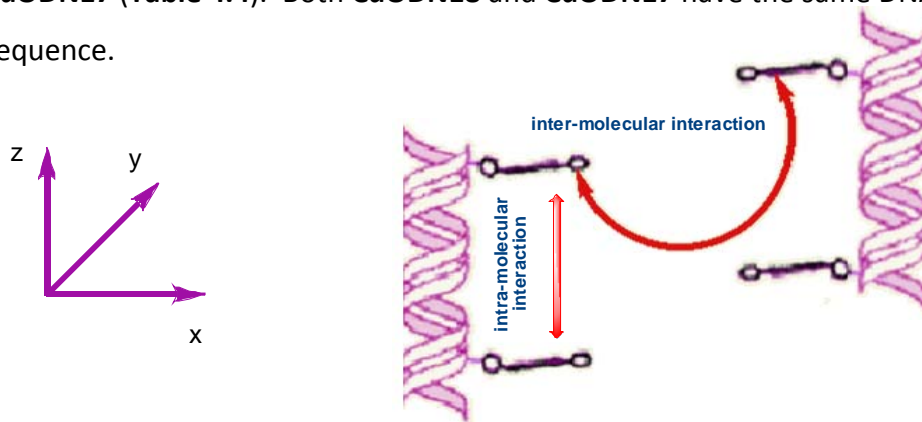


Figure 4.32: Inter and intra-molecular interactions along z-axis of porphyrin-DNA.¹⁷³

The differences in $g_{//}$ and $A_{//}$ values of copper porphyrin-DNA compared to copper porphyrins raise a question on whether the spectra belong to copper bound to nitrogen in the porphyrin ring, or a consequence of copper bound elsewhere in the molecule. The most likely copper binding position outside the porphyrin ring is at the oxygen that carries a negative charge on the phosphate backbone. EPR spectra of **uridine CuTPP 18** (**Figures 4.33, 4.34**), which are water soluble porphyrin

nucleosides prepared by Eugen Stulz and Jonathan R. Burns, University of Southampton, however help eliminate this possibility. When Cu(II) is not bound inside the porphyrin ring, but to oxygen outside the ring then the spectra look very different from that of **CuTPP 16** (Figure 4.18) and **CuTPP-DNA** (Figure 4.27).

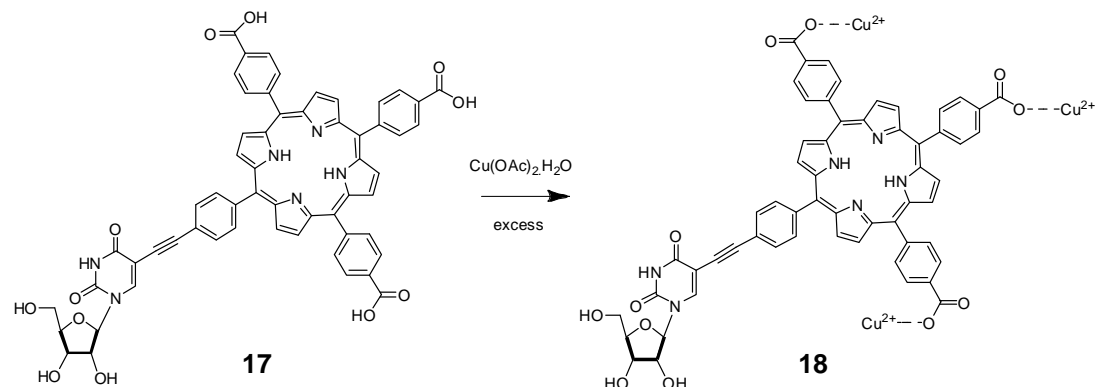


Figure 4.33: Copper metallation of **uridine TPP 17**.

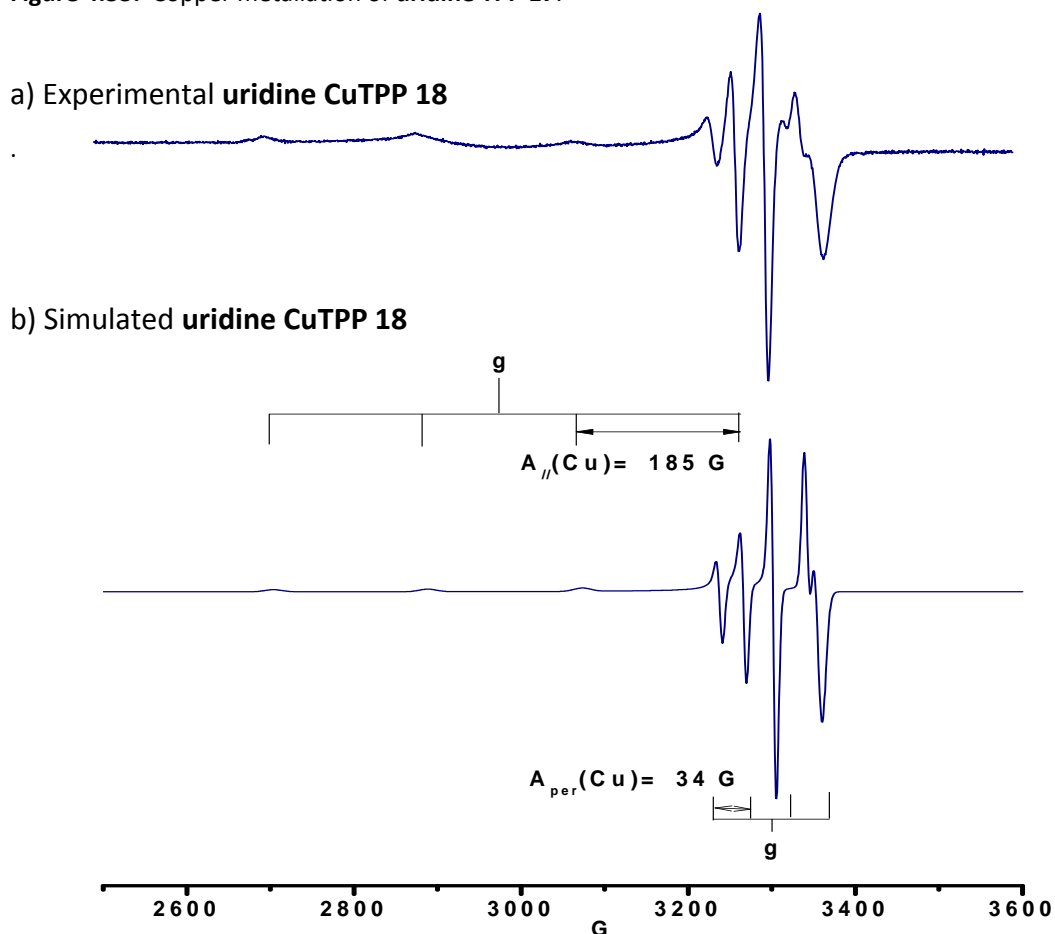


Figure 4.34: a) Experimental 1st derivative frozen solution EPR spectrum of **uridine CuTPP 18**. acquired with 3.99 mW microwave power, 5 Gauss modulation amplitude and approx. 9.5 GHz microwave frequency and b) Simulated frozen solution spectrum of **uridine CuTPP 18** having $g_{\perp} = 2.051$, $g_{\parallel} = 2.266$, $A_{\parallel}(\text{Cu}) = 185$ Gauss, $A_{\perp}(\text{Cu}) = 34$ Gauss, Lorentzian/Gaussian lineshape = 1, $\Gamma_{\perp} = 7$ Gauss, $\Gamma_{\parallel} = 20$ Gauss.

Table 4.6: g and A values from simulated EPR spectra of frozen solutions of **CuTPP 16** and **uridine CuTPP 18**.

Complex	g_{\perp}	$g_{//}$	$A_{\perp}(\text{Cu})/G$	$A_{//}(\text{Cu})/G$	$A_{\perp}({}^{14}\text{N})/G$	$A_{//}({}^{14}\text{N})/G$
CuTPP 16	2.060	2.187	32.0	200	17.0	13.5
Uridine CuTPP 18	2.051	2.266	34.0	185	N/D	N/D

The EPR spectrum of **uridine CuTPP 18** has four copper peaks with the 4th copper peak split into 4 peaks, an indicator of splitting by a nucleus that has $I = 3/2$, which is not that of ${}^{14}\text{N}$ $I = 1$. Indeed, this splitting is caused by a Cu(II) $I = 3/2$ nucleus. Compared to **CuTPP 16**, a small change in $A_{//}\text{Cu}$, g_{\perp} values and a significant increase in $g_{//}$ value are also observed (**Table 4.6**). These findings confirm that the EPR signals from **uridine CuTPP 18** arise from porphyrin complexes that do not have the copper bound inside the porphyrin ring. The likelihood of Cu(II) bound to the oxygen on the carboxylic acid (**Figure 4.33**) is however quite high. Even though a full spectral analysis is required to solidly determine the exact position of Cu(II) in **uridine CuTPP 18**, it is sufficient to conclude that the porphyrin-DNA EPR spectra are not those derived from copper(II) bound outside of the porphyrin ring. A magnification of the 4th copper peak in the experimental **CuTPP**-DNA spectrum shows more than just four signals, which is a strong indication of Cu-4 ${}^{14}\text{N}$ bonding, as found in **CuTPP 16**. The poor quality of experimental porphyrin-DNA spectra due to sample limitation, however does make it hard to simulate and derive ${}^{14}\text{N}$ superhyperfine constants accurately.

A narrow scan, focussing on the half-field signal produced only a broad peak at $g = 4.3$. This helps to rule out the possibility of triplet state radical, as could occur in dimeric species because if it were true, splittings would have been observed in the half-field signal. Besides, the large size of copper porphyrin molecules should prevent the formation of a triplet state. Even though on DNA, the copper

porphyrins seem to be closer to each other than in porphyrin building blocks, the separation between these chromophores is still not small enough to enable copper-copper centres to have rapid electron exchange. If copper porphyrins were bound to each other *via* the DNA backbone then the broad half-field peak would have been split into 7 lines, following the hyperfine splitting = $(2I_{\text{eff}}+1)$ with the total $I_{\text{eff}}= 3$ from two Cu(II) centres.

Dimerisation of porphyrins to form a cofacial configuration *via* a covalent link, as reported by Eaton and colleagues¹⁶⁸ is another possibility which was investigated, and was tested by performing a pyridine binding study on porphyrin-DNA. The porphyrin-DNA did not show any affinity for pyridine, as evidenced by no change in the EPR spectra. However, although this result is consistent with the blocking of the porphyrin z-axis by DNA, it could also simply be a consequence of steric hindrance. Future experiments should investigate stronger binding reagents.

We next considered that half-field signals could be a result of the porphyrin π - π stacking. This was tested for all porphyrin-DNA single and double strands by dilution experiments, since if the interaction between porphyrins is the consequence of π - π stacking, and thus distance dependent, then addition of water should drive molecules further apart. Thus a lower concentration should shift the equilibrium of π - π stacking and decrease the intensity of the interspin transition. However, as indicated in **Table 4.7**, increases in relative intensities of the half field transitions occurred when samples were diluted from 300 μM to 200 μM to 100 μM . These increases are consistent for all porphyrin-DNA complexes. The only exception is the duplex of **CuODN18**, where the ratio decreases slightly at 200 μM . Nevertheless, this could be due to instrumental factors rather than an intrinsic property of the strand, since the spectrum of the **CuODN18** duplex was measured on a different spectrometer, which had a poorer background signal. Despite this aberration, the duplex of **CuODN18** still shows a comparable increase in its relative intensity at 100 μM concentration.

Table 4.7: Relative intensities of all diphenyl porphyrin and tetraphenyl porphyrin-DNA upon dilutions with water. The relative intensity is the ratio of the height of half-field peak at $g = 4.3$:height of main field peak at $g = 2$.

Porphyrin-DNA	Relative intensity 300 μM	Relative intensity 200 μM	Relative intensity 100 μM
ss CuODN4 (TPT)	0.08:1	0.08:1	0.09:1
ss CuODN1 (PAP)	0.06:1	0.08:1	0.08:1
ds CuODN1 (PAP)	0.28:1	0.29:1	0.29:1
ss CuODN17 (PAP)	0.10:1	0.11:1	0.15:1
ds CuODN17 (PAP)	0.37:1	0.41:1	0.43:1
ss CuODN16 (APA)	0.08:1	0.10:1	0.11:1
ds CuODN16 (APA)	0.24:1	0.28:1	0.30:1
ss CuODN18 (PP)	0.12:1	0.13:1	0.16:1
ds CuODN18 (PP)	0.37:1	0.34:1	0.35:1

Increasing trend



Thus diluting the samples enhances the stacking of porphyrins on DNA. In contrast to the expected equilibrium shift, the stacking of porphyrins seems to be induced by DNA and it seems that porphyrin hydrophobic interactions are favoured in the porphyrin-modified DNA models. However, the exact reason for this unusual, though consistent, equilibrium shift is not yet fully understood.

The above results open a new hypothesis for porphyrin-DNA interactions, which will eventually contribute to understanding of porphyrin-DNA stability. A novel porphyrin-DNA stacking model made from a bundle of two to four DNA strands (**Figure 4.35**), which is consistent with recent SAX results from Stulz's group could be a possible structure that porphyrin-DNA adopts. Any conclusions as to whether they take up two or four bundle configurations cannot be determined at this stage, due to limitations in EPR spectral resolution.

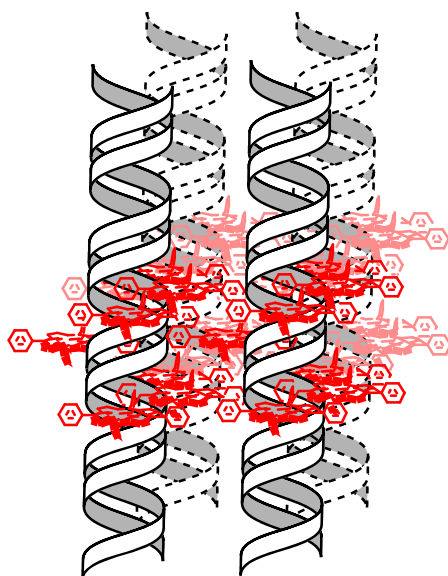


Figure 4.35: Bundle model of porphyrin-DNA stacking.

4.2.2.6 Distance calculation of porphyrin-DNA by EPR

The original aim of the EPR investigation was to provide information on the interspin distance between Cu porphyrins bound to DNA. Schiemann and Kato estimated the separation between Cu^{2+} - Cu^{2+} ions inside a DNA helix to be 3.7 \AA ¹⁵⁷ by simulating EPR spectra to give dipolar coupling constants. In the present work, it was not possible to perform unambiguous simulations, since the parameters would not have been accurate due to the poor resolution of porphyrin-DNA spectra. Even addition of glycerol did not help improve the poor glassing of porphyrin-DNA with water. Therefore, a different method of distance calculation was employed. This method, which was developed by Eaton and Eaton involves the use of half-field transition to determine the interspin distance in a system with two *unpaired* electrons, *via* the following equation.^{155, 174}

$$\text{Relative intensity} = \frac{\text{half-field integration}}{\text{main-field integration}} = \frac{(19.5 + 0.5)(9.1)^2}{r^6 \nu^2}$$

Equation 4.8

Where r is the interspin distance in \AA and ν is the microwave frequency in GHz.

Method for calculating interspin distance r

Calculated Cu(II)-Cu(II) distances of porphyrin-DNA strands at different concentrations are summarised in **Table 4.8**. The calculation is performed by first obtaining the magnitude of the relative intensity. This is the ratio of the height of the half-field peak over the height of the main field peak, which are measured from the spectrum after it has been subtracted from the background spectrum (*i.e.* frozen water spectrum). By inputting the values of relative intensity and microwave frequency ν , which is taken from the instrument and rearranging **Equation 4.8**, the Cu(II)-Cu(II) distance r is then derived.

To satisfy **Equation 4.8**, both anisotropic exchange must be negligible and $r > 4\text{-}5 \text{ \AA}$, because only in this case can the relative intensity become a function of r and be independent of the exchange coupling constant J . All calculated r values (**Table 4.8**), however are $< 4 \text{ \AA}$. Hence, this strategy of Cu(II)-Cu(II) distance calculation is not suitable for porphyrin-DNA models, especially when the DNA seems to have induced porphyrins to be closer to their neighbouring chromophores than normally expected. The range 1.83 \AA - 2.46 \AA of calculated r values of porphyrin-DNA is, however significantly smaller than the distances derived by either point-dipole approximation (8.18 \AA) or standard DNA model (13.6 \AA).³² Method-wise, obtaining r *via* half-field to main-field signal intensities may also carry a large error, since the main field may contain other monoradical impurities from other unwanted paramagnetic species in the sample. Therefore, this method is, in general less precise, especially since the integration of the peak involves subtraction of background spectra.¹⁶⁹ The errors here are intensified by the low spectral resolution.

Table 4.8: Calculated interspin distances of porphyrins attached on DNA.

Porphyrin-DNA	r Cu(II)-Cu(II) 300 μ M (Å)	r Cu(II)-Cu(II) 200 μ M (Å)	r Cu(II)-Cu(II) 100 μ M (Å)
ss CuODN4 (TPT)	2.50	2.48	2.45
ss CuODN1 (PAP)	2.59	2.50	2.46
ds CuODN1 (PAP)	2.02	2.00	2.00
ss CuODN17 (PAP)	2.40	2.34	2.24
ds CuODN17 (PAP)	1.92	1.82	1.83
ss CuODN16 (APA)	2.48	2.40	2.34
ds CuODN16 (APA)	2.06	2.01	1.99
ss CuODN18 (PP)	2.32	2.28	2.21
ds CuODN18 (PP)	1.92	1.97	1.94

Decreasing trend



While it is not possible to derive a dipolar coupling constant **D** for use in **Equation 4.9** to obtain an accurate **r**, the present results can still provide qualitative information on the interspin interactions between porphyrins attached on DNA.

$$D = 2786/r^3$$

Where **D** is the dipolar coupling constant in mT

and **r** is the Cu(II)-Cu(II) separation in Å.

Equation 4.9¹⁷⁵

These qualitative data in **Table 4.8** can provide some structural information for porphyrin-DNA. For example, a decreasing trend in the interspin distance at lower sample concentrations supports the hypothesis for a porphyrin-DNA bundle model, whereupon addition of water improves the stacking of porphyrins. All duplexes show a clear decrease in **r** values compared to single porphyrin-DNA strands, indicating that DNA helps stack porphyrins closer to each other than previously expected. Hence DNA, especially duplexes, can be used as a scaffold for molecular

functionalisation, and DNA is an efficient scaffold for hosting chromophores in well-organised and pre-arranged configurations. It also seems that increasing the number of porphyrins induces a higher degree of stacking on DNA. The value of r is smaller in **CuODN18** than in **CuODN16** (both have the same DNA sequence), where there are two adjacent porphyrins instead of one.

4.3 Conclusion

The EPR spectra of porphyrins confirm that copper is successfully bound inside porphyrin rings, and hence support the authenticity of compounds. The similarities in EPR spectral parameters for all the copper porphyrin building blocks indicate both diphenyl porphyrins and tetraphenyl porphyrins have similar copper environments, and that the porphyrin structure remains intact in the presence of different functional groups (*i.e.* phenyls). By studying the binding with pyridine, it was shown that the interactions between porphyrins are dipolar in nature, and can be disrupted by the addition of a binding reagent. However, for future measurements, it is recommended that a single copper isotope is used to prepare the complexes to improve spectral resolution and simplify their analyses.

Copper is successfully incorporated into the porphyrin-DNA by post-automated solid-phase synthesis. The reaction is controllable, and is not due to spontaneous metallation resulting from concentrated aqueous ammonia that contains traces of numerous metals (*e.g.* copper and zinc).¹⁷⁶ The magnitudes of the nitrogen shfs are consistent with the successful attachment of porphyrins to DNA, and the EPR spectra of porphyrin-DNA are different from those of porphyrins in solutions. All EPR spectra of porphyrin-DNA show a consistent half-field transition, which is not observed in porphyrin building blocks, and may indicate DNA influence on the π - π stacking of porphyrins. The larger relative intensity of this transition, and the decreasing trend of Cu(II)-Cu(II) interspin distance from hybridisation of single strands to duplexes demonstrate a stronger porphyrin π - π interaction in duplexes (**Table 4.7**). DNA double strands are, therefore, better scaffolds for porphyrins stacking than DNA single strands.

The possible bundle model (**Figure 4.35**) promotes porphyrin hydrophobic interactions, and the EPR spectra show that DNA functionalised with porphyrins may not behave like simple molecules. Both the inter- and intra-molecular interactions should be considered when designing future porphyrin-DNA arrays, so that one can explore their promising supramolecular scaffold applications. Eventually, this study may lead to the attachment of molecules which have high

optoelectrical and biological activities to the DNA scaffold, for making the next generation of nanowires and nanochips.

EPR is an ideal technique for checking samples for paramagnetic centre impurities, and there seems to be no major contribution from any other paramagnetic species in the spectra of porphyrins and porphyrin-DNA. Although such measurements help to confirm the authenticity of the sample, the absolute purity of these samples cannot be determined by EPR alone, because diamagnetic materials are invisible to this technique. Thus other techniques, such as mass-spectrometry and HPLC for metallated porphyrin-DNA, hitherto unsuccessful (**Chapter 2, Section 2.4**), are still required for the identification of the presence of impurities.

4.4 Future work

The interspin distance for Cu(II) porphyrins attached to DNA, which are based on the relative intensity calculated from the heights of half-field:main field signals can only provide qualitative information on the separation between chromophores. Developments for a more refined calculation method to derive accurate relative intensity are ongoing. Specifically, a more thorough method to deduce quantitative signal integrations to replace their heights will be investigated in collaboration with Prof. B. A. Goodman at Guangxi University, China.

During the EPR study in this project, an unexpected observation was made in which signals from the single strand **CuODN4** completely disappeared after 3 days in water. Although this discovery was purely accidental, it might tell an interesting story about modified DNA design. Redox chemistry of Cu²⁺ is the most likely explanation,¹⁷⁷ in which Cu²⁺ in diphenyl porphyrin is reduced to Cu¹⁺. Since the redox potentials of purines and pyrimidines have been established (e.g. $E_G = 0.72 < E_A = 0.75 < E_T = 0.79 < E_C = 0.81$ V),¹⁷⁸ the **CuODN4** signal loss may suggest the possibility for electron transfer from the nucleobase onto porphyrin. During photochemical reactions, Kittler and Berg *et al.*¹⁷⁹ reported that all A, C, G, T nucleobases can donate electrons onto photoactive chromophores. These findings may open more doors to the developed area of photo-induced DNA damage *via* oxidative decay,¹⁸⁰ whereupon the porphyrins-DNA designs can trigger singlet oxygen formation that may lead to DNA damage.

One EPR biological application was to probe primary ion radicals of A, C, G, T nucleobases in the early 1990s.¹⁸¹ With regards to porphyrin-DNA strands, the way to look for evidence of a free radical signal around $g=2$ is to perform a fairly narrow scan, but more importantly with a small microwave power to prevent signal saturation. Hence, future EPR experiments could be designed to explore the biological impacts of porphyrin-DNA, especially since certain types of porphyrin (*i.e.* protoporphyrin IX) have been shown to be phototoxic to human cells.¹⁸² An issue that may arise for a radical-probing EPR experiment is the short lifetime of the free radical. Because of the *unpaired* electron, most free radicals are very reactive. The rate of forming enough radical porphyrin-DNA may not be slow enough for the species to be measured. One then may need to consider designing a spin trap system, such as the addition of nitron to produce a longer living free radical for detection.¹⁸³ All of these points will certainly be considered in designing future experiments to continue this investigation.

Up until now, guanine is the easiest nucleobase to be oxidised to form cation radical $G^{\bullet+}$, due to its low redox potential while thymidine and especially cytosine are more likely to be reduced to anion radical $T^{\bullet-}$ and $C^{\bullet-}$, because of their higher redox potentials.^{179, 181} If it is true that the loss of EPR signal in **CuODN4** is a result of electron transfer from DNA, then perhaps irradiation of porphyrin with light could have either encouraged T to be oxidised (**Figure 4.36**), or the through-space reducing of neighbouring G is a possibility.¹⁸⁴ If these issues could be addressed then porphyrin-DNA may have potential for treatments of certain illnesses. Porphyrins may induce radical formation on DNA, which could eventually result in DNA damage.

Once the purity of the metallated oligomers has been confirmed (*e.g.* by HPLC), the next step to pursue will involve *in-vitro* assays of porphyrin-DNA for photodynamic therapy and sequence specific DNA cleavage. Skin cells (*i.e.* keratinocytes) will be cultured for *in-vitro* tests with porphyrin-DNA. The first step will involve observing positive porphyrin-DNA cell transfections, before the detection of cell deaths can be investigated.

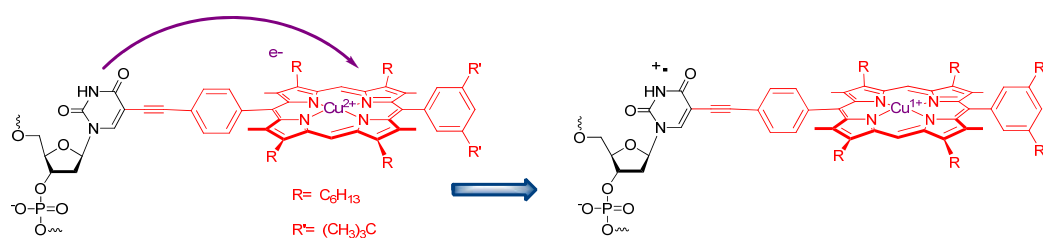


Figure 4.36: Potential of radical transfer from copper diphenyl porphyrins onto DNA.

CHAPTER 5: EXPERIMENTAL

5.1 General synthetic procedures

Reactions involving air or moisture sensitive reagents were carried out under nitrogen using standard vacuum line techniques. All glasswares for these reactions were flame-dried and allowed to cool under vacuum before use. Reactions described as being performed at $-10\text{ }^{\circ}\text{C}$ were in an acetone/dry ice bath and reactions at $0\text{ }^{\circ}\text{C}$ were performed in an ice bath. All organic solutions were dried over sodium sulphate or magnesium sulphate, unless otherwise stated.

Solvents

Dried solvents were purchased from Fisher Scientific and Aldrich. Dry acetone was produced in laboratory by distilling over calcium sulphate (9.00 g of CaSO_4 for 80 mL of wet acetone).

Reagents

All commercial grade chemicals were used as supplied, without further purification, unless otherwise stated. The organic solvents were purchased from Fisher Scientific and deuterated NMR solvents were supplied by Apollo Scientific. DNA synthesis reagents and purifications were obtained from Glen Research, Link Technology, Berry&Associates and ATD Bio. All other chemicals were purchased from either Fisher Scientific or Sigma-Aldrich.

Chromatography

Column chromatography was performed on either silica gel (Kieselgel 60) or silica gel type H, and lipophilic Sephadex size exclusion column chromatography was performed using 25-100 μm beads. Thin layer chromatography was performed on Merck aluminium sheets coated with 0.2 mm silica gel 60 F_{254} . Plates were visualised by UV light (254 nm, 365 nm) or with the aid of anisaldehyde dip.

5.2 Analytical experiments

5.2.1 NMR spectroscopy

^1H NMR spectra were recorded at 300 or 400 MHz on Bruker ADVANCE DPX-300, DPX-400, or AV-400 spectrometers. Chemical shifts (δ_{H}) are reported in parts per million (ppm) and are referenced to the residual solvent peak. Coupling constants (J) are quoted in Hz. ^{13}C and ^{31}P 55

NMR spectra were recorded on a Bruker ADVANCE DPX-400 spectrometer at 100.62 and 161.98 MHz, respectively; chemical shifts (δ_{C}) are quoted in ppm and referenced to residual undeuterated solvent signals or standards.

5.2.2 EPR spectroscopy

All samples of copper porphyrin building blocks were investigated under three separate conditions, namely pure solid powder, fluid solution and frozen solution. For initial slow motion lineshape investigations of porphyrins, temperature dependent measurements from 193 – 301 K were also performed. However, porphyrin-DNA complexes were only measured as frozen solutions at 120 K, because of insufficient sample for pure solid measurements and the high molecular mass which produced rigid limit spectra from fluid solutions. Spectra from pure solids were obtained from a few milligrams of sample. For porphyrin building blocks DCM, and DCM/toluene were used as solvents for fluid and frozen solution spectra, respectively, and porphyrin-DNA complexes were investigated in DNA grade water.

The EPR spectra were acquired using Bruker EMX-X band (9 GHz), Bruker EMX Micro-X band (9 GHz) or Bruker Elexsys-Q band (34 GHz) spectrometers, equipped with Bruker high sensitivity cavities and using built-in frequency counters. Low temperature spectra were acquired with variable temperature cryostats using liquid nitrogen as coolant for measurements in the temperature range 120 – 301 K and liquid helium for measurements at 5 K. All samples were measured in tubes made from quartz with internal diameters of 3mm (X-band) and 1mm (Q-band). Spectra were acquired with 100 Hz modulation frequency in the field range 0 – 8000 Gauss

using the Bruker WIN-EPR program. The porphyrin building blocks were typically recorded with 2048 points as 1st and 2nd derivatives of the microwave absorption, whereas the porphyrin-DNA complexes were usually recorded as 1st derivatives only, but with 3072 points to improve spectral resolution.

Initial peak positions were estimated using WIN-EPR and these were then used to provide a basic interpretation of the spectra; all hyperfine coupling constants (A_{iso} , $A_{//}$, A_{\perp}) are quoted in gauss. For copper porphyrin building blocks, where there was good signal-to-noise and resolution, spectral interpretations and parameters were refined using the Bruker Simfonia simulation software.

Simulations of frozen solution samples assumed axial (square planar) symmetry. In addition, the A_{\perp} (Cu) values were refined by reference to the A_{iso} value from simulated fluid solution spectra, *via* the relationship of $A_{iso} = 1/3(A_x + A_y + A_z)$.^{185, 186} Interpretation of the spectra of the fluid solution samples was complicated by the molecular tumbling rates being insufficiently rapid to completely average the anisotropy, and simulations used the expression $a + bm_l + cm_l^2$ for the linewidths (L/W) of the copper peaks. Furthermore, all spectra were complicated by the presence of two copper isotopes, ⁶³Cu and ⁶⁵Cu with similar, but not identical magnetic properties, so simulations were based on just the main ⁶³Cu isotope.

5.2.3 UV-vis spectroscopy

UV-vis spectra (UV-vis) of porphyrin-DNA complexes were recorded on Cary-4000 Bio, Cary-400 Bio, Cary-300 Bio or Cary-50 Bio UV-Vis spectrophotometers using DNA grade water as solvents. Spectra were measured from 800 nm – 200 nm, and absorption maxima (Abs._{max.}) were recorded by wavelength (nm) together with molar extinction coefficients ϵ in L mol⁻¹ cm⁻¹. Concentrations of oligonucleotides in samples were calculated using the Beer-Lambert Law, where

$$A = \epsilon[C]l$$

Equation 5.1 Beer-Lambert Law¹¹¹

A= absorption (arbitrary unit)

ε= molar absorption coefficient or extinction coefficient (L mol⁻¹ cm⁻¹)

[C]= concentration (mol L⁻¹)

l= pathlength (cm)

The extinction coefficient at 260 nm, ϵ_{260} , of oligonucleotides was calculated by the Ambion® Oligonucleotide MW and Extinction Coefficient Calculator program, which uses the following equation:

$$\text{ODN } \epsilon_{260} = [(8.8 \times nT) + (7.3 \times nC) + (11.7 \times nG) + (15.4 \times nA)] \times 0.9$$

Equation 5.2¹⁸⁷

The extinction coefficient at 260 nm ϵ_{260} of **DPP**-oligonucleotides was calculated by first subtracting the extinction coefficient of the thymidine nucleobase(s), which provide sites for porphyrin attachment **dU**, from the extinction coefficient at 260 nm ϵ_{260} of the non-modified DNA sequence, followed by addition of the extinction coefficient at 260 nm ϵ_{260} of monomer(s) **5'-O-DMT-dU^{DPP}**. This calculation can be expressed as:

$$\text{DPP-ODN } \epsilon_{260} = \text{ODN } \epsilon_{260} - \text{TdU } \epsilon_{260} + \text{5'-O-DMT-dU}^{\text{porphyrin}} \epsilon_{260}$$

Equation 5.3

The extinction coefficient at 260 nm ϵ_{260} of monomer(s) **5'-O-DMT-dU^{DPP}** was previously measured by Dr. Bouamaied. **5'-O-DMT-dU^{DPP} ϵ_{260} = 4904.**

5.2.4 UV-vis melting studies

UV-melting studies of porphyrin-DNA were performed using Cary-4000 Bio, Cary-400 Bio, or Cary-300 Bio UV-visible spectrophotometers on 1 μ M samples at pH 7.0 in a buffer of 100 mM NaCl, 50 mM KH_2PO_4 . A standard melt programme was used (15 – 80 $^\circ\text{C}$ at 0.5 - 1.0 $^\circ\text{C}/\text{min}$, 1 min hold) with 5 heat/anneal cycles in total. Evaporation at high temperature (*i.e.* 80 $^\circ\text{C}$) and condensation at low temperature (*i.e.* 15 $^\circ\text{C}$) were not major problems. Solutions of samples were measured in Hellma[®] SUPRASIL synthetic quartz cuvettes (1.0 cm pathlength, 1.0 mL sample volume) with monitoring at 260 nm and 410 nm using Cary WinUV thermal software. Absorbances for porphyrin-DNA were plotted against temperature to produce a melting curve using Origin[®] software. The derivative of the melting curve was then deduced, and the temperature at the turning point of the derivative was taken as the melting temperature T_m of that porphyrin-DNA strand.

5.2.5 Fluorescence emission spectroscopy

Emission spectra of porphyrin-DNA complexes were recorded on Perkin Elmer LS50B and Cary Eclipse spectrometers using DNA grade water as solvents. Spectra were measured from 550 nm – 900 nm with excitation wavelengths set at 406 – 425 nm, and the wavelengths (nm) of the maxima of the major emissions (Emis_{max}) were recorded.

5.2.6 Fluorescence emission melting studies

Fluorescence emission melting studies were performed with 1 μ M sample concentrations at pH 7.0 in a buffer of 100 mM NaCl, 50 mM KH_2PO_4 on Perkin Elmer LS50B and Cary Eclipse spectrometers. Temperatures were adjusted manually in the range 15 – 85 $^\circ\text{C}$. Solutions were measured in Hellma[®] SUPRASIL synthetic quartz cuvettes with 3 windows (1.0 cm pathlength, 0.2 mL - 1.0 mL sample volume), and monitored at excitation wavelengths of 410 - 425 nm.

5.2.7 Circular dichroism spectroscopy

Circular dichroism measurements were performed on a CD spectrophotometer at Cambridge University Chemistry department and on an Olis DSM20 CD spectrophotometer at Diamond Light Source. All strands were measured at room temperature in water and buffer, unless explained otherwise. All CD spectra were originally recorded in molar ellipticity θ (millidegree), which were subsequently converted to standardised units of $\Delta\epsilon$ for ease of comparisons between spectra of different strands. The standardised molar ellipticity of CD spectra reported in this thesis were calculated after taking into account the differences in sample concentrations and cell pathlengths, and is governed by the following expression:

$$\Delta\epsilon = \theta / (10 \times C \times l \times 3298)$$

Equation 5.4^{187, 188}

θ = intensity of CD spectrum (millidegree)

C = concentration (mol L⁻¹)

l = pathlength (cm)

- For single strands, spectra are presented in standardised units of **$\Delta\epsilon$ per base**.
- For duplexes, spectra are presented in standardised units of **$\Delta\epsilon$ per base-pair**.

The following settings were used for the spectrophotometers:

Olis DSM20 CD spectrophotometer

Scan range: 330 nm to 180 nm.

Slit width: 0.5 mm.

Integration time: 4 s/nm so that total experimental time was kept \leq 60 minutes to exclude possible DNA denaturing by prolonged exposure to high energy light.

Number of repeated scans: 2 – 4.

Cuvettes: quartz cuvettes (0.05 - 0.1 cm pathlengths, 0.16 – 0.40 mL volume).

Solvent: water only because buffer produces absorbance below 220 nm.

Chirascan Circular Dichroism Spectrometer

Scan range: 600 nm to 200 nm.

Slit width: 3.0 mm.

Integration time: 1-3 s/nm.

Cuvettes: quartz cuvettes (1.0 cm pathlength, 1.0 – 3.0 mL volume).

Solvent: 100 mM NaCl, 50 mM KH₂PO₄, pH 7.0 buffer.

5.2.8 Mass spectrometry**MALDI-ToF MS**

Matrix-assisted Laser Desorption Ionisation Time-of-Flight Mass Spectrometry (MALDI-ToF MS) of compounds in this work was performed on a DYNAMO spectrometer for positive ions. The signals are referred to the unfragmented, single charged ions [M]⁺, and data are presented as unit mass per charge (m/z).

Matrix preparation and spectrometer calibration

2 - 6 mg of p-nitroaniline was dissolved in DCM (0.2 - 0.5 mL) to be used as a matrix for MALDI-ToF MS. Reference materials employed for calibration of the spectrometer included tetraphenyl porphyrin (RMM= 614.2) and Zn di-tert-butyl diphenyl porphyrin **10** (RMM= 1140.8).

5.2.9 Analytical HPLC

Analytical HPLC analyses of oligonucleotides were performed on a Varian 920-LC HPLC system with UV-vis detector (260 nm, 410–420 nm) and a reversed phase Waters Xbridge OST C₁₈ 2.5 μm, 4.6 × 50 mm column. The samples were run using 35 and 60 minutes gradient methods. The mobile phase solvents were 8.6 mM TEA/100 mM HFIP (hexafluoroisopropanol) buffer, at pH 8.3 and MeCN. All the chromatograms presented in **Chapter 2, Section 2.4** were obtained from using either method A (**Table 5.1**) or method B (**Table 5.2**).

Table 5.1: Method A: A= 8.6 mMTEA/100 mM HFIP buffer, pH 8.3; B= MeCN.

Time (min)	% A	% B	Flow (ml/min)
0	88	12	0.6
0.1	88	12	0.6
18	1	99	0.6
25	1	99	0.6
30	88	12	0.6
35	88	12	0.6

Table 5.2: Method B: A= 8.6 mMTEA/100 mM HFIP buffer, pH 8.3; B= MeCN.

Time (min)	% A	% B	Flow (ml/min)
0	88	12	0.6
0.1	88	12	0.6
40	40	60	0.6
45	30	70	0.6
50	1	99	0.6
58	88	12	0.6
60	88	12	0.6

5.2.10 Gel electrophoresis

Duplex formations of DNA were analysed by native PAGE at room temperature. The 12 % loading gel was prepared by mixing 40 % polyacrylamide (21 mL) with 10 × TBE buffer (0.9 M tris, 0.9 M boric acid, 0.02 M EDTA, pH 8.2) (7 mL), H₂O (42 mL), 10 % APS (560 µL) and TMED (56 µL). Prior to sample loading, the native gel was pre-run for 30 min at 120 V, then cooled to room temperature for 30 min. DNA samples were prepared in 2:1 buffer (PCR buffer + MgCl₂)/glycerol. A constant voltage (120 V) was supplied and the gel was run for 13-15 h in 1 × TBE buffer. UV shortwave and fluorescence imaging of gel was carried out on a Syngene G-box gel visualiser.

5.3 DNA syntheses and purifications

5.3.1 DNA solid phase synthesis¹⁰²

Some early non-modified and porphyrin-modified oligonucleotides in this work were synthesized by Dr. Dorcas Brown (ATD Bio) on an ABI 394 synthesiser, and later by myself using an Expedite automated solid-phase DNA synthesiser. All nucleobases were dissolved in dry and deoxygenated acetonitrile prior to use. All solvents (*i.e.* acetonitrile, TCA, tetrazole, acetic anhydride, N-methylimidazole, tetrahydrofuran, pyridine, iodine in water) were kept dry, apart from iodine and under an inert atmosphere during the course of the synthesis. Coupling times were between 5-10 minutes. The columns used on the synthesiser were for 0.2 μmol and 1.0 μmol scale DNA syntheses, and were pre-packed with solid beads and a DMT protected nucleoside. Further discussion on the principle of DNA solid phase synthesis can be found in **Chapter 1, Section 1.1.2.2** and **Chapter 2, Section 2.2.1**.

5.3.2 DNA hybridisation

DNA duplex was annealed by first mixing complementary single strands at the same concentration in 100 mM NaCl, 50 mM KH_2PO_4 buffer, pH 7.0. The mixture, stored in an Eppendorf vial, was then heated from room temperature to 85 °C on an Eppendorf thermomixer (3 °C/min, 1000 rotations/min), and then maintained at 85 °C for 5 minutes. The machine was then switched off and the sample cooled slowly to room temperature over 1 hour to form the stable duplex.

5.3.3 DNA purifications

Non-modified and porphyrin-modified DNA were purified through a variety of bought-in pre-packed columns/cartridges.

5.3.3.1 Fluorous affinity purification of oligonucleotides^{103, 104}

The discussion of the principle behind fluorous affinity purification is detailed in **Chapter 2, Section 2.2.2.1.**

Synthesis of fluorous-tagged oligonucleotides

The fluorous dimethoxytrityl group FDMT-N²-iBu-dN CEP (N= C, G, T) (**Figure 5.1**) was incorporated onto diphenyl porphyrin modified oligonucleotides at the 5' position using an ABI 394 DNA synthesiser (ATD Bio) and an Expedite automated solid-phase DNA synthesiser with 10 and 5 minutes coupling times, respectively for each machine. The coupling was set on trityl-on mode in order to retain the FDMT group at the 5' terminus. The crude product was cleaved off the solid support and the DNA was deprotected by ammonia solution (33 %).

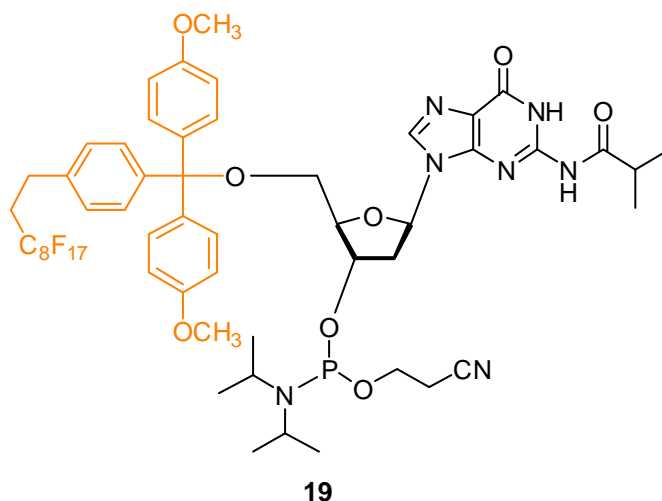


Figure 5.1: Fluorous dimethoxytrityl molecule FDMT-N²-iBu-dG CEP as an example for fluorous-tagged end modifier.

Conditioning the column

The Fluoro-Pak II column, containing 150 mg adsorbent and designed for purification of 1 μ mol DNA, was washed with the following solvents to waste at 2 s/drop rate. Note that a luer adaptor was used to attach a syringe onto the column for flow rate control.

1. MeCN (2 mL), after which the first few drops produced a yellow colour.
2. 0.1 M (2 mL) aq. triethylammonium acetate TEAA.
3. Berry and Associates loading buffer (5 % *N,N*-dimethylformamide in 100 mg/mL aq. NaCl) (2 mL).

Loading FDMT-oligonucleotides onto the column

All synthesised FDMT-oligonucleotides were dissolved in aqueous ammonia solution, diluted with equal amounts of loading buffer so that the final volume for each loading was 4 - 6 mL. The loading buffer was essential for binding the FDMT-oligonucleotides to the adsorbent media. Crude solutions were loaded onto Fluoro-Pak II columns at 5 s/drop rate, which was slow enough to allow one-pass loading.

Elution of non-fluorous sequences

The following solvents were passed through the column at 2 s/drop rate:

1. 10 % MeCN in 0.1 M aq. TEAA (2 mL) to wash out the non-fluorous molecules (*i.e.* failure sequences) first.
2. Water (2 mL) to wash the TEAA buffer out before introducing acid for detritylation in the next step.

Detritylation on the column

The following were passed through the column at 2 s/drop rate:

1. 3 % aq. trifluoroacetic acid TFA (3 mL) to deprotect the FDMT group from the modified oligonucleotides as trityl cation. A strong green colour was observed on column due to the porphyrin protonation.
2. 0.1 M aq. TEAA (1 mL) was passed to neutralise the remaining TFA and to provide the counter lipophilic triethylammonium anion to retain the trityl cation on the adsorbent.
3. Water (1 mL) to wash out the excess TEAA buffer.

Elution of the desired detritylated modified oligonucleotide

The following were passed through the column at a rate of 4 s/drop rate:

1. 50 % MeCN in water (1 mL) to elute the final product.
2. MeOH (1 mL) to elute the remaining product bound to the adsorbent.

The purified modified oligonucleotides were dried *in vacuo* and stored at -15 °C.

5.3.3.2 Nap-5 purification of oligonucleotides

The principle behind Nap-5 purification is discussed in **Chapter 2, Section 2.2.2.2.**

Conditioning the column

The following solvents were passed through a NAP-5 column designed for ≤ 1 mg/mL DNA purification without applying positive pressure to enable solvents to enter the gel bed.

1. Column buffer (distilled water containing 0.15 % Kathon) (2 mL) to enhance the flow rate.
2. Water (10 mL) to remove residual storage solution.

Loading oligonucleotides onto the column

Oligonucleotides were dissolved in 0.5 mL DNA grade water then loaded onto the column and allowed to enter the gel bed completely.

Elution of desired oligonucleotides

The solvent used in the previous step (*i.e.* DNA grade water) (1 mL) was passed through column to elute the purified oligonucleotide.

5.3.3.3 Poly-pak II purification of oligonucleotides

Poly-pak II cartridges were used to purify DMT-ON non-modified oligonucleotides after automated solid-phase synthesis, such as for the following strand¹⁸⁹

5'-DMT-GAG TAC GGT ATA CCG TAC TC-3'



5'-GAG TAC GGT ATA CCG TAC TC-3' **ODN7**

Conditioning the cartridge

Poly-Pak II cartridge designed for 1 μ mol DNA purification was treated with the following solvents to waste at 1 drop per second rate:

1. MeCN (4 mL) to wash organic residues from the resin and wet it.
2. 2 M aqueous TEAA (4 mL) to enhance the binding of oligonucleotides to the resin because TEAA can act as an ion pairing reagent.

Sample Preparation

3 parts of DNA grade water were added to 1 part of DMT-oligonucleotide **ODN7** in aqueous ammonia, so that the final loading volume was \leq 10 mL.

Loading DMT-oligonucleotides onto the column

Samples in \leq 10 mL were loaded onto the cartridge at 1 s/drop rate. The eluted fraction was collected and passed through the cartridge again to maximise the amount of DMT-ON oligonucleotides that bind to the polymeric packing.

Elution of failure sequences

The following solvents were passed through the cartridge at 1 s/drop rate:

1. NH_4OH / DNA grade water 1:20 (6 mL) to remove the remainder of the failure sequences from the cartridge.
2. DNA grade water (4 mL) to wash aqueous ammonia out of cartridge before introducing acid for detritylation in the next step.

Detritylation on the column

The following were passed through the column at 1 s/drop rate:

1. 2 % aqueous TFA (4 mL) to deprotect DMT from oligonucleotides as trityl cations.
2. DNA grade water (4 mL) to wash excess TFA while retaining the trityl cations on resin.

Elution of the desired detritylated oligonucleotide

20 % aqueous MeCN (3 mL) were passed through the column at 1 s/drop rate and fractions of the purified sample were collected in 3 different Eppendorf vials.

5.3.3.4 Glen-pak purification of oligonucleotides

Glen-pak cartridges were most efficiently used to purify post-synthesis metallation of porphyrin-DNA with $\text{Cu}(\text{OAc})_2 \cdot \text{H}_2\text{O}$ (**Figure 5.2**). Also, Glen-pak could replace Poly-pak II in purifying DMT-ON non-modified oligonucleotides.

Conditioning the cartridge

The following solvents were passed through Glen-pak columns at 0.5 - 1 s/drop rate:

1. MeCN (1 mL) to wet the resin and wash out organic residues.
2. 2 M aqueous TEAA (1 mL) to help DMT-ON oligonucleotides bind to the resin.

Sample loading

Samples (≤ 2.0 mL) were loaded onto columns at 1 s/drop rate, so that failure sequences eluted first while DMT-ON sequences were bound to the resin.

Elution of impurities

The following solvents were passed through the column at 0.5 – 1 s/drop rate:

1. 0.1 M TEAA (3 mL) to remove the excess CuEDTA and Cu(OAc)₂·H₂O.
2. Water (3 mL) to remove the remaining TEAA.

Elution of copper metallated porphyrin-DNA

MeCN/water 1:1 (2.0 mL) was finally used to elute the product.

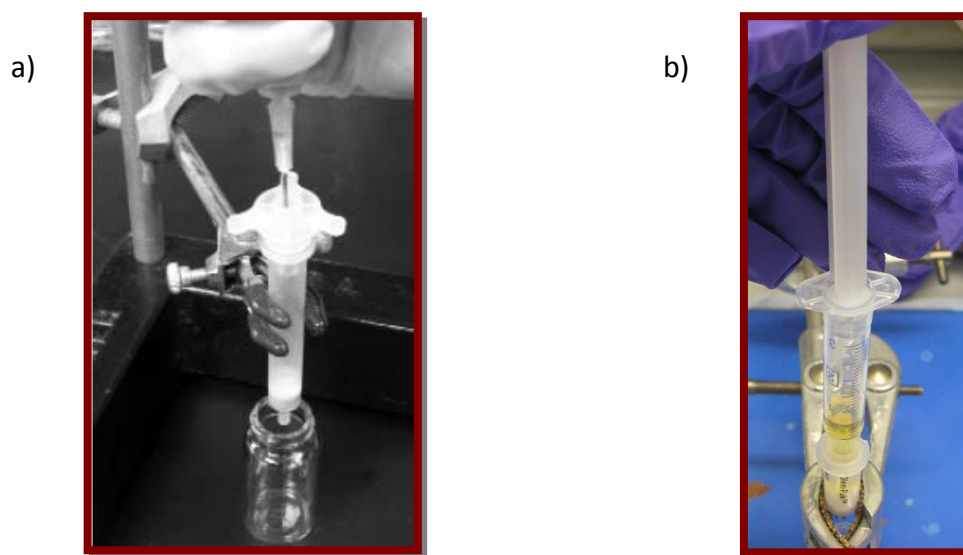


Figure 5.2: a) Fluoro-Pak II¹⁰⁴ and b) Glen-pak columns for DNA purifications.

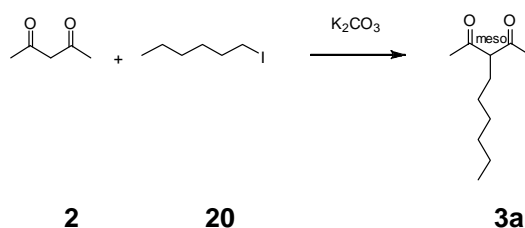
5.3.4 Solvents for DNA chemistry

Water: The water used to make up reagents for DNA metallations (*i.e.* 50 mM Zn(OAc)₂·2H₂O, 16 mM Cu(OAc)₂·H₂O, 500 mM EDTA pH 8.0, buffer) and DNA purifications (*i.e.* 0.1 M TEAA, 50 % aq. MeCN, *etc.*) were Fisher Scientific DNA grade and sterile (*i.e.* DNAase and protease-free filtered through a 0.2-micron filter and autoclaved).

Buffer: The main buffer used for metallations and DNA analytical studies was 100 mM NaCl, 50 mM KH₂PO₄, at pH 7.0, made by dissolving NaCl (585 mg, 10.0 mmol) and KH₂PO₄ (680 mg, 5.0 mmol) in 100 mL water. NaOH pellets or 10 M NaOH solution were added and the mixture was stirred and checked until its pH reached 7.0.

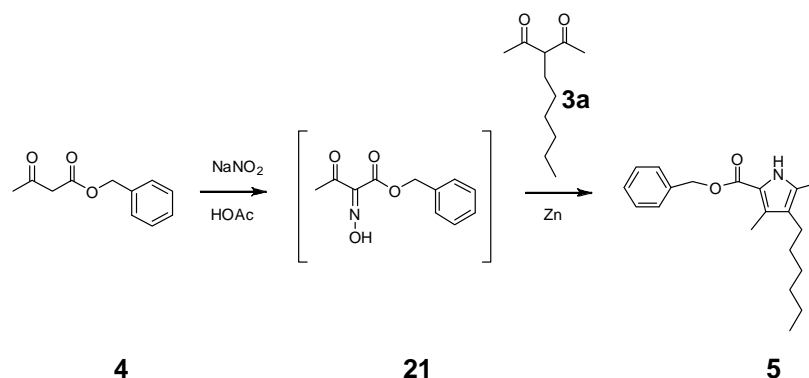
5.4 Experimental procedure

Synthesis of 3-hexylpentane-2,4-dione **3a**



Pentane-2,4-dione **2** (6.50 mL, 63.3 mmol) and 1-iodo-hexane **20** (10.0 mL, 67.8 mmol) were added to a suspension of potassium carbonate (9.36 g, 67.8 mmol) in 50 mL of distilled acetone. The reaction mixture was refluxed under nitrogen at 85 °C for 24 h then filtered, washed with acetone (20 mL) and concentrated *in vacuo*. The crude product was purified *via* vacuum distillation to give 3-hexyl-pentane-2,4-dione **3a** (4.93 g, 26.8 mmol, 42 %) as a colourless oil. R_f 0.38 (7:3 petrol ether 40-60/EtOAc); ^1H NMR (300 MHz, CDCl_3): δ_{H} (ppm) showed contamination with 5 % of side product **3b**, which was confirmed by signals at 5.37 (0.1H, s, CH_2 -meso) and 3.68 (0.1H, t, J 6.5, CH_2 - α); main product **3a** δ_{H} (ppm) 3.52 (1H, t, J 7.2, CH -meso), 2.07 (3H, s, CH_3), 2.03 (3H, s, CH_3), 1.73 (2H, dt, J 7.6, 7.2, $\text{CH}_2\text{C}_5\text{H}_{11}$), 1.17-1.07 (8H, m, $\text{CH}_2\text{C}_4\text{H}_8\text{CH}_3$), 0.77 (3H, app t, J 6.7, $\text{C}_5\text{H}_{10}\text{CH}_3$); $^{13}\text{C}\{^1\text{H}\}$ NMR (100 MHz, CDCl_3): δ_{C} (ppm) 68.6 (CH -meso), 68.0 (CH_2 - α), 31.2, 30.4, 22.4, 22.2 ($4 \times \text{CH}_2$), 28.7 (CH_3), 28.1 ($\text{CH}_2\text{C}_5\text{H}_{11}$), 22.5 (CH_3), 13.7 ($\text{C}_5\text{H}_{10}\text{CH}_3$). The analytical results are consistent with reported data.^{98, 99, 190}

Synthesis of benzyl 4-hexyl-3,5-dimethyl-1H-pyrrole-2-carboxylate **5**

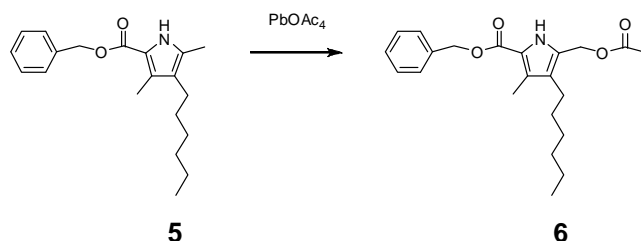


Sodium nitrite (16.5 g, 239 mmol) was added slowly and carefully to H₂O (37 mL) at 0 °C and this light yellow solution was added to a solution of benzyl acetoacetate **4** (41.4 mL, 239 mmol) in acetic acid (46.6 mL, 814 mmol) at 10 °C over 75 min. The reaction mixture was then stirred at 10 °C for 5 h, followed by further stirring at room temperature for 18 h.

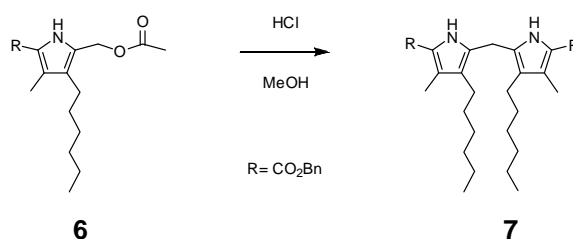
Zinc powder (47.0 g, 718 mmol) was added slowly to 3-hexyl-2,4-diketone **3a** (44.1 g, 239 mmol) in acetic acid (65 mL) at 60 °C over 2 h to form a grey suspension. The previous reaction mixture was then added to the grey suspension at 60 °C over 1 h and the resulting suspension was refluxed under nitrogen at 100 °C for 1 h and further stirred at room temperature for 24 h. The green suspension was filtered and washed with DCM (100 mL). The organic layer was then washed with H₂O (3 × 60 mL), dried over MgSO₄ and co-evaporated with toluene *in vacuo*. The crude product was purified *via* column chromatography (silica, 5:1 petrol ether 60-80/Et₂O) to give benzyl 4-hexyl-3,5-dimethyl-1H-pyrrole-2-carboxylate **5** (15.2 g, 48.5 mmol, 25 %) as a light green solid. *R*_f 0.25 (5:1 petrol ether 60-80/Et₂O); ¹H NMR (300 MHz, CDCl₃): δ_H (ppm) 8.73 (1H, s, NH), 7.73-7.16 (5H, m, CH_{Ar}), 5.20 (2H, s, OCH₂CH_{Ar}), 2.25 (2H, t, *J* 7.4, CH₂C₅H₁₁), 2.20 (3H, s, CH₃), 2.08 (3H, s, CH₃), 1.32 (2H, m, CH₂CH₂C₄H₉), 1.20 (6H, m, C₂H₄C₃H₆CH₃), 0.80 (3H, t, *J* 6.6, C₅H₁₀CH₃). The analytical results are consistent with reported data.^{101, 190}

Synthesis of benzyl 5-(acetoxymethyl)-4-hexyl-3-methyl-1H-pyrrole-2-carboxylate

6

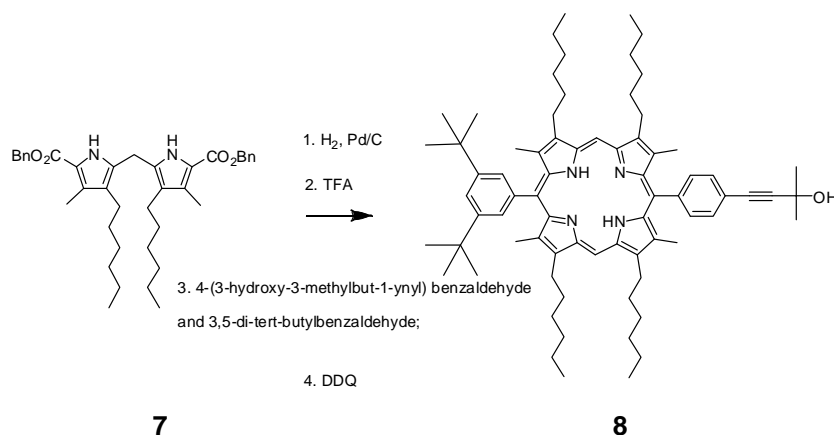


Benzyl 4-hexyl-3,5-dimethyl-1H-pyrrole-2-carboxylate **5** (20.3 g, 64.7 mmol) and lead (IV) acetate (28.7 g, 64.7 mmol) were added to acetic acid (113 mL) and the reaction mixture was refluxed under nitrogen at 140 °C for 1 h, followed by further stirring at room temperature for 2 h. The black reaction mixture was concentrated *in vacuo* to a volume of 50 mL. Cold MeOH (50 mL) was then added and the reaction mixture was cooled to -18 °C for 68 h. The precipitate formed was filtered, washed with MeOH (100 mL), dried *in vacuo* for 18 h and kept under inert atmosphere to prevent product turning pink to give benzyl 5-(acetoxymethyl)-4-hexyl-3-methyl-1H-pyrrole-2-carboxylate **6** (9.73 g, 26.2 mmol, 41 %) as a light grey solid. ¹H NMR (300 MHz, CDCl₃): δ_H (ppm) 8.98 (1H, br s, NH), 7.43-7.30 (5H, m, CH_{Ar}), 5.31 (2H, s, OCH₂), 5.01 (2H, s, OCH₂), 2.42 (2H, t, *J* 7.5, CH₂C₅H₁₁), 2.28 (3H, s, CH₃), 2.06 (3H, s, CH₃), 1.47-1.38 (2H, m, CH₂CH₂C₄H₉), 1.35-1.21 (6H, m, C₂H₄C₃H₆CH₃), 0.88 (3H, app t, *J* 6.3, C₅H₁₀CH₃). The analytical results are consistent with reported data.^{101, 190}

Synthesis of hexyl substituted dipyrromethane 7

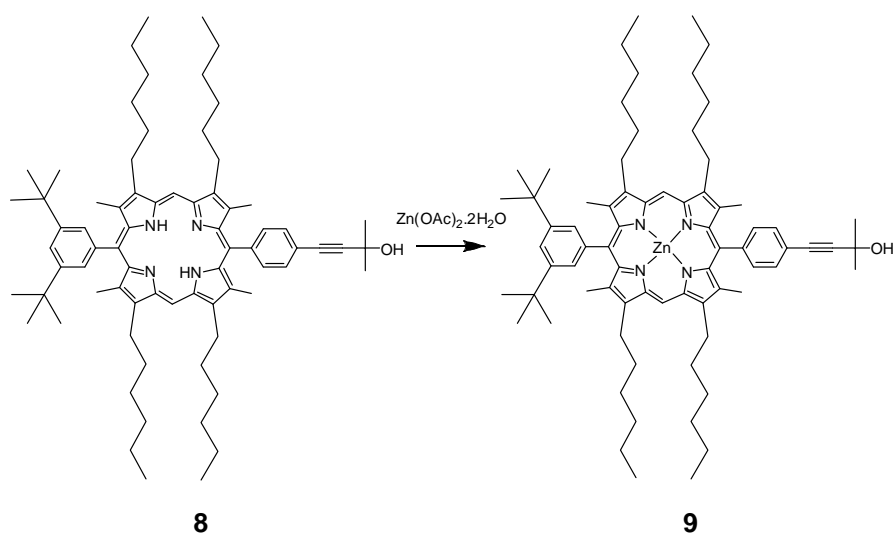
A suspension of benzyl 5-(acetoxymethyl)-4-hexyl-3-methyl-1H-pyrrole-2-carboxylate **6** (9.73 g, 26.2 mmol) in HCl (5.18 mL, 52.5 mmol) and MeOH (150 mL) was refluxed under nitrogen at 82 °C for 10 h. The reaction mixture was then concentrated *in vacuo*, and the residue dissolved in DCM (130 mL), washed with NaHCO₃ sat./H₂O (3 × 30 mL) to neutralise excess HCl, followed by concentration *in vacuo*. Hot MeOH (10 mL) was then added and the reaction mixture was kept at –18 °C for 5 days. Excess MeOH was removed carefully *via* pipette and the precipitate formed was dried *in vacuo* for 10 h. The crude product was purified *via* column chromatography (silica, 100:0.5 to 100:1 to 100:2 DCM/MeOH), followed by recrystallisation in hot MeOH (7 mL) to give benzyl 5,5-methylenebis(4-hexyl-3-methyl-1H-pyrrole-2-carboxylate) **7** (2.91 g, 4.77 mmol, 36 %) as a light yellow crystalline solid. *R_f* 0.51 (100:0.5 DCM/MeOH); ¹H NMR (300 MHz, CDCl₃): δ_H (ppm) 8.44 (2H, br s, NH), 7.40-7.28 (10H, m, CH_{Ar}), 5.26 (4H, s, CH₂CO₂), 3.82 (2H, s, CH₂-meso), 2.34 (4H, app t, *J* 7.4, CH₂C₅H₁₁), 2.28 (6H, s, CH₃), 1.39-1.25 (16H, m, CH₂C₄H₈CH₃), 0.88-0.84 (6H, m, C₅H₁₀CH₃). The analytical results are consistent with reported data.^{101, 190}

Synthesis of protected acetylene diphenyl porphyrin **8**



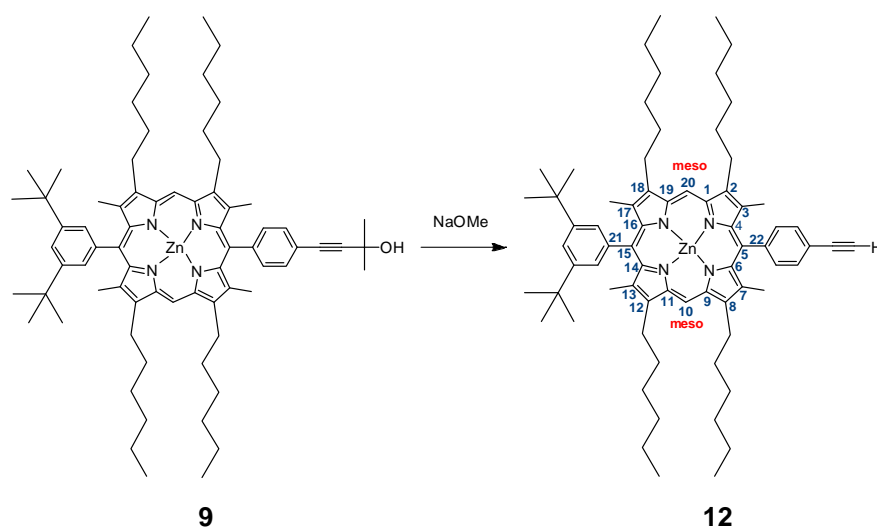
Pd/C (10 %) (119 mg, 0.112 mmol) was added to a solution of dipyrromethane **7** (1.50 g, 2.46 mmol) in triethylamine (1 mL), dry THF (19 mL) and dry MeOH (3 mL). The black suspension was purged with H₂ for 30 min and stirred under H₂ for 2 h. The reaction mixture was filtered *via* cannula under an inert atmosphere, and the residue washed with 5:1 deoxygenated mixture of dry THF/MeOH (12 mL), concentrated *in vacuo* to give a white foam. TLC at this point has R_f = 0 (1:1 DCM/EtOAc). The resulting deprotected dipyrromethane was dissolved in deoxygenated TFA (13 mL) at 0 °C, stirred in the dark for 10 min, and then at room temperature for 30 min. A solution of 4-(3-hydroxy-3-methylbut-1-ynyl) benzaldehyde (363 mg, 1.93 mmol) and 3,5-di-tert-butylbenzaldehyde (281 mg, 1.29 mmol) in dry MeOH (24 mL) were added to the reaction mixture *via* cannula at –10 °C, stirred in the dark under inert atmosphere for 30 min, followed by further stirring at room temperature for 2 h. DDQ (859 mg, 3.78 mmol) was then added and the reaction mixture was stirred for 15 h in the light. The reaction mixture was then diluted with DCM (20 mL) and neutralised with triethylamine (15 mL) in an ice bath. The organic layer was washed with water (3 × 30 mL), followed by drying over Na₂SO₄ and concentrated *in vacuo* to give the crude product **8** as a dark purple solid. At this stage, the crude product was used for the next synthesis step for ease of purification of the final porphyrin.^{101, 191, 192}

Synthesis of protected zinc acetylene diphenyl porphyrin **9**



Protected acetylene diphenyl porphyrin **8** (1.83 g, 1.74 mmol) and excess of zinc(II) acetate dihydrate (6.42 g, 29.2 mmol) were dissolved in MeOH (15 mL) and CHCl_3 (30 mL). The purple suspension was heated carefully with a heat gun for 3 min. The reaction mixture was then concentrated *in vacuo*, and the residue dissolved in DCM (100 mL), filtered and washed with cold DCM (100 mL), followed by concentration *in vacuo*. The crude product was purified *via* column chromatography (silica, 20:1 DCM/EtOAc) to give the protected zinc acetylene diphenyl porphyrin **9** (0.42 g, 0.38 mmol, 21 %) as a dark purple solid. R_f 0.78 (20:1 DCM/EtOAc); ^1H NMR (300 MHz, CDCl_3): δ_{H} (ppm) 10.2 (2H, s, CH-meso), 8.06 (2H, d, J 8.2, CH_{Ar}), 7.95 (2H, d, J 1.8, $\text{CH}_{\text{Ar}}\text{CC}(\text{CH}_3)_3$), 7.84-7.81 (2H, m, CH_{Ar}), 7.74 (1H, s, CH_{Ar}), 3.99 (4H, t, J 6.5, $\text{CH}_2\text{C}_5\text{H}_{11}$), 3.97 (4H, t, J 6.6, $\text{CH}_2\text{C}_5\text{H}_{11}$), 2.50 (6H, s, CH_3), 2.46 (6H, s, CH_3), 2.26-2.14 (8H, m, $\text{CH}_2\text{CH}_2\text{C}_4\text{H}_9$), 1.80 (6H, s, CCH_3OH), 1.76-1.66 (8H, m, $\text{C}_2\text{H}_4\text{CH}_2\text{C}_3\text{H}_7$), 1.53 (18H, s, $\text{C}(\text{CH}_3)_3$), 1.43-1.35 (16H, m, $\text{C}_3\text{H}_6\text{C}_2\text{H}_4\text{CH}_3$), 0.93 (12H, t, J 7.2, $\text{C}_5\text{H}_{10}\text{CH}_3$); LRMS (MALDI-ToF): calculated for $\text{C}_{73}\text{H}_{98}\text{N}_4\text{OZn}^+$ $[\text{M}]^+$ 1113.0, found 1114.0 $[\text{M}+\text{H}]^+$. The analytical results are consistent with reported data.^{192, 193}

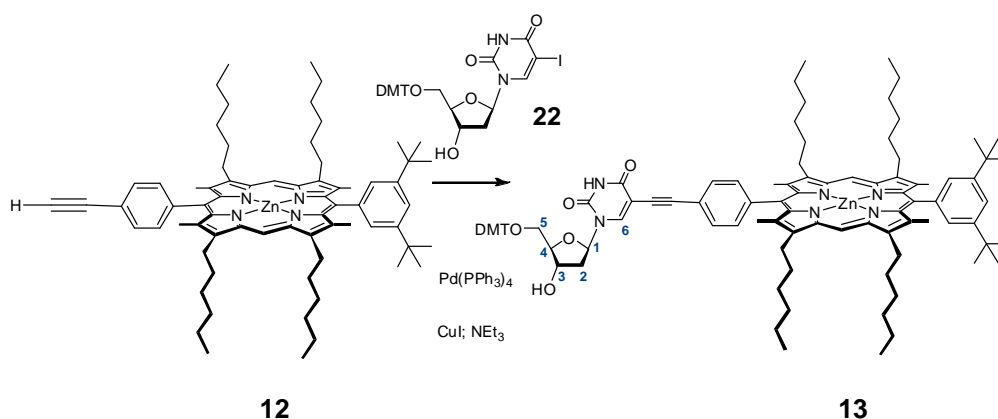
Synthesis of the deprotected zinc acetylene diphenyl porphyrin **12**



Sodium methoxide (675 mg, 12.5 mmol) was added to a solution of protected zinc acetylene diphenyl porphyrin **9** (418 mg, 0.38 mmol) in dry toluene (40 mL). The dark suspension was refluxed under nitrogen at 135 °C for 4 h then diluted with toluene (50 mL). The organic layer was washed with HCl 2 M (2 × 20 mL), brine (2 × 20 mL), followed by drying over Na₂SO₄ and concentration *in vacuo*. Further excess zinc(II) acetate dihydrate (198 mg, 0.90 mmol) in MeOH (5 mL) and CHCl₃ (5 mL) was added and the reaction mixture was heated carefully with a heat gun for 3 min, diluted with DCM (25 mL) and the reaction mixture was filtered, washed with DCM (100 mL) and concentrated *in vacuo*. The crude product was purified *via* column chromatography (silica, 98:2 DCM/MeOH) to give the deprotected zinc acetylene diphenyl porphyrin **12** (208 mg, 0.20 mmol, 53 %) as a dark purple solid. *R_f* 0.90 (98:2 DCM/MeOH). ¹H NMR (300 MHz, CDCl₃): δ_H (ppm) 10.2 (2H, s, CH-meso), 8.08 (2H, d, *J* 7.5, CH_{Ar}), 8.00 (2H, s, CH_{Ar}CC(CH₃)₃), 7.92 (2H, d, *J* 7.6, CH_{Ar}), 7.87 (1H, s, CH_{Ar}), 4.02 (4H, t, *J* 7.2, CH₂C₅H₁₁), 3.94 (4H, t, *J* 7.1, CH₂C₅H₁₁), 3.36 (1H, s, CH), 2.50 (6H, s, CH₃), 2.48 (6H, s, CH₃), 2.30-2.10 (8H, m, CH₂CH₂C₄H₉), 1.90-1.65 (8H, m, C₂H₄CH₂C₃H₇), 1.57 (18H, s, C(CH₃)₃), 1.44-1.30 (16H, m, C₃H₆C₂H₄CH₃), 0.96 (12H, t, *J* 6.8, C₅H₁₀CH₃); ¹³C {¹H} NMR (100 MHz, CDCl₃): δ_C (ppm) 148.1 (C(4), C(6)), 147.4 (C(14), C(16)), 146.6 (C(1), C(9)), 146.4 (C(11), C(19)), 143.7 (C(2), C(8)), 143.5 (C(12), C(18)), 138.8 (C(3), C(7)), 137.7 (C(13), C(17)), 136.4 (C(5)), 133.5 (2 × CH_{Ar}), 131.3 (2 × CH_{Ar}), 129.0 (C(15)),

128.2 ($2 \times \text{CH}_{\text{Ar}}\text{CC}(\text{CH}_3)_3$), 124.3 (CCCH), 121.9 (C(21)), 121.0 (CH_{Ar}), 97.8 ($2 \times \text{CH}$ -meso), 84.3 (CCH), 78.0 (CH), 33.5 ($4 \times \text{CH}_2\text{C}_4\text{H}_9$), 32.2 ($2 \times \text{C}(\text{CH}_3)_3$), 31.9, 29.9 ($4 \times \text{C}_3\text{H}_6\text{C}_2\text{H}_4\text{CH}_3$), 30.2 ($4 \times \text{C}_2\text{H}_4\text{CH}_2\text{C}_3\text{H}_7$), 27.0 ($2 \times \text{CH}_2\text{C}_5\text{H}_{11}$), 26.8 ($2 \times \text{CH}_2\text{C}_5\text{H}_{11}$), 15.7 ($2 \times \text{CH}_3$), 15.1 ($2 \times \text{CH}_3$), 14.3 ($4 \times \text{C}_5\text{H}_{10}\text{CH}_3$); LRMS (MALDI-ToF): calculated for $\text{C}_{70}\text{H}_{92}\text{N}_4\text{Zn}^+$ $[\text{M}]^+$ 1054.7, found 1055.0 $[\text{M}+\text{H}]^+$. The analytical results are consistent with reported data.^{192, 193}

Synthesis of the 5'-O-DMT-dU^{ZnDPP} **13**

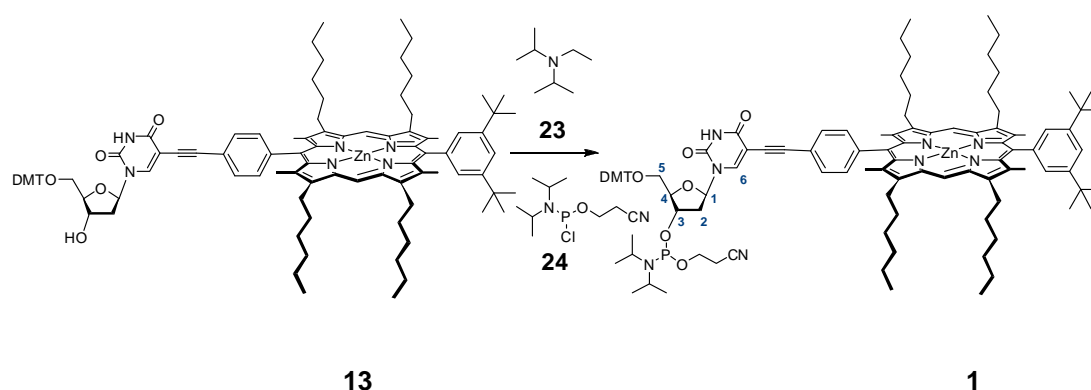


Copper iodide (7.20 mg, 38.0 μmol) was added in the dark and under inert atmosphere to a deoxygenated suspension of 5'-O-DMT-iodouracile **22** (93.3 mg, 142 μmol) in dry DMF (1 mL) with molecular sieves (4 \AA). The creamy suspension was stirred and deoxygenated by purging with N₂ for 15 min until all the copper iodide was dissolved. Triethylamine (66.1 μL , 474 μmol) was then added and the reaction mixture was stirred and deoxygenated for 10 min. A solution of zinc acetylene diphenyl porphyrin **12** (50.0 mg, 47.4 μmol) in dry DMF (2 mL) was added to the reaction mixture *via* cannula and washed with DMF (1 mL).

Tetrakis(triphenylphosphine)palladium (21.9 mg, 19.0 μmol) was then added and the reaction mixture was stirred at room temperature under inert atmosphere, and in the dark for 45 h. The purple solution was diluted with EtOAc (80 mL), filtered to remove molecular sieves and the organic layer was washed with a solution of 1:1 H₂O/brine (6 \times 30 mL), followed by drying over Na₂SO₄ and concentration *in vacuo*. The crude product was purified *via* column chromatography (silica, 100:0.5 to 100:1 DCM/MeOH) to remove the zinc porphyrin **12** and further purified *via* column chromatography (silica, 100:3 to 100:4 DCM/MeOH) to separate the desired porphyrin from 5'-O-DMT-iodouracile **22** to give 5'-O-DMT-dU^{ZnDPP} **13** (35.0 mg, 22.1 μmol , 47 %) as a dark purple solid. Occasionally, a lipophilic Sephadex size exclusion column chromatography (25-100 μm beads gel, DCM/MeOH 1:1) was required to purify the product from Pd(PPh₃)₄. R_f 0.26 (100:4 DCM/MeOH); ¹H NMR (300 MHz, CDCl₃): δ_{H} (ppm) 10.1 (2H, s, CH-meso), 8.31 (1H, br s, NH), 8.19 (1H, s, C(6)H), 7.93 (2H, d, *J* 1.8, CH_{Ar}C(CH₃)₃), 7.88 (2H, d, *J* 8.1, CH_{Ar}), 7.81 (1H, app t, *J* 1.7,

$CH_{Ar}C(CH_3)_3$, 7.49 (2H, app d, J 7.5, CH_{Ar}), 7.42-7.31 (5H, m, CH_{Ar}), 7.26 (4H, s, $CH_{Ar}CC_6H_5$), 6.88 (4H, d, J 7.7, $CH_{Ar}COCH_3$), 6.27 (1H, m, C(1) H), 5.65 (1H, s, C(3) OH), 4.53 (1H, m, C(3) H), 4.03 (1H, m, C(4) H), 3.92-3.87 (8H, m, $CH_2C_5H_{11}$), 3.72-3.71 (6H, s, OCH_3), 3.66 (1H, m, C(5) H), 3.47 (1H, m, C(5) H), 2.36 (6H, s, CH_3), 2.33 (6H, s, CH_3), 2.15-2.05 (8H, m, $CH_2CH_2C_4H_9$), 1.89 (2H, m, C(2) H_2), 1.69-1.64 (8H, m, $C_2H_4CH_2C_3H_7$), 1.43 (18H, s, C(CH_3) $_3$), 1.34-1.27 (16H, m, $C_3H_6C_2H_4CH_3$), 0.84 (12H, t, J 7.2, $C_5H_{10}CH_3$); LRMS (MALDI-ToF): calculated for $C_{100}H_{120}N_6O_7Zn^+$ $[M]^+$ 1583.5, found 1584.4 $[M+H]^+$. The analytical results are consistent with reported data.^{90, 192,}

Synthesis of 5'-O-DMT-dU^{ZnDPP} phosphoramidite **1**



5'-O-DMT-dU^{ZnDPP} **13** (64.3 mg, 40.7 μmol) was co-evaporated with dry pyridine (3×2 mL) and dried *in vacuo* overnight. Dry, deoxygenated DCM (2 mL) and molecular sieves (4 Å) were added. The reaction mixture was stirred and deoxygenated by purging with N₂ for 5 min. Deoxygenated diisopropylethylamine **23** (28.3 μL , 163 μmol) was added *via* syringe and the reaction mixture was stirred for 10 min, followed by slow addition of cyanoethyl diisopropylchlorophosphoramidite **24** (27.2 μL , 122 μmol). The reaction mixture was then stirred in the dark, under inert atmosphere for 2.5 h at room temperature and concentrated *in vacuo* to halve the volume. The crude product was loaded onto a dry, deoxygenated flash column chromatography (silica, PPh₃, 1:1 DCM/EtOAc + 0.5 % Et₃N) *via* cannula and purified to give 5'-O-DMT-dU^{ZnDPP} phosphoramidite **1** (35.0 mg, 19.6 μmol , 48 %) as a purple solid. R_f 0.9 (1:1 DCM/EtOAc); ¹H NMR (400 MHz, CDCl₃): δ_H (ppm) 10.2 (2H, s, CH-meso), 8.46 (0.5, s, NH), 8.42 (0.5H, s, C(6)H), 7.92 (2H, d, J 1.8, CH_{Ar}C(CH₃)₃), 7.88-7.84 (2H, m, CH_{Ar}), 7.80 (1H, t, J 1.8, CH_{Ar}CC(CH₃)₃), 7.75-7.70 (2H, m, CH_{Ar}), 7.56-7.52 (3H, m, PPh₃), 7.47-7.43 (5H, m, CH_{Ar}CO), 7.38-7.33 (4H, m, CH_{Ar}CC₆H₅), 6.92-6.88 (4H, m, CH_{Ar}COCH₃), 6.46-6.40 (1H, m, C(1)H), 4.71-4.67 (1H, m, C(3)H), 4.32-4.31 (1H, m, C(4)H), 3.96 (8H, app t, J 7.0, CH₂C₅H₁₀), 3.79 (3H, s, OCH₃), 3.78 (3H, s, OCH₃), 3.68-3.57 (4H, m, OCH₂CH₂CN), 3.38-3.36 (1H, m, C(5)H), 3.35-3.34 (1H, m, C(5)H), 2.68-2.65 (2H, m, CH(CH₃)₂), 2.49-2.48 (1H, m, C(2)H), 2.46 (1H, m, C(2)H), 2.43 (6H, s, CH₃), 2.40-2.38 (6H, m, CH₃), 2.22-2.13 (8H, m, CH₂CH₂C₄H₉), 1.75-1.70 (8H, m, C₂H₄CH₂C₃H₇), 1.50 (18H, s, C(CH₃)₃), 1.40-1.31 (16H, m, C₃H₆C₂H₄CH₃), 1.26 (12H, br s, C(CH₃)₂), 0.91 (12H, J 7.2, C₅H₁₀CH₃); ³¹P {¹H} NMR (162 MHz, CDCl₃):

δ_p (ppm) 149.8, 149.3; LRMS (MALDI-ToF): calculated for $C_{109}H_{137}N_8O_8PZn^+$ $[M]^+$ 1783.7, found 1795.5 $[M+O]^+$. The analytical results are consistent with reported data but the difference between calculated MS and obtained MS is due to manual calibration of the instrument.^{32, 90, 195}

Synthesis of modified oligonucleotides

5'-CAT CGT AGT TTT **PAP** TTT TCC GTA CTC-3' **ODN1**

5'-CAT CGT AGT **APA PAP APA** TCC GTA CTC -3' **ODN2**

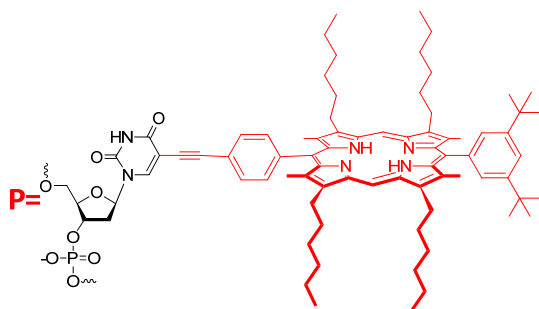
5'-GAG TAC **GGP APA** CCG TAC TC-3' **ODN3**

5'-TAC GAT TCG **TPT** CTA GCT AGC-3' **ODN4**

5'-GAG TAC GGA AAA **APA** AAA ACT ACG ATC-3' **ODN13**

5'-GAT CGT AGT TTT **PAP** TTT TCC GTA CTC-3' **ODN14**

5'-GCT AGC TAG **PPP** CGA ATC GTA-3' **ODN15**

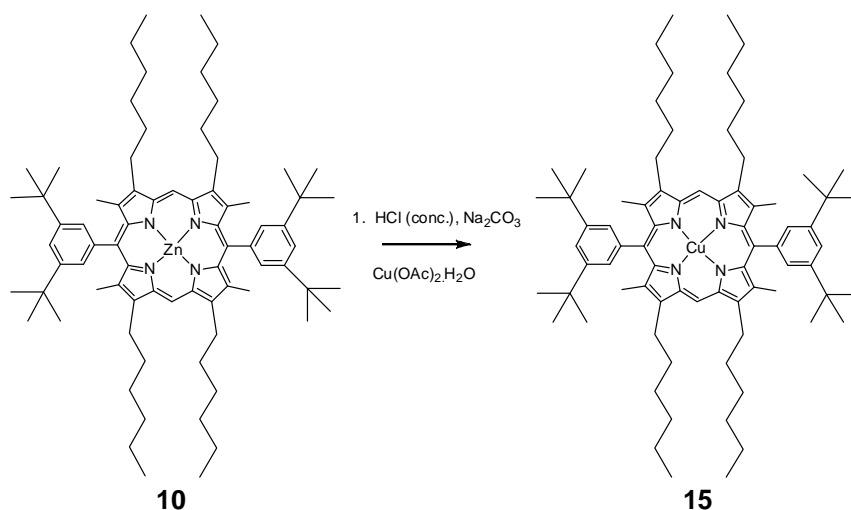


5'-O-DMT-dU^{ZnDPP} phosphoramidite **1** (31.0 mg, 17.0 μmol) was dissolved in dry and deoxygenated DCM (0.7 mL) and MeCN (1.0 mL) to make up a 10 mM solution.

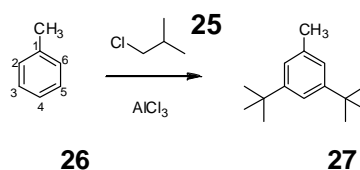
Incorporation of 5'-O-DMT-dU^{ZnDPP} phosphoramidite **1** in DNA sequences was done *via* solid phase synthesis on a 0.2 μM scale with 10 min set for each coupling of **1** to **ODN1**, **ODN2**, **ODN3** on an ABI 394 DNA synthesiser and 5 min for each coupling of **1** to **ODN4**, **ODN13**, **ODN14**, **ODN15** on an Expedite DNA synthesiser. A solution of FDMT-N²-iBu-dN CEP (N= C, G, T) (129 mg, 100 μmol) in MeCN (1.2 mL) was then used to incorporate the corresponding fluorous tag into all oligonucleotides with 6 min coupling time for **ODN1**, **ODN2**, **ODN3** on an ABI 394 DNA synthesiser and 5 min for **ODN4**, **ODN13**, **ODN14**, **ODN15** on an Expedite DNA synthesiser.

Aqueous ammonia solution (33 %) (2 mL) was then added to each modified DNA strand and the sequences were stirred in a thermomixer at 40 °C overnight to cleave modified DNA from the solid beads and to deprotect the bases and phosphate groups from amides, amidines and 2-cyanoethyl group, respectively.

Each modified oligonucleotide sequence was filtered to remove solid beads, washed with water (200 μL) and concentrated *in vacuo*. The crude products were finally purified *via* fluorous affinity column chromatography (see **Section 5.3.3.1**) to give the porphyrin modified oligonucleotides as brown solids. UV-vis (H_2O , $c = 1 \times 10^{-6} \text{ M}$): λ_{max} (log ϵ) **ODN1** 264 (5.38), 407 (5.33) nm; **ODN2** 260 (5.39), 370 (5.26), 420 (5.26) nm; **ODN3** 261 (5.27), 408 (4.97) nm, **ODN4** 262 (5.26), 408 (4.12) nm; **ODN13** 257 (5.49), 412 (4.31), 440 (4.15) nm; **ODN14** 262 (5.39), 412 (4.45), 437 (4.66) nm.

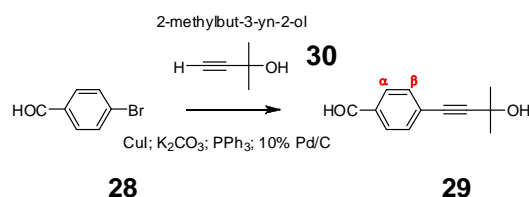
Synthesis of copper(II) di-tert-butyl diphenyl porphyrin **15**^{196, 197}


Hydrochloric acid (20 mL, 203 mmol, 10.1 M) was added to a solution of zinc di-tert-butyl diphenyl porphyrin **10** (52.0 mg, 45.5 μ mol), which is a side product separated from synthesis in DCM (50 mL).¹⁹³ A solution of sodium carbonate (50 mL, 100 mmol, 2.0 M) was added to the green reaction mixture and the organic layer was washed with water (3 \times 30 mL) until the reaction mixtures changed to pink colour. The organic layer was dried over Na₂SO₄ and concentrated *in vacuo* to give the intermediate demetallated di-tert-butyl diphenyl porphyrin. A suspension of copper(II) acetate monohydrate (247 mg, 1.36 mmol) in acetic acid (10 mL) was added to a solution of the demetallated di-tert-butyl diphenyl porphyrin intermediate (49.0 mg, 45.4 μ mol). The reaction mixture was heated carefully with a heat gun for 3 min then diluted with DCM (30 mL). The organic layer was washed with water (6 \times 50 mL), followed by drying over Na₂SO₄, filtered through cotton wool and concentrated *in vacuo* to give copper(II) di-tert-butyl diphenyl porphyrin **15** (67.0 mg, quantitative) as a purple solid. R_f 0.95 (DCM); UV-vis (DCM, $c = 5 \times 10^{-6}$ M): $\lambda_{\max}(\log \epsilon)$ 407 (5.27), 529 (3.88), 566 (3.78) nm; LRMS (MALDI-ToF): calculated for C₇₆H₁₀₈N₄Cu⁺ [M]⁺ 1139.8, found 1139.8; isotopic pattern 1139.8/1140.8/1141.8/1142.8/ 1143.8/1144.8 [M]⁺, 21:16:15:9:4:1; EPR (X-band simulated, 9.43 GHz): $g_x = g_y = 2.0445$, $g_z = 2.183$, $A_x = A_y = 21.3$ mT, $A_z = 1.95$ mT.

Synthesis of 3,5-di-tert-butyltoluene 27

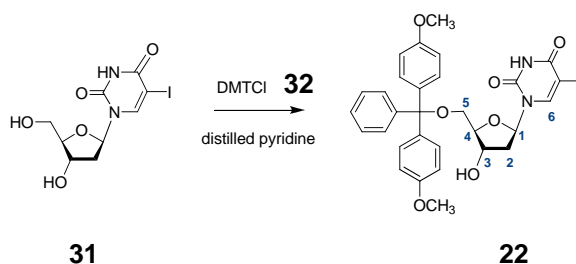
Aluminium trichloride (2.00 g, 15.0 mmol) was added over 5 h to a rapidly stirred solution of 1-chloro-2-methylpropane **25** (50.6 mL, 465 mmol) in dry toluene **26** (24.0 mL, 225 mmol) under an inert atmosphere and the brown suspension was stirred for a further 15 h. Water (40 mL) was then added and the green solution was extracted into diethyl ether (2 × 30 mL), followed by concentration *in vacuo*. The crude product was purified *via* Vigreux distillation under reduced pressure. Fractions of distillate were collected and stored at 4 °C for 64 h. The white crystalline product formed was filtered to give 3,5-di-tert-butyltoluene **27** (9.89 g, 48.4 mmol, 22 %). R_f 0.83 (petrol ether 40-60); ¹H NMR (300 MHz, CDCl₃): δ_H (ppm) 7.16 (1H, s, C(4)H), 6.95 (2H, s, CH), 2.27 (3H, s, CH₃), 1.24 (18H, s, C(CH₃)₃). The analytical results are consistent with reported data.¹⁹⁰

Synthesis of 4-(3-Hydroxy-3-methyl-but-1-ynyl)benzaldehyde **29**



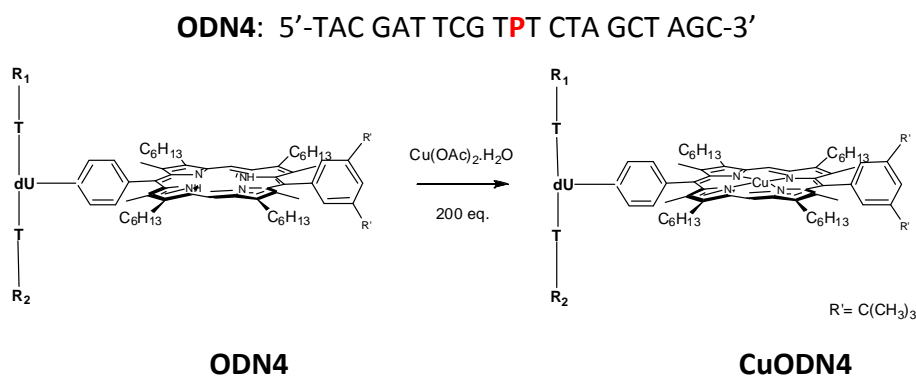
Copper iodide (153 mg, 0.80 mmol), potassium carbonate (6.86 g, 49.6 mmol), triphenyl phosphine (426 mg, 1.62 mmol), Pd/C (10 %) (420 mg, 0.40 mmol) and 4-bromobenzaldehyde **28** (2.00 g, 10.8 mmol) were added to a solution of 1:1 DME/H₂O (45 mL). The black suspension was deoxygenated by purging with N₂ and stirred at room temperature for 30 min. 2-methyl-3-butyn-2-ol **30** (4.90 mL, 50.6 mmol) was then added *via* syringe and the reaction mixture was refluxed under nitrogen at 80 °C for 5 h. The reaction mixture was filtered through Celite[®], washed with EtOAc (100 mL) and diluted in EtOAc (100 mL). The combined organic extracts were washed with a mixture of H₂O/K₂CO₃ (30 mL) and water (2 × 30 mL), followed by drying over MgSO₄ and concentration *in vacuo*. The crude product was purified *via* column chromatography (alumina, DCM) to give 4-(3-Hydroxy-3-methyl-but-1-ynyl)benzaldehyde **29** (1.28 g, 6.81 mmol, 63 %) as a brown oil. R_f 0.21 (3:1 Hexane/EtOAc); ¹H NMR (300 MHz, CDCl₃): δ_H (ppm)= 10.0 (1H, s, CHO), 7.82 (2H, d, *J* 8.2, CH_{Ar}-α), 7.55 (2H, d, *J* 8.2, CH_{Ar}-β), 1.96 (1H, br s, OH), 1.63 (6H, s, CH₃). The analytical results are consistent with reported data.^{190, 198}

Synthesis of 5'-O-(4,4'-dimethoxytrityl)-5-iodo-2'-deoxyuridine **22**



5-iodo-2'-deoxyuridine **31** (2.00 g, 5.65 mmol) was co-evaporated with distilled pyridine (3 × 3 mL) and dissolved in distilled pyridine (15 mL) to give a light cream solution. 4,4'-dimethoxytrityl chloride **32** (2.01 g, 5.93 mmol) was then added over 2.5 h in five portions and the reaction mixture was left to stir under inert atmosphere for 1.5 h, followed by quenching with 1:1 mixture of H₂O/MeOH (2 mL) and further stirring for 10 min. The light yellow solution was concentrated *in vacuo*, followed by co-evaporation with 1:20 mixture of MeOH/toluene (21 mL) then dissolved in DCM (40 mL). The organic layer was washed with KCl sat./H₂O (3 × 50 mL), dried over NaSO₄ and concentrated *in vacuo*. The crude product was purified *via* column chromatography (silica, 1:1 EtOAc/hexane + 0.5 % Et₃N → 6:4 EtOAc/hexane + 0.5 % Et₃N → 8:2 EtOAc/hexane + 0.5 % Et₃N → 9:1 EtOAc/MeOH + 0.5 % Et₃N) to give 5'-O-(4,4'-dimethoxytrityl)-5-iodo-2'-deoxyuridine **22** (1.78 g, 2.71 mmol, 48 %) as a creamy white foam. R_f 0.54 (95:5 DCM/MeOH + 0.3 % Et₃N); ¹H NMR (300 MHz, CDCl₃): δ_H (ppm) 9.81 (1H, br s, NH), 8.06 (1H, s, C(6)H), 7.33 (2H, d, *J* 7.4, CHCCO), 7.26-7.23 (4H, m, CH_{Ar}CC₆H₅), 7.21-7.18 (2H, m, CH₂CHCHCO), 7.14-7.10 (1H, m, CH_{Ar}CHCHCCO), 6.76 (4H, app d, *J* 9.0, CH_{Ar}COCH₃), 6.24 (1H, app t, *J* 5.7, C(1)H), 4.47-4.45 (1H, m, C(3)H), 4.04 (1H, app q, *J* 2.3, C(4)H), 3.34-3.24 (2H, tdt, *J* 3.4, 3.8, C(5)H), 2.48-2.41 (1H, ddd, *J* 1.9, 5.7, 17.3, C(2)H), 2.21-2.11 (1H, m, C(2)H), 1.82 (1H, br s, C(3)OH); LRMS (MALDI-ToF): calculated for C₃₀H₂₉IN₂O₇ [M]⁺ 656.1, found 679.4 [M+Na]⁺. The analytical results are consistent with reported data.^{199, 200}

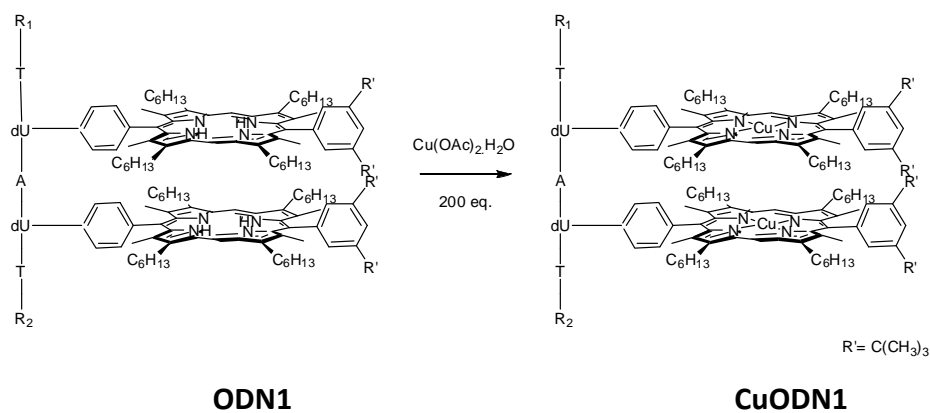
Synthesis of copper(II) diphenyl porphyrin oligonucleotide ODN4



$Cu(OAc)_2 \cdot H_2O$ (50 μ L, 4 mM, 200 nmol, 200 eq.) was added to **ODN4** (100 μ L, 10 μ M, 1 nmol **DPP**, 1 eq.) and immediately deoxygenated by purging with N_2 for 10 seconds then stirred vigorously on a thermomixer at 85 $^{\circ}C$ for 5 min. The reaction mixture was then left to cool to room temperature for 5 min. EDTA pH 8.0 (50 μ L, 400 mM, 20 μ mol, 20000 eq.) was then added to quench excess $Cu(OAc)_2$, followed by addition of buffer (100 μ L, 100 mM NaCl, 50 mM KH_2PO_4 , pH 7.0). 6 batches of this reaction were performed simultaneously, combined, followed by addition of water (200 μ L) and the reaction mixture was immediately purified *via* Glen-Pak cartridge (see **Chapter 2, Section 2.3.2**) to give **CuODN4** (5410 nmol, 90 %) as a dark purple solid. UV-vis (H_2O , $c = 5 \times 10^{-6}$ M): λ_{max} (log ϵ) 261 (5.28), 410 (4.17) nm; Emission (H_2O , $c = 5 \times 10^{-6}$ M): λ_{ex} 410 nm, λ_{em} (rel int) 632 (1), 693 (0.96) nm.

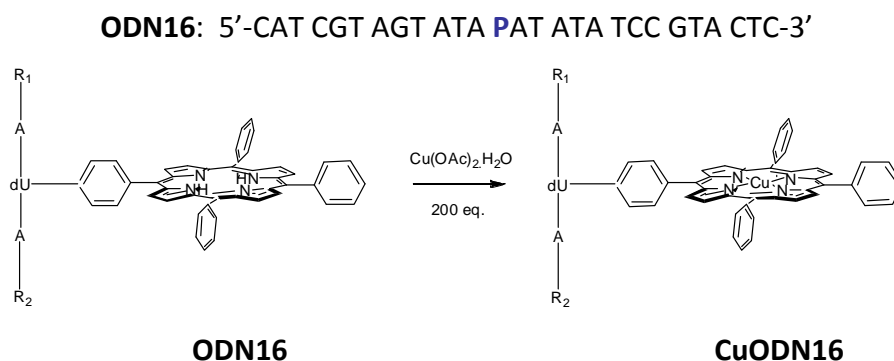
Synthesis of copper(II) diphenyl porphyrin oligonucleotide ODN1

ODN1: 5'-CAT CGT AGT TTT **PAP** TTT TCC GTA CTC-3'



Cu(OAc)₂.H₂O (25 μL, 16 mM, 400 nmol, 200 eq.) was added to **ODN1** (100 μL, 10 μM, 2 nmol **DPP**, 1 eq.) and immediately deoxygenated by purging with N₂ for 10 seconds then stirred vigorously on a thermomixer and at 85 °C for 5 min. The reaction mixture was then left to cool to room temperature for 5 min. EDTA pH 8.0 (100 μL, 400 mM, 40 μmol, 20000 eq.) was then added to quench excess Cu(OAc)₂, followed by buffer (100 μL, 100 mM NaCl, 50 mM KH₂PO₄, pH 7.0). 6 batches of this reaction were performed simultaneously, combined, followed by addition of water (200 μL) and the reaction mixture was purified *via* Glen-Pak cartridge to give **CuODN1** (5550 nmol, 93 %) as a dark purple solid. UV-vis (H₂O, c= 5×10⁻⁶ M): λ_{max} (log ε) 265 (5.38), 409 (5.37) nm; Emission (H₂O, c= 5×10⁻⁶ M): λ_{ex} 409 nm, λ_{em} (rel int) 637 (1), 695 (0.75) nm.

Synthesis of copper(II) tetraphenyl porphyrin oligonucleotide **ODN16**



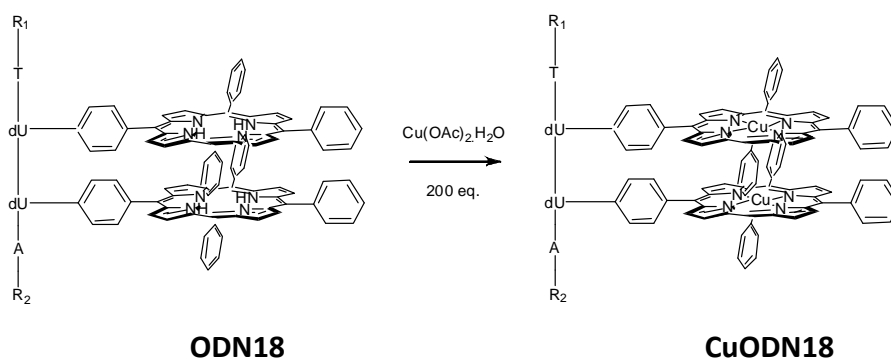
$\text{Cu}(\text{OAc})_2 \cdot \text{H}_2\text{O}$ (50 μL , 4 mM, 200 nmol, 200 eq.) was added to **ODN16** (100 μL , 10 μM , 1 nmol **TPP**, 1 eq.) and immediately deoxygenated by purging with N_2 for 10 seconds then stirred vigorously on a thermomixer at 85 $^\circ\text{C}$ for 5 min. The reaction mixture was then left to cool to room temperature for 5 min. EDTA pH 8.0 (50 μL , 400 mM, 20 μmol , 20000 eq.) was then added to quench excess $\text{Cu}(\text{OAc})_2$, followed by addition of buffer (100 μL , 100 mM NaCl, 50 mM KH_2PO_4 , pH 7.0). 6 batches of this reaction were performed simultaneously, combined, followed by addition of water (200 μL) and the reaction mixture was immediately purified *via* Glen-Pak cartridge to give **CuODN16** (4670 nmol, 78 %) as a dark purple solid.

UV-vis (H_2O , $c = 5 \times 10^{-6}$ M): λ_{max} (log ϵ) 260 (5.46), 422 (4.81) nm;

Emission (H_2O , $c = 5 \times 10^{-6}$ M): λ_{ex} 422 nm, λ_{em} (rel int) 651 (1), 713 (0.32) nm.

Synthesis of copper(II) tetraphenyl porphyrin oligonucleotide ODN18

ODN18: 5'-CAT CGT AGT ATP PAT ATA TCC GTA CTC-3'

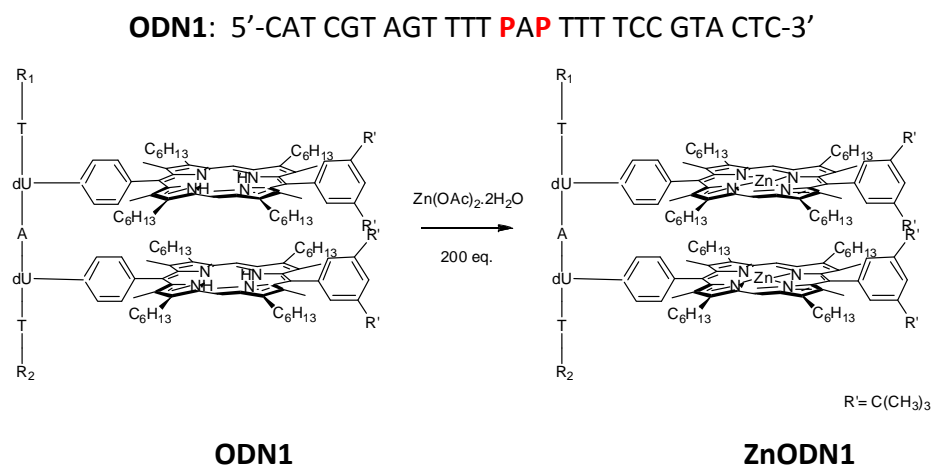


Cu(OAc)₂.H₂O (25 μL, 16 mM, 400 nmol, 200 eq.) was added to **ODN18** (100 μL, 10 μM, 2 nmol **TPP**, 1 eq.) and immediately deoxygenated by purging with N₂ for 10 seconds then stirred vigorously on a thermomixer at 85 °C for 5 min. The reaction mixture was left to cool to room temperature for 5 min. EDTA pH 8.0 (100 μL, 400 mM, 40 μmol, 20000 eq.) was then added to quench excess Cu(OAc)₂, followed by addition of buffer (100 μL, 100 mM NaCl, 50 mM KH₂PO₄, pH 7.0). 6 batches of this reaction were performed simultaneously, combined, followed by addition of water (200 μL) and the reaction mixture was immediately purified *via* Glen-Pak cartridge to give **CuODN18** (4310 nmol, 72 %) as a dark purple solid.

UV-vis (H₂O, c= 5×10⁻⁶ M): λ_{max} (log ε) 260 (5.49), 423 (5.28) nm;

Emission (H₂O, c= 5×10⁻⁶ M): λ_{ex} 423 nm, λ_{em} (rel int) 654 (1), 716 (0.28) nm.

Synthesis of zinc(II) diphenyl porphyrin oligonucleotide ODN1



Zn(OAc)₂·2H₂O (100 μL, 20 mM, 2000 nmol, 1000 eq.) was added to **ODN1** (200 μL, 5 μM, 2 nmol **DPP**, 1 eq.) and stirred on a thermomixer at 65 °C for 1 min. EDTA pH 8.0 (100 μL, 20 mM, 2000 nmol, 1000 eq.) was then added to quench excess Zn(OAc)₂, followed by addition of buffer (100 mM NaCl, 50 mM KH₂PO₄, pH 7.0) (50 μL) and water (50 μL). The crude product was purified *via* Nap-5 column (see **Chapter 2, Section 2.3.1**) to give **ZnODN1** (750 nmol, 75 %) as a brown solid. UV-vis (H₂O, c = 0.75×10⁻⁶ M): λ_{max} (log ε) 267 (5.38), 414 (5.36) nm; Emission (H₂O, c = 0.75×10⁻⁶ M): λ_{ex} 413 nm, λ_{em} (rel int) 587 (1), 636 (5.41), 654 (5.69), 698 (4.89) nm.

REFERENCES

1. Watson, J. D.; Crick, F. H. C. *Nature* **1953**, *171*, 737-738.
2. Wilkins, M. H. F.; Stokes, A. R.; Wilson, H. R. *Nature* **1953**, *171*, 738-740.
3. Franklin, R. E.; Gosling, R. G. *Nature* **1953**, *171*, 740-741.
4. Clayden, J.; Greeves, N.; Warren, S.; Wothers, P. *Organic chemistry*, Oxford University Press: New York **2001**, p 1347-1351.
5. Kool, E. T.; Morales, J. C.; Guckian, K. M. *Angew. Chem. Int. Ed.* **2000**, *39* (6), 990-1009.
6. Sinden, R. R. *DNA structure and function*, Academic Press: London **1994**, p 179.
7. Blackburn, G. M.; Gait, M. J. *Nucleic acids in chemistry and biology*, Oxford University Press: New York **1990**, p 6-10.
8. Blackburn, G. M.; Gait, M. J.; Loakes, D.; Williams, D. M. *Nucleic acids in chemistry and biology*, 3rd ed., RSC Publishing: Cambridge **2006**, p 24-33.
9. Wheeler, R. *University of Oxford*, presentation of figures with kind permission.
10. Corbett, S. A.; Foty, R. A. *Cell structure, function, and genetics*. In *Surgery basic science and clinical evidence*, 2nd ed.; Norton, J. A.; Barie, P. S.; Bollinger, R. R.; Chang, A. E.; Lowry, S. F.; Mulvihill, S. J.; Pass, H. I.; Thompson, R. W. Eds, Springer: New York **2008**, p 40.
11. Flavell, A. J.; Barr, G. C. *DNA sequence information and transmission*. In *Nucleic acids in chemistry and biology*, Blackburn, G. M.; Gait, M. J. Eds, Oxford University Press: New York **1990**, p 192-193.
12. Beaucage, S. L.; Iyer, R. P. *Tetrahedron* **1992**, *48* (12), 2223-2311.
13. Blackburn, G. M.; Gait, M. J.; Loakes, D.; Williams, D. M. *Nucleic acids in chemistry and biology*, 3rd ed., RSC Publishing: Cambridge **2006**, p 144-153.
14. Septak, M. *Nucleic Acids Res.* **1996**, *24* (15), 3053-3058.
15. Gait, M. J. *Oligonucleotide synthesis: A practical approach*, IRL Press: Oxford **1984**, p 8-14.
16. *WHO model list of essential medicines* **2005**.

17. Mokhir, A. A.; Tetzlaff, C. N.; Herzberger, S.; Mosbacher, A.; Richert, C. J. *Comb. Chem.* **2001**, *3* (4), 374–386.
18. Balaz, M.; Li, B. C.; Steinkruger, J. D.; Ellestad, G. A.; Nakanishi, K.; Berova, N. *Org. Biomol. Chem.* **2006**, *4* (10), 1865-1867.
19. Mukae, M.; Ihara, T.; Tabara, M.; Jyo, A. *Org. Biomol. Chem.* **2009**, *7* (7), 1349-1354.
20. Bandy, T. J.; Brewer, A.; Burns, J. R.; Marth, G.; Nguyen, T.; Stulz, E. *Chem. Soc. Rev.* **2011**, *40* (1), 138-148.
21. Yang, H.; Rys, A. Z.; MacLaughlin, C. K.; Sleiman, H. F. *Angew. Chem. Int. Ed.* **2009**, *48* (52), 9919-9923.
22. Brotschi, C.; Mathis, G.; Leumann, C. J. *Chem. Eur. J.* **2005**, *11* (6), 1911-1923.
23. Kool, E. T. *Acc. Chem. Res.* **2002**, *35* (11), 936–943.
24. Tanaka, K.; Clever, G. H.; Takezawa, Y.; Yamada, Y.; Kaul, C.; Shionoya, M.; Carell, T. *Nature Nanotechnology* **2006**, *1* (3), 190-194.
25. Takezawa, Y.; Maeda, W.; Tanaka, K.; Shionoya, M. *Angew. Chem. Int. Ed.* **2009**, *48* (6), 1081-1084.
26. Malinovskii, V. L.; Samain, F.; Häner, R. *Angew. Chem. Int. Ed.* **2007**, *46* (24), 4464-4467.
27. Sonogashira, K.; Tohda, Y.; Hagihara, N. *Tetrahedron Lett.* **1975**, *16* (50), 4467-4470.
28. Vrabel, M.; Horakova, P.; Pivonkova, H.; Kalachova, L.; Cernocka, H.; Cahova, H.; Pohl, R.; Sebest, P.; Havran, L.; Hocek, M.; Fojta, M. *Chem. Eur. J.* **2009**, *15* (5), 1144-1154.
29. Tanaka, K.; Tengeiji, A.; Kato, T.; Toyama, N.; Shiro, M.; Shionoya, M. *J. Am. Chem. Soc.* **2002**, *124* (42), 12494-12498.
30. Jager, S.; Rasched, G.; Kornreich-Leshem, H.; Engeser, M.; Thum, O.; Famulok, M. *J. Am. Chem. Soc.* **2005**, *127* (43), 15071-15082.
31. Barbaric, J.; Wagenknecht, H.-A. *Org. Biomol. Chem.* **2006**, *4* (11), 2088-2090.
32. Bouamaied, I.; Nguyen, T.; Rühl, T.; Stulz, E. *Org. Biomol. Chem.* **2008**, *6* (21), 3888-3891.
33. Datta, B.; Schuster, G. B. *J. Am. Chem. Soc.* **2008**, *130* (10), 2965-2973.

-
34. Fendt, L. A.; Bouamaied, I.; Thöni, S.; Amiot, N.; Stulz, E. *J. Am. Chem. Soc.* **2007**, *129* (49), 15319-15329.
35. Nguyen, T.; Brewer, A.; Stulz, E. *Angew. Chem. Int. Ed.* **2009**, *48* (11), 1974-1977.
36. Mayer-Enthart, E.; Wagenknecht, H.-A. *Angew. Chem. Int. Ed.* **2006**, *45* (20), 3372-3375.
37. Feynman, R. P. *Miniaturization*, Reinhold: New York, **1961**.
38. Rao, C. N. R.; Cheetham, A. K. *Materials science at the nanoscale*. In *Nanomaterials handbook*, Gogotsi, Y. Ed, CRC Press: Boca Raton **2006**, p 1-12.
39. Di Ventra, M.; Evoy, S.; Heflin, J. R. *Introduction to nanoscale science and technology*, Springer: New York **2004**, p 1.
40. Balzani, V.; Credi, A.; Venturi, M. *Molecular devices and machines*, WILEY-VCH: Weinheim **2003**, p 4.
41. Seeman, N. C. *Nature* **2003**, *421* (6921), 427-431.
42. Scott, A. *Chemistry World* **2004**, *1* (11), November.
43. Benenson, Y.; Gil, B.; Ben-Dor, U.; Adar, R.; Shapiro, E. *Nature* **2004**, *429* (6990), 423-429.
44. Yan, H.; Park, S. H.; Finkelstein, G.; Reif, J. H.; LaBean, T. H. *Science* **2003**, *301* (5641), 1882-1884.
45. Liu, H.; Chen, Y.; He, Y.; Ribbe, A. E.; Mao, C. *Angew. Chem. Int. Ed.* **2006**, *45* (12), 1942-1945.
46. Notman, N. *Chemistry World* **2010**, *7* (1), 36-37.
47. Zheng, J.; Birktoft, J. J.; Chen, Y.; Wang, T.; Sha, R.; Constantinou, P. E.; Ginell, S. L.; Mao, C.; Seeman, N. C. *Nature* **2009**, *461* (3), 74-77.
48. Gross, M. *Chemistry World* **2009**, *6* (4), 50-53.
49. Fischler, M.; Sologubenko, A.; Mayer, J.; Clever, G.; Burley, G.; Gierlich, J.; Carell, T.; Simon, U. *Chem. Comm.* **2008**, (2), 169-171.
50. Ackermann, D.; L. Schmid, T.; Hannam, J. S.; Purohit, C. S.; Heckel, A.; Famulok, M. *Nature nanotechnology* **2010**, *5* (6), 436-442.

-
51. Chapman, V. *Chemical Science* **2008**, 5 (2), 12.
 52. Andersen, E. S.; Dong, M.; Nielsen, M. M.; Jahn, K.; Subramani, R.; Mamdouh, W.; Golas, M. M.; Sander, B.; Stark, H.; Oliveira, C. L. P.; Pedersen, J. S.; Birkedal, V.; Besenbacher, F.; Gothelf, K. V.; Kjems, J. *Nature* **2009**, 459 (7243), 73-77.
 53. Broadwidth, P. *Chemistry World* **2009**, 6 (6), 27.
 54. Thaxton, C. S.; Elghanian, R.; Thomas, A. D.; Stoeva, S. I.; Lee, J.-S.; Smith, N. D.; Schaeffer, A. J.; Klocker, H.; Horninger, W.; Bartsch, G.; Mirkin, C. A. *Proc. Natl. Acad. Sci. U. S. A.* **2009**, 106 (44), 18437-18442.
 55. Stoeva, S. I.; Lee, J.-S.; Smith, J. E.; Rosen, S. T.; Mirkin, C. A. *J. Am. Chem. Soc.* **2006**, 128 (26), 8378-8379.
 56. Lo, P. K.; Karam, P.; Aldaye, F. A.; McLaughlin, C. K.; Hamblin, G. D.; Cosa, G.; Sleiman, H. F. *Nature Chem.* **2010**, 2 (4), 319-328.
 57. Sealy, C. *Nano today* **2010**, 5 (3), 161.
 58. Urquhart, J. *Chemistry World* **2010**, 7 (4), 27.
 59. Drabkin, D. L. *Selected landmarks in the history of porphyrins and their biologically functional derivatives*. In *The porphyrins*, Dolphin, D. Ed, Academic Press: New York **1978**, Vol. 1, p 32-33.
 60. Kim, J. B.; Adler, A. D.; Longo, F. R. *Synthesis of porphyrins from monopyrroles*. In *The porphyrins*, Dolphin, D. Ed, Academic Press: New York **1978**, Vol. 1, p 85-87.
 61. Bouamaied, I. *DNA as supramolecular scaffold for porphyrin arrays*, PhD thesis, University of Basel: Basel **2007**, p 21-59.
 62. Huang, X.; Nakanishi, K.; Berova, N. *Chirality* **2000**, 12 (4), 237-255.
 63. Clayden, J.; Greeves, N.; Warren, S.; Wothers, P. *Organic chemistry*, Oxford University Press: Oxford **2005**, p 1177-1180.
 64. Fleischer, E. *Advan. Inorg. Chem. Radiochem.* **1970**, 3 (3), 105-112.
 65. Berezin, B. D. *Coordination compounds of porphyrins and phthalocyanines*, John Wiley: **1981**, p 23-26.
 66. Buchler, J. W. *Synthesis and properties of metalloporphyrins*. In *The porphyrins*, Dolphin, D. Ed, Academic Press: New York **1978**, Vol. 1, p 390-404.

67. Harvey, P. D. *Recent advances in free and metalated multiporphyrin assemblies and arrays; a photophysical behaviour and energy transfer perspective*. In *The porphyrin handbook*, 1st ed.; Kadish, K. M.; Smith, K. M.; Guilard, R. Eds, Academic Press: Netherlands **2003**, Vol. 18, p 65-68.
68. Smith, K. M. *Porphyrins and metalloporphyrins*, Elsevier scientific publishing: Amsterdam **1975**, p 9-11.
69. Hopf, F. R.; Whitten, D. G. *Photochemistry of porphyrins and metalloporphyrins*. In *Porphyrins and metalloporphyrins*, Smith, K. M. Ed, Elsevier Scientific Publishing: Amsterdam **1975**, p 687.
70. Beer, P. D.; Gale, P. A.; Smith, D. K. *Supramolecular chemistry*, Oxford University Press: New York **1999**, p 1-4.
71. Cram, D. J.; Kaneda, T.; Helgeson, R. C.; Lein, G. M. *J. Am. Chem. Soc.* **1979**, *101* (22), 6752-6754.
72. Behr, J.-P.; Lehn, J.-M.; Vierling, P. *J. Chem. Soc., Chem. Commun.* **1976**, (16), 621-623.
73. Pedersen, C. J. *J. Am. Chem. Soc.* **1967**, *89* (26), 7017-7036.
74. Beer, P. D.; Gale, P. A.; Smith, D. K. *Supramolecular chemistry*, Oxford University Press: New York **1999**, p 19-26.
75. Brown, A.; Mullen, K. M.; Ryu, J.; Chmielewski, M. J.; Santos, S. r. M.; Felix, V.; Thompson, A. L.; Warren, J. E.; Pascu, S. I.; Beer, P. D. *J. Am. Chem. Soc.* **2009**, *131* (13), 4937-4951.
76. Hiscock, J. R.; Caltagirone, C.; Light, M. E.; Hursthouse, M. B.; Gale, P. A. *Org. Biomol. Chem.* **2009**, *7* (9), 1781-1783.
77. Smith, E. E.; McClean, J. N.; Cooke, L. A.; Duprey, J.-L.; McCourt, M.; Fabani, M. M.; Tucker, J. H. R.; Vyle, J. S. *Tetrahedron Lett.* **2007**, *48* (37), 6569-6572.
78. Anderson, S.; Anderson, H. L.; Bashall, A.; McPartlin, M.; Sanders, J. K. M. *Angew. Chem. Int. Ed.* **1995**, *34* (10), 1045-1129.
79. Stulz, E.; Scott, S. M.; Ng, Y.-F.; Bond, A. D.; Teat, S. J.; Darling, S. L.; Feeder, N.; Sanders, J. K. M. *Inorg. Chem.* **2003**, *42* (20), 6564-6574.
80. Yokoyama, A.; Kojima, T.; Ohkubo, K.; Fukuzumi, S. *Chem. Comm.* **2007**, (39), 3997-3999.

81. Cormode, D. P.; Davis, J. J.; Beer, P. D. *J. Inorg. Organomet. Polym.* **2007**, *18* (1), 32-40.
82. Alexandre S. Boutorine; Daniel Brault; Masashi Takasugi; Olavio Delgado; Hélène, C. *J. Am. Chem. Soc.* **1996**, *118* (40), 9469-9476.
83. Mestre, B.; Jakobs, A.; Pratviel, G.; Meunier, B. *Biochemistry (Mosc).* **1996**, *35* (28), 9140-9149.
84. Schuberta, A.; Klütscha, T.; Cech, D. *Nucleosides, Nucleotides and Nucleic acids* **1997**, *16* (3), 277-289.
85. Balaz, M.; Li, B. C.; Steinkruger, J. D.; Ellestad, G. A.; Nakanishi, K.; Berova, N. *Org. Biomol. Chem.* **2006**, *4* (10), 1865-1867.
86. Endo, M.; Shiroyama, T.; Fujitsuka, M.; Majima, T. *J. Org. Chem.* **2005**, *70* (19), 7468-7472.
87. Endo, M.; Seeman, N. C.; Majima, T. *Angew. Chem. Int. Ed.* **2005**, *44* (37), 6074-6077.
88. Börjesson, K.; Tumpene, J.; Ljungdahl, T.; Wilhelmsson, L. M.; Nordén, B.; Brown, T.; Mårtensson, J.; Albinsson, B. *J. Am. Chem. Soc.* **2009**, *131* (8), 2831-2839.
89. Bouamaied, I.; Stulz, E. *Synlett* **2004**, *9*, 1579-1583.
90. Bouamaied, I.; Stulz, E. *Chimia* **2005**, *59* (3), 101-104.
91. Clayden, J.; Greeves, N.; Warren, S.; Wothers, P. *Organic chemistry*, Oxford University Press: New York **2001**, p 1177-1180.
92. Ethirajan, M.; Chen, Y.; Joshi, P.; Pandey, R. K. *Chem. Soc. Rev.* **2011**, *40* (1), 340-362.
93. Nierkens, S.; Brok, M. H. d.; Roelofsen, T.; Wagenaars, J. A. L.; Figdor, C. G.; Ruers, T. J.; Adema, G. J. *PLoS One* *4* (12), e8368.
94. Lodish, H.; Berk, A.; Matsudaira, P.; Kaiser, C. A.; Krieger, M.; Scott, M. P.; Zipursky, S. L.; Darnell, J. *Molecular cell biology*, 5th ed., W. H. Freeman and Company: New York **2004**, p 246.
95. Bouamaied, I. *DNA as supramolecular scaffold for porphyrin arrays*, PhD thesis, University of Basel: Basel **2007**, p 59-127.
96. Bouamaied, I. *DNA as supramolecular scaffold for porphyrin arrays*, PhD thesis, University of Basel: Basel **2007**, p 147-179.

-
97. Bouamaied, I.; Fendt, L.-A.; Wiesner, M.; Häussinger, D.; Amiot, N.; Thöni, S.; Stulz, E. *Pure Appl. Chem.* **2006**, *78* (11), 2003–2014.
98. Shono, T. K., S.; Sawamura, M.; Soejima, T. *J. Org. Chem.* **1988**, *53* (4), 907-910.
99. Zhang, Y.; Jiao, J.; Flowers, R. A. *J. Org. Chem.* **2006**, *71* (12), 4516-4520.
100. Finkelstein, H. *Berichte der Deutschen Chemischen Gesellschaft* **1910**, *43* (2), 1528-1532.
101. Twyman, L. J.; Sanders, J. K. M. *Tetrahedron Lett.* **1999**, *40* (36), 6681-6684.
102. Brown, T. *Nucleic acids primer*, in press.
103. Pearson, W. H.; Berry, D. A.; Stoy, P.; Jung, K.-Y.; Sercel, A. D. *J. Org. Chem.* **2005**, *70* (18), 7114-7122.
104. Berry&Associates. *Fluorous affinity purification of oligonucleotides user guide*, p 1-7.
105. GE-Healthcare. *Illustra NAP-5 columns protocol*, p 6.
106. Scheer, H.; Inhoffen, H. H. *Hydroporphyrins: reactivity, spectroscopy, and hydroporphyrin analogues*. In *The porphyrins*, Dolphin, D. Ed, Academic Press: New York **1978**, Vol. 2, p 62.
107. Banu, B. S.; Ishaq, M.; Danadevi, K.; Padmavathi, P.; Ahuja, Y. R. *Food Chem. Toxicol.* **2004**, *42* (12), 1931-1936.
108. Tkeshelashvili, L. K.; McBride, T.; Spence, K.; Loeb, L. A. *J. Biol. Chem.* **1991**, *266* (10), 6401-6406.
109. Bales, B. C.; Kodama, T.; Weledji, Y. N.; Pitié, M.; Meunier, B.; Greenberg, M. M. *Nucleic Acids Res.* **2005**, *33* (16), 5371-5379.
110. Fortner, A.; Wang, S.; Darbha, G. K.; Ray, A.; Yu, H.; Ray, P. C.; Kalluru, R. R.; Kim, C. K.; Rai, V.; Singh, J. P. *Chem. Phys. Lett.* **2007**, *434* (1-3), 127-132.
111. Atkins, P. W. *The elements of physical chemistry*, 2nd ed., Oxford University Press: Bath **1996**, p 411-414.
112. Atkins, P. W. *Physical chemistry*, 6th ed., Oxford University Press: New York **1998**, p 6.
113. Blackburn, G. M.; Gait, M. J.; Loakes, D.; Williams, D. M. *Nucleic acids in chemistry and biology*, 3rd ed., RSC Publishing: Cambridge **2006**, p 19.

114. Bouamaied, I. *DNA as supramolecular scaffold for porphyrins arrays*, PhD thesis, University of Basel: Basel **2007**, p 109-119.
115. Nguyen, T. *Synthesis of bis(thiosemicarbazone) complexes with fluorescent marker and for peptide bond formation*, Master thesis, University of Oxford: Oxford **2006**, p 4.
116. Scheer, H.; Inhoffen, H. H. *Hydroporphyrins: reactivity, spectroscopy, and hydroporphyrin analogues*. In *The porphyrins*, Dolphin, D. Ed, Academic Press: New York **1978**, Vol. 2, p 68.
117. Becker, R. S.; Kasha, M. *J. Am. Chem. Soc.* **1955**, 77 (13), 3669-3670.
118. Lakowicz, J. R. *Principles of fluorescence spectroscopy*, 3rd ed., Springer: New York **2006**, p 6.
119. Santalucia, J. J.-R. *Proc. Natl. Acad. Sci. USA* **1998**, 95 (4), 1460-1465.
120. Wada, T.; Umemoto, T. *Tetrahedron Lett.* **2005**, 46 (24), 4251-4253.
121. Davis, T. M.; McFail-Isom, L.; Keane, E.; Williams, L. D. *Biochemistry (Wash.)* **1998**, 37 (19), 6975-6978.
122. Yang, J. T. *Remembrance of things past: A career in chiroptical research*. In *Circular dichroism and the conformational analysis of biomolecules* Fasman, G. D. Ed, 1996 Plenum Press: New York **1996**, p 3.
123. Rodger, A.; Nordén, B. *Circular dichroism and linear dichroism*, Oxford University Press: Oxford **1997**, p 3.
124. Bloomfield, V. A.; Crothers, D. M.; Jr. Tinoco, I.; with contributions from Hearst, J. E.; Wemmer, D. E.; Kollman, P. A.; Turner, D. H. *Nucleic acids: Structures, properties, and functions*, University Science Books: Sausalito **2000**, p 188.
125. Berova, N.; Nakanishi, K. *Exciton chirality method: Principles and applications*. In *Circular dichroism principles and applications*, 2nd ed.; Berova, N.; Nakanishi, K.; Woody, R. W. Eds, Wiley-VCH: Canada **2000**, p 353.
126. Cai, G.; Bozhkova, N.; Odingo, J.; Berova, N.; Nakanishi, K. *J. Am. Chem. Soc.* **1993**, 115 (16), 7192-7198.
127. Bouamaied, I.; Fendt, L.-A.; Häussinger, D.; Wiesner, M.; Thöni, S.; Amiot, N.; Stulz, E. *Nucleosides, Nucleotides and Nucleic Acids* **2007**, 26 (10-12), 1533-1538.
128. McMillin, D. R.; Shelton, A. H.; Bejune, S. A.; Fanwick, P. E.; Wall, R. K. *Coord. Chem. Rev.* **2005**, 249 (13-14), 1451-1459.

129. Bejune, S. A.; Shelton, A. H.; McMillin, D. R. *Inorg. Chem* **2003**, *42* (25), 8465-8475.
130. Pasternack, R. F.; Ewen, S.; Rao, A.; Meyer, A. S.; Freedman, M. A.; Collings, P. J.; Frey, S. L.; Ranen, M. C.; de Paula, J. C. *Inorg. Chim. Acta* **2001**, *317* (1-2), 59-71.
131. Lee, S.; Jeon, S. H.; Kim, B.-J.; Han, S. W.; Jang, H. G.; Kim, S. K. *Biophys. Chem.* **2001**, *92* (1-2), 35-45.
132. Balaz, M.; Bitsch-Jensen, K.; Mammana, A.; Ellestad, G. A.; Nakanishi, K.; Berova, N. *Pure Appl. Chem.* **2007**, *79* (4), 801-809.
133. Endo, M.; Fujitsuka, M.; Majima, T. *Tetrahedron* **2008**, *64* (8), 1839-1846.
134. Bandy, T. J. *University of Southampton*, publication in preparation.
135. Ferancová, A.; Rengaraj, S.; Kim, Y.; Labuda, J.; Sillanpää, M. *Biosens. Bioelectron.* **2010**, *26* (2), 314-320.
136. Goodsell, D. S. *Oncologist* **2001**, *6* (3), 298-299.
137. Britt, A. B. *Photosynth. Res.* **2004**, *81* (2), 105-112.
138. Ravanat, J.-L.; Douki, T.; Cadet, J. *J. Photochem. Photobiol., B* **2001**, *63* (1-3), 88-102.
139. Ziegler, A.; Leffell, D. J.; Kunala, S.; Sharma, H. W.; Gailani, M.; Simon, J. A.; Halperin, A. J.; Baden, H. P.; Shapiro, P. E.; Bale, A. E.; Brash, D. E. *Proc. Natl. Acad. Sci. U. S. A.* **1993**, *90* (9), 4216-4220.
140. Yang, S.-J.; Hao, W.; Ekuni, A.; Fujiwara, Y.; Ono, T.; Munakata, N.; Hayatsu, H.; Negishi, K. *Mutat. Res.* **1999**, *438* (1), 53-62.
141. Westermeier, R. *Electrophoresis in practice*, 4th ed., WILEY-VCH: Damstadt **2005**, p 24-34.
142. Stephenson, A. W. I. *Supramolecular helical arrangement of porphyrins along DNA*, PhD thesis, Massey University: Palmerston North **2010**, p 76-105.
143. Stulz, E. *University of Southampton*, personal communication.
144. Kochelaev, B. I.; Yablokov, Y. V. *The beginning of paramagnetic resonance*, World Scientific Publishing: Singapore **1995**, p 3.
145. Rieger, P. H. *Electron spin resonance: Analysis and interpretation*, RSC Publishing: **2007**, p 1-2.

-
146. Shriver, D. F.; Atkins, P. W. *Inorganic chemistry*, 3rd ed., Oxford University Press: Belgium **1999**, p 457-459.
147. Weber, R. T.; Jiang, J.; Barr, D. P. *Bruker's EMX user's manual version 2.0*, **1998**, p 2-1 - 2-9.
148. Goodman, B. A.; Raynor, J. B. *Electron spin resonance of transition metal complexes*. In *Advances in inorganic chemistry and radiochemistry*, Emeléus, H. J.; Sharpe, A. G. Eds, Academic Press: New York **1970**, Vol. 13, p 137-149.
149. Petrakis, L. *J. Chem. Educ.* **1967**, 44 (8), 432-436.
150. Goodman, B. A. *Guangxi University*, personal communication.
151. Fleischer, E. B. *Acc. Chem. Res.* **1970**, 3 (3), 105-112.
152. Collison, D. *EPSRC EPR national service centre*, collaboration.
153. Goodman, B. A.; Raynor, J. B. *Electron spin resonance of transition metal complexes*. In *Advances in inorganic chemistry and radiochemistry*, Emeléus, H. J.; Sharpe, A. G. Eds, Academic Press: New York **1970**, Vol. 13, p 314-324.
154. Nguyen, T. *Synthesis of bis(thiosemicarbazone) complexes with fluorescent markers and for peptide bond formation*, Master thesis, University of Oxford: Oxford **2006**, p 30-38.
155. Eaton, S. S.; More, K. M.; Sawant, B. M.; Eaton, G. R. *J. Am. Chem. Soc.* **1983**, 105 (22), 6560-6567.
156. Blankenship, R. E. *Acc. Chem. Res.* **1981**, 14 (6), 163-170.
157. Tanaka, K.; Tengeiji, A.; Kato, T.; Toyama, N.; Shionoya, M. *Science* **2003**, 299 (5610), 1212-1213.
158. Nguyen, T. *Synthesis of bis(thiosemicarbazone) complexes with fluorescent markers and for peptide bond formation*, Master thesis, University of Oxford: Oxford **2006**, p 25-31.
159. Subczynski, W. K.; Pasenkiewicz-Gierula, M.; Antholine, W. E.; Hyde, J. S. *J. Am. Chem. Soc.* **1999**, 121 (16), 4054-4059
160. Edge, R. *EPSRC EPR national service centre*, collaboration.
161. Goodman, B. A.; Cheshire, M. V. *Nature New Biology* **1973**, 244 (135), 158-159.
162. Goodman, B. A.; Cheshire, M. V. *Eur. J. Soil Sci.* **1976**, 27 (3), 337-347.
163. Didenko, V. V. *BioTechniques* **2001**, 31 (5), 1106-1121.

-
164. Holden, S. J.; Uphoff, S.; Hohlbein, J.; Yadin, D.; Le Reste, L.; Britton, O. J.; Kapanidis, A. N. *Biophys. J.* **2010**, *99* (9), 3102-3111.
165. Burns, J. R.; Stulz, E. *University of Southampton*, manuscript in preparation.
166. Giese, B.; Carl, B.; Carl, T.; Carell, T.; Behrens, C.; Hennecke, U.; Schiemann, O.; Feresin, E. *Angew. Chem. Int. Ed.* **2004**, *43* (14), 1848-1851.
167. Goodman, B. A.; Green, H. L.; McPhail, D. B. *Geochim. Cosmochim. Acta* **1984**, *48* (10), 2143-2150.
168. Eaton, S. S.; Eaton, G. R.; Chang, C. K. *J. Am. Chem. Soc.* **1985**, *107* (11), 3177-3184.
169. Schiemann, O. *University of St. Andrews*, personal communication.
170. Kato, T. *Josai University*, personal communication.
171. Dougherty, G.; Pasternack, R. F. *Inorganic Chimica Acta* **1992**, *195* (1), 95-100.
172. Suzuki, T.; Maeda, Y.; Sakai, H.; Fujimoto, S.; Morita, Y. "*J. Biochem., Tokyo*" **1975**, *78* (3), 555-560.
173. Brown, A. *University of Oxford*, presentation of figure with kind permission.
174. Eaton, S. S.; Eaton, G. R. *Distance measurements by CW and pulsed EPR*. In *Biological magnetic resonance*, Berliner, L. J.; Eaton, S. S.; Eaton, G. R. Eds, Plenum Publishers: New York **2000**, Vol. 19, p 13-14.
175. Eaton, S. S.; Eaton, G. R. *Distance measurements by CW and pulsed EPR*. In *Biological magnetic resonance*, Berliner, L. J.; Eaton, S. S.; Eaton, G. R. Eds, Plenum Press: New York **2000**, Vol. 19, p 8.
176. Mammana, A.; Asakawa, T.; Bitsch-Jensen, K.; Wolfe, A.; Chaturantabut, S.; Otani, Y.; Li, X. X.; Li, Z. M.; Nakanishi, K.; Balaz, M.; Ellestad, G. A.; Berova, N. *Biorg. Med. Chem.* **2008**, *16* (13), 6544-6551.
177. McInnes, E. *EPSRC EPR national service centre*, collaboration.
178. Jovanovic, S. V.; Simic, M. G. *J. Phys. Chem. A* **1986**, *90* (5), 974-978.
179. Kittler, L.; Löbera, G.; Gollmick, F. A.; Berg, H. *Bioelectrochem. Bioenerg.* **1980**, *7* (3), 503-551.

-
180. Bohne, C.; Faulhaber, K.; Giese, B.; Häfner, A.; Hofmann, A.; Ihmels, H.; Köhler, A.-K.; Perä, S.; Schneider, F.; Sheepwash, M. A. L. *J. Am. Chem. Soc.* **2005**, *127* (1), 77-85.
181. Sevilla, M. D.; Becker, D.; Yan, M.; Summerfield, S. R. *J. Phys. Chem* **1991**, *95* (8), 3409-3415.
182. Böhm, F.; Edge, R.; Foley, S.; Lange, L.; Truscott, T. G. *J. Photochem. Photobiol. B: Biol.* **2001**, *65* (2-3), 177-183.
183. Rehorek, D. *Chem. Soc. Rev.* **1991**, *20* (3), 341-353.
184. Meggers, E.; Dussy, A.; Schäfer, T.; Giese, B. *Chem. Eur. J.* **2000**, *6* (3), 485-492.
185. Bonomo, R. P.; Cucinotta, V.; Giuffrida, A.; Impellizzeri, G.; Magri, A.; Pappalardo, G.; Rizzarelli, E.; Santoro, A. M.; Tabbi, G.; Vagliasindi, L. I. *Dalton Trans.* **2005**, (1), 150-158.
186. Sealy, R. C.; Hyde, J. S.; Felix, C. C.; Menon, I. A.; Prota, G.; Swartz, H. M.; Persad, S.; Haberman, H. F. *Proc. Natl. Acad. Sci. U. S. A.* **1982**, *79* (9), 2885-2889.
187. Bouamaied, I. *DNA as supramolecular scaffold for porphyrin arrays*, PhD thesis, University of Basel: Basel **2007**, p 132-142.
188. Woody, R. *Theory of circular dichroism of proteins*. In *Circular dichroism and the conformational analysis of biomolecules*, Fasman, G. D. Ed, Plenum Press: New York **1996**, p 28.
189. GlenResearch. *Poly-Pak purification user guide*, p 8-9.
190. Bouamaied, I. *DNA as supramolecular scaffold for porphyrin arrays*, PhD thesis, University of Basel: Basel **2007**, p 143-160.
191. Anderson, H. L.; Sanders, J. K. M. *J. Chem. Soc., Perkin Trans. 1.* **1995**, (18), 2223-2229.
192. Bouamaied, I.; Stulz, E. *Synlett* **2004**, (9), 1579-1583.
193. Bouamaied, I. *DNA as supramolecular scaffold for porphyrin arrays*, PhD thesis, University of Basel: Basel **2007**, p 161-172.
194. Bouamaied, I. *DNA as supramolecular scaffold for porphyrin arrays*, PhD thesis, University of Basel: Basel **2007**, p 173-181.
195. Bouamaied, I. *DNA as supramolecular scaffold for porphyrin arrays*, PhD thesis, University of Basel: Basel **2007**, p 183-189.

-
196. Rothmund, P.; Menotti, A. R. *J. Am. Chem. Soc.* **1948**, *70* (5), 1808-1812.
 197. Fleischer, E. B.; Miller, C. K.; Webb, L. *J. Am. Chem. Soc.* **1964**, *86* (12), 2342-2347.
 198. Bleicher, L. S.; Cosford, N. D. P.; Herbaut, A.; McCallum, J. S.; McDonald, I. A. *J. Org. Chem.* **1998**, *63* (4), 1109-1118.
 199. Classon, B.; Samuelsson, B. *Acta Chem. Scand. Ser. B.* **1985**, *39b*, 501-504.
 200. Gerrard, S. R. *Novel nucleotide analogues for forming stable DNA triple helices*, PhD thesis, University of Southampton: Southampton **2009**, p 158.

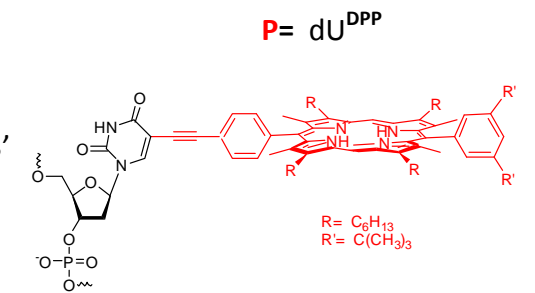
LIST OF OLIGONUCLEOTIDES INCLUDED IN THESIS

Non-modified oligonucleotides:

- ODN5 5'-GAG TAC GGA AAA ATA AAA ACT ACG ATG-3'
 ODN6 5'-GAG TAC GGA TAT ATA TAT ACT ACG ATG-3'
 ODN7 5'-GAG TAC GGT ATA CCG TAC TC-3'
 ODN10 5'-GAG TAC GGA AAA ATA AAA ACT ACG ATC-3'
 ODN11 5'-GAT CGT AGT TTT TAT TTT TCC GTA CTC-3'
 ODN12 5'-TAC GAT TCG AAA CTA GCT AGC-3'
 ODN19 5'-CAT CGT AGT ATA TAT ATA TCC GTA CTC -3'

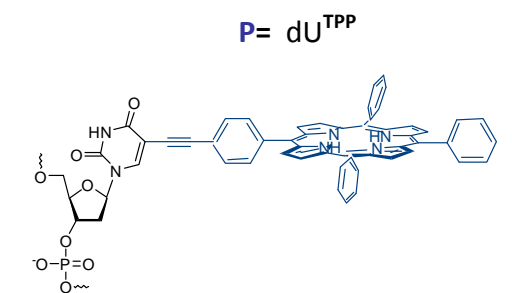
Diphenyl porphyrin-modified oligonucleotides

- ODN1 5'-CAT CGT AGT TTT **PAP** TTT TCC GTA CTC-3'
 ODN2 5'-CAT CGT AGT **APA PAP APA** TCC GTA CTC -3'
 ODN3 5'-GAG TAC **GGP APA** CCG TAC TC-3'
 ODN4 5'-TAC GAT TCG **TPT** CTA GCT AGC-3'
 ODN13 5'-GAG TAC GGA AAA **APA** AAA ACT ACG ATC-3'
 ODN14 5'-GAT CGT AGT TTT **PAP** TTT TCC GTA CTC-3'
 ODN15 5'-GCT AGC TAG **PPP** CGA ATC GTA-3'



Tetraphenyl porphyrin-modified oligonucleotides

- ODN8 5'-CAT CGT AGP **APA PAP APA PCC** GTA CTC-3'
 ODN9 5'-GAG TAC GGA **PAP APA PAP** ACT ACG ATG-3'
 ODN16 5'-CAT CGT AGT ATA **PAT** ATA TCC GTA CTC-3'
 ODN17 5'-CAT CGT AGT TTT **PAP** TTT TCC GTA CTC-3'
 ODN18 5'-CAT CGT AGT **ATP PAT** ATA TCC GTA CTC-3'



FAM-modified oligonucleotides

- ODN20 5'-**FAM**GAG TAC GGA TAT ATA TAT ACT ACG ATG-3'